



Provided by the author(s) and University of Galway in accordance with publisher policies. Please cite the published version when available.

Title	Anisotropy Resolved Multidimensional Emission Spectroscopy (ARMES) as a tool for biophysical analysis
Author(s)	Gordon, Fiona
Publication Date	2021-10
Publisher	NUI Galway
Item record	http://hdl.handle.net/10379/17028

Downloaded 2024-04-24T18:18:16Z

Some rights reserved. For more information, please see the item record link above.





National University of Ireland - Galway
College of Science, School of Chemistry
Nanoscale Biophotonics Laboratory

Anisotropy Resolved Multidimensional Emission Spectroscopy (ARMES) as a tool for biophysical analysis.

Thesis presented for the degree of PhD of the National University of
Ireland - Galway

by **Fiona Gordon, B. Sc.**

under the supervision of **Prof. Alan Ryder**

– **October 2021** –

ACKNOWLEDGEMENTS

I wish to thank Prof. Alan Ryder for giving me the opportunity to join his group and for guiding my research throughout my PhD studies.

I also wish to sincerely thank my earlier teachers; parents, grandparents, schoolteachers, and lecturers, who taught me the importance of learning and value of knowledge. I thank my family and friends who were there for me throughout my studies. Finally, I wish to thank my colleagues in the Nanoscale Biophotonics Group, and in the School of Chemistry NUIG for their continuous support throughout and for making the experience an enjoyable one!

This work has emanated from a research grant from Science Foundation Ireland co-funded under the European Regional Development Fund under Grant number (14/IA/2282, Advanced Analytics for Biological Therapeutic Manufacture, to AGR). I thank Science Foundation Ireland for providing this funding without which I could not have pursued this research.

This work is dedicated to my family, who taught me the value of persistence and determination, without them I would not have completed my Doctoral degree. I shall be ever grateful to them.

TABLE OF CONTENTS

Acknowledgements.....	i
Table of Contents.....	ii
Commonly used abbreviations	v
Abstract.....	vi
1 Introduction.....	1
1.1 Fluorescence Spectroscopy	1
1.1.1 Fundamental parameters: Quantum yield and Fluorescence lifetime	3
1.1.2 Fluorescence quenching	4
1.1.3 Fluorescence spectroscopy of proteins	6
1.1.4 Steady-state fluorescence spectroscopy	9
1.1.5 Time-resolved fluorescence spectroscopy	10
1.2 FRET	13
1.2.1 Types of FRET.....	15
1.2.2 Biochemical applications of FRET	16
1.2.3 Methods of measuring FRET	18
1.3 Anisotropy	20
1.4 Multi-Dimensional Fluorescence	23
1.4.1 MDF collection modes: TSFS and EEM	23
1.4.2 ARMES Methodology	25
1.4.3 Factors affecting MDF spectra.....	25
1.5 Chemometric methods.....	28
1.5.1 Background of multi-way analysis.....	28
1.5.2 MCR-ALS	29
1.5.3 PCA.....	31
1.5.4 PARAFAC	32
1.5.5 Tucker3 and Restricted Tucker3	35
1.6 ARMES as a tool for biophysical analysis.....	38

1.6.1	Biopharmaceuticals	38
1.6.2	Liposome Drug Delivery Systems (DDS).....	42
1.6.3	Project I: FRET Study	44
1.6.4	Project II: Protein-liposome interactions	44
1.7	Thesis outline	45
2	Materials & Methods	46
2.1	Materials	46
2.2	Instrumentation.....	49
2.3	Chemometric analysis and data pre-processing operations.....	51
2.4	Experimental system I: HSA-ANS study.....	57
2.4.1	Sample preparation.....	57
2.4.2	Data collection parameters.....	58
2.4.3	Data pre-processing for chemometric analysis	59
2.5	Experimental system II: Liposome Study	61
2.5.1	Sample preparation.....	61
2.5.2	Data collection parameters.....	62
2.5.3	Data pre-processing for chemometric analysis	63
3	Spectral analysis of the interaction between HSA and ANS.....	65
3.1	HSA-ANS model system.....	67
3.2	Determination of FRET parameters	70
3.3	UV-Vis analysis	73
3.4	Fluorescence MDF spectra.....	76
3.4.1	Aniso-t-EEMs and anisotropy analysis.....	77
3.4.2	PCA analysis of MDF spectra.....	80
3.5	Biochemical parameters	83
3.5.1	Jobs plot analysis	83
3.5.2	Stern-Volmer analysis.....	84
3.5.3	FRET efficiency calculation	88
3.6	Lifetime analysis	90
3.7	Conclusions	93
4	Chemometric modelling of the HSA-ANS interaction.....	95

4.1	Modelling of MDF spectra with FRET	96
4.2	Modelling of HSA-ANS interaction: Global emission	98
4.2.1	PARAFAC modelling of the HSA-ANS interaction	100
4.2.2	Tucker3 modelling of HSA-ANS interaction	106
4.3	Modelling of HSA-ANS interaction: Donor emission	111
4.4	Calculation of biochemical parameters using ARMES.....	116
4.4.1	Stern-Volmer analysis.....	116
4.4.2	Multivariate calculation of FRET efficiency.	119
4.5	Conclusions	121
5	Spectral analysis of the interaction between HSA and DMPC liposomes	123
5.1	Introduction	124
5.2	DLS analysis.....	127
5.3	Absorbance spectroscopy	135
5.4	2D fluorescence emission and anisotropy analysis	138
5.4.1	Dil-DiD lipophilic dye fluorescence	141
5.5	Lifetime analysis	143
5.6	Conclusions	147
6	Chemometric modelling of the interaction between HSA and DMPC liposomes	
	149	
6.1	Introduction	150
6.2	PCA analysis	151
6.3	PARAFAC modelling	155
6.3.1	PARAFAC models on buffer specific datasets.....	156
6.3.2	PARAFAC models on global datasets.....	161
6.3.3	Anisotropy analysis of PARAFAC components.....	163
6.3.4	Evaluation of PARAFAC scores.....	165
6.4	Conclusions	167
7	Conclusions.....	169
8	Appendix.....	175
	References.....	183
	Publications and research presentations	200

COMMONLY USED ABBREVIATIONS

ABC	Ammonium bicarbonate buffer
ANS	1-anilino-8-naphthalenesulfonate
ARMES	Anisotropy-resolved multi-dimensional emission spectroscopy
DLS	Dynamic light scattering
DMPC	1,2-dimyristoyl-sn-glycero-3-phosphocholine
EEM	Emission-excitation matrix
t-EEM	EEM collected in TSFS mode and converted to EEM layout
FRET	Förster resonance energy transfer
G	G-factor
HSA	Human serum albumin
I	Intensity
IFE	Inner filter effect
LOD	Limit of detection
MDF	Multidimensional fluorescence
PARAFAC	Parallel factor analysis
PBS	Phosphate buffered saline
PC	Principal component
PCA	Principal component analysis
Phe	Phenylalanine
QY	Quantum yield
<i>r</i>	Anisotropy
RSD	Relative standard deviation
SNR	Signal-to-noise ratio
τ	Lifetime
TCSPC	Time correlated single photon counting
TSFS	Total synchronous fluorescence spectroscopy
Tucker3	3-way Tucker analysis
Trp/W	Tryptophan
Tyr/Y	Tyrosine
UV-Vis	Ultraviolet-Visible spectroscopy

ABSTRACT

The development of analytical tools for the biophysical analysis of biological samples is an area of tremendous application and potential. In this work the use and efficacy of an analytical methodology, known as anisotropy resolved multi-dimensional emission spectroscopy (ARMES) [1, 2], as a tool for biophysical analysis is explored.

ARMES comprises of a 4-D measurement method used in combination with multi-way data analysis. The ARMES methodology is being developed with the aim of addressing some of the challenges surrounding the analysis of biological therapeutics. At present, many available methods used in biological therapeutic manufacture are either destructive, time-consuming, or alter the sample [3]. Protein analysis by intrinsic fluorescence is attractive as it is fast, sensitive, inexpensive and non-invasive, with good robustness, high sample throughput, ease of use and low cost required for use as a process analytical technology (PAT) tools [4]. Proteins are generally multi-fluorophore systems, with overlapping emission from the aromatic amino acids (Trp, Tyr and Phe) which makes multidimensional fluorescence spectroscopy (MDF) measurement techniques like excitation-emission matrix (EEM) and total synchronous fluorescence scan (TSFS) potentially beneficial [5-7]. These MDF methods can be further developed by coupling with factor based chemometric methods to resolve the individual fluorophore contributions of the intrinsic emission. In ARMES, an additional dimension of anisotropy (r) is collected, which is related to rotational speeds, hydrodynamic volumes, and thus molecular size, and adds further information to the MDF measurement. This ARMES methodology forms the foundation for this research [2, 8].

In the first project presented in this thesis work, the application of ARMES in the analysis of Förster resonance energy transfer (FRET) is investigated (**Chapter 3 & 4**) [9]. FRET is a widely used technique to study the structure and dynamics of biomolecular systems, and also causes the non-linear fluorescence response observed in multi-fluorophore proteins, so accurate FRET analysis is critical. Here, a model system of human serum albumin (HSA) as a FRET donor and 1,8-anilinonaphthalene sulfonate as a FRET acceptor was used. The results of this work found ARMES

enabled resolution of the fluorescence emission into its constituent fluorophore emission and facilitated a more accurate analysis of the interactions and photophysical processes occurring in the HSA-ANS system. This enabled a new way of calculating biophysical parameters including quenching constants and FRET efficiencies using the multi-dimensional emission of individual donor fluorophores, and a significant increase in the FRET efficiency values recovered using the ARMES method was observed. In addition, ARMES enabled the extraction of the emission arising from indirect excitation via FRET, which is of significance in understanding the effects of FRET on MDF spectra.

In the second project of my thesis research, the use of ARMES in investigating protein-liposome interactions is explored (**Chapter 5 & 6**). Studying the interaction between plasma proteins and liposomes is critical for many different scientific applications, particularly in their use as drug delivery systems (DDS) [10, 11], such as those used in COVID-19 vaccines [12]. Here, a model system of HSA and DMPC liposomes was used, and their interactions were monitored in three different aqueous environments: water (pH \sim 7.9), NH_4HCO_3 (ABC) (50 mM, pH \sim 7.8), and phosphate buffered saline (PBS) (10 mM, pH \sim 7.4). Interestingly, a dramatically different interaction mechanism was observed in each environment with HSA observed to penetrate the lipid bilayer in water and ABC, but not in the case of PBS. Here, ARMES enabled the resolution of fluorescence emission into interacting populations of HSA which had penetrated the lipid bilayer from populations of HSA which were surface bound or free in aqueous solution and provided an informative approach for monitoring protein-liposome interactions.

In conclusion, the application of ARMES methodology for biophysical analysis on two different molecular systems is demonstrated in this thesis work. ARMES facilitated a more detailed analysis of the photophysical of FRET, providing a new means of calculating biochemical parameters (FRET efficiencies and quenching constants) and provided a new way of assessing protein-liposome interactions using intrinsic protein emission. The studies show ARMES has tremendous potential as a tool of biophysical analysis of interacting molecular systems.

1 INTRODUCTION

The work presented in this thesis is quite interdisciplinary, the aim of this introductory chapter is to outline the key concepts and theories which form the cornerstones of research discussed in subsequent chapters. The analytical technology used in this thesis, anisotropy resolved multidimensional emission spectroscopy (ARMES), combines the use of fluorescence spectroscopy and chemometrics and these topics are explored in this introductory chapter. The relevance of the research is outlined, along with the two major projects used to explore and demonstrate the application of ARMES as a tool for biophysical analysis.

1.1 FLUORESCENCE SPECTROSCOPY

The term ‘luminescence’ was introduced by Eilhard Widemann in 1888 for all phenomena of light not solely caused by a rise in temperature (incandescence). There are various types of luminescence classified by their mode of excitation including; photoluminescence, chemiluminescence, bioluminescence, and electroluminescence [13]. ‘Photoluminescence’ in particular, refers to the emission of photons from excited electronic states following absorption of light, and can be formally divided into two categories: fluorescence and phosphorescence [4, 13].

The term ‘phosphorescence’ stems from the term ‘phosphor’ which has been used since the Middle Ages to describe materials which glow in the dark after exposure to light. On the other hand, the term ‘fluorescence’ was first introduced in the middle of the 19th century when Sir George G. Stokes, a native of Co. Sligo Ireland, observed that the mineral fluorspar exhibits fluorescence when illuminated under ultraviolet light. In his famous paper ‘On the refrangibility of light’ in 1852 [14], he demonstrated the phenomenon of emission of light followed absorption, and that the emission had longer wavelengths than the exciting light (red-shifted), which is now well-known as Stokes law. In his first paper Stokes called the phenomenon ‘true internal dispersion’

or ‘dispersive reflexion’ but later in his second paper coined the term ‘Fluorescence’ which is widely used today [15, 16].

‘Phosphorescence’, and ‘fluorescence’ can be separated based on the quantum mechanics of excited species, using this approach, fluorescence can be defined as photoluminescence where the radiative transition does not involve a change in spin multiplicity, and phosphorescence as photoluminescence where the radiative transition involves a change in spin multiplicity. This phenomenon was stated for the first time by Francis Perrin in 1929 [17].

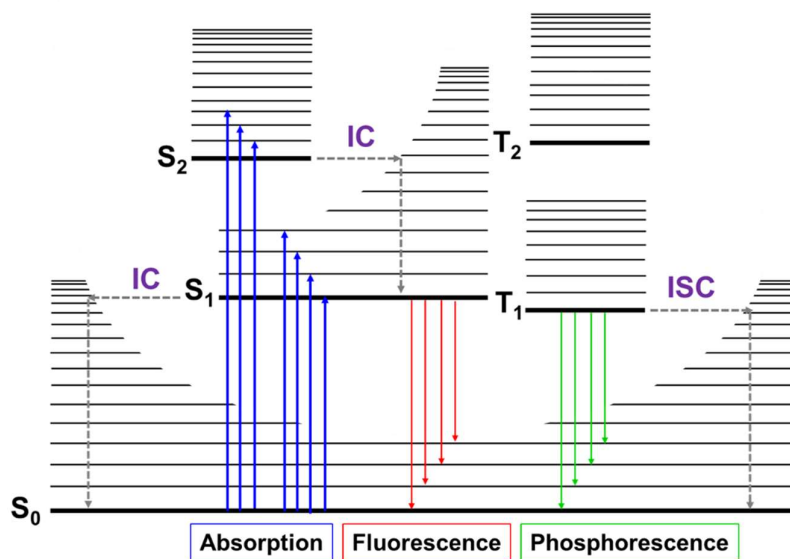


Figure 1.1: The Jablonski diagram showing the processes of internal conversion (IC) and intersystem crossing (ISC) that occur between the absorption and emission of light (fluorescence or phosphorescence) (Image adapted from Valeur, 2002 [18]).

The processes that occur between the absorption and emission of light are illustrated by the Jablonski diagram (**Figure 1.1**) [4, 18]. The singlet ground, first, and second electronic states are denoted by S_0 , S_1 , S_2 , respectively, at each of these electronic levels, fluorophores can exist in different vibrational and rotational energy levels. Absorbance refers to the transition from ground state to excited state, the absorption spectrum of a fluorophore is the result of all electronic, vibrational and rotational transitions [4, 18]. At room temperature, most molecules occupy the lowest vibrational level of the ground electronic state (S_0), but when a molecule is excited

with the appropriate energy it occupies an upper electronic state and can return to the ground electronic state (S_0) in several different ways.

First, the molecule will rapidly undergo internal conversion (IC) and electrons return to the lowest vibrational energy level of the excited state (S_n), continuing to the lowest energy excited electronic state (S_1) by dissipating part of the energy to the surrounding environment (Kasha's rule) [19], this step generally occurs on a time scale of 10^{-14} to 10^{-10} s and is followed by vibrational relaxation in S_1 , a process which takes 10^{-12} to 10^{-10} s [20]. Next, the molecule returns from the excited state S_1 to S_0 via a variety of competitive excited-state processes. Fluorescence is one such process and represents the transition to S_0 by the emission of a photon, fluorescent lifetimes have time scales of 10^{-10} to 10^{-7} s [18]. Other pathways of reaching the ground state include intersystem crossing (ISC) followed by emission (phosphorescence), dissipation of absorbed energy as heat (non-radiative process) and the release of energy to nearby molecules (collisional quenching and energy transfer, such as FRET) [20].

The timescales of these excited-state processes have important experimental consequences. The long lifetime of phosphorescence means the process is vulnerable to quenching, and for this reason phosphorescence is not usually observed in fluid solutions at room temperature because there are many deactivation processes that have faster rate constants, such as non-radiative decay and quenching processes. The fact fluorescence measurements occur on a shorter timescale than phosphorescence means they are less prone to deactivation process and, thus, can be made at a wider range of conditions than phosphorescence [21].

1.1.1 Fundamental parameters: Quantum yield and Fluorescence lifetime

The quantum yield (Φ) and fluorescence lifetime (τ) are two fundamental characteristics of a fluorophore. The quantum yield is a measurement of the efficiency of fluorescence emission relative to all possible pathways of relaxation, it gives the probability that an excited fluorophore will emit a photon. The quantum yield of a fluorophore is generally expressed by the ratio of the number of emitted photons to the number of photons absorbed (**Equation 1.1**).

Equation 1.1

$$\Phi = \frac{\textit{photons emitted}}{\textit{photons absorbed}} = \frac{\Gamma}{\Gamma + k_{nr}}$$

where Γ is the rate constant for fluorescence decay and k_{nr} is the rate of non-radiative decay to S_0 .

The fluorescence lifetime (τ) of a fluorophore is the average time a molecule remains in an excited state before photon emission occurs [4]. Few molecules emit at $t = \tau$, and a fluorophore can undergo processes during the excited state lifetime, such as conformational changes and interactions with other molecules that affect the fluorescence lifetime decay. The lifetime of a fluorophore can be described by **Equation 1.2**.

Equation 1.2

$$\tau = \frac{1}{\Gamma + k_{nr}}$$

where Γ is the rate constant for fluorescence decay and k_{nr} is the rate of non-radiative decay to S_0 .

The fluorescence lifetime (τ) is related to the quantum yield by **Equation 1.3**.

Equation 1.3

$$\tau = \Phi/k_r$$

1.1.2 Fluorescence quenching

The intensity of fluorescence can be decreased by a variety of processes, and such decreases in intensity are referred to as fluorescence quenching. There are two main types of fluorescence quenching: dynamic and static quenching (**Figure 1.2**) [4].

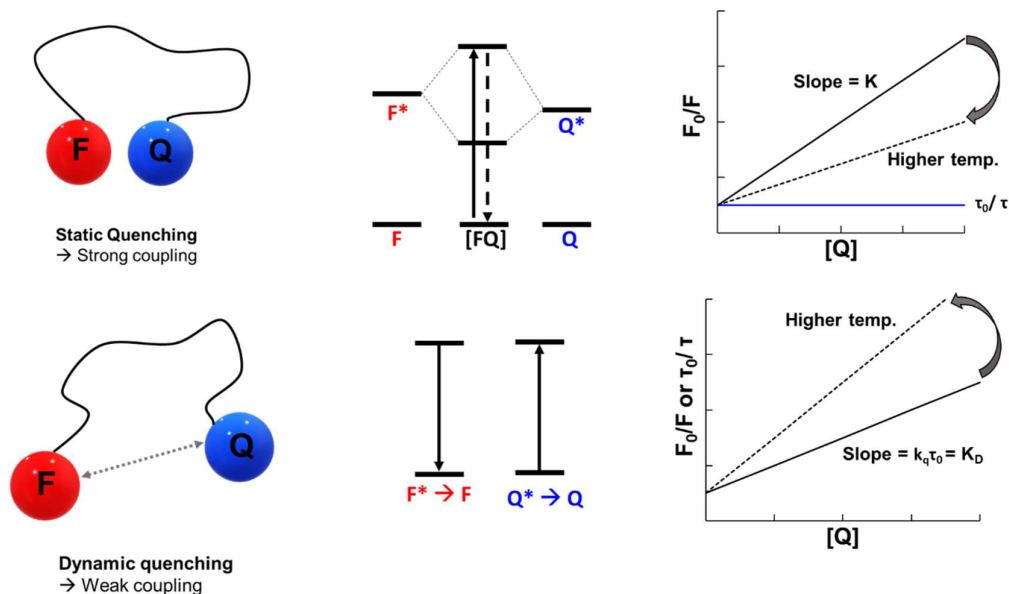


Figure 1.2: Static quenching mechanism (*top*) showing the decrease in quenching with an increase in temperature and the independence of fluorescence lifetime to the process and dynamic quenching mechanism (*bottom*) showing the increase in quenching with an increase in temperature, and the dependence of fluorescence lifetime to the process.

Dynamic (or collisional) quenching occurs when a fluorophore (F^*) in its excited state encounters another molecule in solution called a quencher (Q) and is deactivated. The fluorophore in this case returns to the ground state through a non-radiative transition ($F^* \rightarrow F$), without the emission of a photon. In dynamic quenching there is no chemical modification of the fluorophore [4, 18].

The Stern-Volmer plot or F_0/F plot (or alternatively τ_0/τ) is a widely used way to represent the sensitivity of the fluorophore to a quencher (**Equation 1.4**). For a quenching process involving dynamic quenching only a linear relationship is given by the Stern-Volmer plot.

Equation 1.4

$$\frac{F_0}{F} \text{ or } \frac{\tau_0}{\tau} = 1 + k_q \tau_0 [Q] = 1 + K_D [Q]$$

where F_0 and F is the absence (F_0) and presence (F) of the quencher, K_D is the Stern-Volmer quenching constant for dynamic quenching, k_q is the bimolecular quenching constant, τ_0 is the unquenched lifetime, and $[Q]$ is the quencher concentration.

Quenching of fluorescence can also occur via static quenching. In static quenching the fluorophore is quenched ($F^* \rightarrow F$) upon formation of a non-fluorescent complex (FQ) with another molecule. Static quenching does not rely on diffusion of molecular collisions in contrast of dynamic quenching [4, 22]. In cases of pure static quenching a change in fluorescence lifetime with increasing quencher concentration should not occur (**Equation 1.5**), thus a τ_0/τ versus $[Q]$ plot can be used to differentiate the two mechanisms of quenching ($\tau_0/\tau=1$ for static quenching, and $\tau_0/\tau= F_0/F$ for dynamic quenching). In addition, the dependence of the quenching process on temperature can be used to differentiate the two mechanisms of quenching. In dynamic quenching an increase in temperature will cause increased quenching and steeper slope in the Stern-Volmer plot due to an increase in the rate of collisions between the fluorophore and the quencher, whereas in static quenching decreased quenching and lesser slope will be observed as increasing temperature tends to disfavour the binding of fluorophore and the quencher (**Figure 1.2**).

Equation 1.5

$$\frac{F_0}{F} = 1 + K_S[Q], \text{ where } K_S = \frac{[F - Q]}{[F][Q]}$$

1.1.3 Fluorescence spectroscopy of proteins

Fluorescence spectroscopy is one of the most popular and useful techniques for the analysis of proteins. The growth in application and use of fluorescence spectroscopy as an analytical technique is due to the significant advantages it possesses [4]. It is a non-invasive technique that is both highly specific and exceptionally sensitive, allowing routine nanoscale detection of fluorescent substances such as proteins [23]. The study of proteins using fluorescence spectroscopy can be achieved in three ways: using intrinsic protein fluorescence, using extrinsic covalent probes, or using extrinsic noncovalent probes.

The intrinsic fluorescence of proteins, is a unique feature that facilitates direct analysis of proteins using fluorescence techniques (**Figure 1.3**) [4]. The three aromatic amino acids tryptophan (Trp, W), tyrosine (Tyr, Y) and Phenylalanine (Phe, F), are responsible for the intrinsic fluorescence of proteins [24-26]. Trp usually dominates the fluorescence emission of proteins where Trp is present, due to the fact it has a significantly higher quantum yield (QY) in both exposed and limited exposure

environments (QY \sim 0.20-0.30) and has a similar quantum yield to Tyr when it is completely buried (QY \sim 0.11) (**Table 1.1**). Tyr has significantly lower quantum yield (QY \sim 0.13) than Trp but is often used as an intrinsic fluorescent probe in Trp-lacking proteins (e.g., insulin). The spectral overlap of Tyr with Trp means FRET can occur to Trp residues in close enough proximity which further weakens Tyr fluorescence (see section 1.2) in Trp containing proteins. Phe emission is not usually observable in most proteins due to its low QY (QY \sim 0.02) and ability to participate in FRET to both Tyr and Trp (**Table 1.1**). Thus, close proximity of Phe to Tyr or Trp, and Tyr to Trp, can influence the quantum yield of Trp and Tyr through FRET [4].

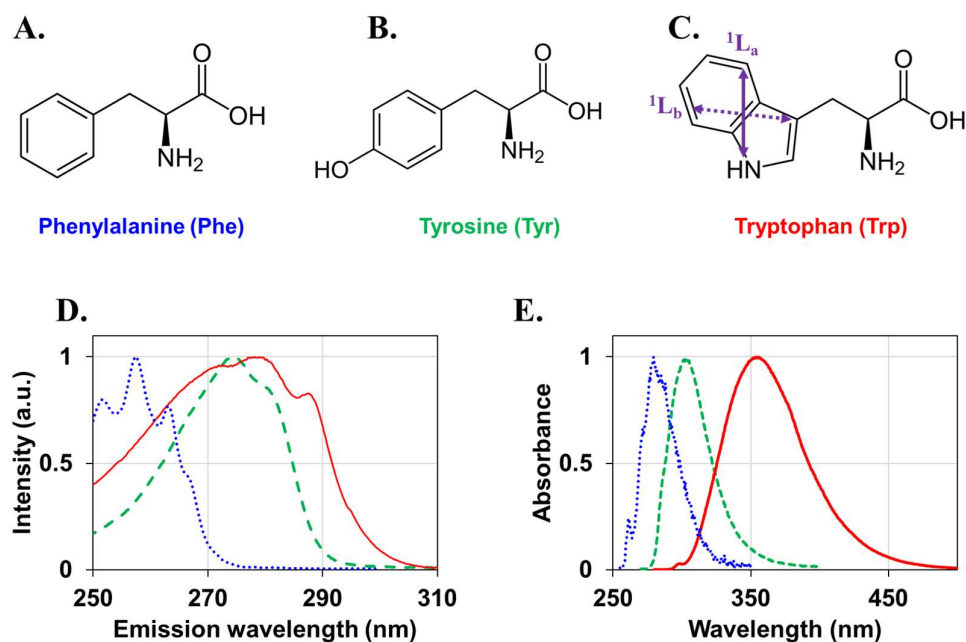


Figure 1.3: Aromatic amino acids Phenylalanine (Phe), Tyrosine (Tyr), and Tryptophan (Trp) (**A-C**) responsible for the intrinsic fluorescence of proteins. The normalised absorbance and fluorescence emission spectra are shown for L-Phe, L-Tyr and L-Trp, in **D** and **E** respectively (*spectra obtained from photochemcad.com*).

Table 1.1: Fluorescence properties of the three intrinsic fluorophores Phe, Tyr, and Trp in different environments; in a buried (hydrophobic) environment, where emission is blue-shifted, in an environment with limited exposure to water showing a red-shift in comparison to buried Trp, and in an environment with exposure to water showing a more significant red-shift in emission (measured at room temperature) [4, 22, 27].

Fluorophore		$\sim\lambda_{\text{ex}}$ (nm)	Absorptivity ($\text{M}^{-1} \text{cm}^{-1}$)	$\sim\lambda_{\text{em}}$ (nm)	τ (ns)	QY (Φ)
Phe		260	195	282	6.8	0.02
Tyr		275	1405	304	3.6	0.13
Trp	Buried	>295	5500	330	2.1	0.11
	Limited exposure			340	4.4	0.30
	Exposed to water			350	5.4	0.20

A valuable feature of intrinsic protein fluorescence is the high sensitivity of Trp to its local environment [4]. The emission spectra of Trp can change in response to changes in the local environment surrounding the indole ring, the emission maxima can shift from as low as $\lambda_{\text{em}} = 308$ nm in non-polar environment to $\lambda_{\text{em}} = 355$ nm in polar environments [28]. Another important characteristic of Trp emission is the existence of two excited states commonly referred to as $^1\text{L}_a$ and $^1\text{L}_b$ [4]. In a completely non-polar environment, the $^1\text{L}_b$ state ($\tau \sim 2$ ns, $\Phi \sim 0.1$) has the lowest energy and is the dominant emitter, whereas in more polar environments the $^1\text{L}_a$ becomes the major emitter ($\tau \sim 4\text{-}5$ ns, $\Phi \sim 0.3$) (**Table 1.1**). The observed difference between the $^1\text{L}_a$ and $^1\text{L}_b$ excited states, is thought to be due to the different dipole moments. The $^1\text{L}_a$ involves the nitrogen of the -NH group which has a stronger dipole moment and interacts with polar solvents via hydrogen bonding.

In addition, proteins can also be studied via extrinsic fluorescence [4]. A wide variety of fluorescent probes have been developed with different affinities and spectroscopic properties, and can either be covalently attached or attach to a protein via association (non-covalent) [4]. The ability to select the extrinsic probe properties, is a significant advantage over intrinsic fluorescence, as many unwanted effects (e.g., scatter contamination, low QY or poor signal-to-noise ratio) can be avoided [4, 29].

However, a significant disadvantage of using extrinsic fluorescence is that the modified proteins characteristics (e.g., binding affinity, hydrophobicity, protein-folding etc.) may differ to that of the native molecule [29].

1.1.4 Steady-state fluorescence spectroscopy

Steady-state spectra generally report on equilibrium conditions when all vibrational and solvent induced relaxation of the excited species are completed and the rate of excitation and emission are equal (**Figure 1.4/A**) [4, 18]. A steady-state spectrum can be viewed as the average of multiple time-dependent phenomena over the intensity decay of the sample [30], or in other words, the detector adds up all the photons emitted by the sample molecules, starting with the instance of excitation, and ending with the time when the last excited molecule has decayed to the ground state.

As steady-state measurements provide an intensity weighted average of the underlying decay processes, signals are often proportional, not to the most populated state, but to the state that emits the most light [30]. Time-resolved studies on the other hand, can provide information concerning the population distribution of molecular species in the excited state [4].

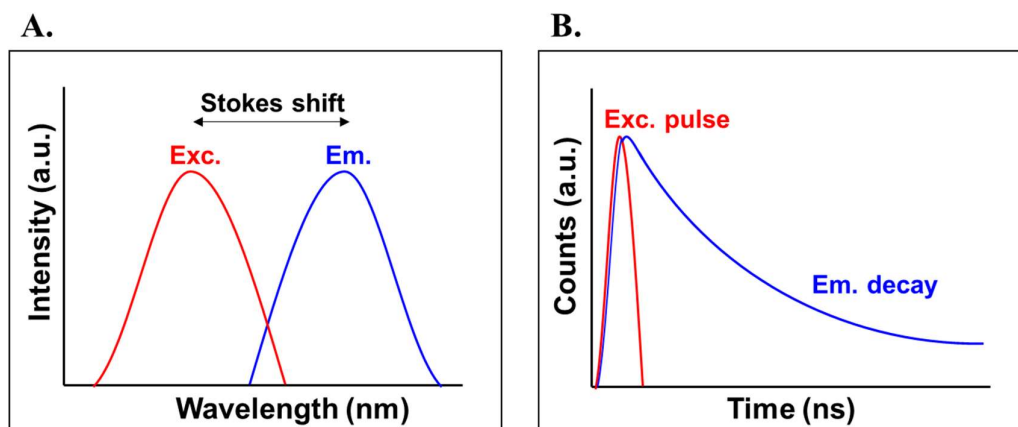


Figure 1.4: Example (A) Steady-state (Wavelength (nm) vs. Intensity (a.u.)) and (B) Time-resolved spectra (Time (ns) vs. Counts (a.u.)).

1.1.5 Time-resolved fluorescence spectroscopy

Time-resolved fluorescence spectroscopy monitors events that occur during the lifetime of the excited state (**Equation 1.7**) and examination of the time-dependence of fluorescence allows investigation of molecular conformation and dynamics of a molecular system in more detail (**Figure 1.4/B**) [31].

Time-resolution in time-resolved fluorescence spectroscopy can be achieved using two methods; time-domain and frequency-domain¹ methods [4]. Time-domain method (pulse-fluorimetry), relies on the use of a short pulsed excitation to excite the fluorophore [4]. The subsequent fluorescence is measured as a function of time (usually in nanoseconds) and the decay time (τ) is calculated from the slope of $\log I(t)$ versus t , or from the time at which the intensity decreases to $1/e$ of the intensity at $t=0$. In our studies, time-domain measurements are used, therefore, any reference to time-resolved measurements can be assumed to be made using time-domain measurements.

The decay law states if a population of fluorophores is excited instantaneously, the excited population (and fluorescence intensity) decays gradually to the ground state (S_0) as a function of time (**Equation 1.6**).

Equation 1.6

$$I(t) = I_0(e^{-\frac{t}{\tau}})$$

where I_0 is the intensity at time $t = 0$, t is the time after the absorption, and τ is the lifetime, (i.e., time when the fraction of the population of molecules in the excited state has decreased by a factor of $1/e$).

Depending on the sample, the lifetime may be described using a single exponential fit, however a single exponential is often not appropriate to describe samples with multiple different populations of excited fluorophores or when factors such as quenching, energy-transfer and molecular rotations/collisions influence the

¹ In frequency-domain method (phase-modulation), the sample is excited using a modulated source of light. When a fluorophore is excited in this manner the emission of the fluorophore responds with the same modulation frequency, but is phase shifted and demodulated. The phase-shift refers to where the lifetime of the fluorophore causes the delay of emission relative to the excitation, and the demodulation refers to the decreased peak-to-peak height of the emission relative to the modulated excitation. Both phase-shift and demodulation are dependent on the lifetime of the sample and therefore can be used to calculate fluorescent lifetimes of excited samples.

fluorescence decay. In such cases, the fluorescence lifetime may be described using a multi-exponential or non-exponential decay-law equation [4, 32].

One of the major advantages of using the fluorescence lifetime is the fact that it is an absolute measurement, unlike the steady state intensity, which is relative [33]. The fluorescence lifetime is an intrinsic molecular property and, within certain constraints, independent of concentration.

1.1.5.1 Time-Correlated Single Photon Counting (TCSPC)

Time correlated single photon counting (TCSPC) is the most popular technique for time-resolution of time domain measurements [4]. In TCSPC, the time between the excitation of the sample by a pulsed laser and the arrival of ideally each individual emitted photon to the detector, are measured using specialised electronics [34].

During a TCSPC measurement, the production of a light pulse “starts” the time measurement clock and a defined “stop” signal occurs when the single photon reaches the detector (**Figure 1.5/A**). The difference in time between the “start” and “stop” signal is outputted to a histogram; number of photons emitted (counts) versus time [4] (**Figure 1.5/B**). The excitation-emission process is repeated many times (~10,000 counts in peak channel).

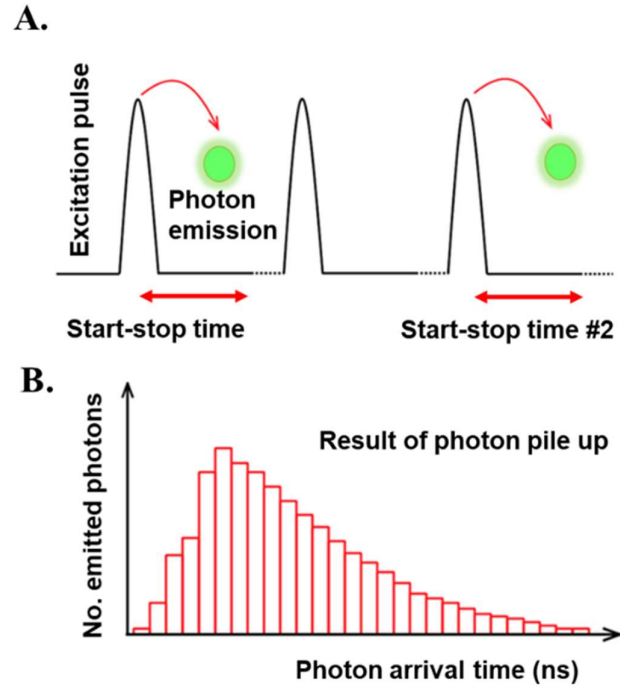


Figure 1.5: The principle of time-correlated single photon counting (TCSPC) **(A)** TCSPC records the start-stop time between the pulse of excitation and detected photon emitted **(B)** Histogram of the number of photons emitted vs. the arrival time at the detector (Image adapted from Fu *et al.* [35]).

1.2 FRET

Förster Resonance Energy Transfer (FRET) is a physical phenomenon first described over 50 years ago, and refers to distance-dependent, non-radiative energy transfer of from a donor molecule to a nearby acceptor molecule following excitation [36]. In order for FRET to occur a number of primary conditions need to be met; **1)** The donor and acceptor molecules must be in close proximity to one another (typically <10 nm), this permits the excitation energy to be transferred from a molecule to another by resonance [37, 38], **2)** The absorption or excitation spectrum of the acceptor must overlap with the fluorescence emission spectrum of the donor, and **3)** The donor and acceptor transition dipole orientations must be approximately parallel or close to parallel (**Figure 1.6**).

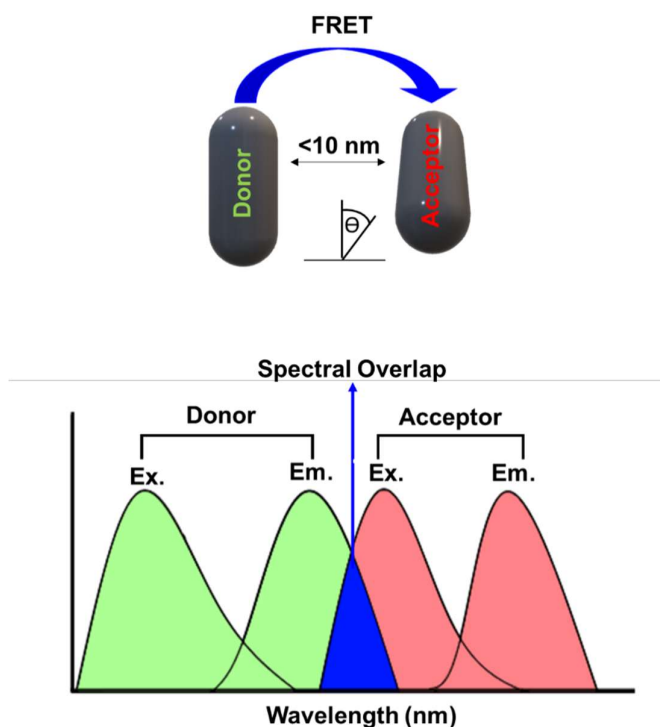


Figure 1.6: Schematic representation of the FRET process that between a donor and an acceptor molecule. The FRET efficiency highly depends on the distance between fluorophores, but also on the angle between dipoles and the extent of overlap (highlighted in blue) between the donor emission and acceptor excitation spectra (Image adapted from Broussard *et al.* [39]).

FRET is a competing pathway to fluorescence for the de-excitation of an excited fluorophore [40, 41]. Considering k_D^0 the fluorescence rate constant of an excited fluorophore in the absence of acceptor and k_{ET} the rate of energy transfer, the FRET efficiency (E) is simply defined by **Equation 1.7**.

Equation 1.7

$$E = \frac{k_{ET}}{k_D^0 + k_{ET}}$$

Förster, demonstrated that the rate of energy transfer (k_{ET}) depends on the inverse sixth-distance between donor and acceptor, which is now called Förster theory [40] (**Equation 1.8**).

Equation 1.8

$$k_{ET} = k_D^0 \left(\frac{R_0}{R}\right)^6 = \frac{1}{\tau_D^0} \left(\frac{R_0}{R}\right)^6$$

where τ_D^0 is the donor lifetime in the absence of acceptor, R the distance between the excited donor (D*) and the FRET acceptor molecule (A), and R_0 the Förster distance.

By combining these equations, a new expression called FRET efficiency (E) is obtained (**Equation 1.9**).

Equation 1.9

$$E = \frac{1}{1 + \left(\frac{R}{R_0}\right)^6}$$

As stated earlier, the degree to which FRET occurs is dependent on the distance, spectral overlap, and orientation of the FRET donor and acceptor dipoles. Both FRET efficiency (E) and the rate of energy transfer (k_{ET}) are strongly dependent on the distance (R) separating the donor/acceptor pairs [42] and rapidly decreases with increasing R as both are proportional to the inverse of its 6th power. Therefore, a short distance (<10 nm) is necessary to enable coupling of the oscillating dipole moments.

Secondly, the extent of spectral overlap between donor emission and acceptor absorbance ($J(\lambda)$) (**Equation 1.10**) also affects E and k_{ET} , where the greater the extent of overlap the higher the FRET Efficiency.

Equation 1.10

$$J(\lambda) = \int E_A(\lambda)F_D(\lambda)\lambda^4 d\lambda$$

where $F_D(\lambda)$ is the normalized donor fluorescence, and $E_A(\lambda)$ is the normalized acceptor excitation spectra.

Finally, the degree of alignment of these dipoles influences the FRET k_{ET} and E, the greater the alignment the FRET efficiency [37, 38]. The κ^2 coefficient is more complex and depends on the angle between the donor/acceptor dipoles, relating the FRET efficiency to their degree of alignment, FRET coupling is maximal if the dipoles are parallel to each other but is negligible for orthogonal orientations [18, 38]. The κ^2 coefficient is difficult to estimate as in almost every realistic case, the fluorophores never have a fixed orientation. For this reason, most studies consider κ^2 to be equal to 2/3, which is the average value obtained by integrating over all possible dipole angles [18, 38].

The spectral overlap and dipole orientation dependencies are contained in the Förster distance (R_0), which corresponds to the distance for which the FRET efficiency (E) of a fluorophore pair is equal to 50%. R_0 can be calculated from the spectroscopic and dipole orientation parameters of the donor and acceptor such as [18, 38] using **Equation 1.11**.

Equation 1.11

$$R_0 = [2.8 \times 10^{17} \times \kappa^2 \times \Phi_D^0 \times \epsilon_A \times J(\lambda)]^{1/6}$$

where ϵ_A is the maximum extinction coefficient of the acceptor, Φ_D^0 is the quantum yield of the donor in the absence of acceptor, κ^2 the dipole orientation factor, and $J(\lambda)$ the integral of the spectral overlap.

1.2.1 Types of FRET

There are two major types of FRET: **1)** hetero-FRET in which FRET occurs between spectroscopically different donor and acceptor molecules, and **2)** homo-FRET

in which the FRET donor and the acceptor molecules are spectroscopically identical [4]. Hetero-FRET is manifested spectroscopically in many ways including an increase in FRET acceptor intensity via indirect excitation via FRET, a decrease FRET donor intensity by quenching via FRET. An increase in FRET donor anisotropy and lifetime and a decrease in FRET acceptor anisotropy due to depolarisation via FRET [4, 18].

Homo-FRET, on the other hand, does not lead to a reduction in donor fluorescence intensity or lifetime, because the donor excited state population is not quenched during the act of energy transfer [43]. Home-FRET is solely manifested in a decrease in the fluorescence anisotropy of the donor [4, 44]. Despite the obvious advantages of Homo-FRET (i.e., requires a single fluorophore and no extrinsic labelling), the use of homo-FRET is more restricted than that of hetero-FRET, as the extent of depolarization due to homo-FRET is much more complex than that of quenching due to hetero-FRET. In homo-FRET processes back-transfer can occur to the directly excited donor, or any donor, which can result in a large number of transfer steps, and, if rotation and FRET occur in the same timescale, the two phenomena are coupled, which complicates quantitative data analysis [43].

1.2.2 Biochemical applications of FRET

FRET has widespread applications in the study of bimolecular systems (**Table 1.2**) [45-47]. It is powerful method in the investigation of molecular structures and is often referred to as a ‘spectroscopic ruler’, due to the nanoscale distance dependency of the process. If the R_0 value is known for a given FRET pair, the measurement of the FRET efficiency enables using **Equation 1.9**, to calculate the distance R separating both fluorophores [48].

There are numerous different biochemical applications of FRET, a few of which are introduced in this section. One application which is particularly relevant to my thesis research is the use of FRET in: (i) protein analysis, FRET is commonly used in structural analysis of proteins and can provide information such as distances between domains in a protein which enables the characterisation of protein structure and can allow detection of protein unfolding and/or aggregation [4]. In addition, FRET can also be used in protein analysis to detect and track interactions between proteins [49-

51] and has been used *in vivo* to detect both location and interactions of proteins including integrins and membrane proteins [52].

There are numerous other applications of FRET in biochemical analysis including: (ii) the investigation of membrane properties (e.g. membrane fluidity, location of membrane proteins and monitoring of interactions) [43, 53], (iii) the study of signalling pathways [4, 54, 55] (such as the well-known example of this application is the characterisation of G-protein coupled receptor activation and subsequent signalling mechanism) [56], (iv) in the creation of biosensors (FRET-based probes) which can detect the presence of various molecules, where binding, structural change or a change in environment can result in switching the FRET process on/off [4, 57, 58] or (v) In kinetic studies of biochemical reaction mechanisms such as the kinetics of a FRET dye movements or the kinetics of enzyme-receptor binding [59, 60]. This is not an extensive list of the biochemical applications of FRET, but rather a list of examples to demonstrate the widespread use of FRET in biochemical studies.

Table 1.2: Examples of biochemical applications of FRET.

	Application	Examples
Proteins studies	Structural analysis of proteins (e.g., characterisation of protein structure and detection of proteins in native, unfolded, and aggregated forms) and analysis of protein interactions.	[49-52]
Membranes studies	Analysis of membrane properties, lipid-protein, and protein-protein interactions in the membrane.	[43, 53, 61]
Biosensor applications	Detection of specific molecules by FRET on/off switch, detection of environmental change (pH, hypoxia, membrane potential) by specifically designed FRET chemosensory probe.	[57, 58]
Signalling pathways	Characterisation of receptor activation and subsequent signalling mechanism.	[4, 54-56]
Kinetic studies	Determination of the kinetics of biochemical reaction mechanisms.	[59, 60]

1.2.3 Methods of measuring FRET

There are several ways of measuring the FRET efficiency by monitoring changes in the fluorescence emitted by the donor or the acceptor molecule [4, 18]. Molecular systems in which FRET occurs are commonly studied via 2D (wavelength vs. intensity) steady-state or lifetime spectroscopic measurements. Parameters, such as FRET efficiency, are conventionally calculated using 2D measurements which utilise the quenching of donor fluorescence intensity, enhancement in acceptor fluorescence intensity (steady-state study) and decrease in donor lifetime (time-resolved study), an increase or decrease in anisotropy of the donor or acceptor, respectively. FRET is also often studied using fluorescence microscopy approaches, where a change in the rate of donor/acceptor photobleaching or a change in FRET donor/acceptor lifetimes (Fluorescence-lifetime imaging microscopy (FLIM)) can be used in the calculation of FRET parameters [4].

Although useful information can be extracted using conventional 2-D spectral measurements, to resolve contributing fluorophores and study the individual fluorophore populations in more detail, multi-dimensional approaches are required (**Chapter 4**).

Table 1.3: Measurement methods commonly used for studying FRET are listed along with methods of measuring FRET presented in this thesis research.

	Method	Examples
Sensitized emission	An increase in acceptor emission is observed when FRET occurs (see Chapter 3). Measuring the increase in acceptor emission intensity (i.e., using microscopy or spectroscopy methods) allows calculation of FRET parameters.	[4, 18]
Donor emission	A decrease in donor emission is observed when FRET occurs (see Chapter 3). Measuring the quenching of donor emission (i.e., using microscopy or spectroscopy methods) intensity allows calculation of FRET parameters.	[4, 18]
Lifetime measurements	FRET from the donor to the acceptor molecule causes a decrease in donor fluorescence lifetime (e.g., lifetime of	[4, 62]

	HSA decreases from ~5.6 ns to ~3.3 ns when participating in FRET (see Chapter 3). Measuring the change in donor lifetime allows calculation of FRET parameters (i.e., using fluorescence lifetime imaging microscopy (FLIM) or time-resolved fluorescence spectroscopy methods).	
Anisotropy	FRET results in a decrease in acceptor anisotropy (see Chapter 3). Measuring the decrease in acceptor anisotropy allows calculation of FRET parameters. Anisotropy measurements can be incorporated into microscopy and spectroscopy measurements by using polarized excitation and collecting polarized emission.	[63, 64]
Photobleaching FRET	Photobleaching is the permanent inactivation of excited fluorophores. Since, FRET from an excited donor to an acceptor fluorophore prevents photobleaching of that fluorophore, photobleaching can be used to determine FRET parameters.	[65, 66]
ARMES measurements	ARMES measurements allow the collection of donor emission, sensitised acceptor emission and anisotropy all in a single measurement providing an information rich measurement of FRET. The application of ARMES in the measurement of FRET is explored in Chapter 4 .	[9]

1.3 ANISOTROPY

Fluorescence anisotropy is based upon the principle of photo-selective excitation of fluorophores by polarized light² [4, 18]. Upon excitation with polarized light, fluorophores with absorption dipoles parallel or close to that of electric oscillations of excitation source will be preferentially excited [4, 67]. If the absorption dipole of a fluorophore is orientated perpendicular to the electric field, then excitation will not occur. In general, the closer the angle between the absorption dipole and the light's electric field is to 0°, the higher the probability of excitation will be [67, 68].

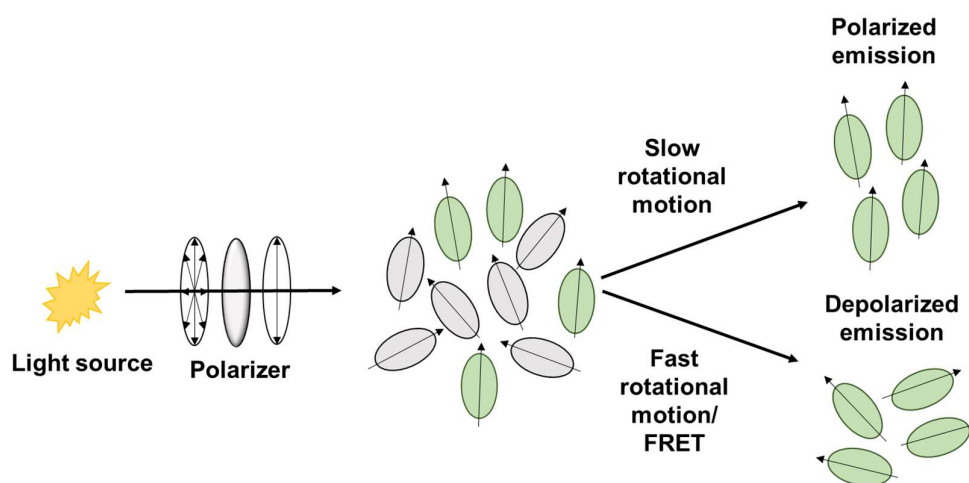


Figure 1.7: Upon polarised excitation of a solution containing randomly oriented fluorophores, the fluorophores with absorption transition dipole parallel or close to that of the excitation light will be preferentially excited through a phenomenon known as photoselection. Following photoselection polarization may be retained, in cases where molecules rotate slowly compared to the time between excitation and emission, or can become depolarised due to fast rotational motion or participation in energy transfer processes.

² Light is an electromagnetic wave consisting of an electric field (E) and a magnetic field (B), both are perpendicular to each other and to the direction of propagation. For natural light these fields have no preferential orientation, but for linearly polarized light the electric field oscillates along a given direction.

Following photo-selective excitation, the emission from fluorophore often exhibits inherent degree of polarisation, known as its ‘limiting anisotropy’ (r_0). The limiting anisotropy of a molecule reflects the angle between the absorption and emission transition moments within the coordinates defined by the molecular structure [69]. The distribution of the angles of the transition moments associated with photoselection and emission means that commonly observable values of r_0 range from 0.4 (for parallel absorption & emission transition moments) to -0.2 (when absorption and emission transition moments are perpendicular) [69]. During the time between excitation and emission (fluorescence lifetime), the fluorescence can become depolarised through a variety of processes including fluorescence quenching, participation in FRET and/or rotational diffusion. A fluorophore in rigid media will show little difference in the degree of polarization of emitted light to that of the excitation, however, in the case of a fluorophore in solution, depolarisation is often observed due to rotational diffusion, quenching FRET (**Figure 1.7**).

Anisotropy (r) values are calculated from the measured fluorescence intensities when linear polarizers set in the excitation and emission beams are configured parallel (I_{\parallel}) and perpendicular (I_{\perp}) to each other (**Equation 1.12**).

Equation 1.12

$$r = \frac{I_{\parallel} - I_{\perp}}{I_{\parallel} + 2I_{\perp}}$$

Instruments will generally have different sensitivities for the two different polarization directions, so a correction factor G (or instrument sensitivity ratio between vertical and horizontal polarized light) is introduced by **Equation 1.13**, where I_{VH} represents the intensity of horizontally polarized fluorescence emission with vertically polarized excitation light. The same applying for I_{VV} , I_{HH} and I_{HV} .

Equation 1.13

$$r = \frac{I_{VV} - G \times I_{VH}}{I_{VV} + 2 \times G \times I_{VH}}, \text{ where } G = \frac{I_{HV}}{I_{HH}}$$

The steady-state anisotropy of a molecule follows the Perrin equation (**Equation 1.14**), and this relationship between the degree of depolarisation and rotation of a molecule during its fluorescence lifetimes [4, 68, 70], led to the development of fluorescence anisotropy techniques to provide information regarding the size, shape, mobility, and flexibility of molecules [70, 71].

Equation 1.14

$$r = \frac{r_0}{1 + \frac{\tau RT}{\eta V}}$$

where r_0 is the value of anisotropy at $t=0$ after short pulse excitation, τ is the fluorescence lifetime of the fluorophore, η is the local viscosity of the solution, and V is the hydrodynamic radius.

1.4 MULTI-DIMENSIONAL FLUORESCENCE

For samples containing multiple fluorophores, conventional 2-D fluorescence spectroscopy, where the emission spectra are collected for a single excitation wavelength, is not ideal and a multi-dimensional approach, which can analyse multiple fluorophores simultaneously are more appropriate. In MDF spectroscopy, emission spectra are measured for a range of excitation wavelengths and the data is combined to form a three-way matrix, referred to as an excitation emission matrix (EEM). The fluorescence EEM represents a three dimensional landscape of fluorophore properties: excitation wavelength (λ_{ex} , plotted on the x-axis), emission wavelength (λ_{em} , plotted on the y-axis), and Intensity ($I_{\text{ex/em}}$, plotted on the z-axis) [72].

1.4.1 MDF collection modes: TSFS and EEM

There are two modes in which steady-state MDF spectra are collected: TSFS and EEM, and each mode offers different advantages and disadvantages. In EEM mode, the excitation and emission monochromators move independently with the full emission spectrum collected at each excitation wavelength, one at a time, and the resulting spectra then combined to produce an EEM plot, with excitation wavelength on the x-axis, the emission wavelength on the y-axis, and the fluorescence intensity on the z-axis (**Figure 1.8/A**). In TSFS mode, excitation and emission monochromators are scanned simultaneously (**Figure 1.8/B**). A 3-D spectrum is obtained by applying a wavelength offset ($\Delta\lambda = \lambda_{\text{em}} - \lambda_{\text{ex}}$), meaning excitation and emission are scanned simultaneously with different wavelength intervals between them, or by applying a variable-angle synchronous fluorescence spectroscopy, in which excitation and emission modes are scanned simultaneously, but at different rates. Constant wavelength synchronous fluorescence spectroscopy is the simplest form of TSFS and is the type of TSFS used in this thesis. The TSFS landscape is obtained by plotting the excitation wavelength on the x-axis, the offset $\Delta\lambda$ on the y-axis, and the fluorescence intensity on the z-axis [73].

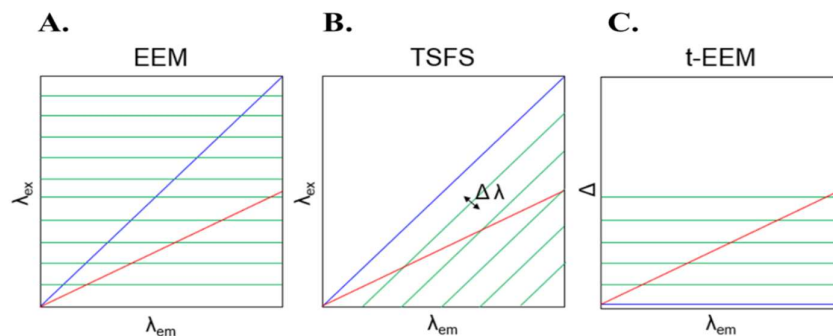


Figure 1.8: Scanning of excitation and emission (green) in: **A)** EEM and **B)** TSFS, **C)** shows the spectra when converted to t-EEM. The blue line represents 1st order Rayleigh scatter and the red line represented 2nd order Rayleigh scatter. Note the reduced spectral range collected in TSFS mode, no data collected at $\lambda_{\text{ex}} > \lambda_{\text{em}}$.

A drawback of TSFS compared to EEM, for chemometric analysis, relates to the tri-linearity of data, an important feature when coupling with multivariate data analysis methods. EEM datasets (sample $\times \lambda_{\text{ex}} \times \lambda_{\text{em}}$) are trilinear while TSFS datasets (sample $\times \lambda_{\text{ex}} \times \Delta\lambda$) are not. In EEM datasets, the spectral profile of an ideal fluorophore does not change over the other two modes. One solution for this is the unfolding of TSFS datasets over one mode to obtain bilinear datasets [74]. *Schenone et al.* have applied unfolded partial least squares and multivariate curve resolution for modelling strong spectral overlapping TSFS data [75]. Another solution is the conversion of TSFS data into EEM layout [76] with the spectra then referred to as t-EEM (**Figure 1.8/C**), this solution to chemometric modelling of TSFS data is used in this thesis research.

One major advantage of TSFS over EEM is reduction of the scanned spectral range. In EEM mode, a significant part of the collected emission where excitation wavelength is longer than the emission wavelength $\lambda_{\text{ex}} > \lambda_{\text{em}}$ does not contain useful information. In TSFS spectra, this region is not included as the wavelength offset $\Delta\lambda = \lambda_{\text{em}} - \lambda_{\text{ex}}$ is always positive. Another advantage of TSFS is the ease of eliminating Rayleigh scatter [77]. In the EEM landscape, the 1st order Rayleigh scatter is positioned diagonally, while in TSFS the 1st order Rayleigh scatter appears as a horizontal line at $\Delta\lambda = 0$ nm (which corresponds to $\lambda_{\text{ex}} = \lambda_{\text{em}}$) (**Figure 1.8**). Thus, in TSFS mode the 1st order Rayleigh scatter can easily be removed by means of selecting a wavelength offset $\Delta\lambda > 10$ nm, whereas in EEM mode it often needs to be removed by computational means.

1.4.2 ARMES Methodology

ARMES methodology adds an additional dimension of anisotropy to MDF measurements like EEM and TSFS through the use of polarized excitation and the measurement of polarization emission [2, 8]. ARMES methodology then combines these polarised measurements of fluorescence with chemometric methods to resolve individual fluorophore contributions [1]. Further information regarding ARMES instrumentation and methodology is given in **Chapter 2**.

1.4.3 Factors affecting MDF spectra

Scattering in MDF

There are several different types of light scattering which can occur in MDF spectra. While scattering is often viewed as an artefact that complicates analysis and removed prior to analysis of emission [78], scattering also contains additional, valuable spectral information which can provide information regarding particle sizes present in the sample. There are two main types of scattering which occur in MDF spectra: Rayleigh scatter and Raman scatter (**Figure 1.9**) [4].

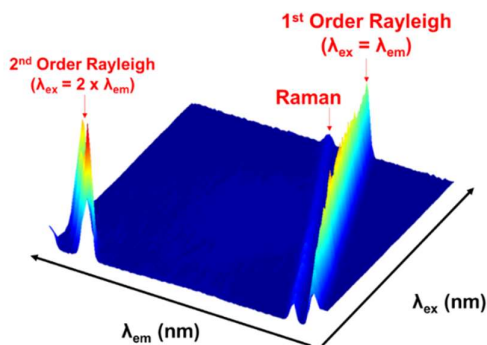


Figure 1.9: Scattering in MDF spectra; Raman scattering, 1st order ($\lambda_{ex} = \lambda_{em}$), and 2nd order ($\lambda_{ex} = 2 \times \lambda_{em}$) Rayleigh scattering.

Rayleigh scatter is a type of elastic scattering of the incident light and can be 1st order or 2nd order. 1st order Rayleigh scattering is the scattered excitation light, and the band appears at positions where excitation and emission wavelengths are equal ($\lambda_{ex} = \lambda_{em}$). 1st Rayleigh scattering it is the most intense scattering present in MDF spectra.

2nd order Rayleigh scattering occurs from second order diffraction from the grating³ of the monochromator and is observed at $\lambda_{\text{ex}} = 2 \times \lambda_{\text{em}}$ [67].

Raman scatter involves the non-elastic scatter of incident photons by molecules in the sample with the incident photons either losing energy (Stokes) or gaining energy (anti-Stokes) by interaction with the vibrational modes of the molecules. The effect is very weak and is generally not observed with strongly fluorescent molecules. However, if the emission is weak then one can observe Raman scatter in EEM spectroscopy, the most likely band being observed, for samples in aqueous solvents, originates from O–H bonds. The centre line of the Raman band is at a constant wavenumber shift compared to the Rayleigh scatter [4].

Although scattering can provide useful information about the chemical and physical properties of the sample, when aiming to analyse fluorescence emission scatter can overcomplicate the spectra. Therefore, scatter is either removed or avoided before chemometric analysis. There are several ways of dealing with scatter effects when modelling spectral data, which are discussed in **Chapter 2** [72].

Inner Filter Effects

Inner filter effect (IFE) is a common problem in fluorescence spectroscopy which occurs particularly in concentrated or turbid samples with high absorption or scatter and leads to an apparent decrease in emission quantum yield and or distortion of the band shape. IFE can be divided into two different types: primary and secondary [4].

Primary IFE refers to the attenuation of the excitation beam due to the absorption by chromophores in the sample and/or presence of scattering particles. Secondary IFE, results from the absorption of emitted fluorescence radiation by chromophores present in solution. IFE also depends on non-molecular properties of the sample, such as the path length of the sample container, optical density of the sample (Absorbance, A), and the geometry of the excitation and emission paths [4, 18]. Most conventional spectrophotometers use a right-angle geometry (**Figure 1.10/A**) and fluorescence is most often collected in a 10 mm pathlength quartz cuvette. Primary IFE can be viewed as the attenuation of the excitation light; and, secondary

³ Monochromators utilise diffraction gratings to isolate a desired wavelength of light.

IFE, attenuation of the emission light. The total attenuation of fluorescence, at a specific wavelength pair ($\lambda_{ex}/\lambda_{em}$), caused both primary and secondary IFE is a function of the absorbance at each wavelength pair (**Figure 1.10/B**). IFE effects are known to be more severe at shorter wavelengths (i.e. blue edge of emission), as absorbance tends to decrease with increasing wavelength [79]. There are four methods commonly used for dealing with IFE: sample dilution, changing the cuvette pathlength, applying mathematical correction, or explicit inclusion of the IFE [72], and these methods are further discussed in **Chapter 2**.

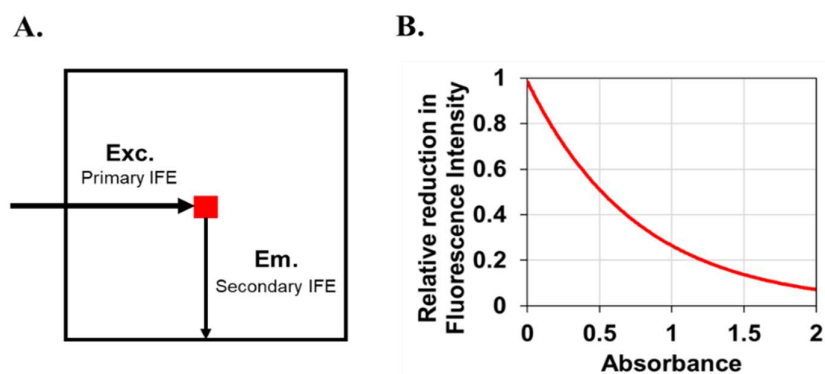


Figure 1.10: (A) Representation of primary and secondary IFE from a sample in a cuvette collected with a spectrophotometer with right-angle geometry. (B) The relationship between the absorbance of the sample (at any excitation/emission wavelength pair) and relative reduction in fluorescence intensity due to IFE in a 10 x 10 mm cuvette. (Image source: Kothwala et al. (2013) [79]).

FRET in MDF

FRET is a major cause of nonlinearity of fluorescence response in MDF measurements. The intrinsic fluorophores of multi-fluorophore protein are spectrally overlapped and usually in close enough proximity for FRET to occur. The presence of FRET in MDF spectra can complicate chemometric analysis when using tri-linear methods in the resolution of fluorescence, such as the commonly used PARAFAC method [7, 80]. The effect of FRET on MDF spectra is discussed in more detail in **Chapters 3 & 4**, where the use of ARMES in modelling FRET processes is explored.

1.5 CHEMOMETRIC METHODS

The concepts of fluorescence, multi-dimensional fluorescence and anisotropy have been introduced so far. In the next section of this introductory chapter the background of multi-way analysis and the main chemometric techniques used in the thesis work will be explored. This section can be used by the reader as a reference when interpreting the results presented in the subsequent experimental chapters.

1.5.1 Background of multi-way analysis

The term “chemometrics” was introduced in 1971 in a grant application, by Swedish scientist Wold, and refers to the discipline of extracting relevant chemical information from often complex data structures of measurements made on chemical or biological samples using multi-way data analysis approaches [81]. In 1974, the International Chemometrics Society was formed by Wold and Kowalski [82], and the pair are often credited with creating chemometrics, however, in reality Wold and Kowalski named an existing discipline which had been founded in the mid-1960s in the area of psychometrics [83-86].

Chemometrics is an area which developed alongside computational and instrumentational advancements [87]. In the past most analytical instruments and techniques generated one-way and two-way data. One-way is often analysed using one-way techniques such as generation of mean and standard deviation of the data. In two-way data, such as a UV-Vis absorption spectrum, the data can be indexed by two indices, one defining the sample (I) and one defining the wavelength number (J), forming a matrix X ($I \times J$). Two-way data can be analysed in more depth using two-way analysis tools such as multivariate curve resolution (MCR) and principal component analysis (PCA) [88-90].

Many modern analytical techniques, however, generate three-way and higher order data, and require more complex multi-way analysis tools. A fluorescence spectrophotometer generating MDF spectra is an example of an instrument which generates three-way data, known as a third order instrument, in this case three-way data results defined by the sample (I), excitation wavelength (J) and emission wavelength (K), resulting in a three-way matrix X ($I \times J \times K$). Such third order instruments have advantage over second order and first order instruments, known as

'higher-order advantage'⁴ [91]. Although this three-way data can be rearranged to a two-way array and analysed using two-way analysis techniques, this entails losing part of the information which may be important in understanding the data as a whole [92]. Therefore, it is more appropriate to use a three-way structure and analyse this data using a three-way analysis technique such as parallel factor analysis (PARAFAC) or Tucker3 modelling.

The main chemometric techniques will be discussed in this section with reference to the spectroscopic data which they were used to analyse in this thesis work. The techniques introduced here include, MCR, PCA, PARAFAC, Tucker3 and restricted Tucker3. It is important to note that MDF spectroscopy is just one example of a modern analytical technique which is suitable for multi-way analysis, but three-way data occur very frequently in chemical sciences, at present however there is a lack of awareness among chemists of the appropriateness and application of multi-way analysis [86, 93-95].

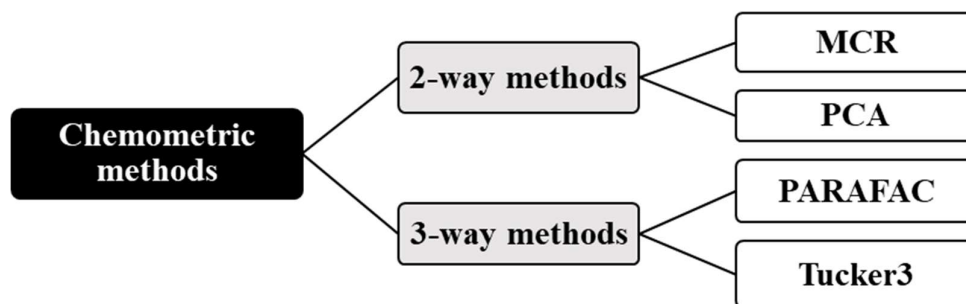


Figure 1.11: Chemometric methods used in this thesis research.

1.5.2 MCR-ALS

MCR-ALS is a commonly used method the decomposition of two-way matrices into smaller two smaller matrices [88], and is often used in the analysis of two-way data generated from measurements such as UV-Vis spectroscopy (**Figure 1.12**) or conventional 2-D fluorescence emission measurement [96-98]. However,

⁴ Higher-order advantage of multi-way analyses refers to the increased sensitivity as increase data dimension increases, and the subsequent ability to resolve overlapped underlying components of the data.

MCR-ALS can also be used on three-way arrays by unfolding the array along the suitable dimensions to form a two-way array [99].

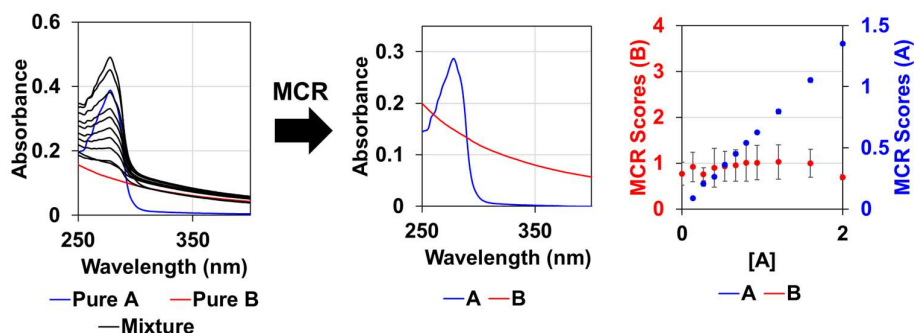


Figure 1.12: Example of the application of MCR to resolve a UV absorbance spectrum. Here the spectra are formed from a mixture of two different components; A and B which have overlapping absorbance spectra, the pure spectra are highlighted in blue (A) and red (B). MCR can resolve two components; A and B, and allows determination of their respective concentration during the interaction using the MCR scores.

The method entails decomposing the two-way matrix using **Equation 1.15** by iterative alternating least-squares (ALS) optimization of **C** (matrix of the concentration profiles) and **S^T** (the spectra matrix) to minimize of the Frobenius norm of **E** (the residuals), for each of the factors (**R**) of a multi-component system. The dimensions of **X**, **C**, **S**, and residual matrix **E** in the expression are **X** ($I \times J$), **C** ($I \times R$), **S** ($J \times R$), and **E** ($I \times J$), respectively (**Figure 1.13**).

Equation 1.15

$$X = CS^T + E$$

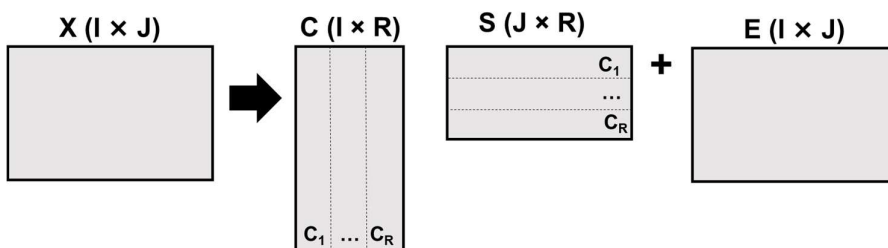


Figure 1.13: Schematic description of an MCR model where, **C**, represents the matrix of concentration profiles, **S**, represents the spectra matrix and, **E**, represents the residuals matrix.

1.5.3 PCA

PCA is a useful tool to get an overview of the data, see initial clustering or detect outliers, and is most often used in exploratory analysis to uncover spectral or sample variance [90, 100]. All methods for the analysis of three-way data presented in this section can be considered as a variant of two-way PCA [89]. The main idea behind PCA is to reduce the dimensionality by representing in the variation of a dataset in PC's (principal components) while retaining as much information as possible. These PCs represent the variation in the dataset in a more concise manner and make it easier to assess similarities and differences between samples.

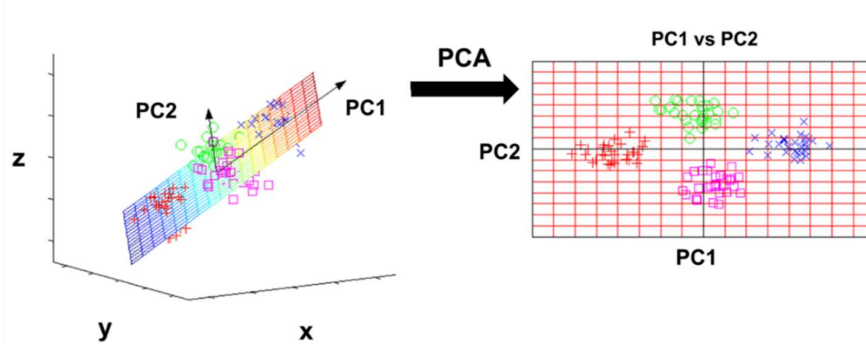


Figure 1.14: An example of PCA analysis to reduce the dimensionality of the data by representing the variation in PC's.

In PCA a two-way data matrix X ($I \times J$) is decomposed as a sum of vector products (**Equation 1.16**) and residual matrix E ($I \times J$).

Equation 1.16

$$x_{ij} = \sum_{r=1}^R a_{ir} b_{jr} g_{rr} + e_{ij}$$

where a_{ir} is a core element called scores and can be collected into a column vector per component \mathbf{a}_r (related to the concentration of a sample), and b_{jr} are called loadings and can be collect into a column vector per component \mathbf{b}_r (related spectral profile of a sample) (**Figure 1.15**). A pair of a loading vectors and it's score vector is called a PC. The g_{ss} are the square roots of the eigenvalues (or singular values) which

represent the standard deviations of the components given the standard centring and normalisations. These PCs represent the variation in the dataset in a more concise manner and make it easier to assess similarities and differences between samples. PCA is a useful tool to get an overview of the data, to see initial clustering or to detect outliers [90, 100].

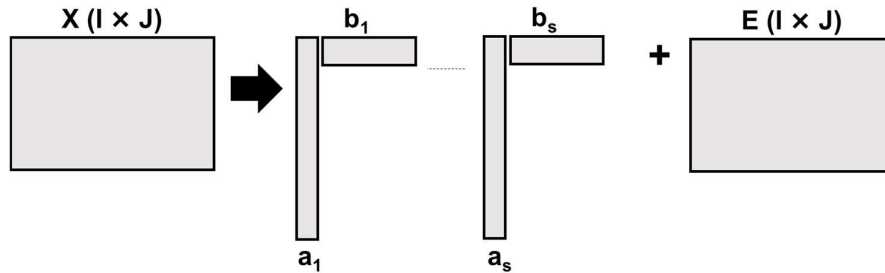


Figure 1.15: Description of a PCA model.

Although, PCA is a method for two-way data, however it can be extended to three-way data. When extending PCA to three-way data unfolding of the data to a two-way matrix is required. For three-way data methods such as PARAFAC or Tucker3 are more appropriate [86].

1.5.4 PARAFAC

At present PARAFAC is one of the most used techniques (along with PCA) for modelling of fluorescence excitation emission matrices (EEMs) [101-103] (**Figure 1.16**). PARAFAC can be considered as a direct extension of bilinear PCA, while the Tucker3 decomposition is another generalization of PCA to higher orders [8]. The fundamental idea underlying the PARAFAC model was first formulated by Cattell in 1944 in the form of the principle parallel proportional profiles [104, 105]. The Parallel factor analysis (PARAFAC) model, however, was first proposed independently by Hitchcock (1927), Carroll and Chang (1970), and Harshman (1970) [101-103].

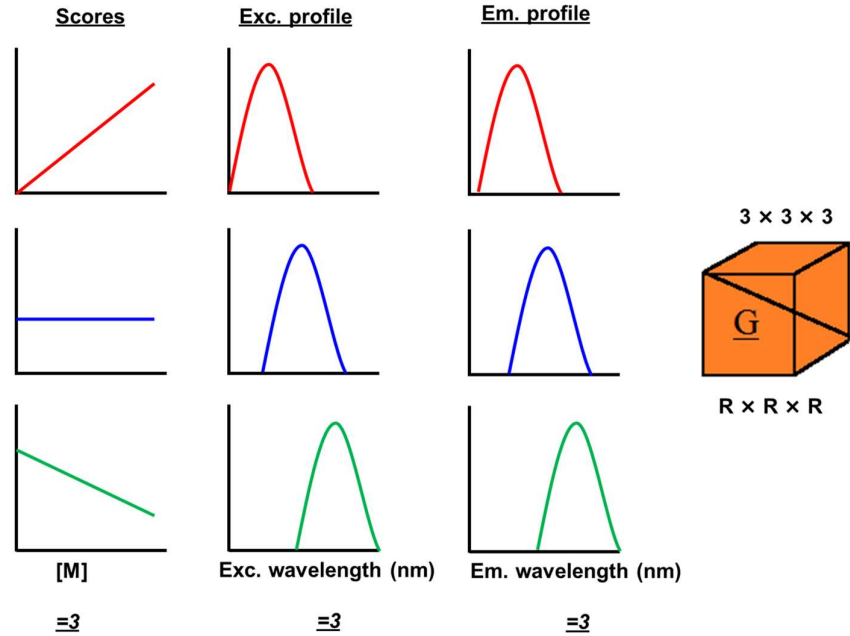


Figure 1.16: An example of PARAFAC resolution of MDF dataset into three components with independent concentration, excitation, and emission profiles where a $3 \times 3 \times 3$ is appropriate.

In PARAFAC a three-way data matrix $X (I \times J \times K)$ can be decomposed into three component matrices $A (I \times R)$, $B (J \times R)$ and $C (K \times R)$, one super-diagonal core array tensor $G (R \times R \times R)$ (and one residual tensor $E (I \times J \times K)$) (**Figure 1.17 & Equation 1.17**) [106]. Where R is the number of components, A corresponds to loadings in the sample and is called the score matrix, B hold the loadings of the second mode and C contains the loadings of the third mode. The super-diagonal core array eliminates the problem of rotational ambiguities by imposing a trilinear constraint and ensures the uniqueness of the PARAFAC solution.

Equation 1.17

$$x_{ijk} = \sum_{r=1}^R a_{ir} b_{jr} c_{kr} g_{rrr} + e_{ijk}$$

In PARFAC, all modes take identical roles so that there is no *a priori* designation of variable coefficients [106]. The weight of the s^{th} component, in the core matrix, g_{sss} , indicates its significance.

The simple application of PARAFAC requires trilinear data of full rank (i.e., the same number of components must be extracted in each mode), or in other words, underlying components of the data must be linearly independent and non-interacting. In practice a lot of datasets, contain components which do not conform to parallel proportional profile principle. One such example is protein MDF spectra, the highly overlapping spectra of the intrinsic fluorophore of proteins (i.e., Phe, Tyr, Trp) along with their close proximity can led to interactions occurring between fluorophore populations which can break the parallel proportional profile principle [6, 7, 107].

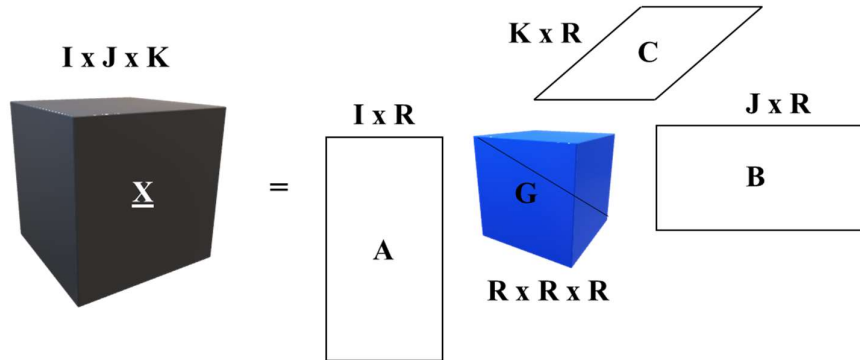


Figure 1.17: Description of the PARAFAC model.

For PARAFAC analysis, the number of components can be selected based on several criteria, one criteria was the CORE CONSistency DIAGNOSTIC test [108], CONCORDIA is a simple method to assess if the model structure is reasonable by assessing the distribution of superdiagonal and off-superdiagonal elements of G , the test reflects how well the Tucker3 core fits to the assumptions of the PARAFAC model. Using the loadings (A , B , and C) from the PARAFAC model and the dataset X , an unconstrained core (G) conditional on the data and loadings can be estimated ($G = A^T X (B \times C)$). The presence of nonzero off-superdiagonal elements in this core compared to the ideal superidentity core reduces the core consistency value below 100%. As the data moves away from low-rank trilinear behaviour, the core consistency parameter becomes lower and moves toward zero and negative values. In addition to the CONCORDIA diagnostic other criteria including; how much of variance was explained by the model, residual analysis, and visual inspection of the recovered

spectral profiles and residuals, was used to select the appropriate number of components. Validation of spectral deconvolution results were performed using split-half analysis [109].

Equation 1.18

$$CONCORDIA = 100 \left(\frac{1 - \frac{\sum_{i=1}^R \sum_{j=1}^R \sum_{k=1}^R (g_{def} - t_{def})^2}{\sum_{i=1}^R \sum_{j=1}^R \sum_{k=1}^R t_{def}^2}}{2} \right)$$

1.5.5 Tucker3 and Restricted Tucker3

The Tucker model was introduced by Tucker (1966) [85] four years prior to the PARAFAC model, and PARAFAC can be considered as a constrained version of Tucker3 [110]. There are many different variants of the basic Tucker model, such as The Tucker2 and Tucker3 models. In this section we will discuss only the Tucker3 model as it is the Tucker model used in this thesis.

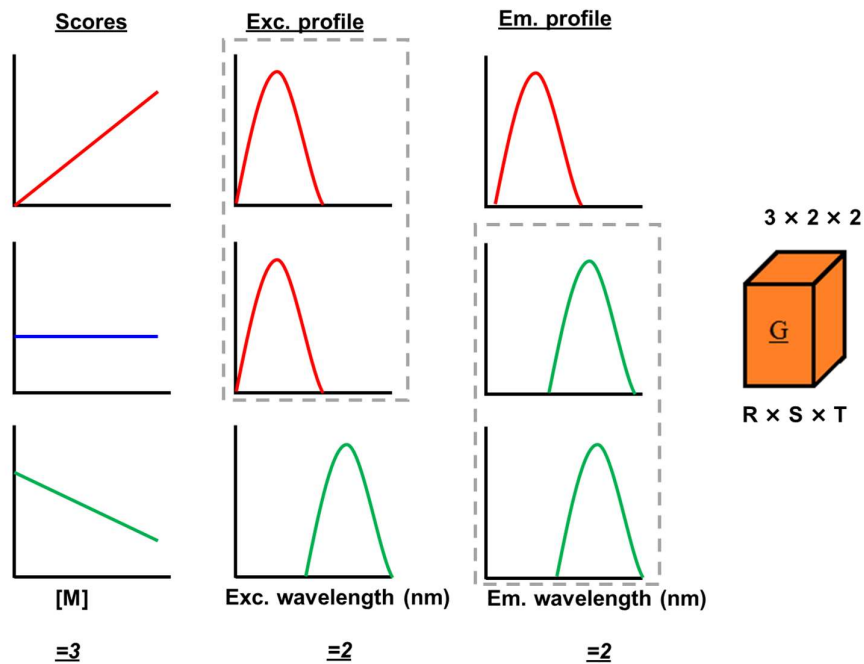


Figure 1.18: A schematic representation of Tucker3 resolution of MDF dataset into three components with independent concentration, but linearly dependent excitation and emission profiles, where a 3x2x2 Tucker core is most appropriate.

The key difference between the Tucker3 model and PARAFAC is that Tucker3 allows for extraction of different numbers of components in each of the three modes (i.e., does not require trilinear data) (**Figure 1.18**). In two-way analysis extracted components are uniquely linked to each other, however, in tucker3 this is not the case, and any component in a certain mode can interact with any component in the other two modes. Whereas in the PARAFAC model, the link between components of different modes is retained.

Equation 1.19

$$x_{ij} = \sum_{r=1}^R \sum_{s=1}^S \sum_{t=1}^T a_{ir} b_{js} c_{kr} g_{rst} + e_{ijk}$$

In Tucker3 the EEM dataset, with dimensions $I \times J \times K$, can be decomposed into three component matrices $A(I \times R)$, $B(J \times S)$ and $C(K \times T)$, one core array tensor G (which can have interactions between any two modes) and one residual tensor E (**Figure 1.19**). In this case, R is the number of components in the first mode, S is the number of components in the second mode, and T is the number of components in the third mode. As in PARAFAC, A , corresponds to loadings in the sample and is called the score matrix, B , hold the loadings in the emission mode and C , contains the excitation loadings.

However, despite the model's ability to handle non-linear data, it has not gained significant attention due to the rotational freedom of the model which leads to complicated and difficult to interpret solutions. In the case where PARAFAC is too restricted and Tucker3 is too flexible, a restricted Tucker3 model offers a potential solution [17-19]. A restricted Tucker3 model minimizes the ambiguity of the solution by harnessing *a priori* chemical knowledge of the system. The tucker core (G) which allows for components in a certain mode to interact with any component in the other two modes, is replaced with a defined core array in which most elements are forced to zero. In this way, the restricted model with a much smaller number of interaction terms is simpler and more interpretable. (Note: PARAFAC is, in essence, a restricted tucker3 model in which the core array contains ones on its super-diagonal and zero in every other position.)

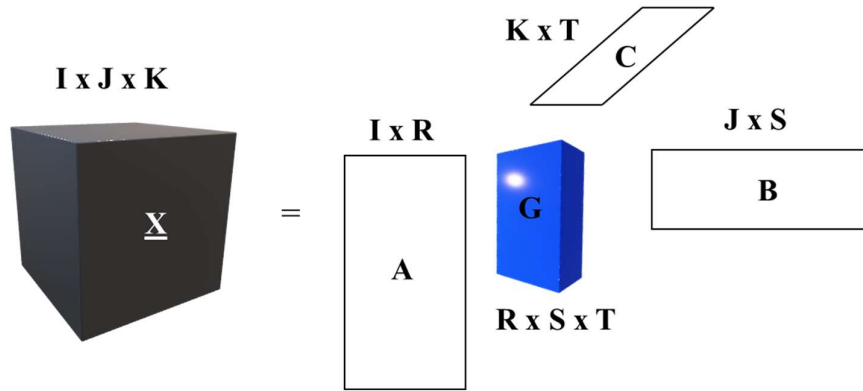


Figure 1.19: Description of the Tucker3 model.

Tucker3 models could be validated in a similar way to PARAFAC but using TuckCorCon in place of CONCORDIA as the diagnostic test (**Equation 1.20**) [111]. TuckCorCon is calculated similar to the PARAFAC core consistency but uses the hypothesized restricted core instead of the superdiagonal array of PARAFAC. Hence, two cores are playing a role in calculation of the TuckCorCon: the restricted final core of the Tucker3 model (G_1) and the unrestricted one (G_2) obtained using the final loadings of the restricted model (A , B , and C) and the data.

Equation 1.20

$$CONCORDIA = 100 \left(\frac{1 - \sum_{i=1}^R \sum_{j=1}^S \sum_{k=1}^T (g_{1,ijk} - g_{2,ijk})^2}{\sum_{i=1}^R \sum_{j=1}^S \sum_{k=1}^T g_{1,ijk}^2} \right)$$

1.6 ARMES AS A TOOL FOR BIOPHYSICAL ANALYSIS

The aim of this thesis research was to explore the use of ARMES methodology in biophysical analysis. The thesis research was part of a larger project to develop advance analytics for biological therapeutic manufacture. Biological therapeutics or biopharmaceuticals are defined as materials manufactured by biological means and used for therapeutic purposes. In the first project, FRET was investigated using ARMES methodology as it was a factor observed to complicate the analysis of biotherapeutic molecules IgG and insulin [6, 7, 107, 112]. In the second project of this thesis work, the application of ARMES as a tool to investigate protein-liposome interactions was investigated. Liposomes have a wide range of uses including their use as drug-delivery systems (DDS). It is of interest to study protein-liposome interactions as these interactions have critical consequence of the use of liposomes as DDS.

In this section, the areas of biopharmaceuticals and liposome-based drug delivery systems will be introduced to provide a context for the research. The two different projects investigating the biophysical applications of ARMES, explored in this thesis, will then be introduced in more detail.

1.6.1 Biopharmaceuticals

Proteins are the molecular machines of the cell with the most diverse range of functions of any macromolecule (**Figure 1.20**). The diversity of protein functions is matched by the variety of three-dimensional structures these complex macromolecules can adopt [113, 114]. Given the fact that misfolded proteins pose an immunological risk in vivo, proteins pose an immense challenge when viewed from the perspective of disease⁵ [115]. However, viewed from the perspective of therapeutics, proteins provide an area of tremendous opportunity and it is for this reason that recent years have seen a surge in growth of the biopharmaceutical industry [116].

⁵ Misfolding of proteins is believed to be the primary cause of a wide range of diseases including: Alzheimer's disease, Parkinson's disease, Huntington's disease, Creutzfeldt-Jakob disease, cystic fibrosis, Gaucher's disease and many other degenerative/neurodegenerative disorders.

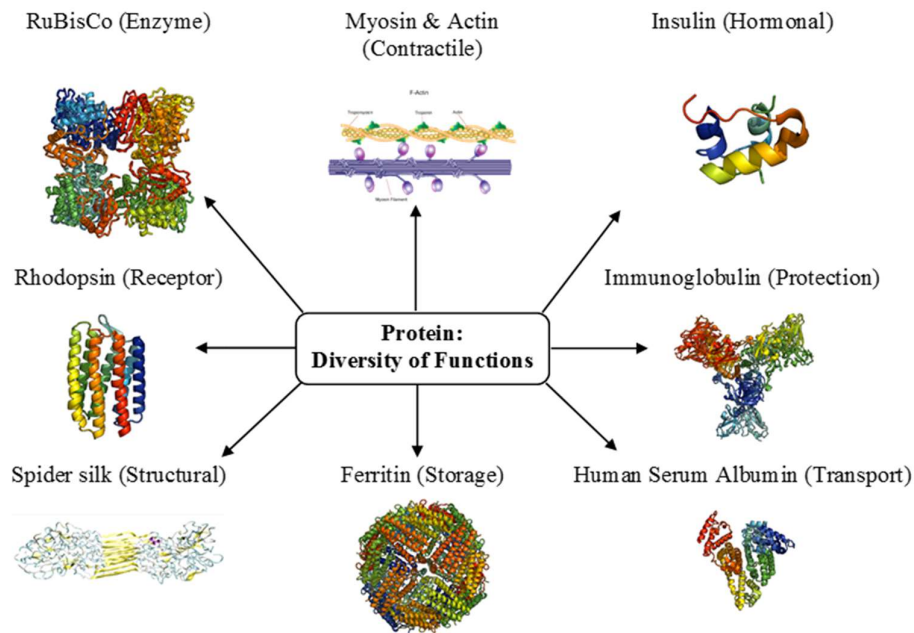


Figure 1.20: The diversity of protein functions (Images sourced from PDB).

Since the introduction of the first recombinant protein therapeutic- human insulin, by Genentech in 1982 [117], this class of therapeutics have grown from being a rarely used subset of medication to now, the most rapidly expanding class of human therapeutics [113, 118]. At the current approval rate of approximately four new products per year, >70 monoclonal antibody products will be on the market by the end of 2021, with combined sale of \$125 billion [119]. Protein therapeutics offer a number of advantages over their small molecule counterparts, namely, better specificity, better tolerability and uniqueness in form and function, these advantages are beneficial not only to the patient but also to the manufacturer with faster approval times and lower costs- saving both time and resources [113].

However, despite the significant advantages and promising market trends, protein therapeutics are still in their infancy. Recombinant DNA technology was only introduced less than 50 years ago in 1972 [120], and so, the manufacture and use of this class therapeutics is not without challenges that limit both their medical applicability and commercial success.

The molecular structures of this class of therapeutics are far more sophisticated in nature than their conventional synthetic small molecule drug counterparts [121].

For example, a molecule of acetylsalicylic acid is composed of 21 atoms, in contrast biopharmaceuticals are typically 100-1000 times larger (**Figure 1.21**) [122]. The specificity of biopharmaceuticals is dependent on the higher-order structure of the molecule which poses a challenge as proteins possess the ability to *breathe*, unfolding and refolding throughout the protein's life cycle. This inherent instability of proteins leads to complexity in both manufacture and analysis and numerous controls are needed to prevent misfolding and or aggregation [121, 123]. Given the threat posed to patients when aggregates are present in therapeutic protein formulations [124], the development of robust, rapid and non-destructive analytical techniques capable of characterising structure and monitoring stability of protein therapeutics is an area of active research and discussion between regulators, industry and academia [125-127].

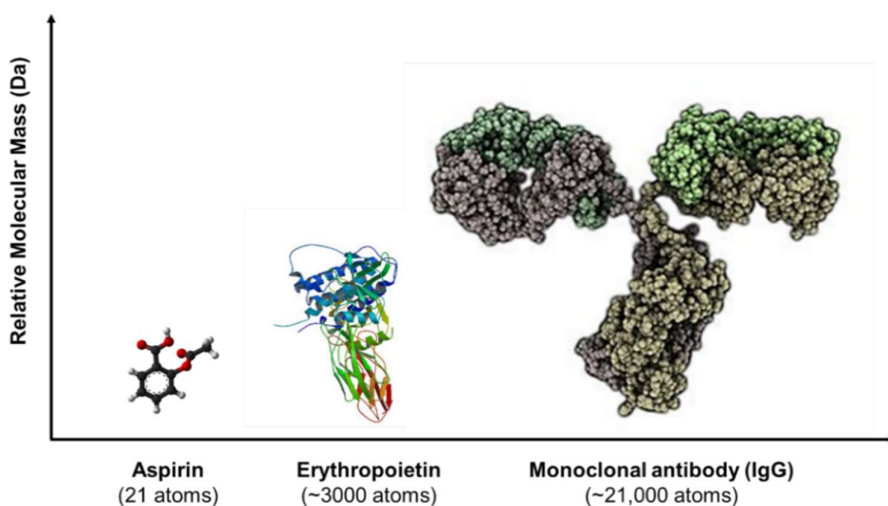


Figure 1.21: Biopharmaceuticals are much larger in size, with a more complex structure than their small-molecule drug counterparts [122].

Current methods for characterising biopharmaceuticals are limited in their capabilities, each technique has advantages and disadvantages, and no single technique can provide all the information required to properly assess protein quality (**Table 1.4**) [128]. Thus, the use of a combination of techniques is often the only alternative, which will add to the analysis time, and may be impractical. The purpose of the project advanced analytics for biological therapeutic manufacture undertaken by the nanoscale biophotonics laboratory was to develop a novel analytical methodology called

ARMES, to characterise and monitor proteins in solution for applications in the biopharmaceutical industry as a PAT technology.

Table 1.4: Some of the advantages and limitations of the main analytical techniques used for assessing the quality attributes of protein-based therapeutics [125, 129].

Technique	Advantages	Limitations	Refs
UV-Vis	<ul style="list-style-type: none"> ✓ Non-destructive ✓ Sensitive (LOD* ~0.05 mg/ml for bovine serum albumin) ✓ Easy to use ✓ Detection of scattering material outside absorption bands 	<ul style="list-style-type: none"> ✗ Limited information on particle properties ✗ Sensitive to scatter 	[130, 131]
SEC	<ul style="list-style-type: none"> ✓ High precision & robustness ✓ Sensitive (~dependent on detector used) ✓ Easy to use 	<ul style="list-style-type: none"> ✗ Alters sample ✗ Time consuming ✗ Limited resolution & particle size range 	[132]
SDS-PAGE	<ul style="list-style-type: none"> ✓ Relatively easy to use ✓ Low cost 	<ul style="list-style-type: none"> ✗ Alters sample ✗ Only qualitative/ semi-quantitative ✗ Low precision ✗ Labour intensive 	[133]
DLS	<ul style="list-style-type: none"> ✓ No change in sample concentration required ✓ Easy to use ✓ Low sample consumption ✓ High sensitivity (dependent on size of molecule measured) 	<ul style="list-style-type: none"> ✗ Only semi quantitative ✗ Low resolution of species with close sizes ✗ Unsuitable for polydisperse samples ✗ Sensitive to contamination 	[134, 135]

CD	<ul style="list-style-type: none"> ✓ Non-destructive ✓ Easy to perform ✓ Low sample consumption ✓ Potential for online detection 	<ul style="list-style-type: none"> ✗ Limited resolution ✗ Complicated data interpretation ✗ Sensitive to contamination 	[136, 137]
FT-IR	<ul style="list-style-type: none"> ✓ Non-destructive ✓ Solid state analysis possible ✓ Little interference from light scattering ✓ Relatively low cost 	<ul style="list-style-type: none"> ✗ Limited information 	[138, 139]
MS	<ul style="list-style-type: none"> ✓ Provides detailed structural information ✓ Very high resolution ✓ High accuracy, precision, and high sensitivity (for typical mass spectrometer the LOD for a 50 kDa protein is ~10 amol) 	<ul style="list-style-type: none"> ✗ Usually requires sample preparation-alters sample ✗ Complex data generated ✗ Expensive 	[140-142]

*LOD refers to limit of detection

1.6.2 Liposome Drug Delivery Systems (DDS)

Alongside the rapid growth in the use of biological therapeutics is the development of drug delivery systems (DDS) to target these biologics to desired cells, and one promising area is liposome-based DDS [143, 144].

Liposomes are sphere-shaped vesicles, typically 50-500 nm in diameter, consisting of one or more phospholipid bilayer surrounding an aqueous core [145, 146]. Liposomes can be composed of natural phospholipids or other surfactant and can be either unilamellar or multilamellar, with sizes ranging from nanometers to micrometres in diameter [145, 147]. The formation of liposomes is a spontaneous

process which occurs when the phospholipids are hydrated [148, 149]. The phospholipids form shells because of hydrophobic effect of acyl chains in aqueous medium [150, 151]. This state is thermodynamically favorable and can be enhanced by hydrogen bonds, van der Waals forces, or other electrostatic interactions.

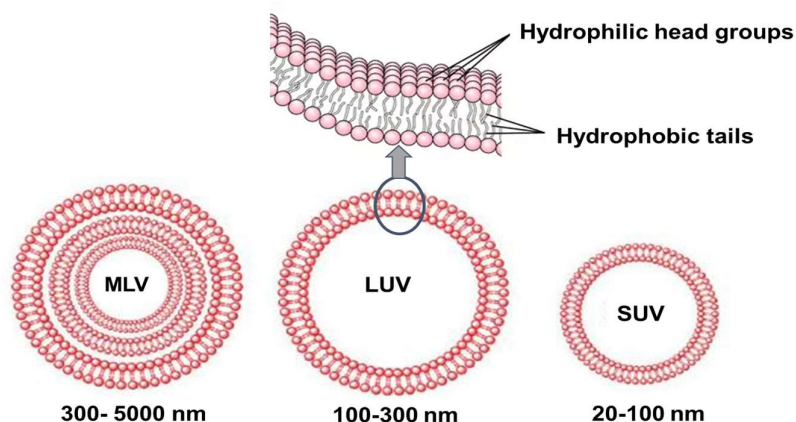


Figure 1.22: Liposome composition and structure, showing liposome assembly of Multi-Lamellar Vesicles (MLV), Large Unilamellar Vesicles (LUV), and Small Unilamellar Vesicles (SUV) (Image adapted from Pandey *et al.* [152]).

Since their discovery in the 1960's [153] liposomes have found use in several different scientific applications [154]. They have long been used as model membrane systems and simple cell models, which permit simple *in vitro* investigation of a broad range of biochemical processes [155, 156]. In addition, due to their biocompatibility and other properties, liposomes have tremendous potential as DDS [12, 144, 157, 158], and can be used to change the pharmacokinetics and pharmacodynamics of entrapped drugs by protecting them against chemical and immunological breakdown, thereby reducing their toxicity and unwanted side-effects [159]. Delivery of the drug is accomplished when the liposome fuses with the lipid membrane of a cell, releasing its contents into the cell cytoplasm. Since approval of the first liposomal based drug, Doxil[®], in 1995 [160], there has been significant development in the area of liposome-based drugs. At present there are >10 FDA approved liposome-based drugs and this growth is likely to continue with many more currently in clinical trials [161, 162].

Protein-liposome interactions

Upon administration of liposome-based DDS in the body, a number of different interactions occur with serum constituents, which leads to the breakdown or fusion of the liposome DDS in the body. In terms of their use as DDS, it is important to characterise the interaction of liposomes with these serum constituents, particularly proteins [10, 163]. The interaction of liposomes with plasma proteins can dramatically affect stability, and thus in vivo behaviour which in turn impacts on therapeutic efficacy (i.e., bioavailability, circulation time etc.) of the liposome DDS [144, 159]

1.6.3 Project I: FRET Study

Previous work investigating the use of ARMES in characterisation of biotherapeutic molecules, Immunoglobulin G (IgG) [7, 112] and Insulin [107], revealed FRET as a factor which introduces non-linearity in the emission, which complicates analysis of the multi-fluorophore emission of intrinsic protein fluorescence. The purpose of the first part of my thesis research was to contribute to the development ARMES, by investigating the process of FRET using ARMES methodology, analysing the effect on the resulting spectra and resolving the FRET sensitized emission using chemometrics. In addition, FRET is an important tool used in biochemical applications, so, the accurate analysis of FRET is not only important for understanding the non-linearity observed in ARMES measurements but also for a wide variety of biochemical applications. In this work, a HSA-ANS model system was used to aim to study the process of FRET, the results of this study are presented in **Chapters 3 & 4**.

1.6.4 Project II: Protein-liposome interactions

The second part of my thesis research explored the use of ARMES in studying the interactions between liposomes and proteins, in combination with conventional spectroscopic, UV absorbance, and DLS measurements. The results of this work have relevance in the analysis of protein-liposome interactions and in the development of quality control measurements for liposome-based therapeutics. In this work a HSA-DMPC model system was used to aim to study the interactions between liposome and proteins, the results of this study are presented in **Chapters 5 & 6**.

1.7 THESIS OUTLINE

In this introductory chapter the fundamental concepts of fluorescence were introduced alongside an overview of the area of chemometrics. The relevance of this thesis research was also outlined by the two areas of application explored in this work - biopharmaceuticals and liposome-based therapeutics. In this final section of this introductory paragraph an outline of the thesis is provided with an overview of the key information presented in each chapter.

In Chapter 2, the materials and methods used in this thesis work are described. An overview of the general pre-processing operations for correction of MDF measurements are explained alongside the specific sample preparation, instrumental parameters and data pre-processing methods used in each study.

Chapters 3 & 4 present the results of the FRET study of the HSA-ANS model system. In Chapter 3, the model system is introduced along with findings from the spectral analysis of the recorded UV-Vis, lifetime and pMDF data and the calculation of conventional biochemical parameters. In Chapter 4, the results from chemometric analysis of the pMDF data are presented (ARMES methodology). The resolved components were used in calculation of biochemical parameters and compared with results from conventional analysis. Most of the findings presented in Chapter's 3 & 4 were published in *Biophysica et Biochemica Acta* in February 2021 [9].

In Chapter 5 & 6 the results from the study of HSA and DMPC interactions in different aqueous environments are presented. As before, the first of these two chapters (Chapter 5), presents the results from the conventional spectral analysis of the collected data (DLS, UV, fluorescence lifetime and emission). In the subsequent chapter (Chapter 6) the results of the chemometric analysis of the molecular systems are presented, highlighted the additional information provided by applying ARMES methodology. Most of the results presented in Chapter's 5 & 6 are submitted to *Colloids and Surfaces B: Biointerfaces* in August 2021.

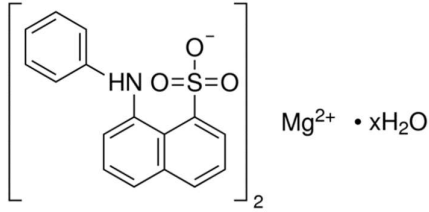
The final chapter of the thesis provided overall conclusions from the work alongside future perspectives of the application of ARMES as a tool for biophysical analysis.

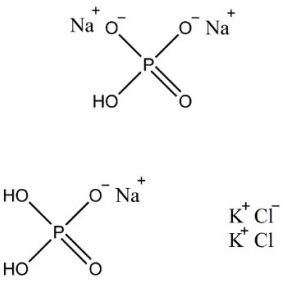
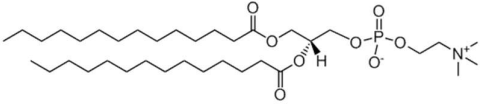
2 MATERIALS & METHODS

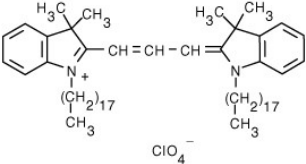
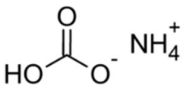
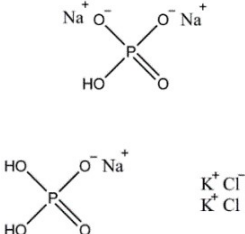
2.1 MATERIALS

All reagents (**Table 2.1**) were used without further purification, except for microfiltration of solutions. Pipette tips were sterilized by autoclaving at above 120 °C. HPLC grade water was used for all solutions (Chromasolv™ Plus, HPLC grade) and did not present any impurities detectable during fluorescence measurements.

Table 2.1: Description of all materials used in this work.

Material	Description	Source
Experimental section 1: HSA-ANS FRET Study		
Isopropanol	99.9 % purity, Chromasolv™ for HPLC	Sigma-Aldrich
Water	Chromasolv™ Plus, HPLC grade	Sigma-Aldrich
Human Serum Albumin (HSA)	≥99 % essentially fatty acid free, lyophilized powder, mol. weight ~66.3 kDa	Sigma-Aldrich (cat. no. A1887, lot no. SLBM7779V)
8-Anilino-1-naphthalenesulfonic acid hemi-magnesium salt hydrate (1,8-ANS)	<div style="display: flex; align-items: center;">  </div> ≥95.0% powder for fluorescence, mol. weight 310.49 g/mol	Sigma-Aldrich (cat. no. 10419)

<p>Phosphate buffered saline (PBS)</p> 	<p>Tablet form to make 0.01 M phosphate buffer (containing 0.0027 M KCl and 0.137 M NaCl)</p>	<p>Sigma-Aldrich (cat. no. P4417)</p>
<p>Ludox</p>	<p>LUDOX[®] AS-40 colloidal silica (SiO₂)</p>	<p>Sigma-Aldrich (cat. no. 420840)</p>
Experimental section 2: Liposome study		
<p>Chloroform</p>	<p>99%+, Extra Pure</p>	<p>Fisher Chemicals</p>
<p>Ethanol</p>	<p>99%+, Absolute, Extra Pure</p>	<p>Fisher Chemicals (CAS no. 64-17-5, lot no. 1922061)</p>
<p>Water</p>	<p>Chromasolv[™] Plus, HPLC grade</p>	<p>Sigma-Aldrich</p>
<p>1,2-dimyristoyl-sn-glycero-3-phosphocholine (DMPC)</p> 	<p>≥99 % purity, white powder, mol. weight 677.93 g/mol</p>	<p>Sigma-Aldrich (cat. no. 850345P, lot no. 850345P-1G-A-274)</p>
<p>1,1'-Dioctadecyl-3,3,3',3'-tetramethylindocarbocyanine Perchlorate (Dil)</p>	<p>≥99 % purity, Red/purple solid, mol. weight 933.88 g/mol</p>	<p>Thermo Fisher (cat. no. D282, lot no. 2095333)</p>

		
<p>1,1'-Dioctadecyl -3,3,3',3'- Tetramethylindodicarbocyanine, 4 - Chlorobenzenesulfonate salt (DiD)</p>	<p>≥99 % purity, Blue solid, mol. weight 1052.08 g/mol</p>	<p>Thermo Fisher (cat. no. D7757, lot no. 2071577)</p>
<p>Ammonium bicarbonate (NH₄HCO₃)</p> 	<p>≥99.5% purity (BioUltra), white powder, mol. Weight 79.06 g/mol</p>	
<p>Phosphate buffered saline (PBS)</p> 	<p>Tablet form to make 0.01 M phosphate buffer (containing 0.0027 M KCl and 0.137 M NaCl)</p>	<p>Sigma-Aldrich (cat. no. P4417)</p>
<p>Human Serum Albumin (HSA)</p>	<p>≥99 % essentially fatty acid free, lyophilized powder, mol. weight ~66.3 kDa</p>	<p>Sigma-Aldrich (cat no. A1887, lot no. SLMBM7779V)</p>
<p>Ludox</p>	<p>LUDOX[®] AS-40 colloidal silica (SiO₂)</p>	<p>Sigma-Aldrich (cat. no. 420840)</p>

2.2 INSTRUMENTATION

UV-Vis absorbance measurements were collected on a Cary 60 UV-Vis spectrophotometer (Agilent Technologies, part no. G6860A). Temperature control was ensured by a Single Cell Peltier Accessory (part no. SPV 1X0).

The fluorescence measurements were performed on a Cary Eclipse Fluorescence Spectrophotometer (Agilent Technologies, part no. G9800A), equipped with a multi-cell holder (Agilent Technologies, part no. G9808A) and a temperature controller (Agilent Technologies, part no. G9844A) (**Figure 2.1**). In this spectrophotometer, polarization of excitation and emission light was achieved using dual wire grid polarizers (dWGP) [8], which allow excitation in the UV region, suited to the analysis of the intrinsic fluorescence of proteins. Before data collection, the several parameters on the spectrometer were checked using the “validate” software delivered with the machine these included the accuracy and reproducibility of excitation and emission wavelengths (Xenon lamp), and the accuracy of spectral bandwidth for various excitation and emission slits. In-house protocols were used to check alignment of polarizers prior to analysis, this included obtaining the anisotropy of a dilute ludox solution in triplicate [164].

Schematic of ARMES system:

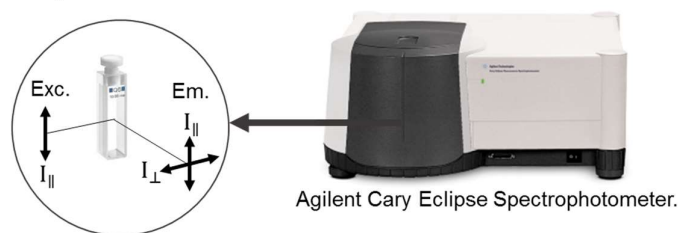


Figure 2.1: Schematic described the Agilent Cary Eclipse spectrophotometer equipped with wire grid excitation and emission polarizers.

Lifetime measurements were carried out using a PicoQuant GmbH TCSPC system, called the FluoTime 200. Fluorescence lifetime decays were recorded at the

magic-angle⁶ to avoid polarization effects [4]. The excitation source used for lifetime of protein sample, was a 295 nm pulsed LED (PLS-8-2-299, PicoQuant GmbH).

Dynamic light scattering (DLS) was collected using a Malvern Zetasizer Nano ZS with temperature control at a 173° detection angle. The hydrodynamic diameter ($d(H)$) was computed from the diffusion coefficients using Zetasizer Software version 7.13 from Malvern Panalytical. DLS is a non-invasive technique used for measuring the size and size distribution of molecules and submicron particles in solution [134]. The measurement principle behind the DLS is Brownian motion, in a DLS measurement the Brownian motion of particles in a solution is correlated with the sizes of the particles. Brownian motion is defined as the random movement of particles due to the collisions between the particles and the solvent molecules which surround them. The Brownian motion of the particles will be slowed down with an increase in the size of the particles with smaller particles moving more rapidly, as they move further from the solvent molecules as they collide. During the measurement, a laser of known wavelength is passed through the sample and is scattered at different intensities due to the random movement of the particles in the solution [134, 165]. The scattered light is collected by the detector and the intensity fluctuations of the scattered light are analysed to obtain the velocity of the Brownian motion and then using Stokes-Einstein relationship, the particle size can be determined. The Stokes-Einstein relationship is given by **Equation 2.1**.

Equation 2.1

$$d(H) = \frac{kT}{3\pi\eta D}$$

where $d(H)$ = hydrodynamic diameter, K = Boltzmann's constant, D = translational diffusion coefficient, T = absolute temperature and η = viscosity.

⁶ A measurement made at precisely defined angle of 54.7° between the emission polarizer and excitation beam polarization, used in order remove or reduce the effects of the chromophore's rotational correlation time.

2.3 CHEMOMETRIC ANALYSIS AND DATA PRE-PROCESSING OPERATIONS

Data analysis was performed using the PLS_Toolbox ver. 8.2.1 (Eigenvector Research Inc.), MATLAB ver. 9.1.0 (The MathWorks Inc.), and in-house written codes (through a programme called FluorS). MDF data had to first be pre-processed to make the data suitable for data analysis. An overview of the main pre-processing techniques which are used in this thesis are provided in this section.

Scatter removal

Since Rayleigh and Raman scatter are generally unrelated to the compositional properties of fluorescence samples and the scatter peaks do not behave trilinearly, both Rayleigh and Raman scatter can complicate chemometric modelling of fluorescence [78]. Raman scatter is generally simply corrected by blank subtraction of the buffer used in the sample. Rayleigh scatter is more complicated to deal with. The use of TSFS measurements provides a simple way of eliminating majority of the 1st order Rayleigh scatter during measurement by using an appropriate wavelength offset (>10 nm), however, often it is not possible to entirely removal Rayleigh scatter even when using TSFS collection mode⁷. Various computational/mathematical methods are available for dealing with the Rayleigh scatter issue in EEM. Firstly, zero values can be inserted outside of the fluorescence data area [166], data point weighting can be used to make the scattering band insignificant during trilinear decomposition [167] or weighted PCA on the unfolded EEM matrix can be used to eliminate scatter before refolding, and subsequent decomposition [168] There are various other strategies available including interpolation [78] and modelling [169, 170] of the scatter affected region. In my work TSFS measurements were used (avoiding 1st order Rayleigh scatter) with the

⁷ Generally, some scattered light will remain especially if using wide slit widths (~5-10 nm) and/or measuring samples which have a short Stokes shifted emission for $\lambda_{ex} < 300$ nm. If the sample solution contains particles, then this will increase further due to Mie and Tyndall scattering.

interpolation method used to fill the region with no data spectral from TSFS measurement mode, and to eliminate any 2nd order Rayleigh scatter (**Figure 2.2**).

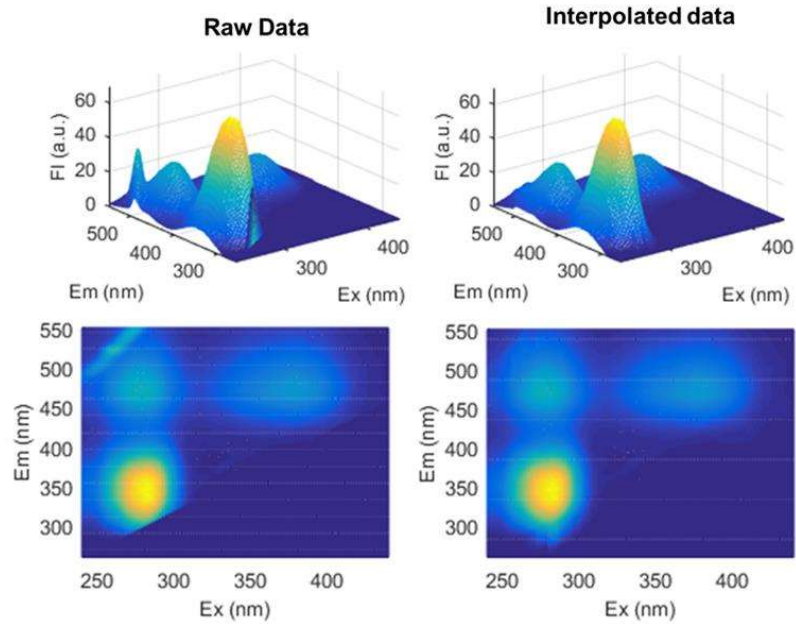


Figure 2.2: An example of the interpolation correction applied to remove 2nd order Rayleigh scatter and fill in area missing data at $\Delta\lambda=0-20$ nm) from TSFS measurements (made at $\Delta\lambda\geq 20$ nm).

G-factor correction

MDF_{HV} and MDF_{HH} measurements were collected to calculate the G-factor ($G=I_{HV}/I_{HH}$). G-factor was calculated with the raw [171] polarized MDF_{HV} and MDF_{HH} spectra, which was then de-noised using a one component PARAFAC model (**Figure 2.3**). These G-factors without noise were used to correct the raw MDF_{VH} spectra into the perpendicular MDF_⊥ spectra.

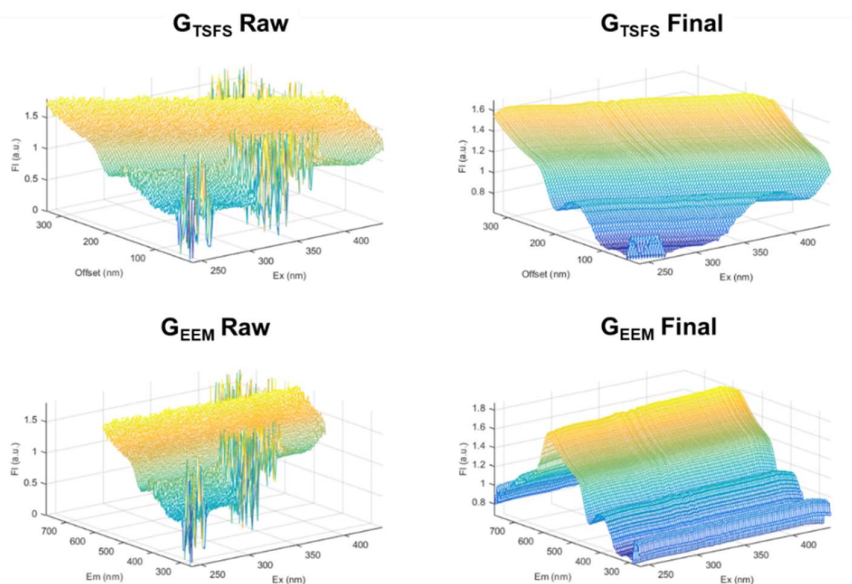


Figure 2.3: De-noised G-factor used for correction of VH spectra.

Inner filter effect (IFE) correction

There are a number of different approaches used to deal with IFE; sample dilution, changing the pathlength by changing cuvette, or using front-surface excitation, applying mathematical correction, or explicit inclusion of the IFE [72]. The simplest way to avoid IFE is to reduce sample concentration, however, in many cases this is not a viable option as reducing sample concentration involves sample handling which can lead to a change in the sample, especially in biological samples⁸ [172], in addition, dilution would also lead to a reduction in fluorescence intensity and signal-to-noise ratio (SNR) [173]. The second option is by the pathlength, this can easily be achieved by changing the cuvette pathlength, however, changing the pathlength may not solve the problem for very high concentration solutions. In addition some spectrometers allow front-face excitation, which allows detection of emission at the same surface as excitation which reduces the pathlength even further and can be used for high concentration solutions [174]. The third option, which is implemented in this thesis work, is a mathematical correction. This approach can be used in cases where the OD of the sample is <1.5 . The most used mathematical correction is known as the

⁸ For example, accurate protein quantification of a sample can be altered by dilution effects on the sample.

absorbance-based approach, the approach used the measured absorbance (A_λ) at a pair of excitation (λ_{ex}) and emission (λ_{em}) wavelengths to convert the fluorescence intensity observed (F_{obs}) into the corrected fluorescence intensity (F_{corr}). Finally, for samples with $OD > 1.5^9$, the mathematical correction method is not an option, and in some cases, changing sample concentration is not a practical solution either [112]. In this case, IFE can be considered as part of the sample fingerprint to provide information about the sample.

Equation 2.2

$$F_{\lambda_{ex},\lambda_{em}}^{corr} = F_{\lambda_{ex},\lambda_{em}}^{obs} \times I = F_{\lambda_{ex},\lambda_{em}}^{obs} \times 10^{(0.5 \times (A_{\lambda_e} + A_{\lambda_{em}}))}, \quad \text{if } F_{\lambda_{ex},\lambda_e}^{obs} > LOR$$

Equation 2.3

$$LOR = F_{\lambda_{ex},\lambda_{em}} = F_{\lambda_{ex},\lambda_{em}}^{Blank} + 10 \times SD(F_{\lambda_{ex},\lambda_{em}}^{Blank})$$

In this thesis work, the use of 4 mm excitation pathlength¹⁰ cuvettes reduced IFE, however, there is still some IFE occurring due to the high optical density at 280 nm [2]. The IFE correction was performed where appropriate, according to the absorbance-based approach (ABA) (**Figure 2.4**) [4]. The ABA method uses the measured absorbance (A_λ) at each pair of excitation (λ_{ex}) and emission (λ_{em}) wavelengths to convert the observed fluorescence intensity (F_{obs}) into the corrected fluorescence intensity (F_{corr}), **Equation 2.2**. IFE correction was limited to the spectral coordinates which had fluorescence intensities that were above the limit of reporting (LOR, **Equation 2.3**) [79].

⁹ Particularly relevant to protein samples which have absorbance (>300 nm) in the same region of the spectrum significantly affected by light scattering, often leading to high OD.

¹⁰ Here, a 4 mm excitation pathlength results in an actual pathlength of 2 mm as emission is collected at a 90° from the centre of the cuvette.

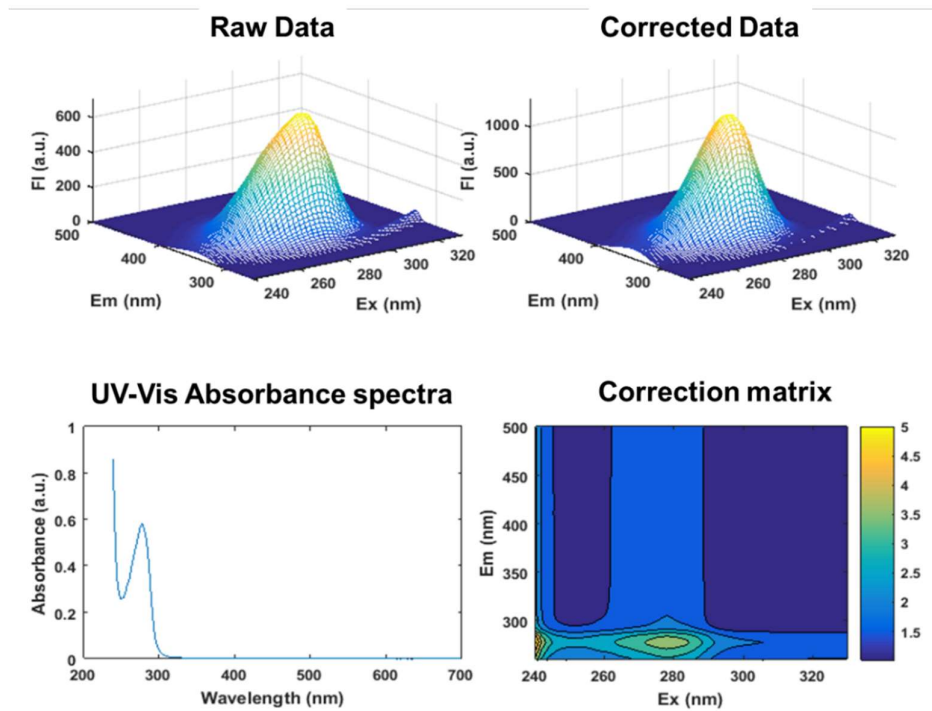


Figure 2.4: An example of a spectra corrected using the IFE correction based on the ABA approach.

Normalization

Normalization techniques (i.e. to the maximum peak or to area under peak =1) can be used to remove variances related with small concentration differences between the replicate samples, and day-to-day measurements [72]. Normalization (to area under peak=1) was used prior to PARAFAC resolution on data where the components of interest had highly varying signal magnitudes, normalisation here could facilitate the resolution of the weaker fluorophore contributions.

Smoothing

Smoothing is used in order to reduce unwanted noise from data. Smoothing used in this work is completed using the Savitzky-Golay algorithm. All smoothing completed in this thesis work used a second-order polynomial with a 15-point window size to reduce unwanted noise (**Figure 2.5**) [175].

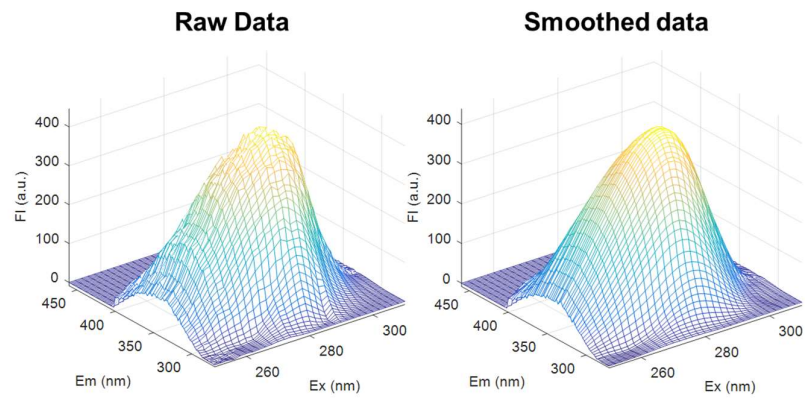


Figure 2.5: Spectra shown before and after Savitzky-Golay smoothing.

2.4 EXPERIMENTAL SYSTEM I: HSA-ANS STUDY

2.4.1 Sample preparation

Stock solutions of Human Serum Albumin (HSA) (3×10^{-5} M) and 1,8-anilinonaphthalene sulphate (3×10^{-4} M) were prepared in phosphate buffered saline (pH 7.4). Twenty samples with molar fractions/labelling ratio of ANS/HSA = 0.05 – 10 were prepared in triplicate (n=60) keeping the concentration of HSA constant (1.5×10^{-5} M) and varying ANS concentration (7.5×10^{-7} – 1.5×10^{-4} M) (**Figure 2.6**). Triplicate samples of the stock HSA (n=3) and stock ANS (n=3) were also prepared by adding equal amounts of stock solution and buffer. Prepared samples were stored in a -70°C freezer. Prior to analysis samples were defrosted overnight in a fridge kept at 2-8°C and pipetted into 0.4 cm × 1 cm quartz cuvettes (Lightpath Optical, UK) under laminar flow conditions. These cuvettes were chosen as the shorter 0.4 cm excitation pathlength lessens the effect of IFEs than standard 1 cm × 1 cm cuvettes, and, in addition, a smaller volume of sample is required to fill the cuvette. After the measurements, cuvettes were rinsed with HPLC grade water, and then rinsed three times with 100% isopropanol before rinsing again with HPLC grade water. The analysed protein samples were preserved by storing again in a -70°C freezer.

Several precautions were taken during sample preparation to prevent any contamination. Firstly, all solutions were prepared in a laminar flow hood and sterile filtered using 5 mL syringes (BD Plastik™) equipped with Minisart filters (Sartorius, 0.2 µm pore size). All pipette tips were sterilized using an Omega Media autoclave (Prestige medical, part no. 220140). Additionally, the stock solutions were prepared in amber volumetric flasks to minimise any photodegradation.

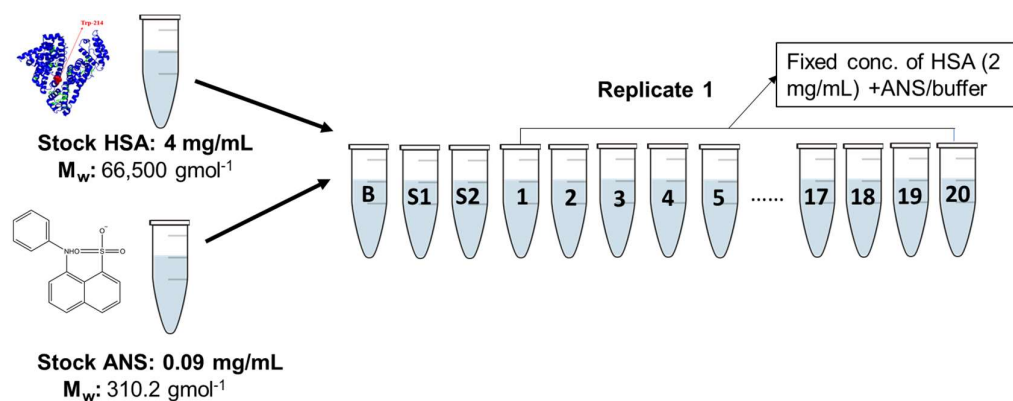


Figure 2.6: Preparation of samples for the HSA-ANS FRET study. Samples labelled 1-20 contain HSA, ANS and buffer, samples labelled S1 and S2 contained HSA and ANS in buffer, respectively and the sample labelled B referred to the blank sample containing buffer only.

2.4.2 Data collection parameters

UV-Vis absorbance spectra (200–800 nm) were obtained using Cary 60 UV-Vis Spectrophotometer along the short 0.4 cm pathlength, using a 5 nm step at a scan rate of 1200 nm min^{-1} and a temperature of 25°C. Fluorescence data were collected using a 2 nm step at a scan rate of 1200 nm min^{-1} and a temperature of 25°C. The short cuvette pathlength (0.4 cm) was used along the excitation, with the longer pathlength (1 cm) in emission, for the fluorescence measurements.

ARMES data was collected using Agilent Cary Eclipse Spectrophotometer in TSFS mode with $\lambda_{\text{ex}} = 240\text{--}440$ nm at varying wavelength offsets of 20–330 nm ($\lambda_{\text{em}} = 260\text{--}570$ nm) with 2 nm step increments for both axes, with 10 and 10 nm excitation/emission slit widths. The photomultiplier tube (PMT) detector voltage was fixed to 555 V in all cases. All samples were measured with four different polarizer settings: VV (vertical-vertical), VH (vertical-horizontal), HH (horizontal-horizontal), HV (horizontal-vertical). The anisotropy (r) was calculated using the standard anisotropy formula, which was then used to construct the corresponding multidimensional anisotropy maps.

Magic-angle fluorescence decays were recorded using PicoQuant FluoTime 200, with 295 nm pulsed LED excitation source and emission was collected at 350 nm. The repetition rate of the excitation laser was set to 4 MHz and decays obtained using

35 ps time resolution. The decays were collected with 20,000 counts in the channel of peak intensity.

2.4.3 Data pre-processing for chemometric analysis

Here, TSFS measurements were used in preference to EEM to minimize the Rayleigh scattering contamination when using wavelength offsets of $\Delta\lambda \geq 20$ nm. TSFS_{HV} and TSFS_{HH} measurements were used to calculate the G-factor ($G = I_{HV}/I_{HH}$) and this was used to correct the TSFS_{VH} spectra, giving the corrected perpendicular TSFS_⊥ spectra. The TSFS_{VV} spectra are referred as the parallel polarized, TSFS_∥, spectra. The total unpolarized TSFS_T spectra were calculated from the pTSFS spectra as follows: $TSFS_T = TSFS_{\parallel} + 2 \times TSFS_{\perp}$, and were used to assess the advantages of using polarized TSFS measurements instead of conventional TSFS measurements. The TSFS_∥ and TSFS_⊥ datasets, were then subjected to Raman scattering minimization by blank subtraction (PBS buffer spectrum) from the TSFS spectrum and IFE correction using the ABA approach [79]. IFE correction was necessary due to the change in the optical density of the samples ($Abs = 0.21 \pm 0.00$ to 0.97 ± 0.01 , at 280 nm, 4 mm pathlength) of solutions with constant HSA and increasing ANS concentrations.

TSFS_⊥ and TSFS_∥ datasets were then transformed from a non-trilinear TSFS layout to a trilinear EEM layout for chemometric data analysis and hereafter designated as t-EEM_T, t-EEM_⊥, and t-EEM_∥ [176]. Interpolation was applied in order to handle the area with no experimentally acquired spectral information in the t-EEM layout, and second-order scatter was also corrected via interpolation [78]. Finally, the t-EEM data were smoothed using Savitzky-Golay smoothing to reduced unwanted noise (**Figure 2.7**).

The pre-processed t-EEM_T, t-EEM_⊥, and t-EEM_∥ data were arranged into a three-way array (**X**) of size $63 \times 131 \times 101$ (samples (excluding ANS stock) $\times \lambda_{em} \times \lambda_{ex}$) and normalized (unit area=1) for the global HSA-ANS emission, and a three-way array (**X**) of size $63 \times 51 \times 31$ for the sub-region of HSA emission (non-normalised), before chemometric analysis.

Fluorescence decay curves were fitted using a tri-exponential decay law. The intensity weighted average (**Equation 2.4**) corresponds to the average amount of time

a fluorophore spends in the excited state, for a collection of fluorophore populations the lifetime of each is weighted by the relative contribution to the total fluorescence [177]. In the case of amplitude weighted average (**Equation 2.5**) the weight factor is the amplitude fraction; the amplitude weighted average is proportional to steady-state measurements.

Equation 2.4

$$\langle \tau \rangle_f = \frac{\sum a_i \tau_i^2}{\sum a_i \tau_i}$$

Equation 2.5

$$\langle \tau \rangle_a = \frac{\sum a_i \tau_i}{\sum a_i}$$

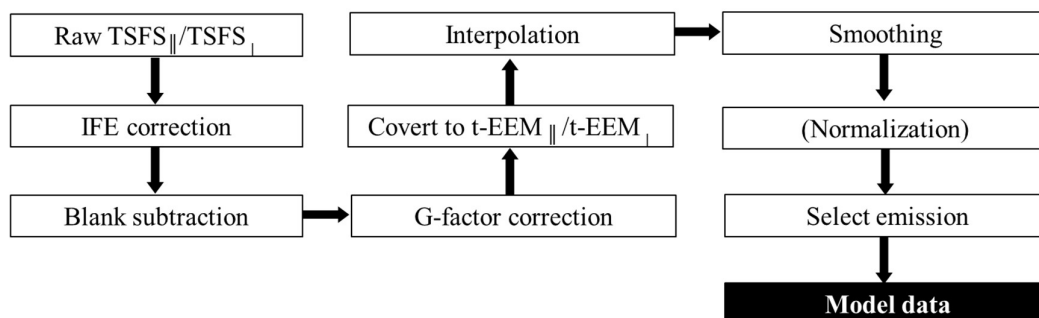


Figure 2.7: Pre-processing operations applied to correct HSA-ANS.

2.5 EXPERIMENTAL SYSTEM II: LIPOSOME STUDY

2.5.1 Sample preparation

Liposome were prepared using extrusion method (**Figure 2.8**). Firstly, stock solutions (1 mM) of lipophilic dyes (DiI and DiD) were prepared in ethanol [178, 179]. Mixtures of lipids (10 mg/mL) and lipophilic dyes (<0.5 % labelling ratio) were homogenously dispersed in chloroform in a glass vial and dried overnight under vacuum. The resulting lipid thin film was re-suspended in water or buffer solution (PBS and ABC) and the solution was vortexed for 5 minutes to give a milky suspension. Extrusion was completed at 25°C (above the phase transition temperature of DMPC) using an Avanti mini-extruder kit with a heating block (part no. 610000), and 200 nm polycarbonate filters (Whatman, 800281), the extruder was thoroughly rinsed before use and a buffer solution was passed through before extrusion. The lipid suspension was passed through the extruder 21 times (ensuring the solution was collected on the opposite syringe to the one used in picking up the lipid suspension). Liposomes were freshly prepared each day and analysed within ~8 hours. Nine separate extrusions were required in total, as the interaction was carried out in three aqueous environments: water, PBS, and ABC and 3 replicate interaction datasets per aqueous environment were measured.

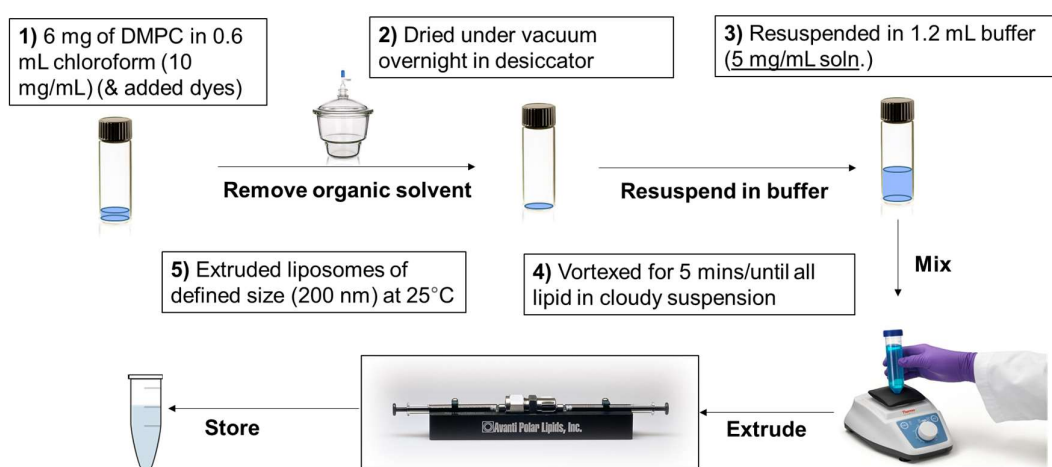


Figure 2.8: An overview of the liposome preparation technique used.

To prepare the protein-liposome samples, stock solutions of HSA (4 mg/ml, 0.2 μm filtered) and extruded DMPC liposomes (5 mg/ml) were prepared in water and buffer solutions (PBS and ABC). Ten different concentrations were prepared keeping the concentration of DMPC constant (0.25 mg/ml or 0.37 mM) and varying the concentration of HSA (0 – 2 mg/mL or 0-0.03 mM), corresponding to 1:185 to 1:12 molar ratios of HSA:DMPC (**Figure 2.9**). All samples were incubated at 25°C for ~2-3 hours prior to analysis to ensure that complete interaction had occurred between the protein and liposome. All samples were analysed within an 8-hour period on the same day as extrusion.

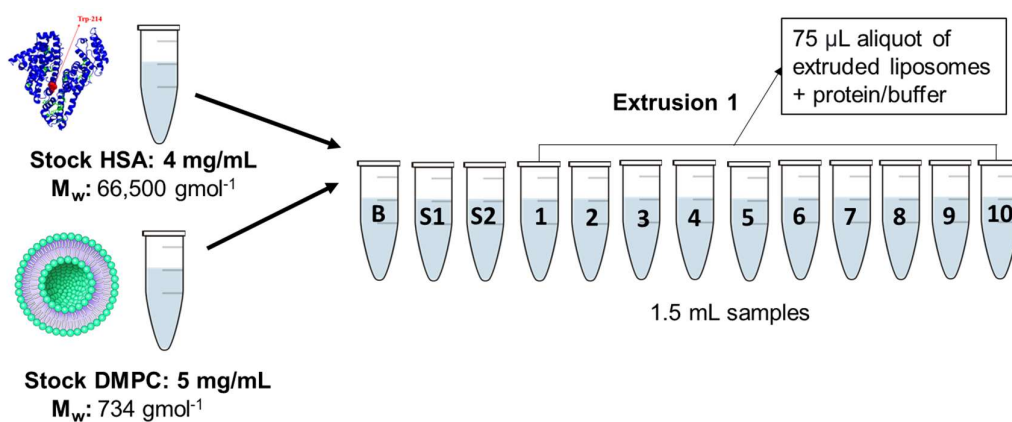


Figure 2.9: Preparation of samples from one extrusion of liposomes (9 extrusions were required in total) for the HSA-DMPC interaction study. Samples labelled 1-10 contain HSA, DMPC and buffer, samples labelled S1 and S2 contained HSA in buffer and DMPC in buffer, respectively and sample labelled B referred to the blank sample containing buffer only.

Again here, the same precautions as previously used in the HSA-ANS study were taken here during sample preparation to prevent any contamination. However in this case only the protein stock solution used was filtered using 5 mL syringes (BD Plastik™) equipped with Minisart filters (Sartorius, 0.2 μm pore size), as the liposomes were already extruded.

2.5.2 Data collection parameters

DLS measurements were used to assess the mean vesicle size and were collected at a 173° detection angle, using a Malvern Zetasizer® Nano ZS (Malvern

Panalytical Ltd.). Each sample was first equilibrated at 25°C for 120 seconds before being measured three times (each measurement was an average of 20 runs of 10 s duration). UV-visible absorption spectra were obtained using Cary 60 UV-Vis Spectrophotometer (Agilent Technologies) along the short axis of the cuvette (4 mm) at a scan rate of 1200 nm min⁻¹ and a temperature of 25°C.

Steady-state emission and pTSFS spectra were collected again using the Cary Eclipse Spectrophotometer (Agilent Technologies), samples were excited along the short axis (4 mm) and emission was collected along the long axis (10 mm). pTSFS data were collected for the intrinsic HSA emission over an excitation range of $\lambda_{\text{ex}}=250\text{--}310$ nm at varying wavelength offsets of 20–150 nm ($\lambda_{\text{em}}=270\text{--}400$ nm) with 2 nm step increments for both axes and a scan rate of 1200 nm min⁻¹ with PMT voltage of 875 V. Again, wavelength offsets of $\Delta\lambda\geq 20$ nm [6] were used, to minimize the Rayleigh scattering contamination. Three different 2D emission scans were also collected measuring HSA emission ($\lambda_{\text{ex/em}}=280 / 310\text{--}420$ nm) and two regions of the lipophilic dye's emission ($\lambda_{\text{ex/em}}=532 / 550\text{--}700$ nm (FRET trace) & $\lambda_{\text{ex/em}}=620 / 640\text{--}740$ nm (direct excitation of FRET acceptor)), all scans were collected with 1 nm increments, at a scan rate of 600 nm min⁻¹, and PMT voltage set to 875 V (for $\lambda_{\text{ex}}=280$ nm), 900 V (for $\lambda_{\text{ex}}=532$ nm), and 800 V (for $\lambda_{\text{ex}}=620$ nm). Excitation and emission monochromators slit widths were 5 nm for all measurements.

All fluorescence emission measurements were collected using two different polarizer settings: VV (vertical-vertical), VH (vertical-horizontal). The instrumental G-factor was calculated each day from the HH (horizontal-horizontal), HV (horizontal-vertical) spectra of the samples with the best SNR, which were the samples containing HSA only. The anisotropy (r) was then calculated as before using the standard anisotropy formula [4, 18]. Magic-angle fluorescence decays were recorded as previously described using Fluotime 200 (see **section 2.4.2**).

2.5.3 Data pre-processing for chemometric analysis

Raman scattering was reduced by blank subtraction of the buffer spectrum (water, PBS, or ABC) from the samples spectrum and spectra were smoothed using the Savitzky-Golay algorithm to reduce unwanted noise.

For the 3D MDF spectra, spectra were corrected as previously described (see **section 2.4.2**). Again, Raman scattering was reduced by blank subtraction from the TSFS spectrum. For PCA analysis, the blank subtraction was made by blank subtraction of the buffer spectrum (water, PBS, or ABC). For PARAFAC analysis the blank subtraction used was of the liposomes only spectrum in each buffer to minimise scatter across the spectrum. IFE [79] correction was not possible here due to strong light scattering from the liposomes in the absorbance spectra.

Prior to PCA, datasets were re-shaped to form a two-way dataset (36×2046 (interaction samples $n=30$, stock DMPC liposomes $n=3$, stock HSA $n=3$)). As before, prior to PARAFAC analysis TSFS data was transformed to a trilinear EEM layout (t-EEM_T, t-EEM_⊥, and t-EEM_∥) and corrected via interpolation to handle the area with no experimentally acquired spectral information [78, 176]. t-EEM data was cut to select the area of interest ($\lambda_{ex/em} = 250-310 / 270-400$ nm), smoothed using the Savitzky-Golay algorithm. The pre-processed t-EEM data (**Figure 2.10**) were arranged in a three-way array (**X**) of size $99 \times 66 \times 31$ and $33 \times 66 \times 31$ (samples $\times \lambda_{em} \times \lambda_{ex}$) for global (all samples, all buffers) and sub-models (per interaction medium), respectively (where interaction samples $n=90/30$, stock HSA $n=9/3$). The fluorescence decay curves were again fitted using a tri-exponential decay law (**Equation 2.4**).

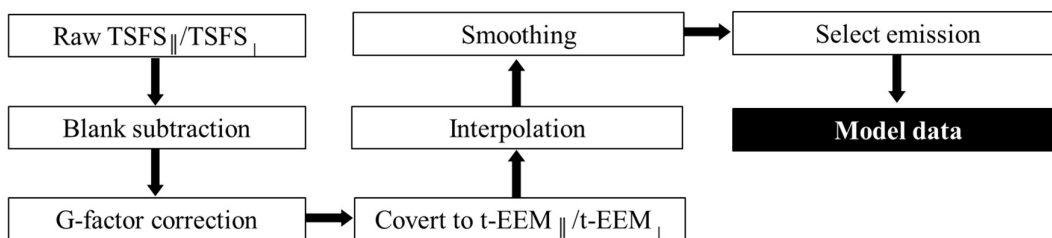
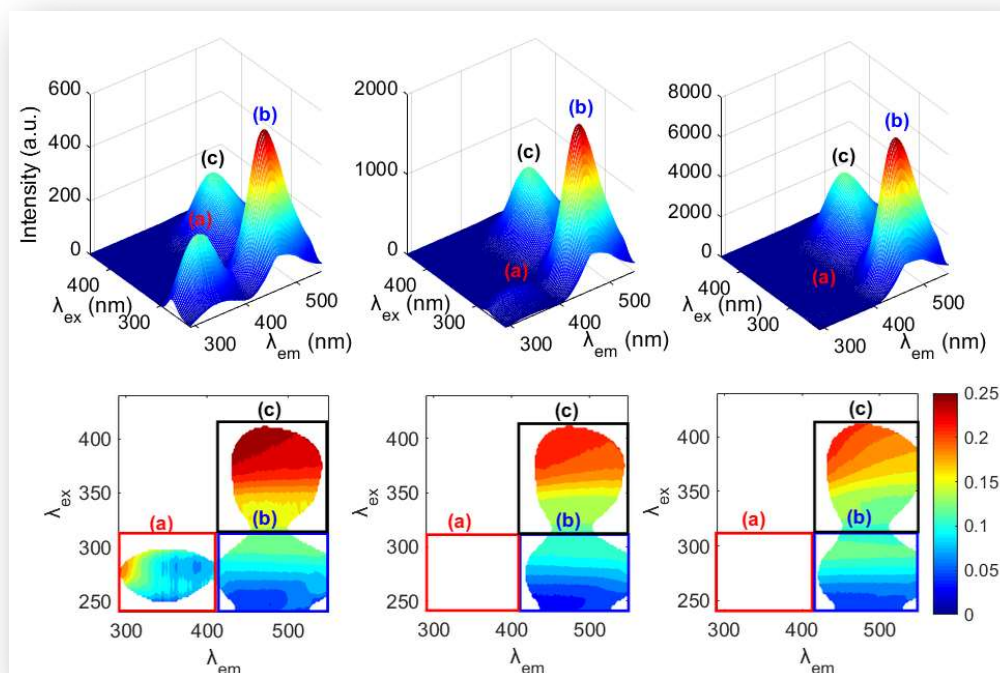


Figure 2.10: Pre-processing operations applied to correct HSA-DMPC data.

3 SPECTRAL ANALYSIS OF THE INTERACTION BETWEEN HSA AND ANS

Graphical abstract:



FRET is an important tool used in biophysical analysis, and also, the main cause of the non-linearity of intrinsic fluorescence emission observed in Immunoglobulin G and insulin [6, 7, 107], therefore, the accurate analysis of FRET¹¹ is critical. Conventionally, parameters, such as FRET efficiency, are calculated using 2-D (wavelength vs. emission intensity) steady-state, or time-resolved, measurements of the quenching of donor fluorescence intensity, the enhancement in acceptor fluorescence intensity or the decrease in the donor lifetime [4, 180]. However, the low information content of simple 2-D spectral measurements from complex samples with overlapping emission from multiple fluorophores makes multi-dimensional

¹¹ In terms of measuring spectral changes, such as donor quenching, FRET sensitized acceptor emission in order to recover accurate FRET parameters such as FRET efficiency values.

fluorescence (MDF) measurements more suitable for analysis of the different spectral changes occurring during the interaction.

This chapter is the first of two which will discuss the findings of studying the HSA-ANS model system using ARMES methodology. Here, the model system and findings from the spectral analysis of the recorded MDF spectra are discussed along with the biochemical applications of studying the photophysical processes occurring the system in a multi-dimensional manner. The main results presented in Chapters 3 and 4 were published in *Biophysica et Biochemica Acta* in February 2021 [9].

3.1 HSA-ANS MODEL SYSTEM

In this study, a human serum albumin (HSA) and 1,8-anilinonaphthalene (ANS) model system was used to study the process of FRET using ARMES methodology. This system was chosen as it is a well-characterised, relatively simple model system, to demonstrate the use of ARMES as a tool to study FRET. In addition, extensive data was available on a similar on a similar bovine serum albumin (BSA) ANS model system [181, 182].

In this model system, HSA acts as a donor molecule and interacts photo-physically via FRET with ANS (acceptor) that is hydrophobically bound to HSA. HSA is the most abundant protein in the blood, accounting for ~52-60% of the total plasma protein, and facilitates the binding and transport of a wide variety of endogenous and exogenous small-molecule ligands [183]. Structurally, HSA is a heart shaped protein [184] consisting of 585 amino acids, in three domains (I, II and III), each of which comprises of two subdomains (A and B) [185]. The intrinsic fluorescence of HSA is dominated by the single tryptophan fluorophore (Trp-214) located between IA and IIB, with a smaller contribution from 17 tyrosine residues that are distributed throughout the protein and are more solvent exposed (**Figure 3.1/A**), whereas the contribution of Phenylalanine is negligible [4]. There are two primary small molecule binding sites referred to as; Sudlow I (which is located in subdomain IIA, in close proximity (~2 nm) to Trp-214 [186, 187]) and Sudlow II (which is located in subdomain IIIA, further from Trp-214 >2nm), along with a number of secondary binding sites [188, 189].

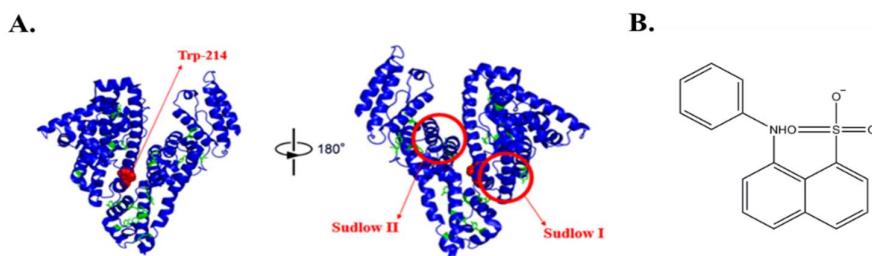


Figure 3.1: (A) Human serum albumin with singular tryptophan residue (red) and 17 tyrosine residues (green) highlighted. The major binding sites (Sudlow I & II) are also indicated above (Image sourced from PDB and edited using Pymol) (B) 1,8-anilinonaphthalene sulfonate, a hydrophobic small molecule probe.

ANS is a commonly used fluorescent probe due to its desirable spectroscopic properties¹² (**Figure 3.1/B**) [190]. The emission of ANS arises from contributions of two distinct excited states; the non-polar (NP) and charge transfer (CT) excited state [191, 192], and is highly sensitive to the polarity of the surrounding environment. The NP excited state of ANS is first reached upon excitation and is localized on the naphthalene ring of ANS (**Figure 3.1/B**). Emission from this NP excited state occurs in non-polar environments (e.g., hydrophobic binding sites of HSA) or in aprotic solvents (e.g., Dimethyl sulfoxide (DMSO)), and shows a significant increase in quantum yield and hypsochromic shift relative to ANS in aqueous buffer (**Figure 3.2/A**). The hypsochromic shift here is due to a decreased Stokes shift in the non-polar environment around polar, solvatochromic dyes [193]. In more polar solvents, the NP excited state undergoes an intramolecular electron-transfer reaction to form the CT excited state and this low-energy state emits at longer wavelengths (**Figure 3.2/B**). In aqueous solution another intermolecular electron transfer (ET) occurs which involves ionization and electron solvation, and this process serves as an efficient quenching mechanism of the CT state which explains the low fluorescence quantum yield of ANS observed in aqueous polar solvents like water (**Figure 3.2/A**) [190, 192]. However, in non-aqueous polar solvents, such as methanol, the deactivation process through ET to solvent does not occur¹³ (**Figure 3.2/A**) [194]. The fact that ANS is weakly fluorescent when free in aqueous buffer, such as water, and shows a large hypsochromic shift, increase in quantum yield along with an increase in anisotropy and fluorescent lifetime upon incorporation into the hydrophobic binding sites of HSA means it can provide a lot of information about the HSA-ANS interaction system under study [21, 193]. The spectral properties of ANS and its derivatives have made these fluorescent probes popular in range of applications such as studying protein binding [195], characterising enzymatic binding sites [21], and investigating properties such as action potentials in neuronal systems [196].

¹² Low quantum yield in aqueous polar buffer, with a significant increase in quantum yield and hypsochromic shift upon hydrophobic binding.

¹³This effect has been attributed to the slowness of solvent reorientations for larger polar molecules compared to water molecules.

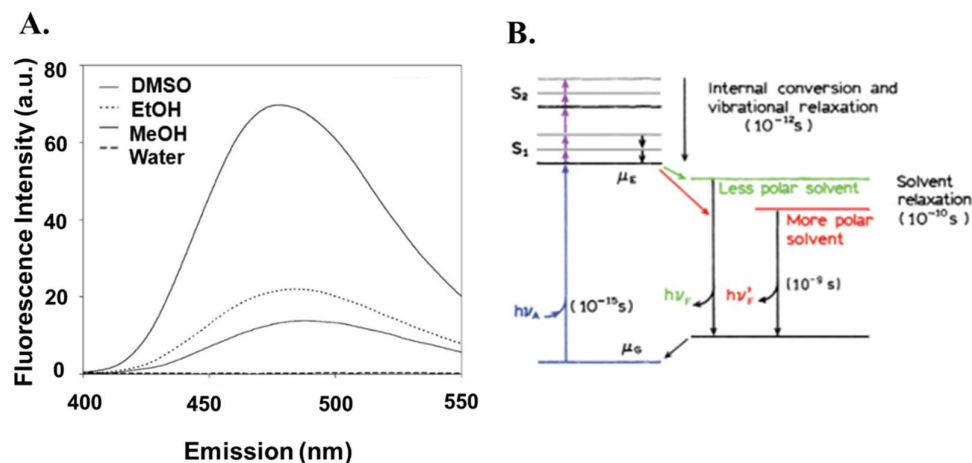


Figure 3.2: (A) Fluorescence emission of ANS (1×10^{-6} M) in aprotic solvent, DMSO, polar non-aqueous solvents, ethanol (EtOH) and methanol (MeOH), and in an aqueous polar solvent, water (Image adapted from Hawe *et al.* [29]), and (B) The Jablonski diagram for solvent relaxation, showing a red shift in more polar solvents (Image adapted from Lakowicz [4]).

There are numerous FRET processes occurring in this HSA-ANS model system, namely, the hetero-FRET between the Trp of HSA and ANS, the hetero-FRET occurring between the Tyr-Trp residues of HSA and homo-FRET processes between Tyr residues of HSA (note: there should be no homo-FRET between Trp residues here as only one Trp residue is present in HSA). The work presented here aims to model the most significant FRET process occurring in this system which is the process of hetero-FRET from the singular Trp of the HSA donor molecule to the ANS, FRET acceptor molecule.

3.2 DETERMINATION OF FRET PARAMETERS

In the HSA-ANS model system, as ANS is added, it becomes hydrophobically bound to the binding sites of HSA [197, 198]. Upon binding, as expected, there is a dramatic increase in the quantum yield of ANS along with a bathochromic/red shift in excitation spectrum and a hypsochromic/blue shift in emission going from the polar environment of the aqueous buffer solution to the non-polar environment of the hydrophobic binding sites of HSA [199]. In addition to the increase in quantum yield and spectral shifts of ANS when bound to the protein, a shoulder is observed in the emission (**Figure 3.3/A**), which is likely due to the presence of more than one binding site in HSA [189, 198], this affect is discussed in more detail in subsequent sections.

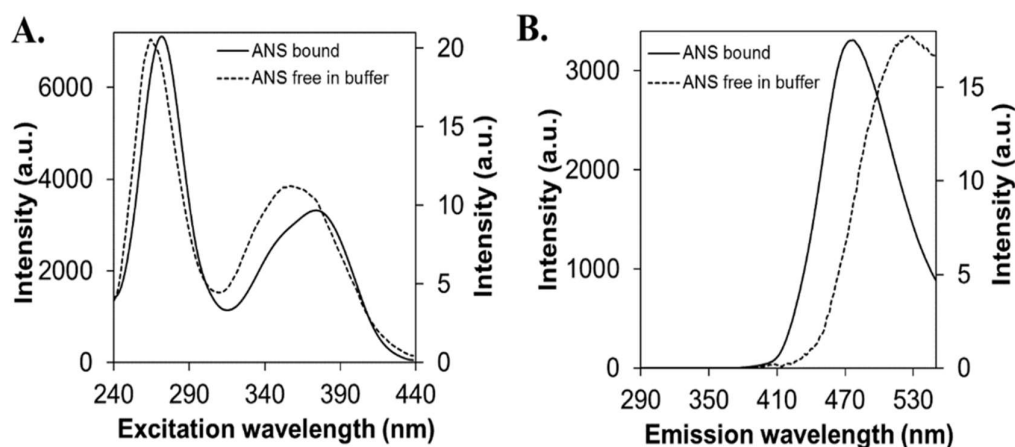


Figure 3.3: Enhancement of ANS fluorescence emission upon incorporation into the hydrophobic binding sites in HSA (Note: Intensity values for ANS bound to HSA and ANS free in buffer shown on left and right axis of plots, respectively). The figure shows the excitation and emission profiles of 1.5×10^{-4} M ANS in aqueous buffer 1.5×10^{-4} M (axis on the right) ANS and when added to 1.5×10^{-5} M solution of HSA, at an emission wavelength of 480 nm (A) and at an excitation of 380 nm (B). The emission becomes blue-shifted (~ 50 nm) upon binding to HSA.

The high degree of spectral overlap between HSA emission and ANS absorbance (**Figure 3.4**), as well as the distance of the ANS binding sites being close enough, to the singular Trp-214 of HSA results in strong FRET as ANS binds to the

protein. The calculated spectral overlap (**Equation 1.10, Chapter 1**) between HSA emission and ANS absorption spectra $J(\lambda) = 5.76 \times 10^{15} \text{ nm}^4 \text{ M}^{-1} \text{ cm}^{-1}$ (**Figure 3.4**) was used to calculate an R_0 of 4.82 nm (value in a similar range to other studies involving HSA [200, 201]) (**Equation 3.1**), estimating the orientation factor $\kappa^2=0.666$ and using values of $\phi_D=0.13$, $\eta=1.33$ for the quantum efficiency of the donor and the refractive index of the sample, respectively. The distances between the donor and acceptor (r) (**Equation 1.9, Chapter 1**) were calculated using the FRET Efficiency values (**Equation 3.2**) at different concentrations of ANS. The distances ($r= 6.4\text{--}4.1$ nm, for $[\text{ANS}]/[\text{HSA}] = 0.25\text{--}10$) fall within the range $0.5R_0 < r < 1.5R_0$ which is clear evidence that FRET occurs as ANS binds to the protein.

Equation 3.1

$$R_0 = 0.211 \times \sqrt[6]{\frac{\kappa^2 \cdot \phi_D \cdot J(\lambda)}{\eta^4}}$$

where, with R_0 (given in Å) is the Förster distance i.e., the D-A distance at which the FRET efficiency is 50%, κ^2 = orientation factor between the donor and acceptor, η = refractive index, ϕ_D = quantum yield of the donor in absence of the acceptor and J = overlap integral.

Equation 3.2

$$E = 1 - \frac{I_{DA}}{I_D}$$

where, I_{DA} and I_D are the total donor fluorescence intensities in presence and absence of the FRET acceptor, respectively.

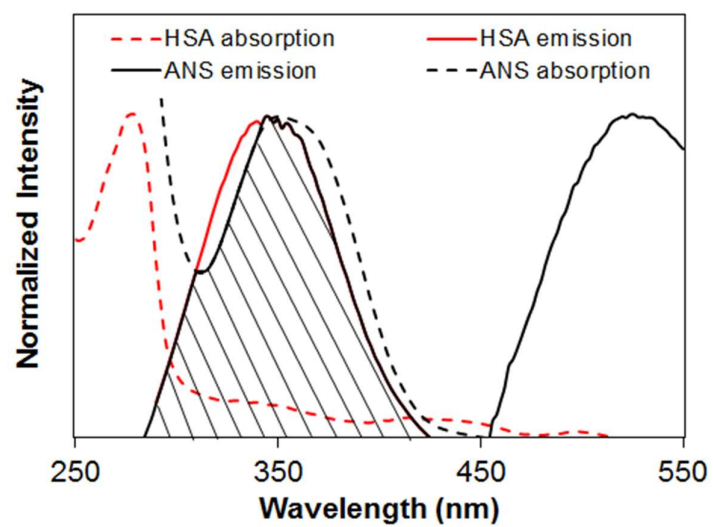


Figure 3.4: Normalised absorbance and emission spectra of HSA and ANS showing the spectral overlap of HSA (solid red line) emission with ANS (dashed black line) absorption spectra resulting in the occurrence of FRET.

3.3 UV-VIS ANALYSIS

The absorbance spectrum (**Figure 3.4**) of ANS shows a bathochromic shift or red-shifted of ~ 5 nm relative to the ANS free in buffer as it is incorporated into the hydrophobic binding sites of HSA. This bathochromic shift, is again caused by the change in the polarity of the ANS environment, going from the polar environment of the aqueous buffer to the non-polar environment of the hydrophobic binding sites of HSA [193].

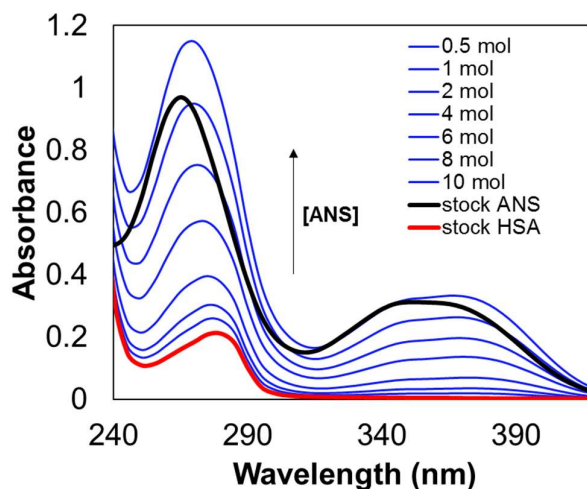


Figure 3.5: UV-Vis absorption spectra of solutions containing HSA only in buffer, ANS only in buffer and the HSA-ANS complexes with increasing molar ratios of ANS/HSA.

As ANS is added to the system the absorbance spectra of the HSA-ANS samples are observed to increase, but the overlapping spectra of the HSA and ANS (**Figure 3.5**) makes quantitative analysis of the underlying components unfeasible using conventional analysis of the absorbance spectra. However, further investigation of the interaction between HSA-ANS using the UV-Vis absorbance spectra by MCR-ALS [202], facilitates the decomposition of the absorbance spectra into the contributing species. MCR-ALS [96] entails decomposing the matrix \mathbf{D} as: $\mathbf{D} = \mathbf{C} \cdot \mathbf{S}^T + \mathbf{E}$ by iterative alternating least-squares (ALS) optimization of \mathbf{C} (matrix of the concentration profiles) and \mathbf{S}^T (the spectra matrix) to minimize of the Frobenius norm of \mathbf{E} (**section 1.5.2, Chapter 1**).

To initialize the optimization process, a SIMPLISMA based algorithm was used. The spectral matrix was decomposed during ALS optimization implementing non-negativity constraints on both concentration and spectral profiles to ensure that the mathematical solution was chemically meaningful. Correspondence among species was used to restrict the rotational ambiguity, i.e. presence/absence of analytes in stock samples was actively set [203]. Singular Value Decomposition (SVD) was used to estimate the number of components and was found to be three in all cases.

Decomposition of the spectra extracted the concentration and pure spectral profiles of the individual species formed during the binding process [204]. Here, the data matrix **D** (66×41) was constructed with rows representing the UV-Vis spectra at the different molar fractions (20 [ANS]/[HSA] molar ratio solutions, n=60) and ANS (n=3) and HSA stock solutions in triplicate (total n=66), and in the columns (41) the absorbance values measured at each spectral wavelength between 240 and 440 nm (every 5 nm). Three profiles were resolved corresponding to free ANS, free HSA, and the HSA-ANS complexes (**Figure 3.6/A**). Using the initial concentrations of each species the concentration of the resolved species could be calculated using the corresponding MCR Scores (**Figure 3.6/B**). The free HSA species is observed to decrease upon complexation with added ANS (from 1.50×10^{-4} M to 8.54×10^{-5} M at [HSA]/[ANS]=10), whereas the free ANS is observed to increase as more ANS is added to the solution (no free ANS observed up to \sim [HSA]/[ANS]=2 i.e. all bound to HSA, free ANS increases to 7.4×10^{-5} M at [HSA]/[ANS]=10) (**Figure 3.6/C-D**).

From Job's plot analysis (see section 3.5.1) it was determined that complex formation took place with 1:2 (HSA: ANS) stoichiometry, therefore the third species resolved which corresponds to the formed complex is a combination of all formed complexes. These individual complexes, unfortunately, were not resolvable using MCR-ALS analysis of UV-Vis data presented here and to do so would require a higher resolution dataset, with smaller increments (<5 nm) and a slower scan speed than used in the study (<1,200 nm min⁻¹) during the spectral measurements [189]. Unfortunately, this was outside the scope of the current study and recollection of the sample spectra to obtain a higher resolution dataset was not feasible, however, this is an area which may be investigated in future studies in the group using similar interaction systems.

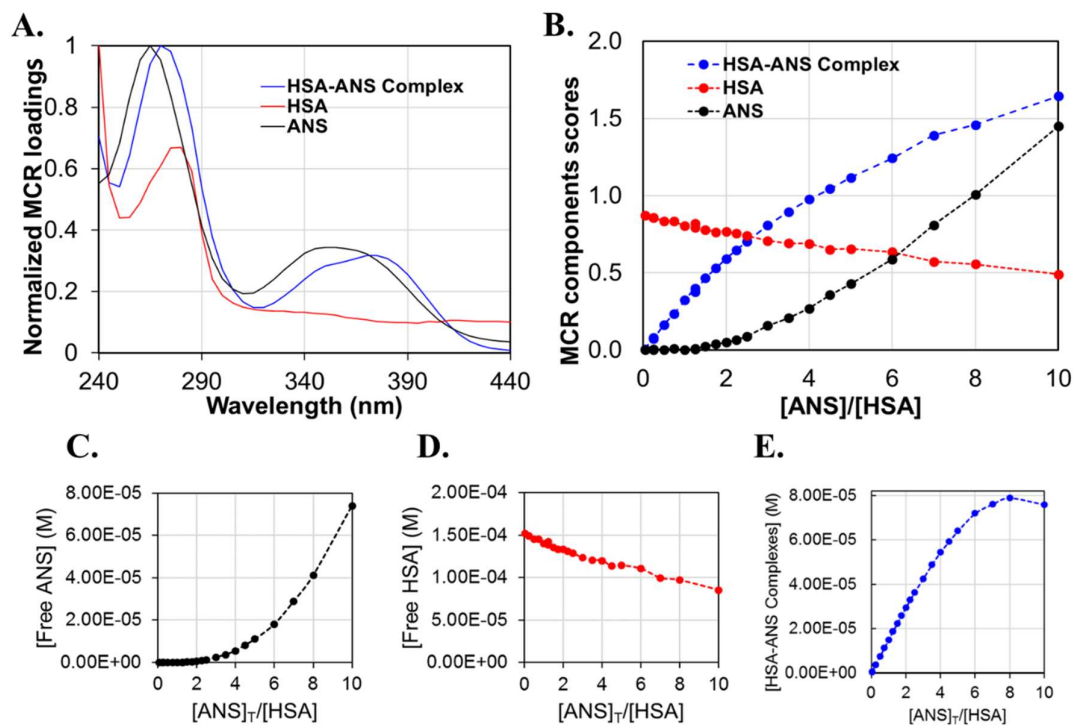


Figure 3.6: MCR modelling of UV-Vis absorption spectra: **(A)** Spectral loadings (absorption spectra), **(B)** scores (relative concentrations) showing the formation of HSA-ANS complexes, **(C-E)** Concentration evolution of: **(C)** free ANS, **(D)** free HSA and **(E)** HSA-ANS complexes (calculated by subtracting free ANS from the total ANS in the system i.e. $[\text{HSA-ANS}] = [\text{ANS}]_T - [\text{ANS}]_F$).

3.4 FLUORESCENCE MDF SPECTRA

The 3D t-EEM spectra recorded for the HSA-ANS complexes show three emission peaks (**Figure 3.7**): peak A ($\sim 280/\sim 350$ nm $\lambda_{\text{ex/em}}$) corresponds to intrinsic HSA emission (combination of Trp and Tyr emission) which is blue-shifted and quenched upon ANS addition. The strong emission blue-shift (~ 24 nm) up to ~ 2 molar equivalents of ANS, correlates with increasing FRET as ~ 2 molecules of ANS become bound to HSA. Peaks B ($\sim 270/470$ nm $\lambda_{\text{ex/em}}$) and C ($\sim 380/470$ nm $\lambda_{\text{ex/em}}$) correspond to fluorescence of ANS in the hydrophobic sites. The ANS peak positioned at $\lambda_{\text{ex}} = \sim 270$ nm (peak B), is expected to increase not only due to an increase in the concentration of ANS added to the system, which is directly excited, but also increases due to FRET from HSA (i.e. ANS indirect excitation), this increase in emission intensity is coupled with depolarisation of the emission as seen from anisotropy analysis (see section 3.4.1).

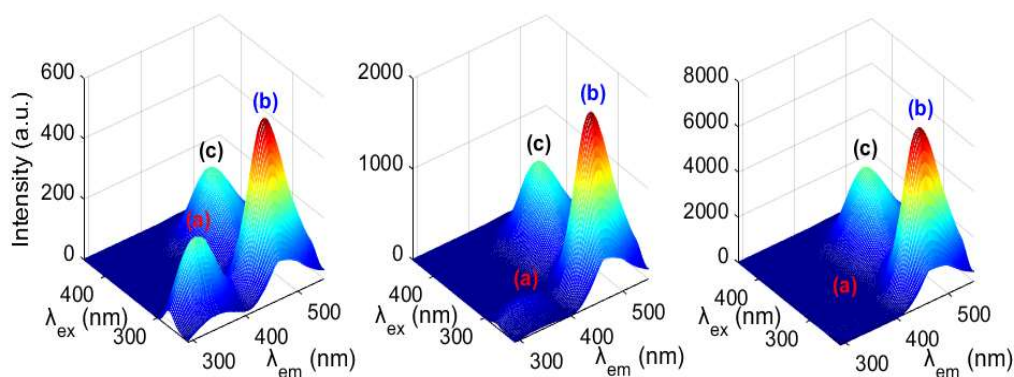


Figure 3.7: t-EEM_T spectra of representative HSA-ANS samples with varying [ANS]/[HSA] ratios: (left) 0.25, (middle) 1.0, and (right) 10. Three main emission bands are observed: **(a)** Intrinsic HSA fluorescence (composed of Tyr & Trp emission); **(b)** ANS fluorescence bound to HSA (composed of direct & indirectly excited emission); and **(c)** ANS fluorescence bound to HSA (direct emission only).

Comparison of the spectral shapes of 2D spectra at the maximum emission of each peak according to polarization shows clear differences are observed in shape of the excitation profile of the directly excited bound ANS (**Figure 3.7**, peak C) in parallel and perpendicular polarizations. The shoulder which appears at ~ 350 nm in

the excitation spectrum (as seen in comparison to ANS in aqueous buffer (**Figure 3.8/C**) of the ANS bound to the protein, was stronger in the t- EEM_⊥ spectra and may be due to a larger contribution from ANS bound to secondary binding sites of HSA in which polarization is not as strongly retained. The blue shifted emission of the shoulder observed may indicate that these sites are more hydrophobic in nature [189].

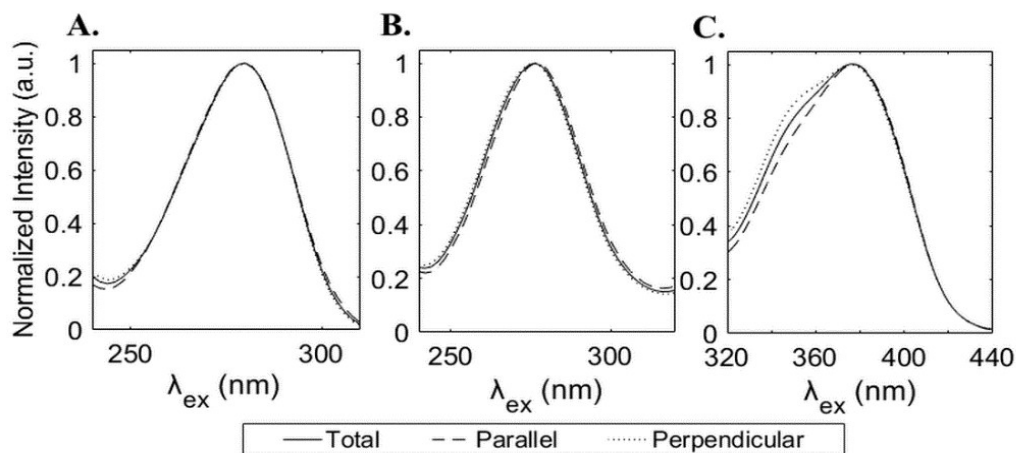


Figure 3.8: Normalized excitation spectra for a representative $[ANS]/[HSA] = 1$ sample of each of the different polarization measurements: **(A)** peak a, $\lambda_{em}=350$ nm, intrinsic HSA fluorescence; **(B)** peak b, $\lambda_{em}=470$ nm, ANS bound to HSA fluorescence, direct & indirect emission; and, and **(C)** peak c, $\lambda_{em}=470$ nm, ANS bound to HSA fluorescence, direct emission only. The shoulder observed at ~ 350 nm in the excitation spectrum was stronger in the t- EEM_⊥ spectra.

3.4.1 Aniso-t-EEMs and anisotropy analysis

From analysis of the anisotropy of a single point at the maximum emission of each peak upon addition of ANS (**Figure 3.9**) we observe; a high anisotropy of the ANS signal arising from direct excitation as the small molecule ANS binds to the larger HSA ($r=0.25-0.18$), a low anisotropy in the case of ANS arising from direct and indirect excitation ($r=0.08-0.09$), and finally a low anisotropy which increases slightly for HSA ($r=0.08-0.11$).

The anisotropy of the ANS signal arising from direct excitation (**Figure 3.7/peak C**) is observed to be higher at lower molar ratio of ANS/HSA, which can be explained by the fact that ANS is known to bind with two different binding modes

[197]; first occupying the Sudlow II site (**Figure 3.1/A**) ($r= 4.85$ nm, i.e., distance from Trp-214) with high affinity leading to tighter binding and higher anisotropy at lower concentrations of ANS, next as ANS is added secondary binding sites are occupied in a more non-specific character [188, 198]. The low anisotropies observed in the case of the ANS signal arising from direct and indirect excitation ($r=0.08-0.09$), and the signal arising from intrinsic HSA emission ($r=0.08-0.11$) are caused by FRET processes occurring in the system. FRET is known to cause depolarization of emission [18, 67, 205], and here analysis of anisotropy clearly shows this depolarization of the ANS emission affected by the indirect excitation via FRET from Trp-214, and also of the intrinsic HSA emission (**Figure 3.9**) as a consequence of the intrinsic FRET processes occurring within the protein; homo-transfer-FRET (homo-FRET), Tyr-Tyr, (there should be no Trp-Trp homo-FRET as HSA contains a single Trp), and hetero-FRET (Tyr-Trp) [22, 30].

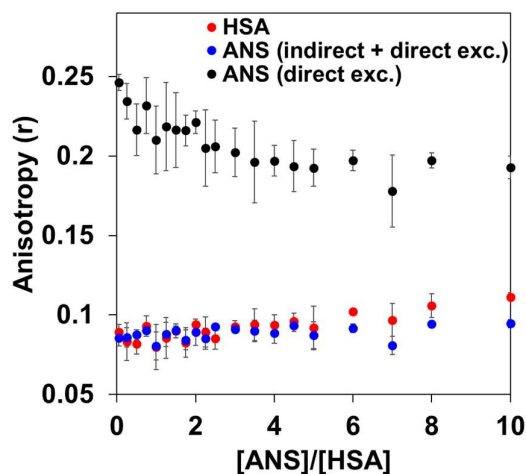


Figure 3.9: Anisotropy values at the maximum emission of each peak; for HSA emission ($\lambda_{\text{ex/em}} = 280/250$ nm), ANS emission arising from direct and indirect excitation ($\lambda_{\text{ex/em}} = 276/470$ nm) and from ANS emission arising via direct excitation only ($\lambda_{\text{ex/em}} = 380/470$ nm).

Although analysis of the anisotropy at a single point of emission provides useful information, aniso-t-EEM could provide a clearer visualisation of FRET processes (**Figure 3.10**). Here, the aniso-t-EEMs clearly showed ANS emission depolarisation ($\lambda_{\text{ex/em}} = 250-310/420-550$ nm), caused by hetero-FRET from the HSA donor (mostly Trp) to ANS (**Figure 3.10/region B**). We can also visualise the

depolarization of intrinsic HSA emission ($\lambda_{\text{ex/em}} = 250\text{--}300/290\text{--}390$ nm) (**Figure 3.10/region A**) [22, 30]. In addition, the *aniso*-t-EEMs also provided information about ANS binding from the variation observed in the directly excited ANS emission region ($\lambda_{\text{ex/em}} = 320\text{--}420/420\text{--}550$ nm) (**Figure 3.10/region C**). The differences observed in spectral shape of the excitation profile (**Figure 3.8**) of directly excited ANS ($\lambda_{\text{ex/em}} = 320\text{--}420/420\text{--}550$ nm), in parallel and perpendicular polarizations also manifests itself in the anisotropy of the directly excited ANS region. The unique anisotropy observed, along with complementary spectral analysis provided information on the nature of the binding sites occupied by ANS in HSA. It appears that as ANS first binds, at low molar ratios, to HSA, the emission anisotropy is more homogenous, whereas at higher ANS molar ratios ($[\text{ANS}]/[\text{HSA}] > 1$), more variation is observed in the anisotropy maps (**Figure 3.10/region C**). As ANS is known to bind to HSA with two different binding modes, it could be hypothesised, as ANS binds to the highest affinity binding site at lower molar ratios of $[\text{ANS}]/[\text{HSA}]$ a more homogenous anisotropy is observed across the emission space and as the secondary binding sites are occupied the emission detected becomes more depolarised, generating anisotropy variation across the emission [188, 198]. As the secondary HSA binding sites are occupied, emission becomes more depolarized due to ANS homo-FRET [195, 206]. Furthermore, in these lower affinity sites, ANS is said to be less strongly bound, than in the Sudlow II site, thus facilitating more rotational diffusion of the molecules within these sites, also leading to depolarization of emission [207].

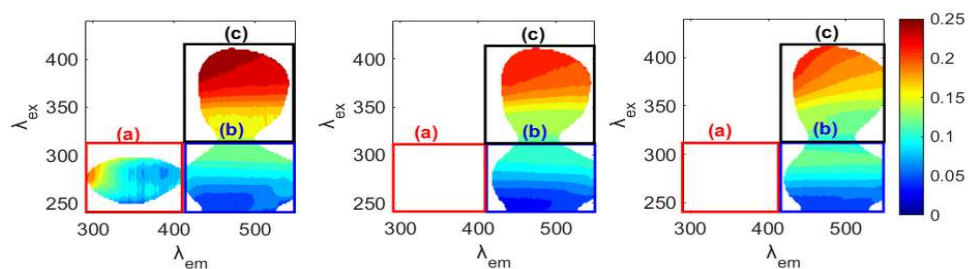


Figure 3.10: Aniso-t-EEMs maps of representative HSA-ANS samples with varying [ANS]/[HSA] ratios: (left) 0.25, (middle) 1.0, and (right) 10. Large changes in anisotropy are observed, induced by FRET. Region **a**, corresponding to intrinsic HSA fluorescence shows depolarisation of emission due to intrinsic homo- and hetero-FRET (Tyr-Tyr/Trp-Trp/Tyr-Trp) within HSA. Region **b**, corresponding to ANS emission (indirect and direct emission) is depolarised due to hetero-FRET (Trp-ANS). Region **c** shows higher anisotropy due to ANS binding to the much larger HSA, upon addition of ANS variation is observed in this region.

3.4.2 PCA analysis of MDF spectra

PCA analysis was used to explore the TSFS data in order to check for outliers and assess the degree of physical sample variance, in each polarization mode [90]. First, PCA analysis was applied to the full emission spectra, and then to the sub-region of donor emission. The data used for PCA analysis was minimally corrected with only IFE correction and blank subtraction of the spectra applied to the spectra in the original TSFS layout. The dataset was re-shaped to give a two-way dataset and normalisation (to area=1) was applied in the case of the global region modelling to account for the variation in signal intensity.

In the case of the global emission, three PCs were required (**Table 3.1**) to explain 99.7- 99.9 % of the total variance, with PC1 and PC2 typically accounting for ~98 % of the explained variance. We observe that PC1 accounts for ~82 % of variance and appears to be arising from ANS (bound to HSA) emission from both direct and indirect excitation (**Figure 3.11/B**), whereas PC2 accounts for ~15 % of variance and appears to be from HSA emission (**Figure 3.11/C**). PC3 accounts for <2 % of the variance explained and appears to be related to unbound ANS present in the system. The relationship between PC1 and PC2 shows little separation between the samples, and thus more advanced methods such as PARAFAC and Tucker3 may provide more useful information (**Figure 3.11/A**).

Table 3.1: Comparison of model parameters and components obtained for PCA modelling of global emission (66×13231) and intrinsic HSA donor emission (66×1271) according to the polarization of the measurement.

Polarization setting	t-EEM _∥	t-EEM _⊥	t-EEM _T	t-EEM _∥	t-EEM _⊥	t-EEM _T
	Global model			Donor model		
Variance explained (%)	99.7	99.9	99.9	99.9	100.0	100.0
PC1 Fit model (%)	82.5	82.1	82.3	99.0	99.2	99.2
PC2 Fit model (%)	15.4	15.8	15.7	0.9	0.8	0.8
PC3 Fit model (%)	1.8	2.0	1.9	-	-	-

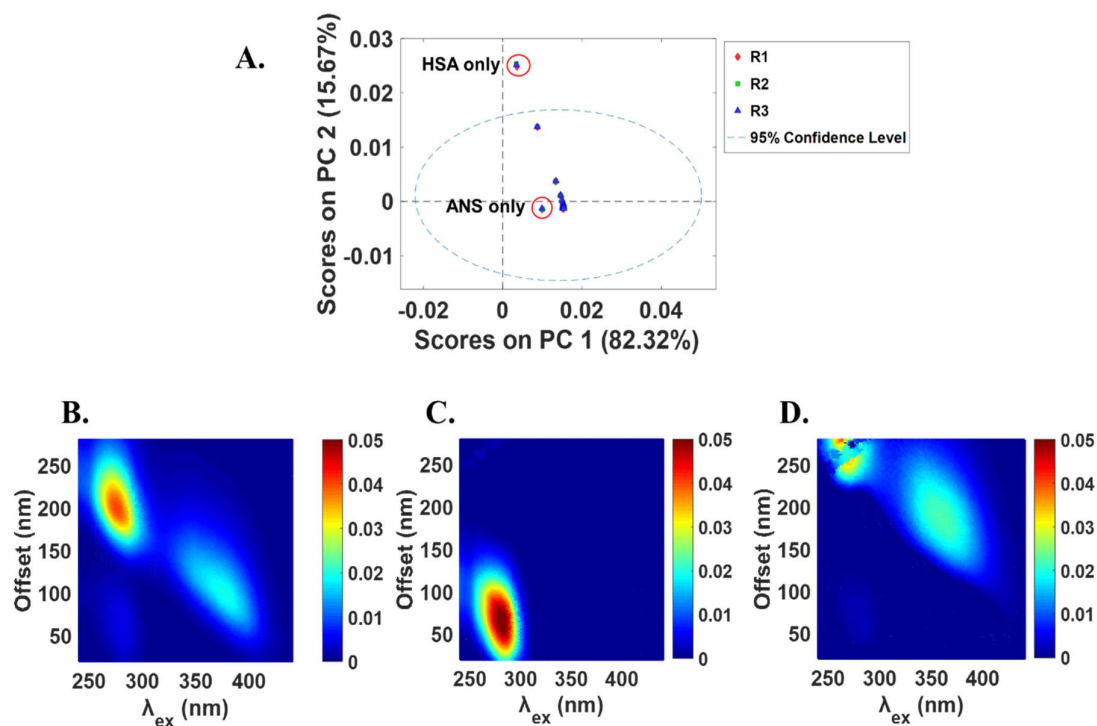


Figure 3.11: (A) PC1 vs PC2 Scores plots from three component PCA model on global emission ($n=63$) in the total polarization mode with the samples containing HSA only and ANS only labelled. The different markers correspond to replicate 1-3 (i.e., R1, R2, R3). (B-D) Show the loadings of PC 1-3 (R-L).

In the case of the PCA modelling of HSA donor emission two PCs were required in all cases (**Table 3.1**) with PC1 and PC2 typically accounting for ~99 % and ~1% of the explained variance, respectively. PC1 appears to be arising from the overall HSA emission (**Figure 3.12/B**), whereas PC2 appears to be more related to Tyrosine emission, with a small amount of ANS bleed through emission also detected (**Figure 3.12/C**). The relationship between PC1 and PC2 shows a curved trajectory due to the different quenching of HSA emission observed in the system (**Figure 3.12/A**). Initially as ANS, the HSA emission is quenching more effectively through dynamic and static processes as FRET occurs ($[ANS]/[HSA] < 2$), as more ANS is added the quenching becomes dramatic ($[ANS]/[HSA] = 2-4$) and eventually all accessible HSA fluorophores are quenched ($[ANS]/[HSA] > 4$) (see section 3.5.2).

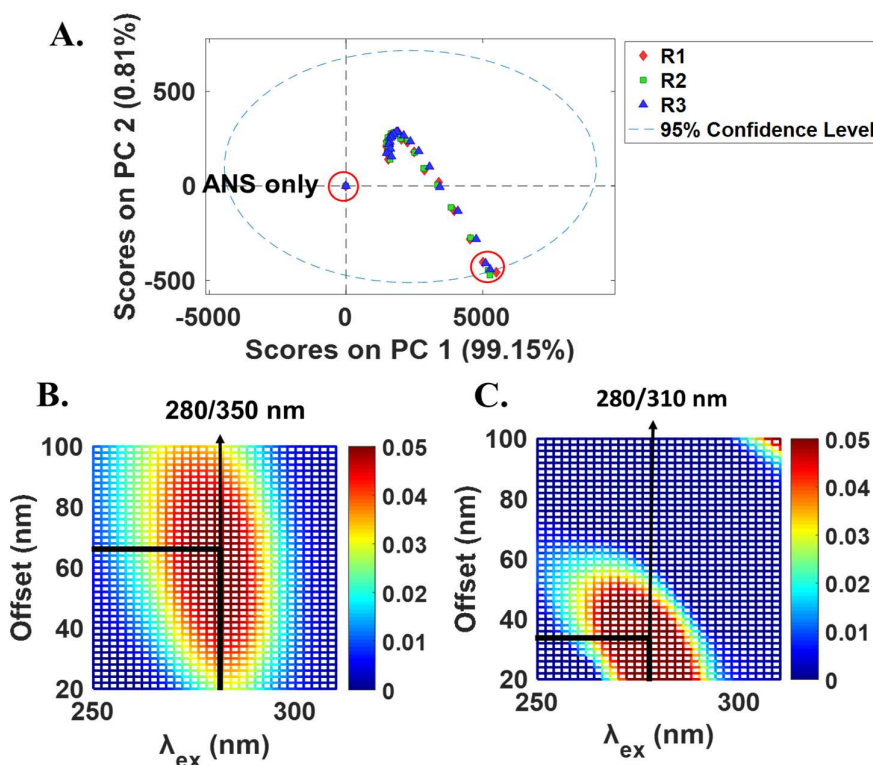


Figure 3.12: (A) PC1 vs PC2 Scores plots from two component PCA model on donor emission ($n=63$) in the total polarization mode with the samples containing HSA only labelled. The different markers correspond to replicate 1-3. (B-C) Show the loadings of PC 1 and 2 (R-L).

3.5 BIOCHEMICAL PARAMETERS

In this section the calculation of conventional biochemical parameters used in analysis of biochemical interactions (Job's plot analysis, Stern-Volmer analysis and determination of FRET efficiency values) are presented.

3.5.1 Jobs plot analysis

A Job's plot [208, 209], also known as method of continuous variation, is a common method used to determine binding stoichiometry. A Job's plot experiment on the HSA: ANS system was found to give a 1:2 binding stoichiometry indicating that at least two complexes were present (**Figure 3.13 & Table 3.2**). The estimated binding stoichiometry, falls within the range of reported literature values for HSA: ANS, with some studies suggesting a 1:3 stoichiometry [210] and others suggesting one or two fluorescent binding sites depending on the HSA:ANS molar ratio used [198, 211].

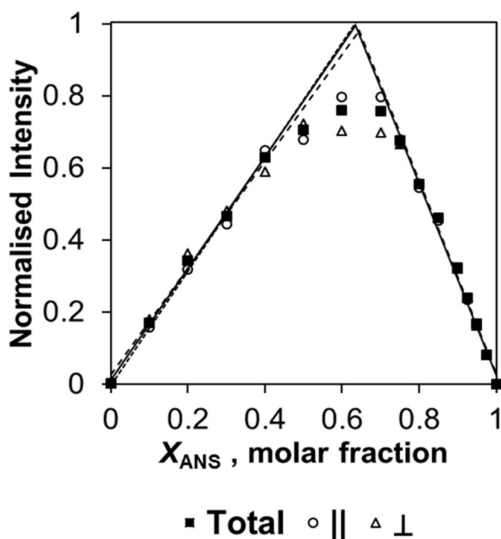


Figure 3.13 Jobs plot for HSA-ANS ANS fluorescence at 380 nm and 470 nm emission, with total concentration of $[HSA] + [ANS] = 2 \times 10^{-5}$ M. Shown for the total (filled square/solid line), parallel (empty triangle, dashed line) and perpendicular (empty circle, dotted line) polarizations.

Table 3.2: Binding stoichiometry obtained using Jobs' plot method.

	$X_{ANS, \text{ mol fraction}}$	Determined stoichiometry	Est. stoichiometry
Total	0.64	1:1.77	~1:2
Parallel	0.66	1:1.94	~1:2
Perpendicular	0.63	1:1.70	~1:2

The results from the Job's plot analysis support the shoulder in the emission spectrum of ANS bound to HSA (**Figure 3.8**) and the heterogeneity observed in the fluorescence anisotropy (**Figure 3.10**), indicating the shoulder and heterogeneity in anisotropy observed, are likely caused by ANS bound in a different location of HSA which experiences a different surrounding environment causing different emission and emission anisotropy. It is interesting to note the slightly higher stoichiometry estimated from the parallel polarization (1:1.94) in comparison to the perpendicular polarization (1:1.70), this may indicate the parallel polarization is a more sensitive measure of the binding stoichiometry than perpendicular polarization, which has a large contribution of ANS with depolarized emission (i.e., ANS which becomes unbound).

3.5.2 Stern-Volmer analysis

Stern-Volmer plots (section 1.1.2, Chapter 1) were used to provide quantitative information about the different quenching mechanisms at play during the HSA-ANS interaction [4, 212-214]. Analysis of the Stern-Volmer plots over the full ANS concentration range (i.e., $[ANS]/[HSA]=0-10$) show three different phases of quenching (**Figure 3.14**).

Table 3.3: Stern-Volmer quenching constants calculated using the unresolved fluorescence emission (classical) fitted for linear region up to $[ANS]/[HSA]=1$.

Polarization	$t\text{-EEM}_{\parallel}$	$t\text{-EEM}_{\perp}$	$t\text{-EEM}_T$
Classical Stern-Volmer	F_0/F at $\lambda_{ex/em}$ 280/350 nm		
$K_{SV} (\times 10^4 \text{ M}^{-1})$	6.0 ± 0.4	6.1 ± 0.5	6.0 ± 0.4
r^2	0.98 ± 0.01	0.99 ± 0.01	0.99 ± 0.01

Firstly, a linear relationship was observed up to a 1:1 ANS/HSA ratio (up to $[\text{ANS}] = 1.5 \times 10^{-5} \text{ M}$) indicative of a single fully collisional quenching process (**Figure 3.14/A**) [4, 18]. This linear quenching region can be attributed to ANS induced quenching (FRET process occurring) [188, 198]. As more ANS was added ($[\text{ANS}]/[\text{HSA}] > 1$) the Stern-Volmer plot curves upward which is symptomatic of a more complex quenching process due to the presence of increasing amounts of static quenching or a second dynamic quenching process occurring (**Figure 3.14/B**). This secondary quenching effect can be explained by the increasing occupancy of ANS in secondary binding sites, thus leading to more complex FRET with Trp-214. From $[\text{ANS}]/[\text{HSA}] = 2$ to $[\text{ANS}]/[\text{HSA}] = 4$ ($[\text{ANS}] = 3 \times 10^{-5} - 6 \times 10^{-5} \text{ M}$), static quenching of Trp-214 emission was observed (**Figure 3.14/C**) which was consistent with fluorescence lifetime measurements (see section 3.6), where the τ/τ_0 value was nearly constant for $[\text{ANS}]/[\text{HSA}] > 2$. For $[\text{ANS}]/[\text{HSA}] > 4$ ($[\text{ANS}] > 6 \times 10^{-5} \text{ M}$), Trp emission was relatively constant indicating that quenching was maximised, and no further changes can be discriminated (**Figure 3.14/D**). A steeper slope (**Figure 3.14/A-B**) and higher values throughout the interaction (**Figure 3.14/A-B**) were observed for the Stern-Volmer plots in the perpendicular polarization modes indicating this polarization mode is potential more sensitive to FRET than the parallel polarization mode.

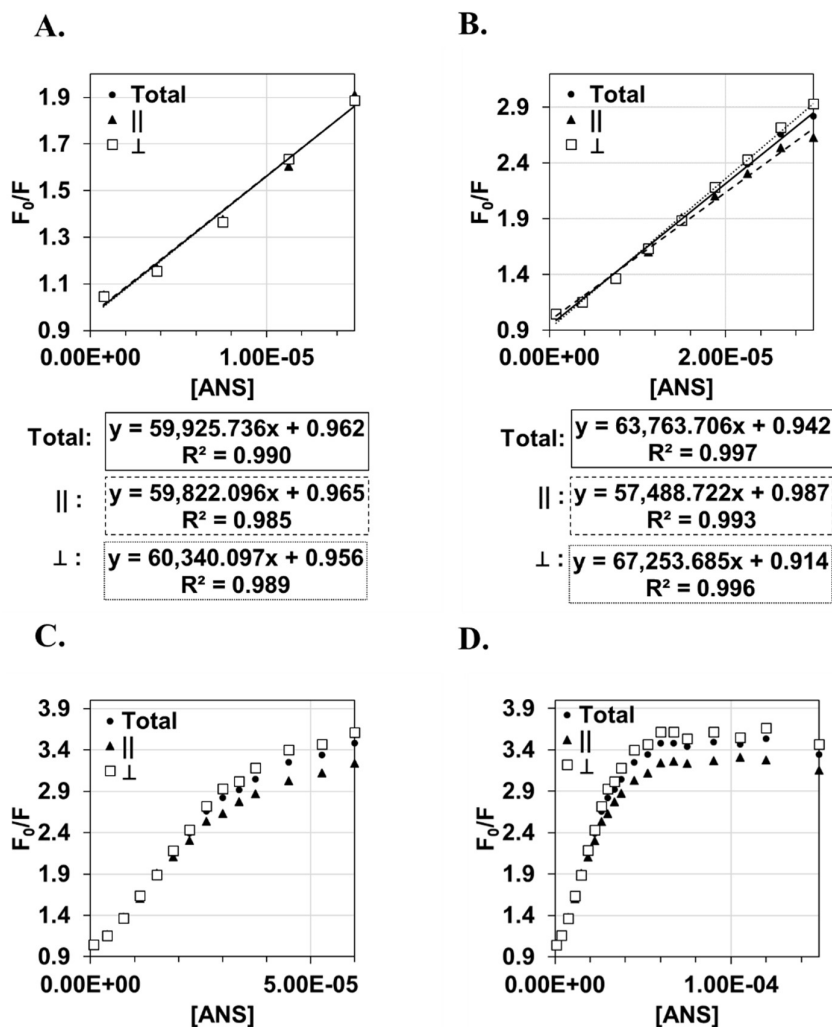


Figure 3.14: Stern-Volmer plots (F_0/F vs $[ANS]$) using t-EEM_T, t-EEM_{||} and t-EEM_⊥ for unresolved spectra based on a single point $\lambda_{ex/em} = 280/350$ nm in absence and presence of quencher. Stern-Volmer plots (A-D) show the quenching up to $[ANS]/[HSA] = 1, 2, 4, 10$, respectively, the linear region, at low ANS concentrations, is associated with FRET quenching.

Changes in fluorescence emission were further analysed using a modified Stern-Volmer analysis [4, 215-218] (**Figure 3.15**). Using this approach, we can get estimates for the relative contributions of static and dynamic quenching [215], which is useful in the context of assessing the reliability of the E_T values produced and determining at which concentration ranges collisional quenching becomes an issue. Plotting K_{app} versus $[ANS]$ shows (**Figure 3.15**) that the quenching behaviour is complex with several linear regions, of which the first (low ANS concentration) is

most important for FRET calculations. More complex behaviour for $[ANS] > 2.0 \times 10^{-5} \text{ M}$ was due to increasing ANS occupancy of the secondary binding sites, inner filter effects, and other interactions. Resolving these effects and their relative contributions would necessitate collecting data at different temperatures which was outside the scope of this work [4]. The most important outcome of the Stern-Volmer and modified Stern-Volmer analysis is that the sample range for FRET calculations must be restricted to those samples with $[ANS]/[HSA]$ ratios of <1 , to avoid bias due to these other processes.

Equation 3.3

$$\frac{F_0}{F} = (1 + K_D[Q])(1 + K_S[Q]) = 1 + K_{app}[Q]$$

Equation 3.4

$$K_{app} = \left[\frac{F_0}{F} - 1 \right] \frac{1}{[Q]} = (K_D + K_S) + K_D K_S [Q]$$

where K_D and K_S are the dynamic and static quenching contributions, respectively.

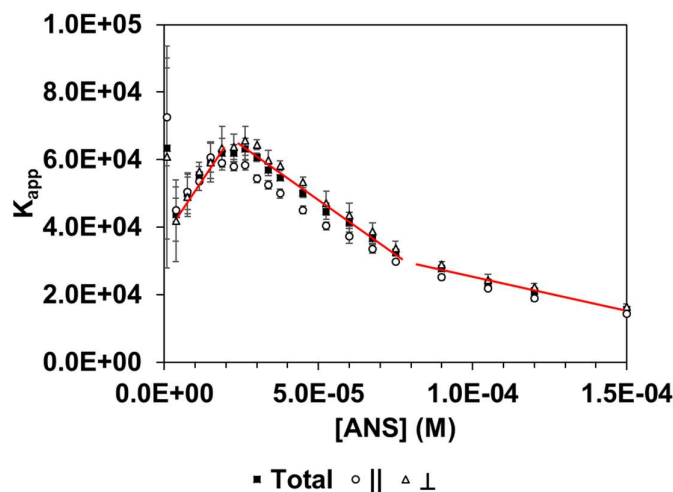


Figure 3.15 (a) Plot of K_{app} versus $[ANS]$ for the HSA-ANS system using data (triplicate samples) measured at $\lambda_{ex/em} = 280/350 \text{ nm}$. The three red lines are guides to show the three different linear quenching regions for this sample system. The first linear region corresponds to ANS/HSA molar ratios of between 0.05 and 1.0, which is the region used for FRET calculations. Note $[ANS] = 3.0 \times 10^{-5} \text{ M}$ is equivalent to an ANS/HSA ratio of 2.

3.5.3 FRET efficiency calculation

FRET efficiency values were calculated using the commonly used method which is based on a single point of the unresolved donor emission (i.e., intrinsic HSA fluorescence) from 2-D spectra [4, 18, 180]. Here, the emission of HSA at the single-point of maximum emission determined from the t-EEM_T spectra ($\lambda_{\text{ex/em}}=280/350$ nm) was measured in the presence (F_{DA}) and in the absence (F_{D}) of FRET acceptor, ANS and used to calculate FRET efficiency (**Equation 3.2**) at different molar ratio of [ANS]/[HSA] (**Table 3.4 & Figure 3.16**).

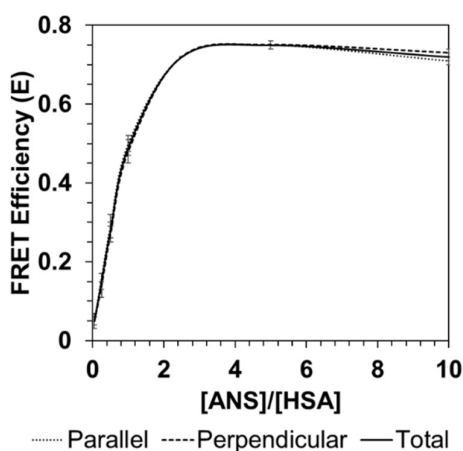


Figure 3.16: [ANS]/[HSA] vs. FRET efficiency calculated using a single point ($\lambda_{\text{ex/em}} = 280/350$ nm) of donor emission (HSA) in the absence (I_{D}) and presence (I_{DA}) of FRET acceptor (ANS).

The maximum FRET efficiency is almost reached at [ANS]/[HSA]=2.5 (~72%), which shows some agreement with Job's plot analysis (see **section 3.5.1**) and lifetime measurements (see **section 3.6**) which show at least ~2 molecules of ANS bind to HSA and cause dynamic quenching (via FRET) up to [ANS]/[HSA] ~2 (**Table 3.4 & Figure 3.16**). The increase in FRET efficiency beyond this point is likely due to the binding of ANS to other secondary binding sites in addition to the two main sites estimated from Job's plot analysis. Little difference is observed between the FRET efficiency value recovered in the different polarization mode, a more sensitive measure with lower measurement errors would be required to see differences in each of the polarization modes here.

Table 3.4: FRET efficiency values (mean and (standard deviation)) calculated for each polarization measurement using the conventional method at $\lambda_{\text{ex/em}}$ 280/350 nm (i.e., point of maximum emission determined from t-EEM_T spectra).

FRET Efficiency values			
ANS/ HSA	t-EEM	t-EEM_⊥	t-EEM_T
0.05	0.05 (0.01)	0.05 (0.02)	0.05 (0.02)
0.25	0.16 (0.01)	0.14 (0.03)	0.15 (0.02)
0.5	0.29 (0.03)	0.27 (0.02)	0.28 (0.02)
1	0.50 (0.02)	0.48 (0.03)	0.49 (0.02)
2.5	0.72 (0.00)	0.72 (0.00)	0.72 (0.00)
5	0.75 (0.00)	0.75 (0.01)	0.75 (0.01)
10	0.71 (0.01)	0.73 (0.01)	0.72 (0.01)

3.6 LIFETIME ANALYSIS

The analysis of the lifetime decay of HSA upon addition of ANS provided further information regarding the different quenching mechanisms at play throughout the interaction. The origin of Trp fluorescence lifetime has been investigated for over 30 years with Trp lifetime in protein suggested to arise from: two lifetimes arising from the Trp structure itself (~ 0.5 ns and ~ 3 ns), and a third lifetime as the result of the Trp surrounding environment [219, 220]. Several models have been suggested for the two lifetimes arising from Trp structure itself, one model assumes the two lifetimes arise from the emission from the two different electronic absorption transitions of Trp known as 1L_a and 1L_b , but the more accepted model suggest the existence of rotameric states of Trp is the source of the multi-exponential decay [221-223]. The third fluorescence lifetime of Trp which is observed in some proteins ($\sim 6 - 9$ ns) such as HSA and BSA, is result of the interactions of the environment surrounding with Trp¹⁴.

Here, the fluorescence lifetime of HSA was calculated using a tri-exponential decay law fit. It is important to note that all fluorescence lifetime measurements were collected at magic angle [224], and therefore results do not correspond directly with polarized measurements. The results show a significant decrease in HSA lifetime up to $[ANS]/[HSA]=2$ ($\langle\tau\rangle_f=5.6 \rightarrow 3.4$ ns) which consistent with dynamic quenching behaviour (i.e., FRET to ANS), and plot of the relative fluorescence lifetime as a function of $[ANS]/[HSA]$ vs τ/τ_0 , shows a negative steep slope for $[ANS]/[HSA] < 2$. Beyond this point, where $[ANS]/[HSA] > 2$, the lifetime remains relative unchanged (i.e., $\tau/\tau_0 \rightarrow 1$) at ~ 3.3 ns indicative that mostly static quenching is occurring beyond this point (**Figure 3.17/A**).

Analysis of the amplitude of each lifetime upon addition of [ANS] shows a strong decrease in the long lifetime decay (~ 7 ns) component, which corresponds to the Trp lifetime arising from interaction with its surrounding environment in HSA (i.e., in hydrophobic interior of HSA molecule (**Figure 3.1/A**)) the up to $[ANS]/[HSA]=2$, consistent with dynamic quenching behaviour. The amplitude of the two shorter lifetimes (~ 3.5 ns and ~ 0.8 ns) are observed increases up to $[ANS]/[HSA] = 2$ (**Figure**

¹⁴ For instance, interactions between Trp residues and neighbouring amino acids.

3.17/B), due to quenching of the overall emission and the amplitudes remain relatively constant beyond $[ANS]/[HSA] > 4$ (where static quenching is mainly occurring).

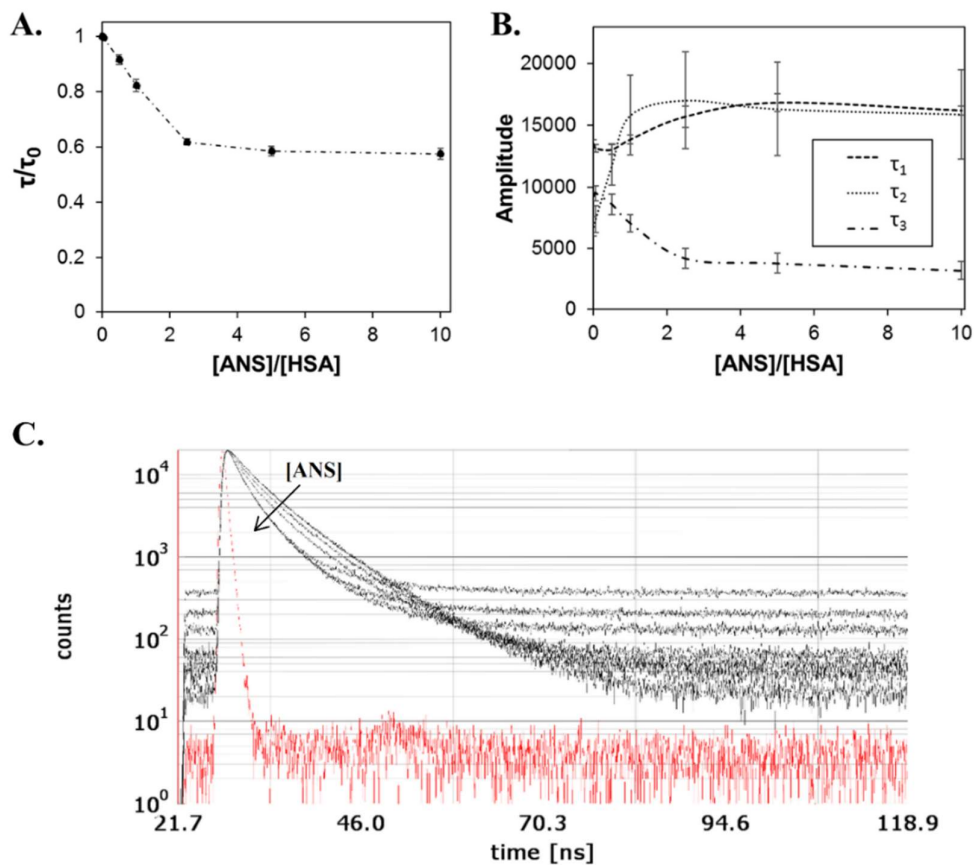


Figure 3.17 (A) Relative fluorescence lifetime as a function of $[ANS]/[HSA]$. τ/τ_0 shows a decrease up to $[ANS]/[HSA]=2$, consistent with dynamic quenching behaviour. At $[ANS]/[HSA] > 2$, τ/τ_0 remains unchanged, indicative of static quenching; (B) Amplitude of each lifetime upon addition of $[ANS]$. A strong decrease in the long lifetime decay (~ 7 ns) is observed up to $[ANS]/[HSA]=2$, consistent with dynamic quenching behaviour. The amplitude of the two shorter lifetimes (~ 3.5 ns and ~ 0.8 ns) is increased up to $[ANS]/[HSA] = 2$. Amplitudes remain relatively constant beyond $[ANS]/[HSA] > 4$. (C) Representative IRF decay curve and HSA-ANS decay curves showing the quenching occurring upon addition of ANS.

Table 3.5: Parameters of fluorescence lifetime from, tri-exponential fitting of HSA-ANS complex, at varying [ANS]/[HSA] molar ratios using 295 nm excitation and 350 nm emission (measurements made in triplicate).

[ANS] /[HSA]	$\langle\tau\rangle_a$	$\langle\tau\rangle_f$	τ_1 (ns)	τ_2 (ns)	τ_3 (ns)	a1	a2	a3	χ^2
0	5.6 ± 0.1	4.1 ± 0.2	3.6 ± 0.2	0.9 ± 0.1	7.4 ± 0.1	13515 ± 342	6808 ± 786	9242 ± 358	1.11 ± 0.06
0.05	5.5 ± 0.02	4.0 ± 0.1	3.5 ± 0.1	0.8 ± 0.1	7.3 ± 0.1	13158 ± 309	7376 ± 1079	9494 ± 627	1.15 ± 0.01
0.5	5.1 ± 0.1	3.3 ± 0.2	3.3 ± 0.2	0.7 ± 0.1	7.0 ± 0.2	13044 ± 374	11800 ± 1673	8582 ± 852	1.12 ± 0.02
1	4.6 ± 2.6	2.6 ± 0.2	2.8 ± 0.1	0.6 ± 0.1	6.8 ± 0.2	13855 ± 378	15826 ± 3233	7056 ± 694	1.14 ± 0.04
2.5	3.4 ± 0.1	2.0 ± 0.2	2.5 ± 0.2	0.6 ± 0.1	6.0 ± 0.3	15700 ± 888	17030 ± 3949	4214 ± 798	1.10 ± 0.04
5	3.3 ± 0.1	2.0 ± 0.2	2.4 ± 0.2	0.6 ± 0.1	5.9 ± 0.4	16819 ± 727	16332 ± 3777	3827 ± 802	1.14 ± 0.03
10	3.2 ± 0.1	1.9 ± 0.2	2.4 ± 0.2	0.6 ± 0.1	6.1 ± 0.5	16193 ± 369	15901 ± 3609	3235 ± 722	1.20 ± 0.03

* $\langle\tau\rangle_f$ -intensity weighted average lifetime; $\langle\tau\rangle_a$ - amplitude weighted average lifetime.

3.7 CONCLUSIONS

The interactions between fluorescent probes, such as ANS, with proteins (e.g., BSA, HSA) have been extensively studied in literature using a variety of analytical techniques including NMR [225, 226], CD [227-229], and fluorescence (lifetime and steady state) [230-232]. In terms of the use of steady-state fluorescence to study the interaction between fluorescent probe and a protein, conventionally measurements are made using 2-D scans of the probe fluorescence emission are used [230, 231]. In this work, the interaction between HSA and ANS was studied using 4-D pMDF that provided information about intensity, emission, excitation, anisotropy in a single measurement. In addition, the use of MDF facilitated the collection of the full emission space of the intrinsic protein emission (i.e., HSA emission) alongside ANS emission, thereby providing more information in a single measurement than conventional 2-D methods.

Firstly, the interaction was investigated using UV absorbance spectra, however, quantitative analysis was complicated by the highly overlapping spectra of HSA, ANS and the HSA: ANS complex. The problem of overlapping signals in absorbance spectra is not uncommon, with a number of methods to resolve overlapping spectra reported in literature, including; derivative treatment of spectra [233, 234], ratio difference method based on the difference in absorbance of at two wavelengths [235, 236], mean centring of ratio spectra [235, 236] and curve fitting methods [237, 238]. Here, MCR-ALS [88], a curve fitting method based on a bilinear model, was applied and found to effectively resolve three components from the spectra corresponding to HSA absorbance, ANS (unbound) absorbance and HSA-ANS complex absorbance, which allowed for determination of the concentrations of the resolved components in the system. A limitation of this work, however, was the fact that individual species of the bound ANS could not be resolved, although we know from Job's plot analysis that at least two different binding sites are occupied.

The analysis of pMDF spectra showed three peaks over the full HSA-ANS emission space: corresponding to ANS (arising via direct and indirect excitation) and intrinsic HSA emission. The aniso-t-EEM map's, which were calculated from the pMDF spectra, clearly showed FRET related depolarisation of emission occurring in

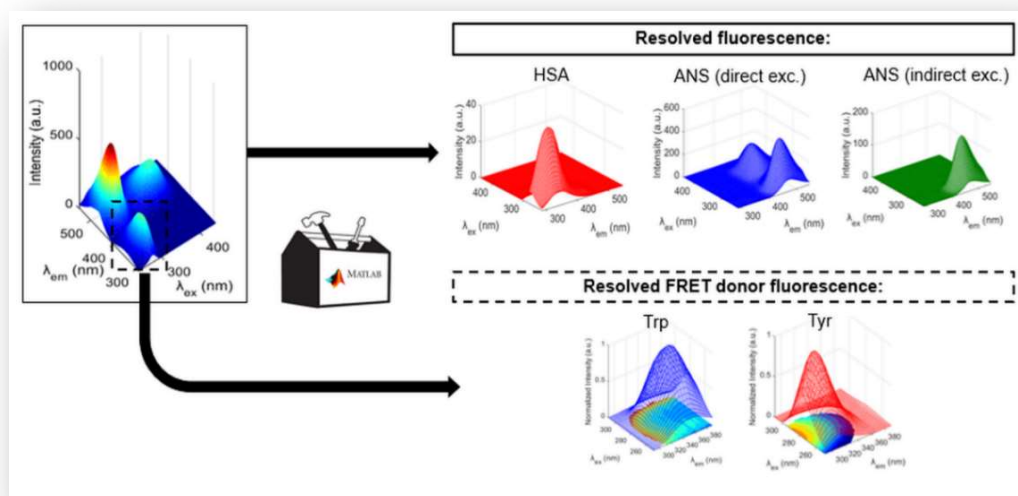
the HSA-ANS interaction system and provided a new way to visually represent the FRET processes occurring more clearly than intensity measurements. In addition, the unique anisotropy patterns observed showed heterogeneity in the emission anisotropy as ANS bind to secondary binding sites ($[ANS]/[HSA] > 1$), whereas more homogenous anisotropy is observed at lower molar ratios when mainly one binding site is occupied ($[ANS]/[HSA] < 1$) [197, 198].

Finally, determination of biochemical parameters including Stern-Volmer quenching constants and FRET efficiency values, and analysis of the fluorescence lifetime of HSA, provided information regarding the quenching mechanism and play during the interaction. From Stern-Volmer analysis of the intrinsic HSA donor emission, quenching was observed to occur in three phases via a combination of dynamic and static quenching: firstly linear quenching was observed as FRET (dynamic quenching) occurred from the, an upward curve then developed up to $[ANS]/[HSA]=2$ as a secondary quenching effect was occur and finally further static quenching is observed up to $[ANS]/[HSA]=4$, and beyond this point it shows majority of accessible fluorophores were quenched.

Overall, the spectral analysis via pMDF of the HSA-ANS system facilitates monitoring of the interaction via spectral shifts, changes in fluorescence intensity, anisotropy and lifetime. MCR analysis of the UV spectra provided an alternative approach for dealing with overlapping UV absorbance spectra and the unique aniso-t-EEM plots provided a new way of visualizing the FRET related depolarisation of emission. Further analysis of the pMDF spectra by PCA analysis was found resolve different variations in the samples, however, to investigate the system further decomposition, using more advanced 3-way methods such as PARAFAC and Tucker3 are required, which are explored in Chapter 4.

4 CHEMOMETRIC MODELLING OF THE HSA-ANS INTERACTION

Graphical abstract:



In this chapter the findings from applying three-way chemometric modelling of the fluorescence t-EEM spectra to study FRET in the HSA-ANS model system will be discussed. Modelling was applied to the global HSA-ANS t-EEM spectra as well as the sub-region of donor emission, using restricted Tucker3 and PARAFAC chemometric models, respectively. The resolved emission was then used to provide a new method of calculating of biochemical parameters and the results compared with those presented in Chapter 3.

4.1 MODELLING OF MDF SPECTRA WITH FRET

Conventional spectroscopic analysis allows investigation of the HSA-ANS interaction via: (i) the decrease of overall HSA donor fluorescence due to quenching via FRET, (ii) the increase in ANS acceptor fluorescence due to both hydrophobic binding and FRET from HSA, (iii) the increase in the anisotropy of directly excited acceptor upon binding, (iv) the decrease in the anisotropy of the indirectly excited acceptor, and (v) the increase in donor anisotropy due to the shortening of the donor fluorescence lifetime.

However, systems exhibiting FRET are inevitably multi-component systems consisting of, at minimum, a donor, and an acceptor molecule (FRET pair), all of which may be fluorescent. Thus, for a given FRET pair, three main spectral contributions often need to be resolved which correspond to the: direct donor fluorescence, direct acceptor fluorescence, and FRET induced acceptor fluorescence (indirect acceptor fluorescence) [239]. Therefore, the application of chemometric methods to MDF spectra to facilitate the decomposition of the emission into individual fluorophore populations is potentially useful. In addition, using the ARMES approach, the fourth dimension, anisotropy, provides additional information and a novel way of chemically validating the chemometric solution.

In the HSA-ANS model system, the various fluorophore spectra present in the system (Tyr, Trp, ANS (direct excitation), ANS (indirect excitation)) all overlap and so here, the use of chemometric methods to resolve the individual emission contributions of the collected MDF spectra is applicable. In this work two different areas of HSA-ANS emission are separately evaluated and modelled to resolve the underlying components of fluorescence. Firstly, the full emission space of the HSA-ANS including the FRET donor (HSA emission) and FRET acceptor (both indirect and direct excitation) is modelled and referred to as the global emission. Secondly, the sub-region of HSA emission was modelled and referred to as the donor emission region.

The most used chemometric model to resolve MDF spectra of multi-component mixtures is PARAFAC [106]. The popularity of PARAFAC in the analysis of MDF spectra is due to the significant advantages it possesses, namely, its ease of

use and unique solutions [240, 241]. A limitation of PARAFAC however, is that the model requires data of full rank [106] (**Figure 1.16, Chapter 1**). In order for an appropriate PARAFAC model of MDF data, it must fulfil Kruskal's condition (**Equation 4.1**) where k_A , k_B , and k_C refer to the rank of loading matrix and R is the number of components [242].

Equation 4.1

$$k_A + k_B + k_C \geq 2R + 2$$

An EEM dataset containing three components, with three components in emission, three components in excitation and three components in the scores matrix (or in other words have full rank in each mode), Kruskal's condition is fulfilled ($3+3+3=9 \geq 8$), and reliable and unique result can be obtained from a PARAFAC model. However, multi-dimensional emission of multi-fluorophore systems which undergo FRET [80], break the conditions necessary to achieve reliable PARAFAC solutions because of proportionality rank deficiency in both the excitation and emission profiles between the donor-acceptor fluorophores. In spectroscopic terms, the acceptor emission arising from indirect excitation (via FRET) will show an excitation profile defined by that of the donor fluorophore and an emission profile defined by that of the acceptor fluorophore. In this case, instead of the dataset having full-rank, we observe two emission components (donor and acceptor), two components in the emission (donor and acceptor), and three components in the scores (donor, directly excited acceptor and indirectly excited acceptor signal), in this case the dataset is referred to as rank-deficient as Kruskal's condition will not be satisfied ($2+2+3=7 \not\geq 9$). A PARAFAC solution in this case, is found to be invalid. In such cases where the trilinear requirement is not satisfied, the data can be modelled using Tucker3 [243].

Tucker3 [85, 89] allows for extraction of different numbers of components in each of the three modes (i.e. does not require trilinear data) (**Figure 1.18, Chapter 1**) [110], however these models often give complicated and difficult to interpret solutions, due to the rotational freedom of the model [244-246]. A restricted Tucker3 (see **section 1.5.5 , Chapter 1**) model minimizes the ambiguity of the solution by harnessing *a priori* chemical knowledge of the system to create a defined core array and is used to model the data presented in this thesis.

4.2 MODELLING OF HSA-ANS INTERACTION: GLOBAL EMISSION

The fluorescence emission spectra of the global t-EEM's of the HSA-ANS interaction system is composed of several underlying components: HSA, composed of direct ex. Tyr, direct ex. Trp, indirect ex. Trp (Tyr-Trp, hetero-FRET), indirect ex. Trp (homo-FRET), indirect Tyr (homo-FRET), hydrophobically bound ANS; composed of direct ex. ANS, indirect ex. ANS (Trp-ANS hetero-FRET), and free ANS in solution (negligible, very weakly fluorescent). Although, chemometric modelling will not achieve resolution of all individual components it can resolve the biggest contributions to the overall fluorescence. Here, we aim to decompose the global emission of HSA-ANS into three components: HSA emission (Tyr + Trp), ANS direct excitation emission and ANS indirect excitation (via FRET) emission. The sub-region of donor emission (composed of Tyr and Trp populations) is further investigated in **section 4.3**.

Prior to commencing data analysis of the spectra the similarity of the replicate MDF spectra for each concentration $[ANS]/[HSA]$ was assessed using a similarity index (SimI) [247]. SimI provides a quick way to compare the degree of similarity between 3-D spectra by comparing each point of the spectra, which is more informative than conventional measurements of the mean and standard deviation. In SimI two matrices $X1$ and $X2$ (e.g., discrete data points of TSFS spectra with dimensions $I \times J$) are used in **Equation 4.2** where the closer SimI value is to one, the more alike the two matrices $X1$ and $X2$. A high degree of similarity is seen between all replicate samples indicating that sample preparation was good (similar replicates) and pre-processing of the dataset did not induce too much variation in the data to be modelled (**Figure 4.1**). Normalisation (norm to area=1) was applied here to account for the large variation in signal intensity of the components of interest and is shown to significantly increase the degree of similarity between the samples.

Equation 4.2

$$SimI = 1 - \lambda \frac{\sqrt{\sum_{i=1}^I \sum_{j=1}^J p_{x1-x2}^2}}{\sqrt{\sum_{i=1}^I \sum_{j=1}^J p_{x1+x2}^2}}$$

where, λ was a penalty parameter, used to set a detectable limit of variance between X1 and X2. Here it was set to 4 which corresponds to 5% variance in the MDF data and was proven quite adequate. p_{x1-x2} and p_{x1+x2} are elements of $(X1-X2)$ and $(X1 + X2)$ respectively.

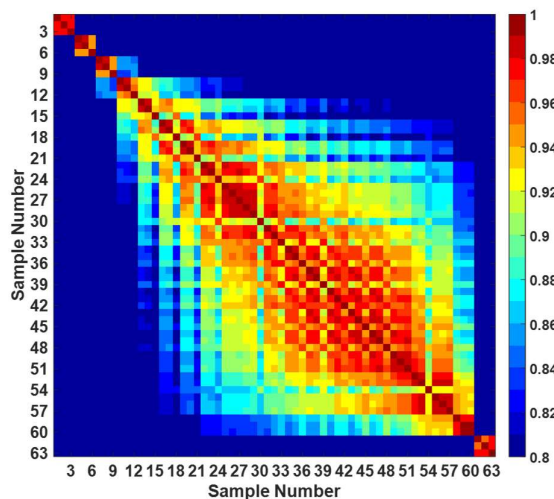
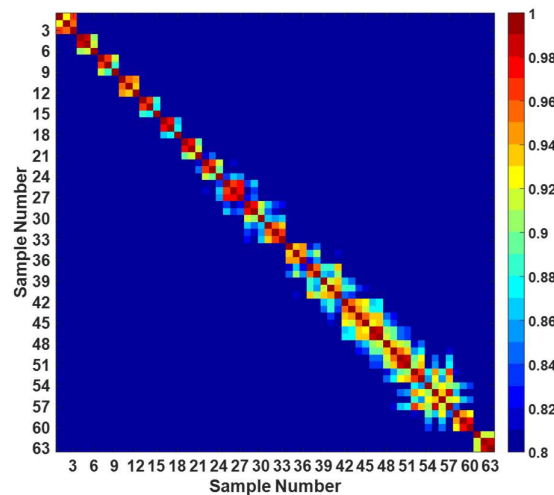


Figure 4.1: Similarity index evaluation of the HSA-ANS dataset ($63 \times 131 \times 101$), before and after normalisation showing good similarity between replicate measurements. Normalisation increases the similarity between samples in the dataset and accounts for the large variation in signal intensity.

In addition, the number of underlying components in the pMDF spectra was estimated using singular value decomposition (SVD) of the unfolded three-way array in all three modes. In all modes, between 2 and 4 components were present (or more correctly resolvable), but with a long tail in both the emission and excitation modes (Figure 4.2/B-C). Photophysically we know that there are many more emitters (i.e., multiple Tyr residues, multiple ANS binding sites), but the dataset (sample numbers, spectral resolution, and signal to noise) is not good enough for resolving the wider population of weak emitters.

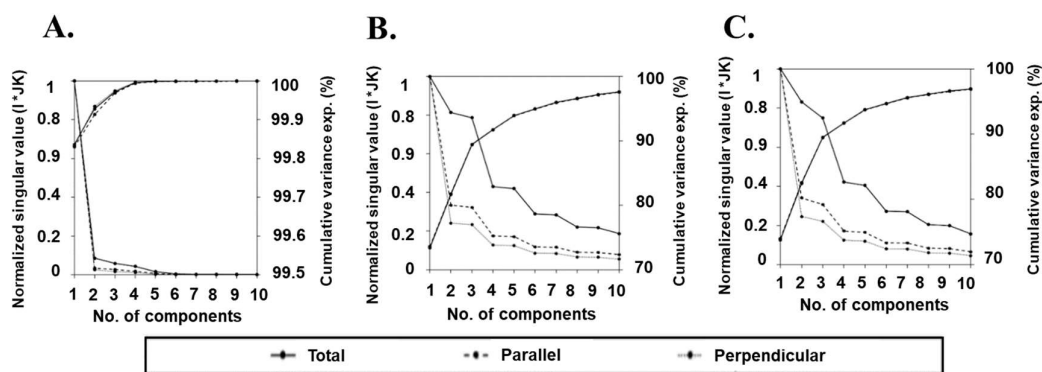


Figure 4.2: Normalized singular values and cumulative variance explained (%) for the first 10 components of the unfolded t-EEM data in the: (A) sample, (B) emission, and (C) excitation modes, respectively, for each polarization setting. A higher number of components is required to explain the variance observed in the excitation and emission modes than in the sample's mode. **Note:** I, denotes the number of samples (63), J, stands for number of emission wavelengths (131), and K, represents the number of excitation wavelengths (101).

4.2.1 PARAFAC modelling of the HSA-ANS interaction

First, the feasibility of PARAFAC modelling of global emission spectrum of HSA-ANS was investigated. The PARAFAC modelling of the global t-EEM is complicated by the FRET induced non-linearity [80]. However, although the requirements for a PARAFAC model are not fulfilled in a FRET affected dataset, useful information about the behaviour and chemical rank of the components of the HSA-ANS system can be extracted.

Two-component PARAFAC model

Firstly, a two component PARAFAC model was observed to explain $\geq 99.8\%$ of the total variance with a core consistency of 100.0 % for all polarization settings (**Table 4.1**). Here, PaC1 appears to be a combination of all ANS emission from both direct and indirect excitation (via FRET), whereas PaC2, appears to be arising from intrinsic HSA emission (composed of Tyr and Trp) (**Figure 4.3**). Little differences are observed between the models in each polarization mode apart from PaC1 showing a significantly higher contribution to the fluorescence emission in the parallel polarization mode (**Figure 4.4/C**), due to the fact that ANS emission arising from direct excitation is expected to show more polarized emission upon binding leading as it has more restricted rotational mobility.

The two-component model provided little additional information than the unresolved spectra of the HSA-ANS samples, the PaC1 and PaC2 signals resolved from the two-component model are already separated in the unresolved spectra showing no spectral overlap (**Figure 3.7**). The results of a two component PARAFAC model, indicated additional components were required here to provide further information about the HSA:ANS interaction than provided by unresolved spectra. The use of an additional component may resolve the ANS emission arising from direct excitation and emission from indirect excitation (i.e., via FRET).

Table 4.1: Comparison of model parameters and components obtained from two component PARAFAC models of total, parallel, and perpendicular polarized datasets.

Polarization setting	t-EEM	t-EEM _⊥	t-EEM _T
PaC1 $\lambda_{ex/em}$ (nm)	276/474	274/474	274/474
PaC1 Fit model (%)	84.2	84.2	84.2
PaC2 $\lambda_{ex/em}$ (nm)	280/344	280/344	280/344
PaC2 Fit model (%)	15.8	15.8	15.9
Variance explained (%)	99.8	99.8	99.8
CONCORDIA (%)	100.0	100.0	100.0
Split-half analysis (%)	99.7	99.3	99.5

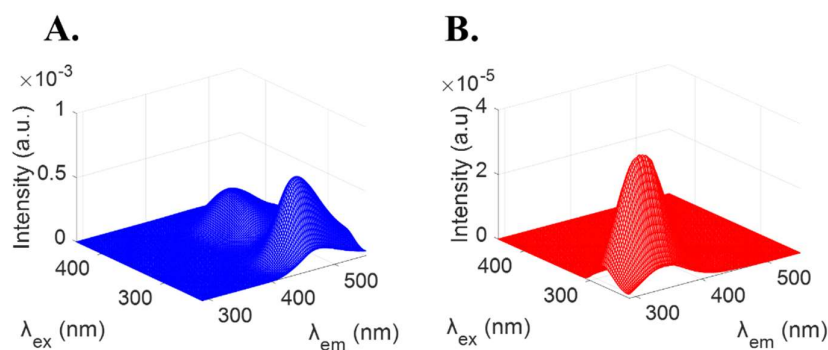


Figure 4.3: Components recovered from two-component PARAFAC modelling of full HSA-ANS emission, a representative example shown for $[ANS]/[HSA]=1$ (for t-EEM_T model). The components recovered correspond to: **(A)** ANS emission arising from indirect and direct excitation; **(B)** Intrinsic HSA emission (composed of Tyr & Trp).

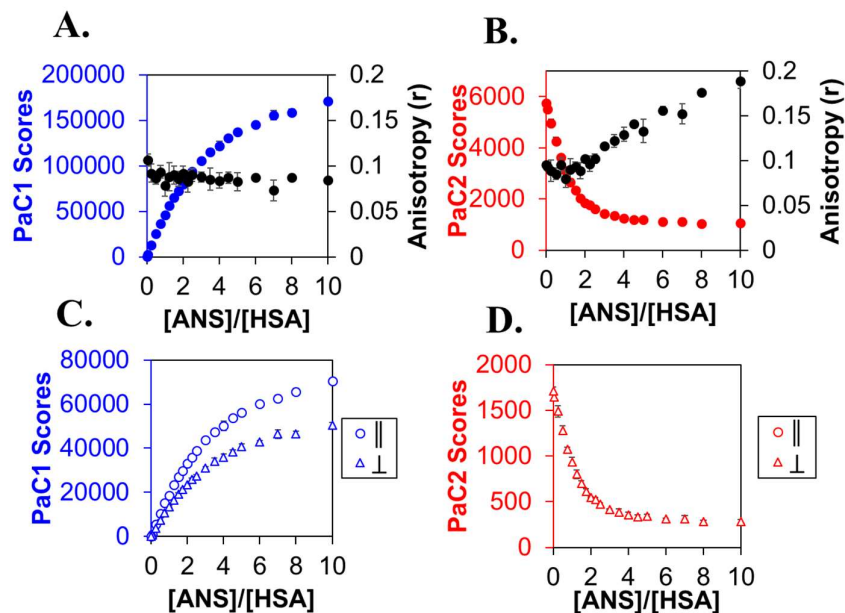


Figure 4.4: Plots of Scores (relative concentrations of components) and anisotropy values taken at the point of maximum emission against $[ANS]/[HSA]$ ratios recovered using two-component PARAFAC models. (First row) t-EEM_T model: **(A)** Component 1, ANS emission from direct and indirect excitation, the low anisotropy at $\lambda_{ex/em} = 274/474$ nm is due to FRET related depolarization; **(B)**; Component 2, HSA intrinsic emission quenched by addition of ANS (anisotropy values unreliable $[ANS]/[HSA] > 4$ as emission is mostly quenched); (Second row) scores from t-EEM_⊥ and t-EEM_∥ models for: **(C)** Component 1 and; **(D)** Component 2.

Three-component PARAFAC model

A three component PARAFAC models showed low (23.9 %) and negative (-1.6 % and -7.4 %) core consistency values (**Table 4.3**) suggesting that the PARAFAC models were here mathematically invalid. The recovered components appeared to be arising from directly excited ANS emission (276/476 nm, >55%) (**Figure 4.5/A**), HSA emission (Tyr +Trp, 280/344 nm, >20%) (**Figure 4.5/B**), and a third component (278/470 nm, >19%) which likely incorporated both the indirect and direct ANS emission in a single component (**Figure 4.5/C**). Thus, these models failed to resolve the indirectly excited ANS emission (arising from FRET) separate from any directly excited ANS emission.

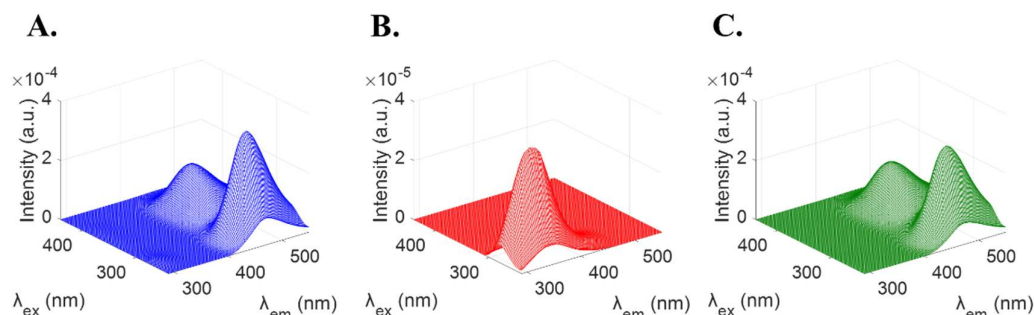


Figure 4.5: Components recovered from restricted three-component PARAFAC modelling of full HSA-ANS emission, a representative example shown for $[ANS]/[HSA]=1$ for the most stable t-EEM_T model). The components recovered correspond to: **(A)** ANS emission arising from indirect and direct excitation (mostly directly excited ANS); **(B)** Intrinsic HSA emission (composed of Tyr & Trp); and **(C)** ANS emission arising from indirect and direct excitation (mostly indirectly excited ANS via FRET).

The difference in the core consistency values observed for the parallel and perpendicular polarizations is indicative of a greater deviation from trilinear behaviour in t-EEM_⊥ (CONCORDIA -1.6 %) than in t-EEM_∥ (CONCORDIA 23.9 %). The core consistency is the lowest in the t-EEM_T (CONCORDIA -7.4 %) due to the method used in calculation of t-EEM_T ($TSFS_T = TSFS_{∥} \times 2TSFS_{⊥}$), making it more difficult to fit due to spectral differences between t-EEM_∥ and t-EEM_⊥. The observed difference between t-EEM_∥ and t-EEM_⊥ is likely due to the difference in the amount of indirect acceptor emission detected in each polarization setting. FRET is known to cause depolarization of emission; thus, we expect more indirectly excited acceptor emission in the t-EEM_⊥ which explains the greater deviation from trilinearity (reflected in the lower core consistency) observed (**Table 4.3**). In addition, more directly excited ANS will be detected in the t-EEM_∥ (**Figure 4.6/D**) as polarization of the bound ANS is expected to be retained.

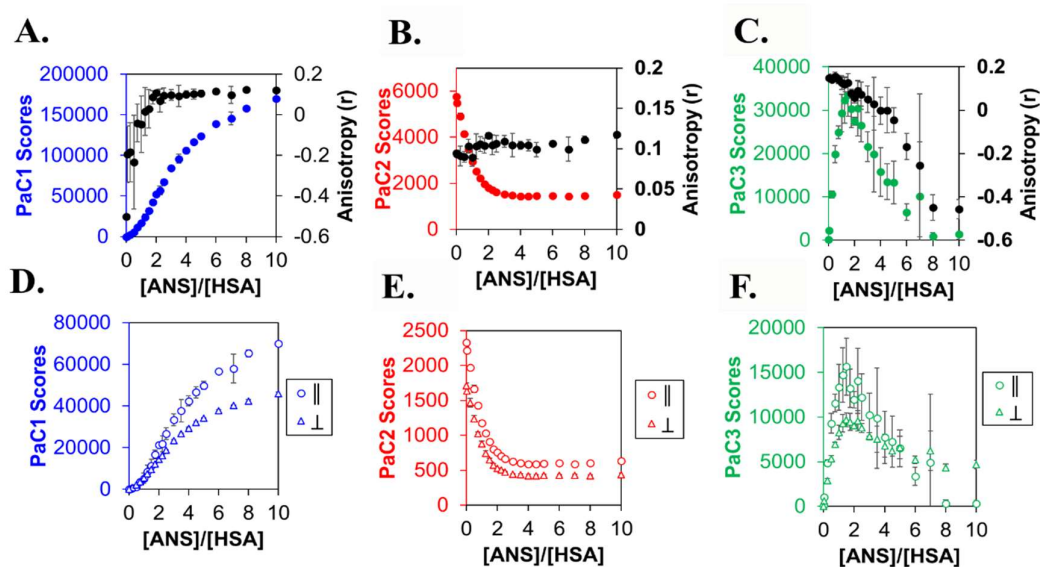


Figure 4.6: Plots of Scores (relative concentrations) and anisotropy values against $[\text{ANS}]/[\text{HSA}]$ ratios recovered using a three component PARAFAC model. **(First row)** t-EEM_T model: **(A)** Component 1, ANS emission from direct and indirect excitation (this is an unstable component); **(B)** Component 2, ; HSA intrinsic emission quenched by addition of ANS **(C)** Component 3, ANS emission arising via indirect excitation by FRET (this is also an unstable component). **(Second row)** scores from t-EEM_⊥ and t-EEM_∥ models for: **(D)** Component 1; **(E)** Component 2; and **(F)** Component 3.

Although, the three component PARAFAC model is not valid due to the rank deficiency of the dataset, the models of both parallel and perpendicular datasets, nonetheless, provide useful information about the behaviour of the underlying components in the system. The significant difference in the recovered components for each polarization measurement supported the restricted Tucker3 results presented in **section 4.2.2**.

Table 4.2: Comparison of model parameters and components obtained from the three component PARAFAC models of total, parallel and perpendicular polarized datasets.

Polarization setting	t-EEM	t-EEM_⊥	t-EEM_T
PaC1 $\lambda_{ex/em}$ (nm)	276/476	274/476	274/476
PaC1 Fit model (%)	55.5	57.3	59.9
PaC2 $\lambda_{ex/em}$ (nm)	278/472	280/344	280/344
PaC2 Fit model (%)	23.8	22.5	21.0
PaC3 $\lambda_{ex/em}$ (nm)	280/342	278/470	278/470
PaC3 Fit model (%)	20.7	20.3	19.1
Variance explained (%)	99.90	99.94	99.93
CONCORDIA (%)	23.9	-1.6	-7.4
Split-half analysis (%)	99.73	99.30	97.17

4.2.2 Tucker3 modelling of HSA-ANS interaction

A restricted Tucker3 model, with a defined core array was used here to accommodate the rank deficient data which results from FRET [244-246]. From theoretical chemical analysis of the FRET interaction HSA-ANS system under study, the fluorescence emission observed can be split into three main constituents: donor emission, acceptor emission due to direct excitation and acceptor emission arising from indirect excitation (via FRET) [246], therefore, using a 3-component model we expect to extract;

1. HSA (composed of Tyr + Trp)
2. ANS (emission arising from direct excitation)
3. ANS (emission arising from indirect excitation via FRET)

In terms of the concentration, excitation, and emission profiles of each of the components, both HSA emission (component 1) and ANS emission arising from direct excitation only (component two) are expected to show linearly independent loadings in all three modes (i.e., independent concentration evolution throughout the interaction, and independent excitation and emission spectra). However, the ANS emission arising from indirect excitation (via FRET) (component three) is expected to show an excitation spectrum like HSA (FRET donor) and an emission spectrum similar to ANS emission arising from direct excitation (i.e., linear dependencies in excitation and emission modes). Using this *a priori* chemical knowledge, the Tucker3 core array could be restricted, extracting fewer components in non-full rank modes (i.e., excitation and emission modes), to create a model which produces interpretable results. Here, a $3 \times 2 \times 2$ core array, corresponding to concentration (1st), emission (2nd), and excitation (3rd) modes respectively, was selected [246].

A variety of different Tucker models were evaluated, constraining the core array which contains 12 possible interaction terms to just 3 or 4 (**Figure 4.7**). In model 1, the emission of indirectly excited ANS was set as the sole source of the third component (i.e., interaction term in excitation of donor and emission of acceptor). Models 2 and 3 allowed that in addition to indirectly excited ANS, the fluorescence of HSA or bound directly excited ANS were the sources of the third component. Finally, model 4 examined the possibility that there was no FRET derived emission and that the third component was composed of a mixture of directly excited emission from HSA and ANS. The most stable solution was achieved using model 1 and are presented here. TuckCorCon [111] was used to validate the obtained solution gave values of >99% in each mode, indicated a good model fit. Three species (**Table 4.3**) were extracted corresponding to: HSA emission comprised of unresolved Tyr and Trp emission, directly excited ANS emission, and ANS emission arising from indirect excitation via FRET (**Figure 4.8**, respectively).

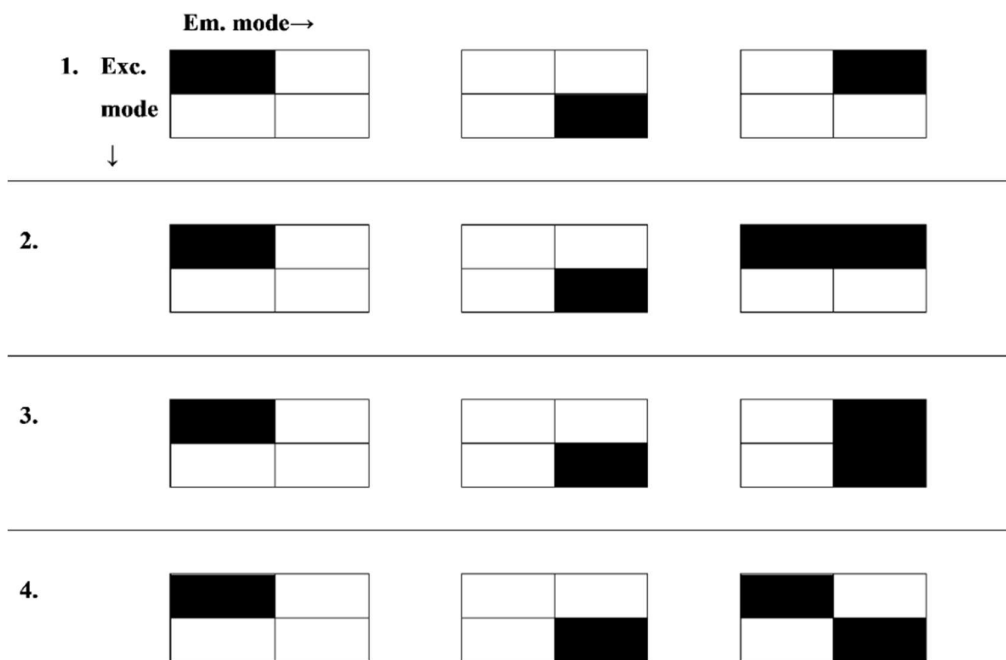


Figure 4.7: Constrained Tucker3 core defined by non-zero elements (black) in the $(3 \times 2 \times 2)$ core array. The model is restricted to 3 or 4 interactions out of 12 possible interactions. The vertical axis represents the excitation mode (2), horizontal axis represents the emission mode (2), and each square shown represents a slice of the sample mode (3).

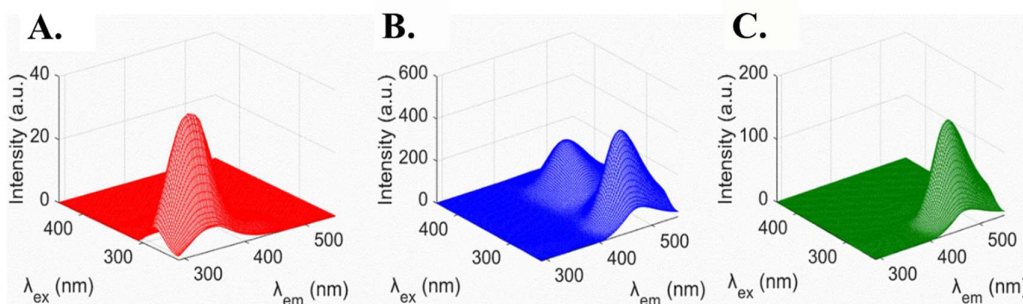


Figure 4.8: Components recovered from restricted Tucker3 modelling of full HSA-ANS emission, a representative example shown for $[ANS]/[HSA]=1$ for the most stable t-EEM $_{\perp}$ model). The components recovered correspond to: **(A)** Intrinsic HSA emission (composed of Tyr & Trp); **(B)** ANS emission arising from direct excitation; and **(C)** ANS emission arising from indirect excitation (via FRET).

Comparison (**Figure 4.9/A-C**) of the obtained scores and anisotropy values showed that the t-EEM $_{\parallel}$ or t-EEM $_{\perp}$ models were not as good at recovering the third component as the t-EEM $_{\perp}$ model, and the t-EEM $_{\perp}$ data-based models produced a more

acceptable result. Significant differences were observed in components 2 and 3 between the $t\text{-EEM}_{\perp}$ and $t\text{-EEM}_{\parallel}$ data (**Table 4.3**), with more directly excited ANS observed in the parallel polarization (**Figure 4.9/E**) and more indirectly excited ANS observed in the perpendicular polarization (**Figure 4.9/F**). This suggests that perpendicular polarization measurements were more sensitive to the indirectly excited acceptor emission presumably because of the FRET orientation factor and the hindered nature of the fluorophores involved [67, 199]. Validating this will require investigation of more controlled, rigid sample systems. However, this chemometric separation of indirect and direction acceptor emission is of significance in understanding the complex non-linear emission and variation in anisotropy of interacting multi-fluorophore mixtures.

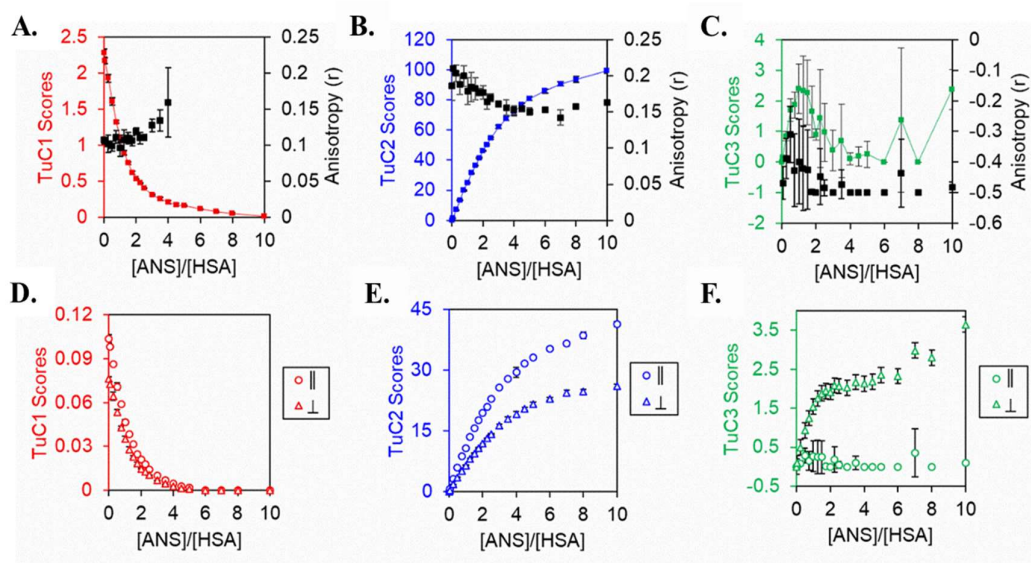


Figure 4.9: Plots of Scores (relative concentrations) and anisotropy values against [ANS]/[HSA] ratios recovered using $3 \times 2 \times 2$ restricted Tucker3 models. **(First row)** $t\text{-EEM}_T$ model: **(A)** Component 1, HSA intrinsic emission quenched by addition of ANS; **(B)** Component 2, ANS emission from direct excitation; **(C)** Component 3, ANS emission arising via indirect excitation by FRET (this is an unstable component). **(Second row)** $t\text{-EEM}_{\perp}$ and $t\text{-EEM}_{\parallel}$ models for: **(D)** Component 1; **(E)** Component 2; and **(F)** Component 3 (stable component in $t\text{-EEM}_{\perp}$).

The recovered anisotropy values (**Figure 4.9/A-C**) provided another insight into the interaction process, and provided a novel way of assessing the Tucker3

solutions. The anisotropy values recovered for HSA (TuC1), showed a slight increase as the concentration of ANS increased (ANS/HSA >2) and as the emission becomes quenched, this increase in anisotropy is consistent with FRET donor behaviour (**Figure 4.9/A**) [4, 18]. The anisotropy of the ANS emission from direct excitation, had a higher anisotropy ($r \sim 0.2$) at low molar ratios of ANS (ANS/HSA <2) due to tighter binding of the low molecular weight ANS to the higher molecular weight HSA, the anisotropy of this species was then observed to decrease slightly to $r \sim 0.18$, possibly as a consequence of homo-FRET/exciplex formation at higher ANS concentrations (**Figure 4.9/B**) [195, 248-251]. Finally, the ANS emission anisotropy arising from indirect excitation via FRET was negative [4, 252, 253] presumably due to a combination of hindered motion and the relative orientations of donor and acceptor dipoles (**Figure 4.9/C**). However, the anisotropy values recovered for component 3 (indirectly excited ANS) are not reliable, as this component was poorly resolved in the parallel polarization dataset.

Table 4.3: Comparison of band maxima for extracted components, and model fit parameters obtained from $3 \times 2 \times 2$ restricted Tucker3 models of the HSA-ANS system.

Polarization setting	t-EEM	t-EEM _⊥	t-EEM _T
TuC1 (HSA):	280/	280/	280/
$\lambda_{ex/em}$ (nm)	342	342	344
TuC1:			
Fit model (%)	4.4	4.6	9.7
TuC2 (ANS):	274/	274/	274/
$\lambda_{ex}/\lambda_{em}$ (nm)	474	474	474
TuC2: Fit model (%)	94.7	81.9	87.1
TuC3 (ANS via FRET):	280/	280/	280/
$\lambda_{ex/em}$ (nm)	474	474	474
TuC3:			
Fit model (%)	0.9	13.5	3.2
Variance explained (%)	99.70	99.70	99.86
TuckCorCon (%)	99.96	99.96	100.00

4.3 MODELLING OF HSA-ANS INTERACTION: DONOR EMISSION

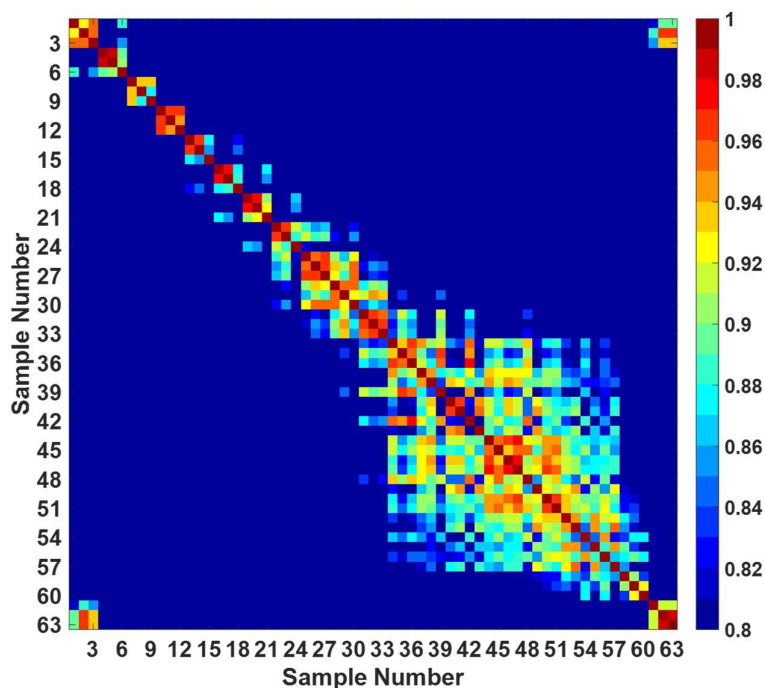


Figure 4.10: Similarity index evaluation of the HSA dataset ($63 \times 51 \times 31$), (non-normalised) showing good similarity between replicate measurements.

The intrinsic HSA fluorescence emission arises from several fluorescent contributions: (i) directly excited Tyr, (ii) directly excited Trp, (iii) indirectly excited Trp, from Tyr-Trp hetero-FRET and Trp homo-FRET, and (iv) indirectly excited Tyr (homo-FRET) [4, 45]. Here, we aim to resolve the HSA emission into two components: Tyr which is mostly non-interacting in FRET with ANS, and Trp, which has a strong FRET interaction with ANS.

Changes in the intrinsic HSA emission ($\lambda_{\text{ex/em}} = 250\text{-}310/290\text{-}390$ nm, peak A, **Figure 3.7**) were evaluated in each polarization mode using two-component PARAFAC models. Models were made on datasets containing all samples at varying $[\text{ANS}]/[\text{HSA}]$ from 0-10 molar ratios ($n=63$) (**Table 4.4** & **Figure 4.11**), as well as on sub-datasets containing samples of $[\text{ANS}]/[\text{HSA}]$ from 0-0.25 ($n=9$), 0.5-0.75 ($n=6$), 1-1.25 ($n=6$), 1.5-3 ($n=9$), and 3.5-10 ($n=9$) molar ratios (**Figure 8.1** & **Table 8.1**,

(Appendix)). PARAFAC modelling of the intrinsic HSA emission region works well because of the more trilinear behaviour of the underlying components. The models made on sub-dataset of HSA emission, show the quenching and emission spectral blue shifts of the intrinsic Tyr and Trp fluorophores during ANS binding (**Figure 8.1** (Appendix), **Figure 4.12**). In all cases, PARAFAC analysis of intrinsic HSA fluorescence recovered two components (explaining >99% of the total variance) for each polarization mode (**Table 4.4** & **Table 8.1** (Appendix)) and the quality parameters indicated that these components behaved in a trilinear fashion.

For the purpose of discussion, the model made on the dataset containing all samples (n=63) is chosen as it provides the best overview and allowed for comparison of all samples. The core consistency of 99.4 %, 99.5 %, and 99.3 % for EEM_T, EEM_I, and EEM_⊥, respectively indicated these models were reliable (**Table 4.4**). PARAFAC Component 1 (PaC1, 83-86 % explained variance) corresponds to mostly Trp-214 emission, which is linked to ANS by FRET and shows non-linear quenching behaviour (**Figure 4.11/C**) with increasing concentrations of ANS. PARAFAC Component 2 (PaC2, 14-17 % explained variance) was related to Tyr emission and shows a more linear quenching behaviour (**Figure 4.11/D**) with increasing concentrations of ANS. Comparison of the models in each polarization mode shows very similar parameters obtained in each mode (**Table 4.4**), slightly higher amount of variance is explained by PaC1 in t-EEM_⊥ than in t-EEM_∥ (and slightly lower amount of variance is explained by PaC2) due to the differences in sensitivity of the polarization modes to the resolved species (i.e., the t-EEM_⊥ polarization mode shows more sensitivity to depolarized emission).

Table 4.4: Comparison of model parameters and components obtained for PARAFAC modelling of intrinsic HSA donor emission from the different polarization measurements.

Polarization setting	t-EEM	t-EEM_⊥	t-EEM_T
PaC1	280/	280/	280/
$\lambda_{ex}/\lambda_{em}$ (nm)	354	356	354
PaC1			
Fit model (%)	82.9	85.8	85.3
PaC2	278/	276/	278/
$\lambda_{ex}/\lambda_{em}$ (nm)	308	310	308
PaC2			
Fit model (%)	17.1	14.2	14.7
Variance explained (%)	99.94	99.95	99.94
CONCORDIA (%)	99.47	99.30	99.55
Split-half analysis (%)	99.74	99.22	99.45

The anisotropy values calculated (**Figure 3.11**) for the recovered components have been used to confirm the accuracy of the resolved components for the small molecule case [254]. Here, with FRET effects, this is less certain but the values, $r = 0.09 \pm 0.01$ for Trp and $r = 0.14 \pm 0.01$ for Tyr (at $[ANS]/[HSA]=1$) are consistent with values cited in the literature [255, 256]. The slight increase in anisotropy, observed for both Trp (PaC1) and Tyr (PaC2), at higher ANS molar ratios of (>2) was ascribed to reductions in lifetime because of quenching and FRET processes [4].

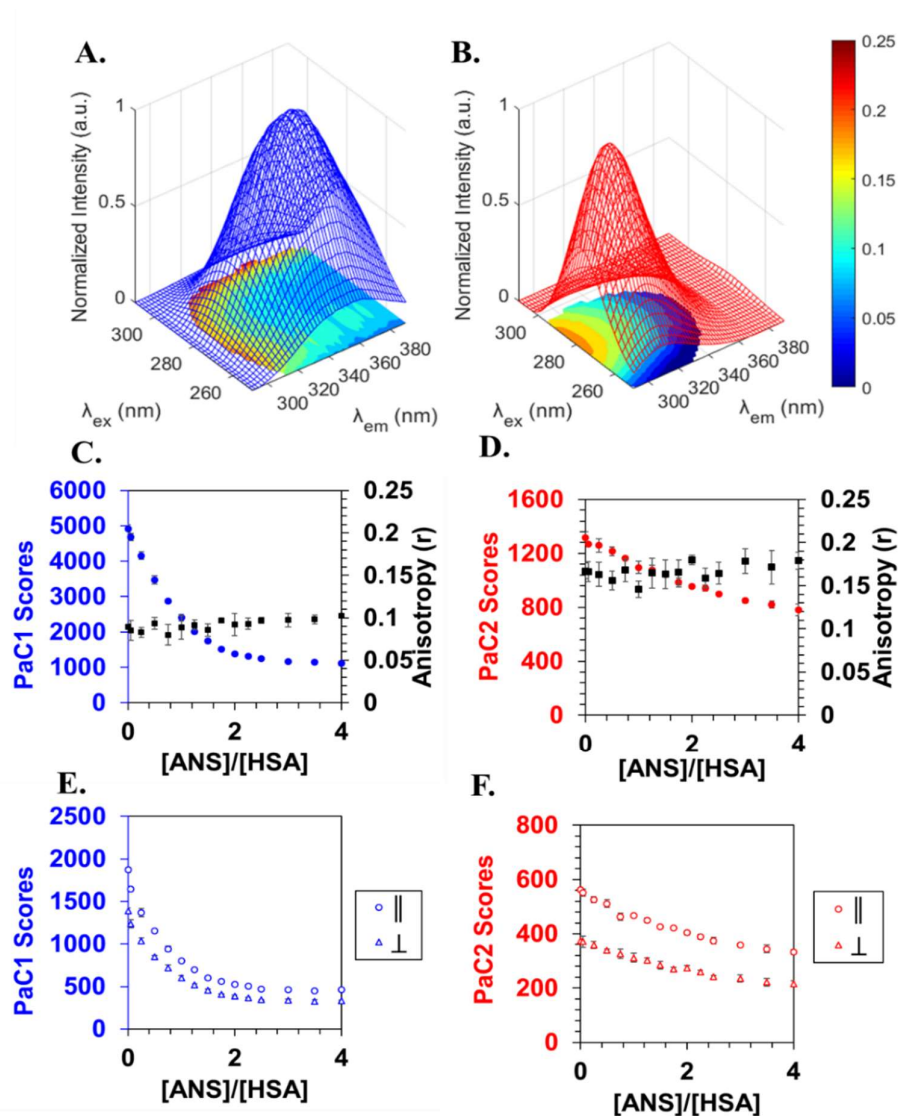


Figure 4.11: Normalised PARAFAC components of: (A) Trp (PaC1); and (B) Tyr (PaC2), obtained from decomposition of intrinsic HSA fluorescence (representative example shown for $[\text{ANS}]/[\text{HSA}]=1$) with the anisotropy maps shown under the signal. (C-D) PARAFAC scores (relative concentrations) for $t\text{-EEM}_T$ and anisotropy values (with standard deviation of triplicate samples) of a single point at emission maximum of: (C) PaC1, $\lambda_{ex}/\lambda_{em}=280/354$ nm; and (D) PaC2, $\lambda_{ex}/\lambda_{em}=278/308$ nm, and (D-F) PARAFAC scores for $t\text{-EEM}_{||}$ and $t\text{-EEM}_T$.

It is interesting to note the correlation of the shift in the maximum emission observed in the raw EEM, with the change in the ratio of the resolved PARAFAC components ($\text{PaC}_1/\text{PaC}_2$), the strong correlation ($r^2=0.81, 0.92, 0.92$ for EEM_T , $\text{EEM}_{||}$, and EEM_{\perp} , respectively) shows the shift in F_{\max} observed is mainly due to the change

in the emission ratio of Trp/Tyr (up to 2 molar equivalents ANS) (**Figure 4.12**). PARAFAC allows us to better evaluate the individual Trp and Tyr components of emission and the change their ratio can be used to explain the shift in the emission maximum, as Trp is quenched via FRET upon addition of ANS. The non-linearity of the correlation between the shift in the HSA emission maximum with the changing ratio of the resolved PARAFAC components (PaC1/PaC2), is due to different quenching mechanisms operating for the Tyr and Trp fluorophores.

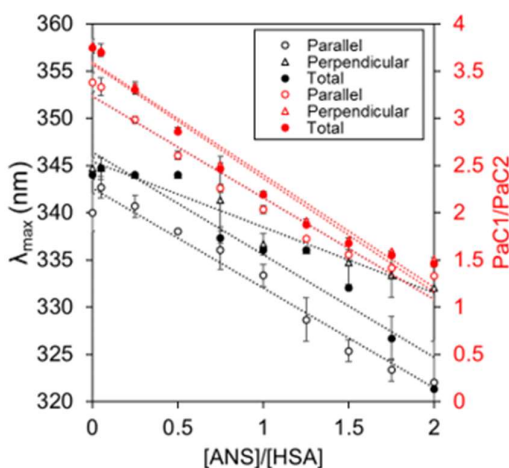


Figure 4.12: Correlation of the shifts in maximum emission wavelength (black) and change in PaC1/PaC2 ratio (red) with $[ANS]/[HSA]$, shown are the data for samples up to $[ANS]/[HSA]=2$ (where strong quenching is occurring).

4.4 CALCULATION OF BIOCHEMICAL PARAMETERS USING ARMES

In this section the calculation of biochemical parameters (Stern-Volmer analysis and FRET efficiency values) using the PARAFAC resolved Tyr and Trp components from the donor emission region are presented and compared with the conventional method of calculation present in **section 3.5, Chapter 3**.

4.4.1 Stern-Volmer analysis

Stern-Volmer and modified Stern-Volmer analysis were completed this time using the PARAFAC resolved Tyr and Trp components, in each polarization mode (**Figure 4.13, Figure 8.2 & Figure 8.3 (Appendix)**) and showed significantly different than those generated using conventional spectra of unresolved donor emission (**Table 4.5**). Large differences were observed between the Trp and Tyr K_{SV} values reflecting the different quenching mechanisms at play for the Trp and Tyr fluorophore populations [4, 212-214].

The Stern-Volmer quenching constants (K_{SV}) calculated using PARAFAC scores (**Table 4.5**) for Trp were significantly higher (~16%) than the Stern-Volmer quenching constant recovered using the conventional unresolved emission data. Over the wider ANS concentration range, PaC1 scores showed that Trp-214 underwent three phases of quenching (**Figure 4.13/A-D**). Firstly, a linear relationship was observed up to a 1:1 ANS/HSA ratio indicative of a single fully collisional quenching process (**Figure 4.13/A**) [4, 18]. This can be attributed to ANS induced quenching [188, 198]. As more ANS was added ($[ANS]/[HSA]>1$), the Stern-Volmer plot first curves upward (**Figure 4.13/B**) which is symptomatic of a more complex quenching process due to the presence of increasing amounts of static quenching or a second dynamic quenching process. From $[ANS]/[HSA]=2$ to $[ANS]/[HSA]=4$, static quenching of Trp-214 (**Figure 4.13/C**) emission was observed which was consistent with fluorescence lifetime measurements, where the τ/τ_0 value was nearly constant for $[ANS]/[HSA]>2$ (**Figure 3.17/A**). For $[ANS]/[HSA]>4$, Trp emission was relatively constant indicating that quenching was maximised (**Figure 4.13/D**), and no further changes can be discriminated.

For the Stern-Volmer plot using PaC2 scores (Tyr emission) (**Figure 4.13/A-D**), an almost linear decrease is observed, caused by quenching up to $[ANS]/[HSA]=4$ ($r^2 > 0.99$) indicating a single type of static quenching [4, 18]. Beyond this point $[ANS]/[HSA]>4$ all accessible fluorophores are quenched. Slight difference in values of K_{SV} are also observed between polarization modes (with higher constants recovered in the parallel polarization mode for both PaC1 and PaC2), indicating this polarization mode may be more sensitive to FRET related quenching of the resolved Tyr and Trp populations (**Table 4.5**).

Table 4.5: Stern-Volmer quenching constants calculated using the unresolved fluorescence emission (classical) and resolved Trp (PaC1) and Tyr (PaC2) emission, for the appropriate linear region (up to $[ANS]/[HSA]=1$).

Polarization	t-EEM	t-EEM _⊥	t-EEM _T
Classical Stern-Volmer	F₀/F at λ_{ex}/λ_{em} 280/350 nm		
K_{sv} (× 10⁴ M⁻¹)	6.0 ± 0.4	6.0 ± 0.5	6.0 ± 0.4
r²	0.98 ± 0.01	0.99 ± 0.01	0.99 ± 0.01
Trp (PaC1)	PaC1₀/PaC1		
K_{sv} (× 10⁴ M⁻¹)	7.2 ± 0.5	7.0 ± 0.4	7.1 ± 0.5
r²	0.98 ± 0.00	0.99 ± 0.01	0.98 ± 0.01
Tyr (PaC2)	PaC2₀/PaC2		
K_{sv} (× 10⁴ M⁻¹)	1.5 ± 0.1	1.1 ± 0.2	1.2 ± 0.2
r²	0.92 ± 0.03	0.96 ± 0.05	0.95 ± 0.03

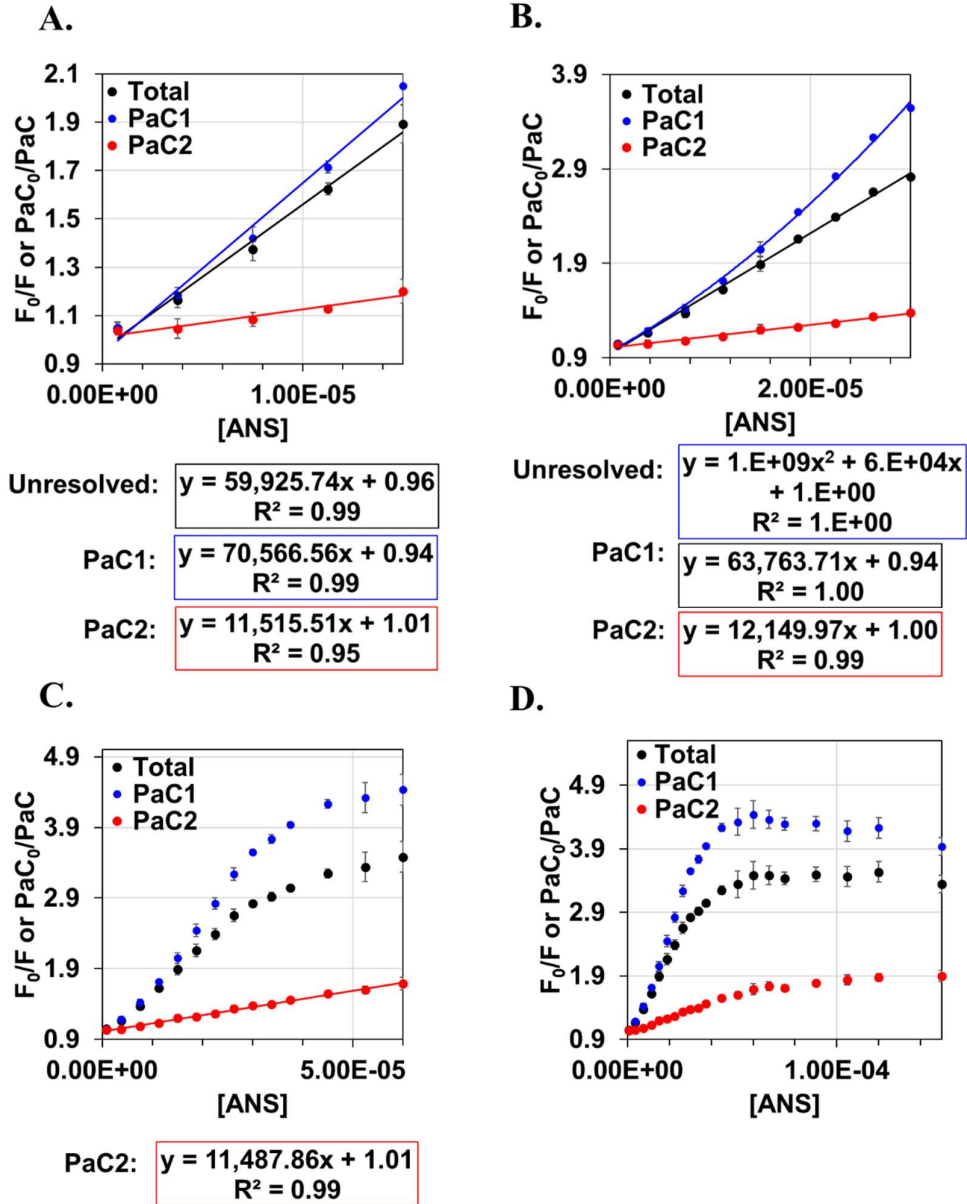


Figure 4.13: Stern-Volmer plots (F_0/F or PaC_0/PaC) using $t-EEM_T$ for unresolved spectra (black) (based on a single point $\lambda_{ex}/\lambda_{em} = 280/350$ nm in absence and presence of quencher) and for the individual Trp (PaC1) (red) and Tyr (PaC2) (blue) populations. Stern-Volmer plots (A-D) show the quenching up to $[ANS]/[HSA]=1,2,4,10$, respectively, and the linear region is at low ANS concentrations is associated with FRET quenching.

4.4.2 Multivariate calculation of FRET efficiency

Using the PARAFAC solution obtained, a new method was proposed for calculating FRET efficiency in a multi-dimensional manner. Commonly FRET efficiency is calculated using a single point of the unresolved donor emission (here, intrinsic HSA fluorescence) from 2-D spectra (**Chapter 3, section 3.5.3**) [4, 18, 180]. Thus, the maximum emission of the FRET donor in the presence of the acceptor (F_{DA}) and in the absence of the acceptor (F_D) are used to calculate FRET efficiency using **Equation 3.2 (Chapter 3)**.

The conventional method, however, does not account for the presence of emission from non-interacting fluorophores (PaC2). PARAFAC decomposition of the donor quenching process enables calculation of FRET efficiency using the interacting species only (PaC1). Our new proposed method replaces the intensity measurements with the recovered components $PaC1_{DA}$ and $PaC1_D$ (**Equation 4.3**).

Equation 4.3

$$E = 1 - \frac{PaC1_{DA}}{PaC1_D}$$

PARAFAC resolution of intrinsic HSA (donor) fluorescence, enabled FRET efficiency calculations using the multi-dimensional emission of the interacting component only. FRET efficiency values calculated using the new proposed PARAFAC method consistently show higher (of up to ~6-7 %), but statistically significant absolute values (p-value < 0.05) for the [ANS]/[HSA] 1.0 > 0.25 samples) than those calculated conventionally using the single point calculations from the unresolved raw t-EEM (**Table 4.6**). The underestimation of the Trp-ANS FRET efficiency using conventional 2D spectra is due to the quenching of the non-interacting Tyr residues whose emission overlaps that of the FRET interacting species. Although the difference observed in this example are small, larger differences would be observed in cases where non-interacting fluorophores had higher quantum yields.

The FRET efficiencies calculated using the emission of the donor, HSA, component (TuC2) recovered from Tucker3 modelling of the global emission (**section 4.2.2**) are also included here for comparison. Although the values follow the same trend, these values cannot be quantitatively relied upon as the Tucker 3 model was not

ideal showing a high degree of error. To improve the Tucker3 solution, a higher resolution dataset is required. In addition, the contribution of the HSA donor emission is very small relative to the overall emission, so this model was less likely to accurately assess donor emission as it becomes quenched. At higher ratios of $[ANS]/[HSA] > 2.5$, where HSA is more quenched, very little signal is resolved leading to unreasonably high values of FRET efficiencies, the values at lower concentrations of ANS are in better agreement with PARAFAC results.

Table 4.6: FRET efficiency values (mean and standard deviation (in brackets)) calculated for each polarization measurement using the conventional, PARAFAC, and Tucker3 methods. Conventional calculations were made using at $\lambda_{ex}/\lambda_{em} = 280/350$ nm (from t-EEM spectra). Values for $[ANS]/[HSA]$ ratios of >1 are unreliable due to the increasing influence of other quenching processes as identified by Stern-Volmer analysis.

ANS/ HSA	Conventional $(E = 1 - \frac{F_{DA}}{F_D})$			PARAFAC $(E = 1 - \frac{PaC1_{DA}}{PaC1_D})$			Tucker3 $(E = 1 - \frac{TuC1_{DA}}{TuC1_D})$			T-test values (conv./ PARAFAC)		
	EEM	EEM _⊥	EEM _T	EEM	EEM _⊥	EEM _T	EEM	EEM _⊥	EEM _T	EEM	EEM _⊥	EEM _T
0.05	0.050 (0.01)	0.045 (0.02)	0.047 (0.02)	0.051 (0.02)	0.045 (0.02)	0.047 (0.02)	0.052 (0.01)	0.047 (0.02)	0.048 (0.02)	0.747	0.929	0.888
0.25	0.16 (0.01)	0.14 (0.03)	0.15 (0.02)	0.16 (0.01)	0.15 (0.03)	0.16 (0.02)	0.17 (0.01)	0.16 (0.04)	0.16 (0.02)	0.009	0.284	0.007
0.5	0.29 (0.03)	0.27 (0.02)	0.28 (0.02)	0.31 (0.02)	0.29 (0.02)	0.30 (0.02)	0.32 (0.02)	0.30 (0.02)	0.30 (0.02)	0.011	0.041	0.002
1	0.50 (0.02)	0.48 (0.03)	0.49 (0.02)	0.52 (0.02)	0.51 (0.02)	0.51 (0.02)	0.55 (0.02)	0.54 (0.02)	0.52 (0.02)	0.004	0.040	0.001
2.5	0.72 (0.00)	0.72 (0.00)	0.72 (0.00)	0.75 (0.00)	0.75 (0.00)	0.75 (0.00)	0.86 (0.00)	0.86 (0.00)	0.82 (0.00)	0.001	0.003	0.001
5	0.75 (0.00)	0.75 (0.01)	0.75 (0.01)	0.76 (0.00)	0.77 (0.01)	0.77 (0.01)	0.98 (0.00)	0.99 (0.00)	0.93 (0.01)	0.001	0.001	0.004
10	0.71 (0.01)	0.73 (0.01)	0.72 (0.01)	0.73 (0.01)	0.75 (0.01)	0.75 (0.01)	1.00 (0.00)	1.00 (0.00)	0.99 (0.01)	0.001	0.0020	0.0038

Note: paired t-test conducted at 95% confidence interval for FRET efficiency calculations based on conventional and proposed PARAFAC approach for each polarization measurement.

4.5 CONCLUSIONS

The separation of the underlying components of a FRET interacting mixture is of interest in many scientific applications for accurate quantitative analysis of FRET parameters [239, 257]. In addition, FRET is also the main cause of non-linearity in MDF spectra of spectrally overlapped, interacting multi-fluorophore mixtures such as proteins [6, 7, 107], thus, to better understand their complex emission, the separation of FRET induced emission is of significant importance. A range of different methods have been suggested in literature for the separation of underlying components in a FRET interaction system, including multispectral FRET microscopy methods [239, 258], and steady state MDF measurements [245, 246] both of which can be coupled with chemometric analysis to resolve the underlying components of the fluorescence.

In this work, the collection of pMDF of the FRET interacting, HSA-ANS, mixture facilitated the decomposition of emission, using chemometrics, into individual the fluorophore species of the interaction in each polarization mode. This decomposition was unfeasible using conventional 2-D emission. Two different chemometric modelling techniques, PARAFAC [106] and restricted Tucker3 [85], were explored and their appropriateness was evaluated in modelling the global HSA-ANS emission and, the quenching effects of the interaction on the sub-region of HSA (FRET donor) emission.

The chemometric modelling of the global t-EEM data was complicated by the non-linearity introduced by the indirect excitation of the ANS (acceptor) via FRET meaning PARAFAC was not an appropriate model. A more flexible, Tucker3 model, was required to handle the non-linearity introduced by the FRET sensitized region of the emission, and *a priori* chemical knowledge of the system was used to restrict the model and reduce the rotational ambiguity. Restricted Tucker3 modelling of FRET interacting MDF has previously been applied by *Kompany-Zareh et al.* [244-246] to model FRET interacting mixtures, however modelling in these studies was completed on unpolarized EEM spectra, of a small sample set [244-246]. Here, the modelling was completed using a larger sample set (n=63) of pMDF collected in TSFS mode, with an additional dimension of anisotropy offering a novel way of validating the chemometric solution achieved. The restricted Tucker3 model was found to effectively

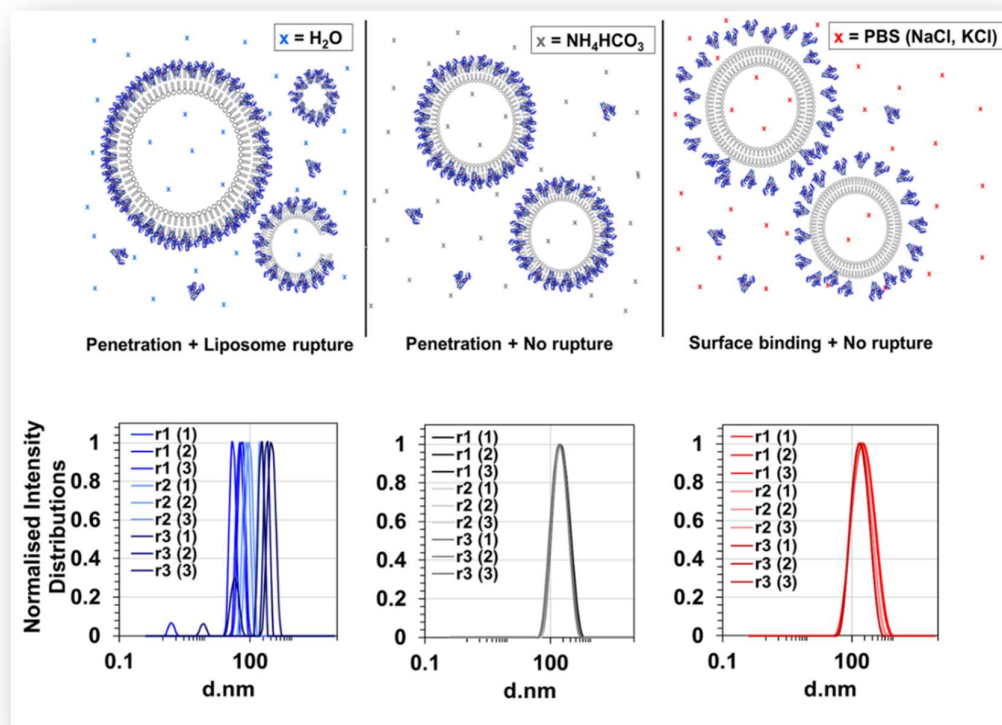
accommodate the non-linearity of the FRET acceptor region and decomposed the fluorescence emission into three components: HSA (Tyr + Trp), directly excited ANS, and ANS indirectly excited via FRET. In addition, the anisotropy values recovered for the resolved components were used for validation of the solution, showing rational values for HSA ($r=0.10-0.15$) [256] and directly excited ANS emission ($r=0.20-0.18$) [195, 249], with the component arising from indirect excitation showing a negative anisotropy, as expected [253]. A significant difference is observed between the restricted Tucker3 models in each polarization mode, with the model on the $t\text{-EEM}_\perp$ showing the most stable solution, showing the advantage of collecting pMDF spectra.

In the analysis of the sub-region FRET donor, HSA emission, PARAFAC was found to successfully decompose the emission into interacting (mainly Trp-214) and non-interacting donor fluorophores (mainly Tyr). This decomposition of the donor emission facilitated the calculation of Stern-Volmer constants and FRET parameters, such as FRET efficiency, using the multi-dimensional signal of individual donor fluorophore populations. Higher values of Stern-Volmer constant ($\sim 16\%$) and FRET efficiencies ($\sim 6-7\%$) were recovered for the interacting donor fluorophore population (Trp-214, PaC1) than the conventional calculation by the removal of the influence of non-interacting donor fluorophores. Although, the difference in FRET efficiency values recovered using the conventional and new proposed PARAFAC approach is relatively small, the method is still useful especially in situations where there is a larger amount of non-interacting fluorophores or in cases where the non-interacting fluorophores have a higher quantum yield.

Overall, chemometric decomposition of the fluorescence emission into contributing fluorophores facilitates a more accurate analysis of molecular interactions and photophysical processes occurring in the system. The comprehensive analysis of FRET using ARMES in this HSA-ANS model system is a first step towards understanding of FRET in more complex multi-fluorophore mixtures and how it manifests itself in the resulting MDF spectra. In addition, the decomposition of the FRET donor fluorescence using PARAFAC analysis was successfully achieved, providing a new quantitative approach for the calculation of biochemical parameters such as quenching constants and FRET efficiencies using the multi-dimensional emission of the interacting and non-interacting fluorophore populations.

5 SPECTRAL ANALYSIS OF THE INTERACTION BETWEEN HSA AND DMPC LIPOSOMES

Graphical abstract:



This chapter is the first of two which will discuss the findings of the interaction between HSA and 1,2-dimyristoyl-sn-glycero-3-phosphocholine (DMPC) liposomes in three different aqueous environments; water (pH ~7.9), ammonium bicarbonate (ABC) (50 mM, pH ~7.8), and phosphate buffered saline (PBS) (10 mM, pH ~7.4). In this chapter, the interaction is investigated using spectral analysis of DLS, conventional absorbance, fluorescence steady-state, and lifetime spectroscopies.

5.1 INTRODUCTION

Liposomes are spherical vesicles containing at least one lipid bilayer, typically ~50-500 nm in diameter, which spontaneously form when certain lipids are hydrated with aqueous media (**Chapter 1, section 1.6.2**) [259]. Liposomes are ideal candidates for drug delivery systems (DDS) due to their multiple advantages including, high biocompatibility and biodegradability, low toxicity and immunogenicity and controlled release [144, 157-159]. Liposomes can carry both hydrophilic (in the aqueous interior of the liposome), and hydrophobic drugs (dissolved in the lipid bilayer) [158-160, 162], and protect the drug from the external environment *in vivo*, thereby increasing the drug's stability, and reducing the drugs toxicity [159].

In the context of their use *in vivo*, it is important to characterise the interaction of liposomes with serum constituents, particularly serum proteins [10, 11]. Interaction of liposomes with plasma proteins can dramatically affect their stability and thus *in vivo* behaviour which in turn impacts on therapeutic efficacy of the DDS [163, 260-262]. In this study, a DMPC / HSA system was used as a model to investigate protein-liposome interactions. HSA was selected as it is the major serum protein present in blood, and it is also a relatively simple protein in terms of structure (8 nm in diameter and 15 nm long [263, 264]) and fluorescence (see **section 3.1, Chapter 3**) [4, 185]. DMPC is neutrally charged and consist of the saturated phospholipid, 1,2-dimyristoyl-*sn*-phosphatidylcholine. DMPC vesicles (~200 nm in diameter) were used for two reasons: first, because they have good stability in water and buffer (**Figure 5.1**), and second, because they are also used in a number of liposome DDS formulations [265, 266]. The liposomes were labelled with a FRET pair of lipophilic dyes; 1,1'-dioctadecyl-3,3,3',3'-tetramethylindocarbocyanine perchlorate (DiI) and 1,1'-dioctadecyl-3,3,3',3'-tetramethylindocarbocyanine, 4-chlorobenzenesulfonate salt (DiD) in order to provide a further means of probing the interaction in terms of dye fluorescence [178, 179].

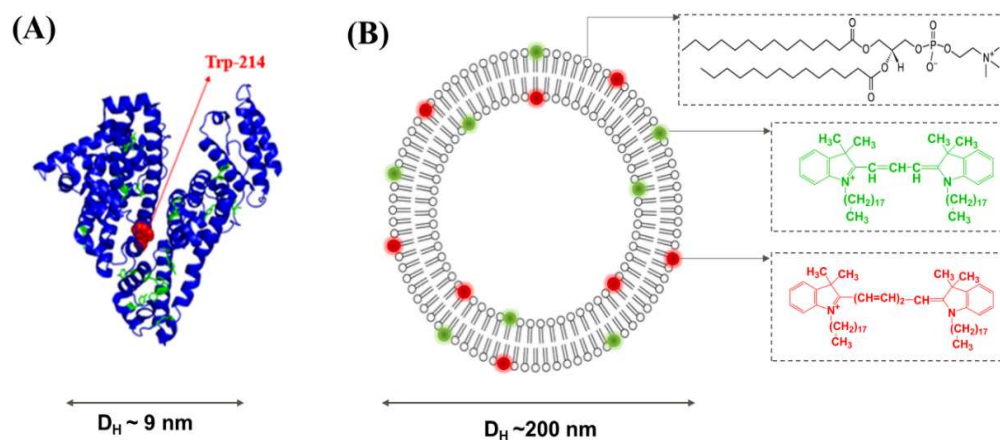


Figure 5.1: Model protein-liposome system studied consisting of: **(A)** HSA (*PBD file 4K2C*) with Tyr (green) and single Trp-214 (red) fluorescent residues of the protein highlighted, and **(B)** DMPC liposomes $\sim 200 \text{ nm}$ in diameter made of 1,2-dimyristoyl-sn-glycero-3-phosphocholine phospholipid (DMPC) labelled with lipophilic dyes Dil (green) and DiD (red).

An important factor to consider when studying protein-liposome interactions is the aqueous environment of the interaction. The aqueous environment (e.g., pH and ionic strength) will dramatically affect the physicochemical properties of both protein and liposome and will therefore influence the interaction [267, 268]. This factor can sometimes be overlooked in the experimental design of studies investigating protein-liposome interactions, with some studies avoiding the use of buffers, using water instead to favour interaction [10, 11]. However, in order to better replicate physiological conditions, it is necessary to employ the use of buffers [269]. The use of buffers is essential to stabilize proteins by increasing their conformational stability thereby preventing protein aggregation in solution [270, 271]. The effects of buffers on liposomes are less commonly studied, however salt composition and ionic strength is known to affect properties such as size and membrane rigidity [272, 273].

In a study by Kandamasy & Larson [268] investigating the interaction of the zwitterionic liposome, POPC, and magainin (an antimicrobial peptide), at different salt concentrations, a decreased interaction was observed with increasing salt concentration. The decreased interaction here, was caused by a combination of factors including an increase in membrane rigidity along with stabilisation of proteins at high salt concentration, which reduces the propensity for interaction [272, 273]. Conversely

in low ionic strength solutions, such as water, the protein is far less stable in the aqueous phase making interactions between hydrophobic regions of the proteins and the zwitterionic lipid bilayer more energetically favourable [268].

Protein–liposome interactions are often investigated using conventional 2D fluorescence measurements of intrinsic protein emission [23, 274, 275]. However, intrinsic protein fluorescence contains overlapping Tyr and Trp emission leading to complex emission spectra. This overlap limits the information available from 2-D spectra, so ARMES provides an attractive approach to study the interaction.

5.2 DLS ANALYSIS

Prior to investigation of the protein-liposome interaction the stability of the liposome preparations was assessed over a two-day period to determine if the liposomes were stable over the timeframe used in the interaction experiments. No major size changes (<4%) were detected in all cases (**Figure 5.2**), indicating the liposomes were sufficiently stable for 8-hours, and thus observed changes would not be caused by the instability of the liposome in the solution but instead caused by interactions occurring with protein.

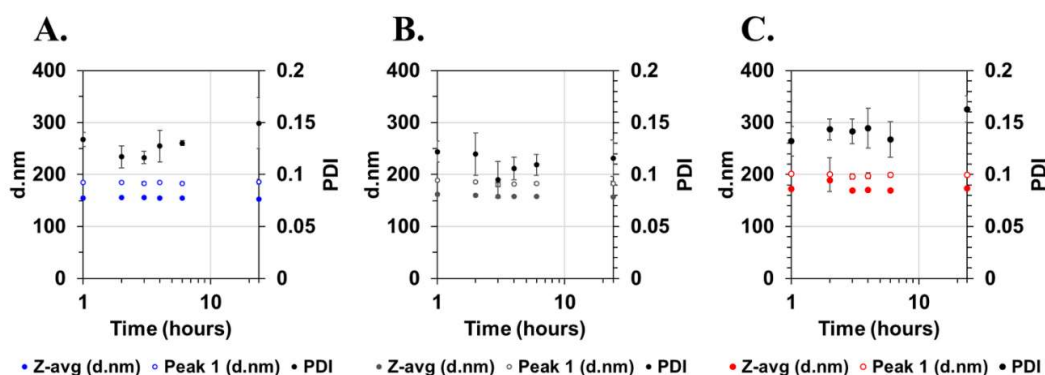


Figure 5.2: Stability of liposomes over time in (A) water, (B) ABC (50 mM), and (C) PBS (10 mM). Low variation in average size and PDI is observed over a 24-hour period, indicating a stable system.

For the interaction between the protein and liposomes, DLS analysis of the freshly extruded liposome solutions was first obtained to validate if successful extrusion had been achieved [276]. The extruded liposomes showed relatively low polydispersity index (PDI) (<0.2) in all solutions [277], with average hydrodynamic diameters of 137.8, 161.6, and 166.3 nm in water, ABC, and PBS, respectively (**Figure 5.3 & Table 5.1**). The liposomes were smaller in water compared to buffers because zwitterionic lipid vesicles are known to swell in salt solutions [276]. This liposome swelling is thought to be primarily driven by weakening of van der Waals (vdW) attraction between lipids and solvent, the strength of the vdW interaction is proportional to the dielectric constant difference between lipid and solvent, the larger the difference, the stronger the attraction between adjacent bilayers [278].

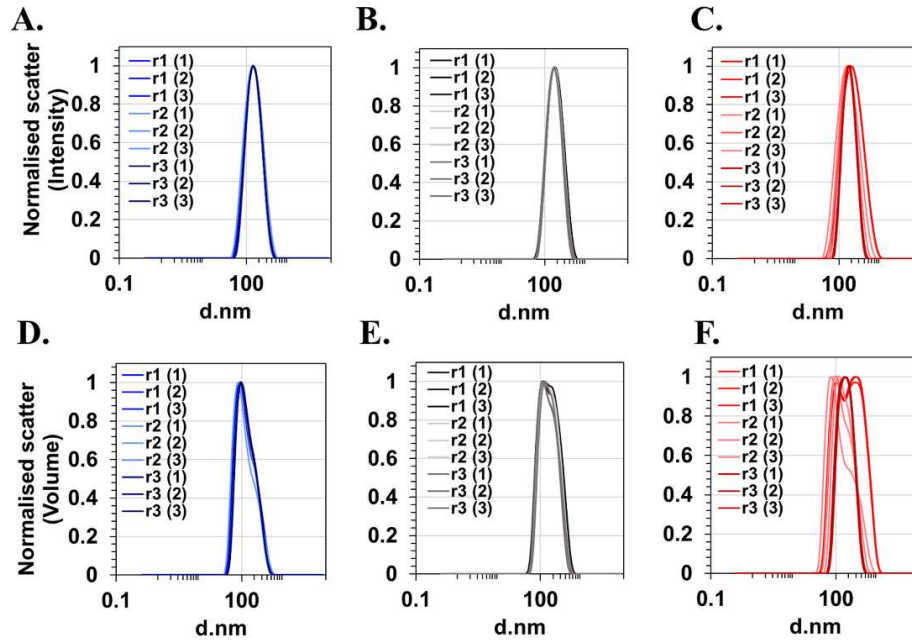


Figure 5.3: DLS Spectra of samples containing extruded DMPC liposomes (0.37 mM) in each of the aqueous environments used in the study, data shown for triplicate measurement of each replicate (i.e., $n=9$). **A-C:** show the DLS spectra calculated by scatter intensity of liposomes in water, ABC (50 mM) and PBS (10 mM), respectively (L-R) & **D-F:** show the DLS spectra calculated by scatter volume of the liposomes in water, ABC (50 mM) and PBS (10 mM), respectively (L-R).

The surface area of the liposome (πr^2) was calculated from the z-average values determined from DLS and total number of lipids per liposome, N_{tot} , were determined, using a simple method suggested by Mozafari *et al.* [279] to give a rough estimate of the numbers of liposome particles present where; $4\pi(d/2)^2$ is the surface area of vesicle's monolayer; d is the diameter of the vesicle; h is the thickness of the phospholipid bilayer (i.e., ~ 5 nm); a is the phospholipid head group area (which was estimated to be ~ 0.71 nm). [64]. **Equation 5.1** could then be simplified to give **Equation 5.2**;

Equation 5.1

$$N_{Tot} = \left[\left(4\pi \left(\frac{d}{2} \right)^2 \right) + \left(4\pi \left(\left(\frac{d}{2} \right) - h \right)^2 \right) \right] / a$$

Equation 5.2

$$N_{Tot} = 17.69 \times \left[\left(\frac{d}{2} \right)^2 + \left(\frac{d}{2} - 5 \right)^2 \right]$$

DLS analysis was also completed on samples containing HSA only and revealed that the hydrodynamic diameter of HSA increased very significantly from 7.8 nm in water, to 9.5 and 9.6 nm in PBS and ABC buffers, respectively (**Table 5.1**). This size difference observed here is due to electrostatic stabilization of the protein structure into a larger extended ellipsoid or oblate ellipsoid conformation by counterions present in PBS and ABC. Conversely in water, HSA is more compact with a smaller hydrodynamic radius due to the lack of pH buffering capacity and counterions present in solution which are necessary to increase the proteins conformational stability through electrostatic stabilization [271, 280]. DLS also revealed a higher PDI (and lower peak 1 contribution) in water which suggests the presence of more aggregates (**Table 5.1 & Figure 5.4**). [281, 282]. These structural and composition differences of HSA in each environment have a significant impact on their interaction with liposomes.

Table 5.1: Average particle size (Z-average, nm), approximate number of lipid molecules per liposome and surface area per liposome (calculated from Z-average) peak 1 size (nm), polydispersity index (PDI), and percentage area calculated from scatter intensity of peak 1 (%) of samples containing liposomes only (*top*); Z-average, HSA binding surface area (calculated from Z-average, end-on and side-on binding assumption), peak 1 size, PDI, and percentage area calculated from scatter intensity of peak 1 (%) of samples containing HSA only (*middle*); Z-average, peak 1 size, PDI, and percentage area of liposome samples incubated with 2 mg/ml HAS (*bottom*) in water, ABC buffer, and PBS (**L-R**).

	Water	ABC	PBS
Liposome only samples:			
Z-average (diameter, nm)	137.8 (± 1.4)	161.6 (± 3.0)	166.3 (± 1.5)
Liposome surface area (nm²)	~59,625	~82,041	~86,882
Approx. no. lipids per liposome [279]	~156,210	~217,132	~230,347
Peak 1,diameter (nm)	162.1 (± 2.7)	188.6 (± 5.8)	197.8 (± 2.1)
Polydispersity index	0.11 (± 0.01)	0.11 (± 0.02)	0.15 (± 0.03)
Peak 1 (% area)	100.0 (± 0.0)	100.0 (± 0.0)	100.0 (± 0.0)
HSA only samples:			
Z-average (diameter) (nm)	7.8 (± 0.9)	9.6 (± 0.5)	9.5 (± 0.2)
HSA Surface area, circular area model from z-avg (πr^2), nm²	~ 47.8	~72.4	~70.9
Surface area per HSA, side on, nm².	~44.8	~44.8	~44.8
Surface area per HSA, end on, nm².	~14.4	~14.4	~14.4
Peak 1 (diameter) (nm)	5.8 (± 0.41)	9.5 (± 0.19)	9.8 (± 0.2)
Polydispersity index	0.32 (±0.05)	0.25 (±0.02)	0.26 (±0.02)
Peak 1 (% area)	73.9 (±1.0)	87.8 (± 3.6)	90.2 (±1.9)
HSA/Liposome complexes (2 mg/mL) :			
Z-average (nm)	2983 (±4077) /Not reliable	170.0 (± 40.3)	214.5 (± 75.6)
Peak 1 (nm)	137 (± 90) / Not reliable	233.3 (± 80.1)	258.1 (± 105.1)
Polydispersity index	0.65 (±0.32) / Not reliable	0.24 (±0.08)	0.29 (±0.05)
Peak 1 (% area)	91.6 (±7.3) / Not reliable	100.0 (± 0.0)	100.0 (± 0.0)

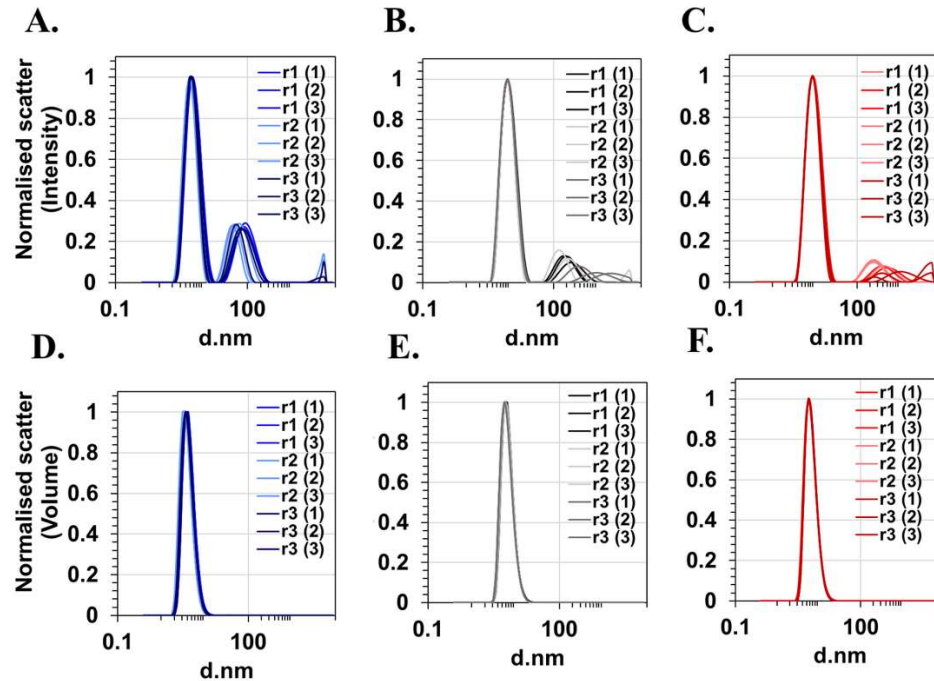


Figure 5.4: DLS Spectra of samples containing HSA free in each of the aqueous environments used in the study, data is the triplicate measurement of each replicate (i.e., n=9). **A-C:** show the DLS spectra calculated by scatter intensity of HSA in water, ABC (50 mM) and PBS (10 mM), respectively & **D-F:** show the DLS spectra calculated by scatter volume of HSA in water, ABC (50 mM) and PBS (10 mM), respectively.

The surface area of the HSA binding surface, which binds to the liposome was estimated using three different binding mechanism assumptions (**Figure 5.5**), firstly the surface area was estimated using the diameter of HSA (z-avg) determined from DLS measurement to estimate the circular surface area (πr^2), secondly, the surface area was calculated using an end-on binding mechanism assumption [283], along the 3.8 nm axis (πa^2), using literature report values of HSA dimensions (i.e. 3.8 (2a) nm in diameter and 15 nm (2b) long [263, 264]) and, thirdly, the surface area was calculated assuming HSA bound using the side on binding mechanism, along the 15 nm (πab) side [283] (**Figure 5.5**). The estimated amount of HSA required to form a monolayer on the liposome surface was then estimated by dividing the surface area of the liposomes (spherical assumption using the diameter determined from DLS) by the surface area of the binding surface of HSA, and from these calculations it is estimated

anywhere between 300 – 8,000 HSA molecules are required to form a uniform monolayer (Table 5.2).

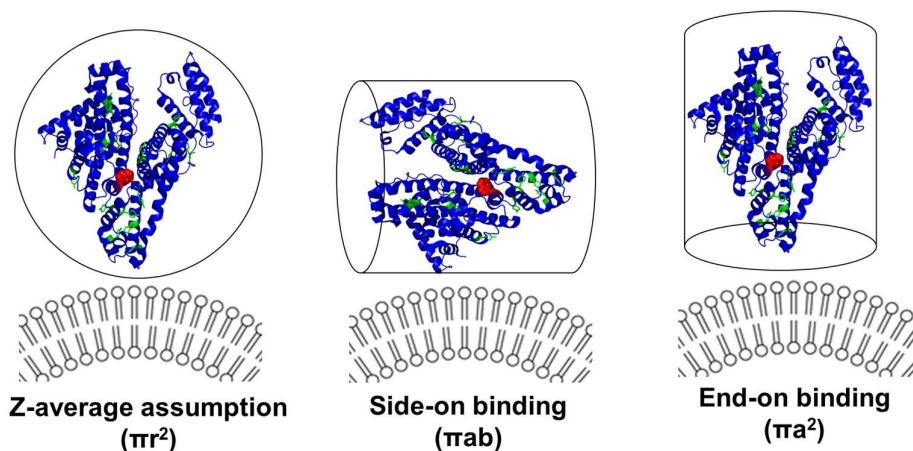


Figure 5.5: Binding mechanism assumptions used for the calculation of HSA binding surface.

Table 5.2: Surface areas of liposome and HSA binding surface using calculations made from the HSA z-average circular area, end-on binding assumption, and side-on binding assumption. The calculated amount of HSA required for a uniform monolayer on the liposome surface is given for each assumption.

Surface area liposome (nm ²)	Est. surface area HSA (nm ²)			Est. max. HSA per monolayer		
	Z-avg	End-on	Side-on	Z-avg.	End-on	Side-on.
Water						
59,625	47.8	11.3	57.0	1247	5260	333.1
HSA: Liposome ratio: 828:1 → 12,740:1						
ABC						
82,000	72.3	11.3	57.0	1134	7238	458.4
HSA: Liposome ratio: 1151:1 → 17,780:1						
PBS						
86,839	70.8	11.3	57.0	1226	7665	485.4
HSA: Liposome ratio: 1221:1 → 18,786:1						

After incubation with HSA, the liposomes were extensively ruptured in water, with the DLS data showing multiple size populations (**Figure 5.6/G**) making quantitative analysis impossible [134, 165]. However, in ABC and PBS, the liposomes appeared much more stable, and DLS showed that there were two populations of particles. For example, for liposomes incubated with 2 mg/ml HSA, in ABC and PBS, polydispersity increased to ~0.24 and ~0.29, and average particle size increased to ~170 and ~215 nm respectively. The bimodal distribution in the volume data showed peaks at ~150-200 nm and at ~250-350 nm (**Figure 5.6/H-I**). The first population is related to a combination of both free unperturbed liposome (if any remains in solution) and the liposome with a protein coating. The second population is likely arising from an aggregated form of the interacting protein-liposome species formed during the interaction [284], previous studies have reported that the formation of a protein monolayer (or protein corona) on the liposome surface can make their surface more adhesive, thus inducing formation of particle clusters which can explain the larger population observed [285, 286].

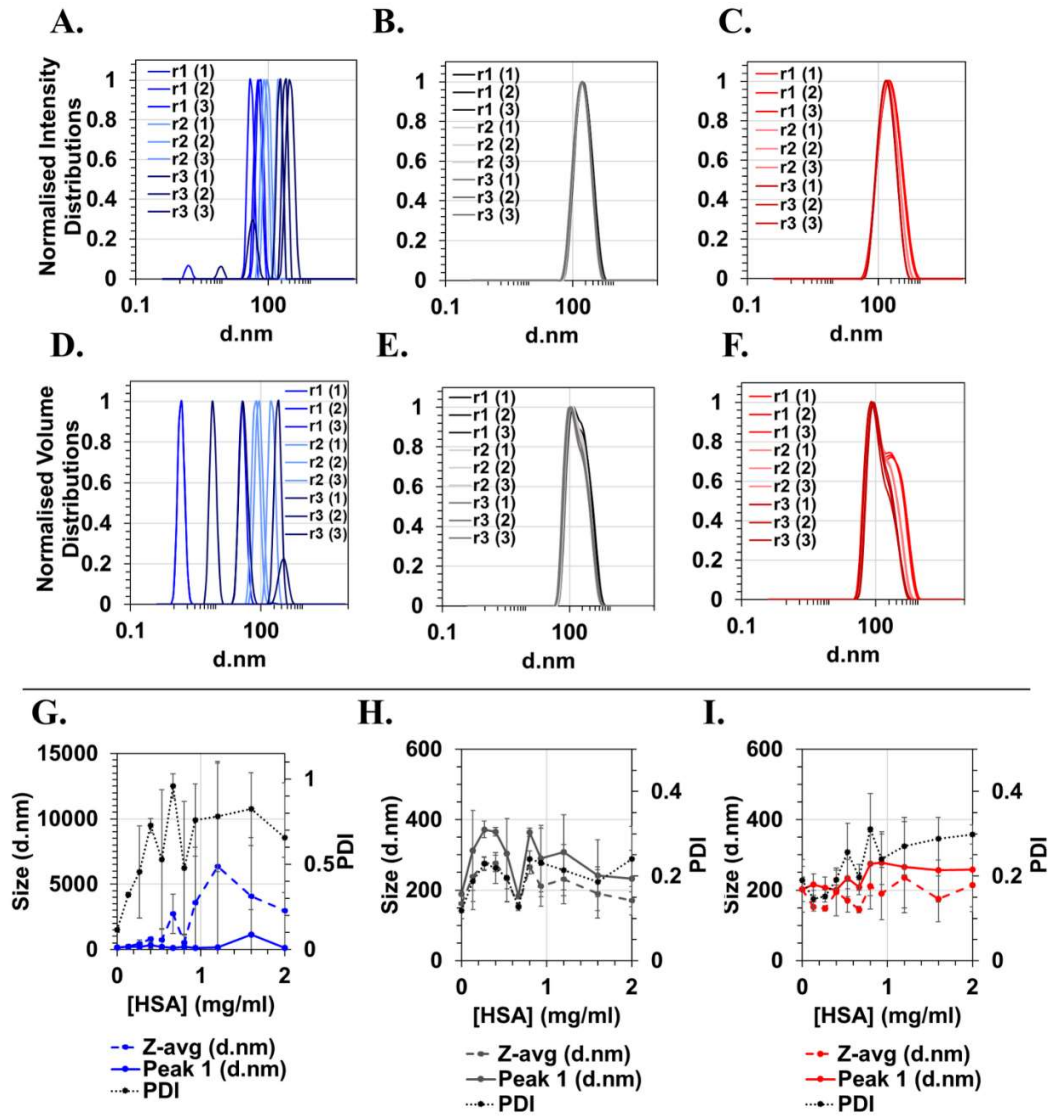


Figure 5.6: DLS measurements of HSA-liposome mixtures (with 0.13 mg/ml HSA) in water (blue), ABC (grey), and PBS (red)). **A-C:** correspond to the intensity based DLS distributions; **D-F:** correspond to volume-based distributions. **G-H:** show changes in average particle size (Z-avg.), peak 1 and PDI of liposomes after addition of varying concentrations of HSA (0-2 mg/ml).

5.3 ABSORBANCE SPECTROSCOPY

Absorbance measurements of the HSA-DMPC samples were significantly affected by scatter arising from the liposome samples (~200 nm) which are of similar size to the wavelengths of light used in absorbance measurements of protein absorbance spectra (250- 400 nm). The impact of this scatter contamination is particularly significant in the analysis of protein absorbance as scatter is significant in this region (i.e., <300 nm). Thus, unresolved absorption spectra could not be quantitatively analysed, which is common problem encountered when analysing systems containing liposomes [300, 301]. Other methods have been suggested in literature to correct scatter interference in absorbance measurements using mathematical corrections of spectra based on equations to approximate scatter contribution (i.e., using Rayleigh-Gans-Debye equation) [301].

Here, an alternative approach using MCR-ALS was applied to extract the concentration and pure spectral profiles of the individual species. MCR models were made on the global dataset (n=108) (**Figure 5.7**) as well specific buffer datasets (**Figure 5.8**). The best results were achieved on the global dataset and these results are used for discussion here. The two-component MCR model here, explained >99.8% of the total variance. Non-negativity constraints were set in both spectral and concentration modes and equality constraints were for one-component in the spectral mode using the pure HSA spectra. This enabled not only better resolution of HSA for lower concentration samples, but also removed any rotational ambiguities compared to using non-negativity constraints alone (**Table 8.2** vs. **Table 8.3** (*Appendix*)). The application of equality constraint also increased only marginally the lack of fit (LOF) as shown in

Table 5.3, showing that the equality constraint did not significantly alter the result indicating these constraints were appropriate for the data being modelled.

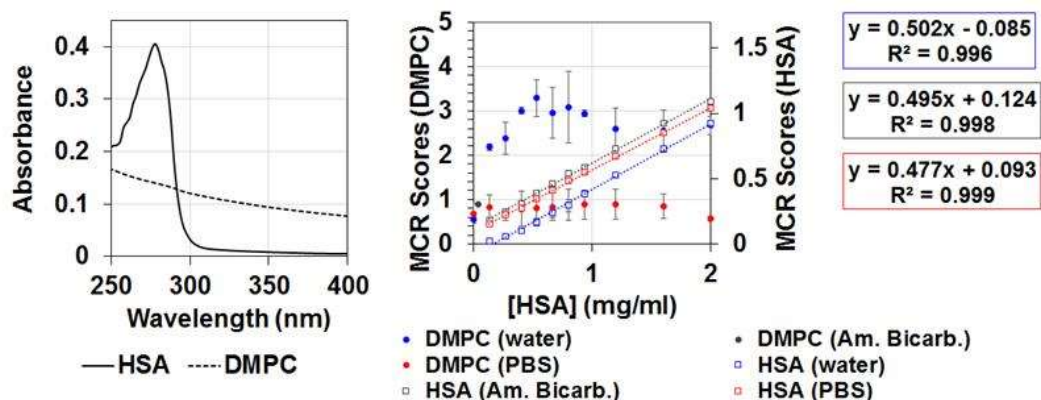


Figure 5.7: (A) MCR resolution of the UV absorbance spectra showing two components corresponding to HSA and DMPC, and (B) the corresponding MCR scores of the recovered components in water, ABC and PBS, with HSA showing a linear behaviour with increasing concentration.

The resolved HSA component accounted for 20.6% of the variance, and the DMPC component accounted for 79.2 %, clearly showing the significant impact particle light scatter on the absorbance spectra. Furthermore, analysis of the resolved scores of each component shows the scatter component scores were much greater in water (**Figure 5.7/B**) which was expected with the larger degree of rupturing occurring in the case (as shown by DLS measurements). For both ABC and PBS, the scatter signal remained nearly constant for all HSA additions which is indicative of a relatively stable particle size and distribution in these environments.

Table 5.3: Results of MCR models on absorbance spectra of all samples (n=108), and only samples in water (n=36), ABC (n=36), and PBS (n=36) respectively.

Dataset modelled	Global	Water	ABC	PBS
<i>Model using non-negativity (C and S^T) and equality constraint on HSA spectra</i>				
Variance explained (%)	99.8	100.0	100.0	100.0
Lack of fit (%)	4.2	0.9	0.7	1.1
C1 (HSA)	20.6	7.3	43.9	42.1
C2 (Scatter)	79.2	92.7	56.1	57.9
<i>Model using non-negativity (C and S^T) only</i>				
Lack of fit (%)	3.5	0.9	0.6	1.0

The scores of the C1 (HSA species) recovered, showed linear behaviour with increasing concentration of HSA in all cases ($r^2 > 0.99$) which shows agreement with the Beer-Lambert law. Thus, MCR appears to accurately resolve the DMPC and HSA contributions. However, this work also shows the limitations of absorbance spectroscopy as there was no evidence for any spectral changes in either component thus, we cannot monitor the protein-liposome interaction apart from saying that in water the liposomes become highly disrupted in the presence of protein. Thus, a more sensitive measurement method is required.

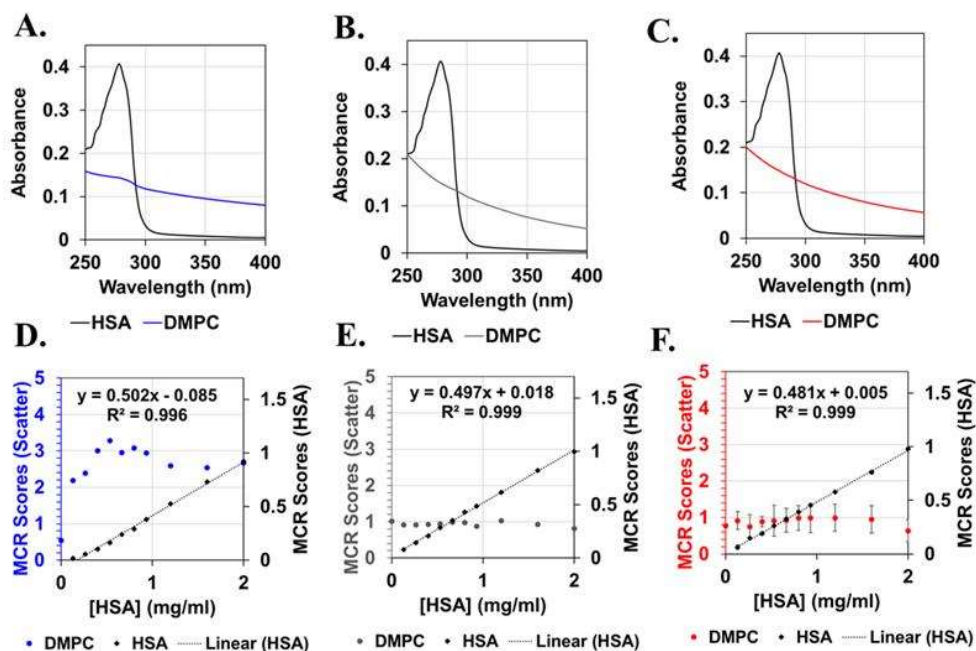


Figure 5.8: MCR resolution of the UV absorbance spectra showing two components corresponding to HSA and DMPC resolved for sub-models on datasets in water, ABC and PBS aqueous environment (A-C), and the corresponding MCR scores of the recovered components, with HSA showing a linear behaviour with increasing concentration (D-F).

5.4 2D FLUORESCENCE EMISSION AND ANISOTROPY ANALYSIS

The interaction between HSA and DMPC liposomes resulted in a significant blue-shift in all polarization modes, with a shift of 22 and 17 nm observed in water and ABC respectively for the sample with [HSA]=0.13 mg/ml in t-EEM_⊥ (Figure 5.9/A-B & Figure 8.4, Figure 8.5 (Appendix)) [4]. In PBS under the same conditions, however, there was far less significant blue-shift of ~ 1 nm (Figure 5.9/C & Figure 8.4, Figure 8.5 (Appendix)). The differences observed in the emission are due to different interaction mechanisms at play in each of the aqueous environments, modulated by their different ionic compositions: (i) Unstable disruption and penetration of HSA in water, resulting in multiple populations (Figure 5.6/A) observed in DLS and a blue-shift in emission (Figure 5.9/A); (ii) Surface binding of HSA and penetration in ABC, with aggregation observed in DLS (Figure 5.6/B) and a blue-shift in emission (Figure 5.9/B); (iii) Non-penetrating protein layer in PBS,

with aggregation observed in DLS (**Figure 5.6/C**) but no significant blue-shift in emission (**Figure 5.9/C**).

From simple calculations (**Table 5.2**) we estimated anywhere between 300 - 8,000 HSA molecules are required to form a 100% monolayer on the liposomes without taking into consideration any structure changes on adsorption. The HSA: liposome ratio ranges from 1:800 to 1:19,000 (**Table 5.2**) in each environment meaning the formation of protein monolayers is possible in the experimental conditions used. In the case the buffered environments of ABC and PBS an increase in Z-average and peak 1 particle size, suggests that protein monolayers are formed on the liposome surface [10, 287].

For PBS, which is the most stable system, the increase in size is ~ 48 nm (ΔZ_{avg}) which is more than that expected for a liposome with a uniform HSA monolayer. The larger increase in size is likely caused by the fact that the formation of a protein monolayer leads to the formation of a more adhesive liposome surface, inducing the formation of larger protein-liposome species [286]. Since neither the emission nor the lifetime (see section 0) change very significantly in PBS we can deduce that HSA appears to remain more in the aqueous phase, associating with the liposome surface without penetration [288].

The blue-shifted emission of HSA in the presence of DMPC in water and ABC environments, suggests that the Trp-214 residue is now surrounded by more a hydrophobic environment [4]. This might mean that for the relatively stable liposomes in water and ABC that the HSA has reoriented on the surface, penetrating the bilayer changing the environment sufficiently to affect the emission [289-291]. In ABC the increase in size is ~ 9 nm (ΔZ_{avg}) which is about that expected for a liposome with a uniform HSA monolayer, in this case we likely have a combination of interacting species including liposomes which have a protein monolayer, liposomes penetrated with protein and aggregated liposomes induced by the interaction of the liposome with HSA.

Finally, in water we have already seen extensive disruption from DLS (**Figure 5.6/A**) measurement, here again we see a significant blue-shift in emission caused by a change in HSA environment, the penetration and disruption of the liposome in water is supported by previous findings by *Sabin et al.* [10] where the penetration of HSA

into the bilayer was characterised using differential scanning calorimetric (DSC) and zeta-potential measurements. This study along with other reported literature supports the assumption that HSA coats the liposome surface, penetrates [289-291], and deforms the lipid bilayer in water [10, 292, 293].

Unfortunately, anisotropy values recovered from conventional measurements of emission (**Figure 5.9/D-F**) are not useful due to the large excess of free HSA in solution and the noise associated with the measurement obscuring any anisotropy changes due to protein adsorption on the liposome. The anisotropy, of HSA at 280/350 nm ($\lambda_{ex/em}$), in all solutions of free HSA in water, ABC, and PBS were nearly identical with similar values of 0.11 (± 0.00), 0.10 (± 0.01), and 0.10 (± 0.01), respectively. To recover useful anisotropy values the emission requires decomposition into its underlying components, this topic will be further explored in **Chapter 6**.

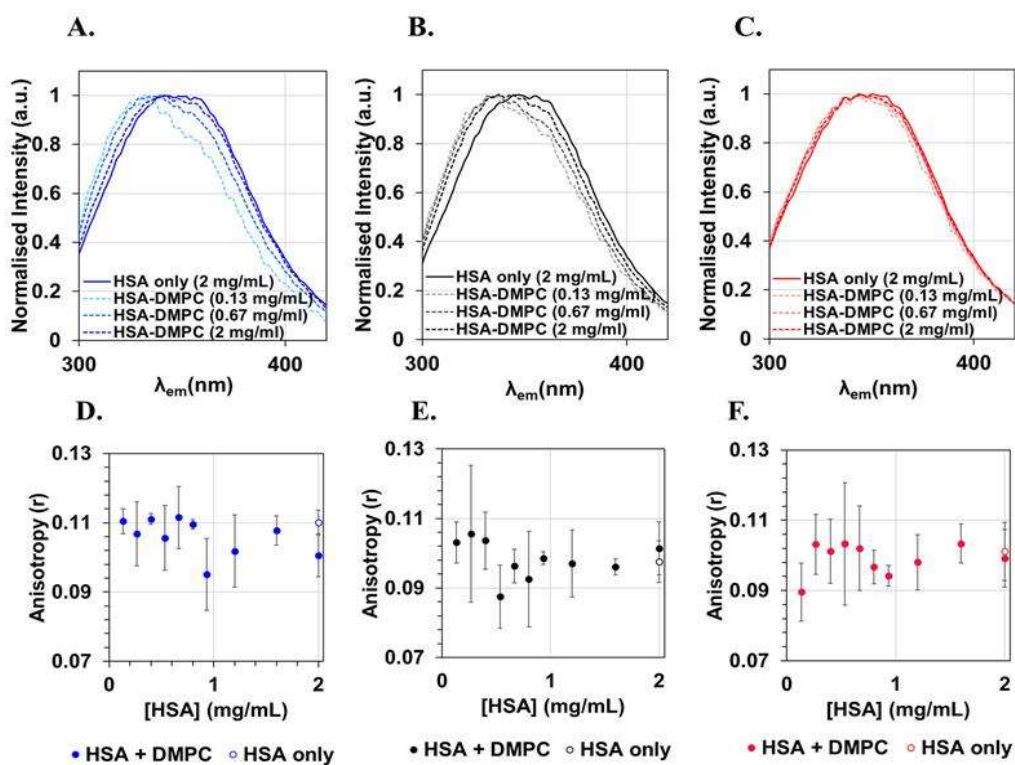


Figure 5.9: A-C: Fluorescence emission of HSA (exc. 280 nm) in t-EEM $_{\perp}$ in: (A) Water, (B) ABC and (C) PBS, in the absence of DMPC liposomes (0.37 mM) (solid lines) and in the presence DMPC liposomes (dashed lines, showing largest shift at the lowest concentration of HSA). D-F: Anisotropy of HSA (280/350 nm ($\lambda_{ex/em}$)) in absence (unfilled circles) and presence of DMPC liposomes (filled circles) at increasing concentrations of HSA in: (D) Water, (E) ABC and (F) PBS.

5.4.1 Dil-DiD lipophilic dye fluorescence

2-D emission spectra were also collected for regions of the FRET pair of lipophilic dye emission, Dil and DiD (**Figure 5.10** & **Figure 5.11**). Lipophilic dyes are in widespread use in both cell biology and in understanding the biophysics of synthetic lipid membranes [294-296]. In previous studies, FRET measurements of Dil and DiD fluorescence emission, was used to study the solubilization mechanism of DMPC liposomes by detergent molecules, where a decrease in FRET efficiency occurred as the liposomes became solubilized [178, 179]. The rationale behind the use of lipophilic dyes in my work was to provide a further means of probing the interaction between by measuring the change in the distance between dyes (located in the liposome bilayer) upon interaction of HSA with the liposome. The emission spectra of Dil and DiD were collected, along with other measurements, at equilibrium after ~3 hours of incubation of the DMPC liposome with HSA.

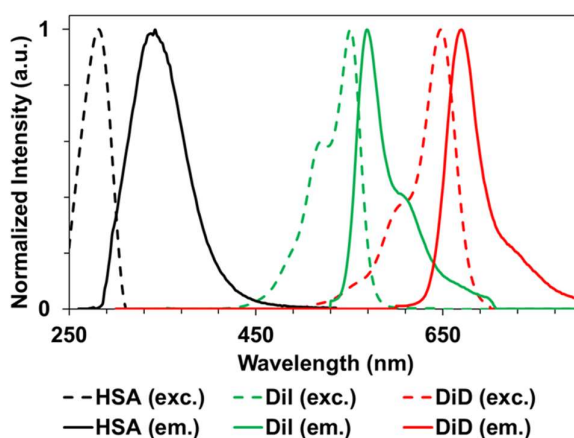


Figure 5.10: Spectral overlap of Dil and DiD lipophilic dyes. The dashed lines are the absorbance spectra and the solid lines the fluorescence emission.

Equation 5.3

$$E_{FRET} = \frac{I_{665}}{I_{665} + I_{565}}$$

where I_{665} and I_{565} represent the fluorescence intensities of the acceptor at 665 nm, and donor at 565 nm, respectively, following excitation at 532 nm.

However, the spectra for the dye emission of collected from the samples show very little change with protein concentration, and unfortunately provided little additional information. There are various reasons to explain this observation: it is likely that liposomes could rupture and reform during the ~3-hour incubation of the protein and liposome (in the case of water), the penetration of the bilayer may not be significant enough to cause a change in FRET efficiency (in the case of ABC) and the liposomes bilayer remains unperturbed (in the case of PBS), in addition, the measurement noise is likely too high to detect small changes in FRET efficiency. One interesting observation from the evaluation of FRET efficiency in the liposomes is the significantly higher FRET efficiency values recovered in the perpendicular polarization (**Figure 5.11**), this supports previous findings which showed the perpendicular polarization was more sensitive to the depolarized emission arising from the indirect excitation via FRET [9].

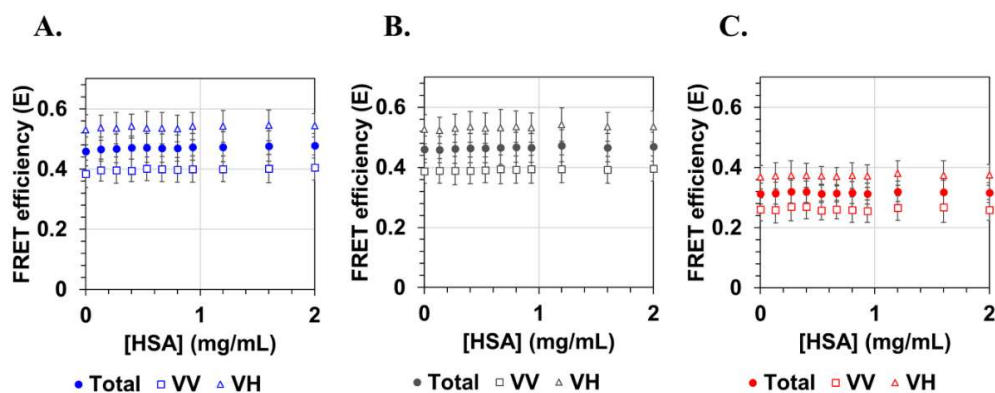


Figure 5.11: FRET efficiency between DiI and DiD lipophilic dyes as HSA is added to DMPC liposomes in (A) Water, (B) ABC (50 mM), and (C) PBS (10 mM). FRET efficiencies were approximated by the apparent FRET efficiency (Equation 3.2, Chapter 3). FRET efficiency values recovered from the perpendicular ($t\text{-EEM}_{\perp}$) polarization are observed to be consistently higher.

5.5 LIFETIME ANALYSIS

The lifetime of HSA was calculated using a tri-exponential fit of the fluorescence decay (**Table 5.4 & Figure 5.12/D**), and results from the analysis of HSA lifetime in the absence and presence of DMPC liposome in each of the aqueous environments supported findings from UV, DLS, and fluorescence emission measurements. In both water (6.2 → 5.2 ns) and ABC buffer (6.3 → 5.6 ns), a decrease in the fluorescence lifetime of HSA is observed upon interaction with the DMPC liposomes (**Table 5.4 & Figure 5.12/AB**).

Although, generally the insertion of Trp fluorophores into a more hydrophobic environment is accompanied by an increase in quantum yield [4], here, other factors are at play which affect the lifetime recovered. The decrease in lifetime observed upon interaction in water and ABC buffer, suggests that HSA undergoes some unfolding, exposing the Trp-214 residue, upon penetration of the DMPC bilayer [297, 298]. This observation is in agreement with other reported literature, where interaction between HSA and similar DPPC liposomes also resulted in a decrease in HSA lifetime [299].

In contrast, for the interaction between HSA and DMPC liposomes in PBS (5.6 → 5.8 ns), quenching of the fluorescence lifetime is not observed indicating again that HSA remains in a similar physicochemical environment to the buffer solution and does not appear penetrate the lipid bilayer (**Table 5.4 & Figure 5.12/C**). Here, there is a slight increase in the fluorescence lifetime was observed, mainly due to a reduction in rotational mobility on surface binding [4, 300, 301], but there may also be a contribution from the increase in the local refractive index in the presence of DMPC liposomes [300].

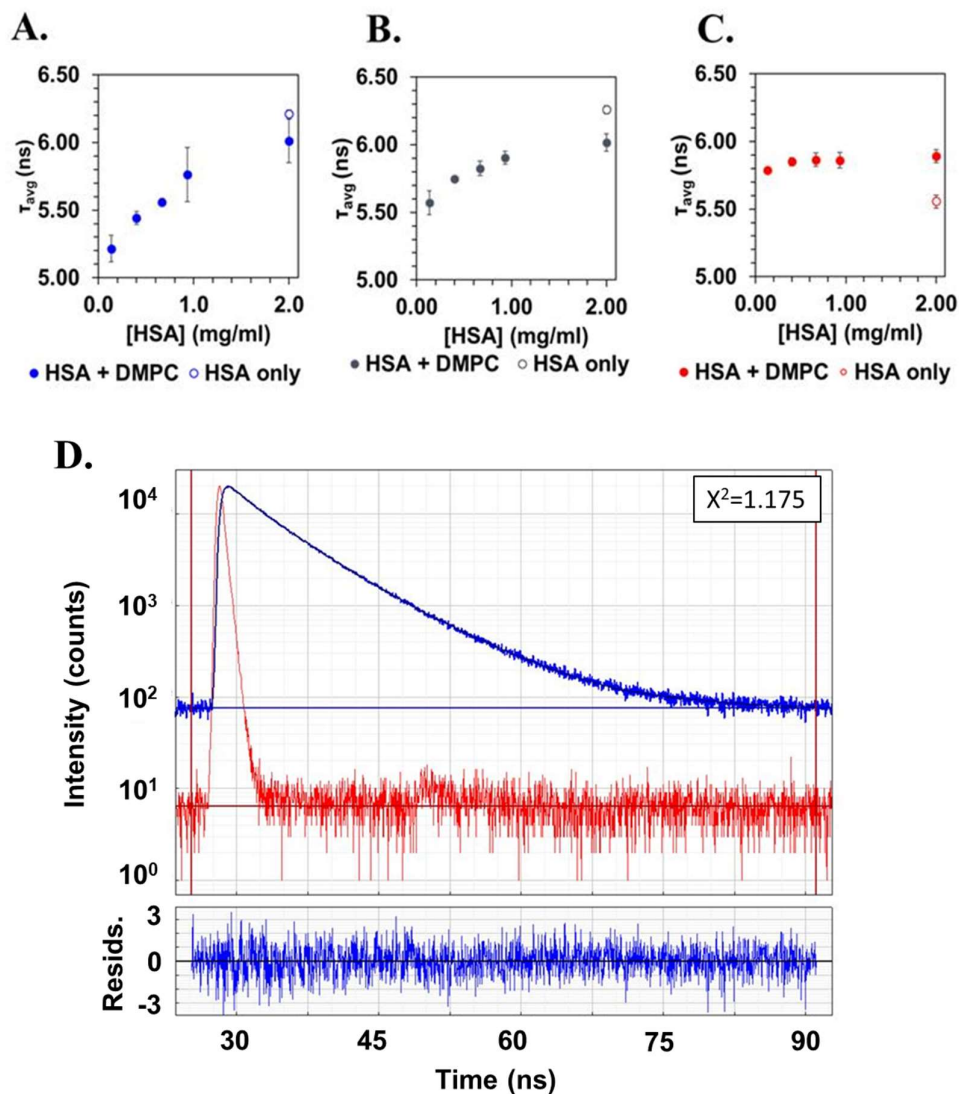


Figure 5.12: A-C: Intensity average lifetime of HSA interaction with DMPC in (A) water, (B) ABC, and (C) PBS aqueous environments, with HSA free in each solution with DMPC lipid present is shown by the unfilled marker in each graph. (D) Shows an example of tri-exponential fitting of the fluorescence lifetime decay of HSA (2 mg/ml) in the presence of DMPC (0.25 mg/ml) in water.

Table 5.4: Tri-exponential reconvolution fitting of HSA emission at 295/350 nm. The intensity and amplitude weighted average ($\langle\tau\rangle_f$ & $\langle\tau\rangle_a$) are shown along with the lifetimes (τ) and their amplitudes (a).

Water										
[HS A] (mg/ ml)	[DM PC]/ [HSA]	τ_1 (ns)	τ_2 (ns)	τ_3 (ns)	a_1	a_2	a_3	$\langle\tau\rangle_f$	$\langle\tau\rangle_a$	χ^2
2	-	7.38 (0.17)	3.61 (0.32)	0.92 (0.41)	13480 (999)	10334 (530)	3817 (871)	6.2 (0.03)	5.1 (0.04)	1.19 (0.02)
0.13	183.7 5	6.62 (0.13)	2.84 (0.18)	0.41 (0.22)	7075 (595)	8079 (635)	6939 (3520)	5.2 (0.10)	3.3 (0.67)	1.19 (0.02)
0.40	61.25	6.74 (0.04)	3.10 (0.09)	0.65 (0.10)	11329 (595)	11817 (474)	4375 (519)	5.4 (0.05)	4.2 (0.12)	1.28 (0.07)
0.67	36.75	6.58 (0.60)	3.22 (0.16)	0.61 (0.22)	11922 (935)	12354 (315)	6989 (2933)	5.6 (0.03)	4.1 (0.36)	1.23 (0.06)
0.93	26.25	7.08 (0.15)	3.33 (0.14)	0.71 (0.24)	12112 (543)	11842 (1222)	5871 (3024)	5.8 (0.25)	4.4 (0.58)	1.25 (0.03)
2	12.25	7.35 (0.15)	3.66 (0.41)	0.93 (0.30)	12040 (1516)	11604 (1435)	4313 (909)	6.0 (0.16)	4.8 (0.15)	1.19 (0.07)
ABC (50 mM)										
[HS A] (mg/ ml)	[DM PC]/ [HSA]	τ_1 (ns)	τ_2 (ns)	τ_3 (ns)	a_1	a_2	a_3	$\langle\tau\rangle_f$	$\langle\tau\rangle_a$	χ^2
2	-	7.44 (0.08)	3.71 (0.16)	1.10 (0.11)	1561 (281)	1063 (187)	3084 (172)	6.3 (0.03)	5.3 (0.05)	1.20 (0.01)
0.13	183.7 5	6.98 (0.21)	3.27 (0.20)	0.90 (0.37)	4867 (226)	5740 (706)	1217 (251)	5.6 (0.05)	4.6 (0.12)	1.17 (0.01)
0.40	61.25	7.27 (0.05)	3.68 (0.04)	1.05 (0.15)	1070 (172)	8603 (455)	2806 (20.1)	5.8 (0.02)	4.7 (0.05)	1.19 (0.04)
0.67	36.75	7.30	3.65	0.92	1028	1229	2871	5.8	4.8	1.21

		(0.09)	(0.03)	(0.11)	(57.7)	(378)	(299)	(0.05)	(0.06)	(0.05)
0.93	26.25	7.18 (0.05)	3.33 (0.02)	0.57 (0.20)	1228 (104)	1205 (100)	3255 (1175)	5.9 (0.05)	4.6 (0.21)	1.22 (0.04)
2	12.25	7.37 (0.12)	3.65 (0.20)	0.95 (0.33)	1213 (973)	1223 (695)	3211 (312)	6.0 (0.06)	5.0 (0.11)	1.19 (0.03)
PBS (10 mM)										
[HS A] (mg/ ml)	[DM PC]/ [HSA]	τ_1 (ns)	τ_2 (ns)	τ_3 (ns)	a_1	a_2	a_3	$\langle\tau\rangle_f$	$\langle\tau\rangle_a$	χ^2
2	-	7.28 (0.34)	3.56 (0.24)	0.99 (0.08)	9900 (1230)	1380 (1403)	5687 (460)	5.6 (0.05)	4.3 (0.03)	1.16 (0.04)
0.13	183.7 5	7.16 (0.14)	3.34 (0.14)	0.60 (0.08)	6474 (434)	7163 (662)	1652 (158)	5.8 (0.02)	5.0 (0.45)	1.19 (0.03)
0.40	61.25	7.40 (0.16)	3.78 (0.17)	0.92 (0.14)	9177 (700)	11662 (380)	3048 (227)	5.9 (0.03)	4.8 (0.06)	1.20 (0.08)
0.67	36.75	7.48 (0.10)	3.88 (0.12)	0.91 (0.11)	9620 (347)	13087 (324)	3327 (123)	5.9 (0.05)	4.8 (0.07)	1.17 (0.05)
0.93	26.25	7.40 (0.07)	3.80 (0.08)	0.80 (0.13)	10243 (586)	13087 (633)	3700 (919)	5.9 (0.06)	4.8 (0.14)	1.21 (0.04)
2	12.25	7.42 (0.29)	3.86 (0.41)	0.83 (0.30)	1063 (1834)	13259 (871)	3781 (508)	5.9 (0.05)	4.8 (0.17)	1.16 (0.02)

5.6 CONCLUSIONS

It is of critical importance to characterise the interaction between liposomes and serum constituents, particularly proteins in the context of their use as DDS as their interaction *in vivo* and therapeutic efficacy [10, 11, 163, 260-262]. Here, the interaction between HSA and 1,2-dimyristoyl-sn-glycero-3-phosphocholine (DMPC) liposomes in different aqueous environments (water, 50 mM ABC, and 10 mM PBS), was investigated.

Conventional DLS measurements of the interactions reported size changes occurring, and clearly showed dramatically different interaction mechanisms were at play for the three different aqueous environments. In water, there was minimal stabilisation of the protein in the aqueous environment and, the interaction was observed to cause extensive liposome disruption [268], ABC and PBS on the other hand, the increased stabilisation of HSA in solution meant the interaction did not lead to significant alteration of the liposome structure [272, 273]. Although DLS provided useful information regarding the different interactions occurring, it did not provide any direct information about the protein. Furthermore, the size measurements become unreliable as the sample solution becomes more polydisperse, making quantitative analysis impossible, so orthogonal methods are required to provide more information about the interactions [134, 165].

Absorbance measurements could provide further information, but spectra were significantly affected by scatter arising from the liposome samples (~200 nm) which are of similar size to the wavelengths of light used in measurements (250-400 nm). This is common problem encountered when analysing systems containing liposomes using absorbance [302, 303], and is particularly significant in the analysis of intrinsic protein absorbance as scatter is often very significant in this region (i.e. <300 nm). Other methods have been suggested in literature to correct scatter interference in absorbance measurements using mathematical corrections of spectra based on equations to approximate scatter contribution (i.e., using Rayleigh-Gans-Debye equation) [303]. Here, an alternative approach for dealing with scatter contamination in absorbance spectra of liposomal systems is present using MCR. Using this approach enabled the simple resolution of protein absorption spectra from the scatter contaminated absorbance spectra, with the recovered protein absorbance signal

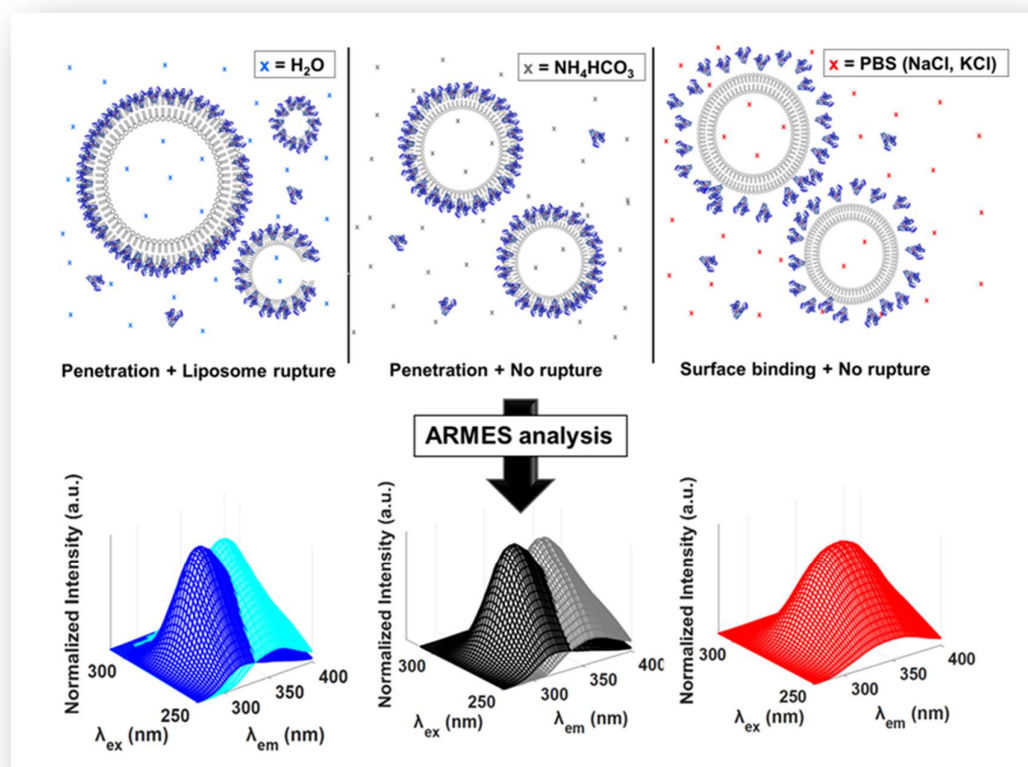
showing agreement with Beer-Lambert law. The MCR solution achieved supported findings from DLS suggesting significantly different interaction mechanisms were occurring, here the highest scores for the scatter component observed in water, with much less significant contributions in both ABC and PBS. Absorbance measurements supported DLS results and provided some information about the different interactions at play, but it gave no explicit information about the protein except for concentration.

Finally, the interaction between HSA and DMPC was analysed using conventional fluorescence steady-state measurement of intrinsic HSA and lipophilic dye emission, along with lifetime measurements of intrinsic HSA fluorescence decay. From analysis of the intrinsic HSA emission in the presence of DMPC liposome information was provided about the protein location in each aqueous environment with clear differences observed between penetrating and non-penetrating liposome coatings. In the cases of water and ABC, a significant blue-shift and decrease in average lifetime, was observed indicating protein penetration of the bilayer [10, 292, 293]. In contrast, in PBS no significant blue-shift but a small increase in lifetime was observed, indicating that the protein remains more in the aqueous environment [288, 300].

Overall, analysis of the interaction by DLS measurements, UV-Vis absorbance, and conventional fluorescence steady-state and lifetime measurements of the system provided a great deal of information regarding the different interactions at play. However, all measurements had limitations for example the measurements of fluorescence emission were significantly affected by noise associated with the highly scattering liposome samples, resulting in anisotropy measurements providing little useful information. Thus, an investigation of information provided using pMDF spectra combined with chemometric analysis (ARMES methodology) to resolve the fluorescence emission signals is explored in **Chapter 6**, to see if additional information about the interaction could be obtained.

6 CHEMOMETRIC MODELLING OF THE INTERACTION BETWEEN HSA AND DMPC LIPOSOMES

Graphical abstract:



In this chapter, the application of chemometric modelling to the pMDF spectra will be presented (ARMES methodology). The details of PCA and PARAFAC models were introduced in Chapter 1, and the specific data pre-processing steps can be found in Chapter 2.

6.1 INTRODUCTION

Although conventional spectroscopic analysis did provide useful information about the HSA-DMPC interaction by allowing investigation using the overall fluorescence emission via shifts in emission and changes in the emission intensity, there is potentially more information which can be obtained about the interaction from pMDF measurements of intrinsic HSA emission when analysed using chemometrics. For instance, anisotropy values recovered using conventional 2-D measurements of polarized HSA emission, did not provide useful because of the large amount of light scatter arising from the liposome samples (**Figure 5.9, Chapter 5**). However, the use of chemometrics to resolve 3-D pMDF measurements of the intrinsic HSA emission, may remove the light scatter artefacts and give the pure fluorescence emission of HSA. Here, the application of ARMES methodology to the intrinsic HSA emission is investigated to see what further information can be obtained from the emission.

As previously stated, we know that the intrinsic fluorescence emission of HSA arises from several fluorescent contributions (see **section 4.3, Chapter 4**) [4, 45]. Along with these fluorescent contributions arising from intrinsic HSA fluorescence emission alone, in the presence of DMPC liposomes there are additional contributions from HSA fluorophores which are interacting and penetrating the lipid bilayer, along with fluorophores which associate with the liposome surface but not penetrating, as well as fluorophores which are not linked to interaction with the bilayer and remain in the aqueous phase. Here we aim to resolve the HSA emission using PARAFAC modelling into two components: HSA emission linked with interaction and penetration of the lipid bilayer and HSA emission linked with non-penetration of the lipid bilayer (i.e., HSA free in aqueous solution or in surface bound states). The resolved species can then be further analysed to assess what additional information is provided by the ARMES methodology.

6.2 PCA ANALYSIS

PCA analysis was first used to explore the minimally corrected TSFS data without scatter subtraction to check for outliers, the degree of physical sample variance, and the effect of residual scatter on data separation. It was found that three PC's were required in all cases (**Figure 6.1 & Table 6.1**) to explain ~99.9 % of the variance of TSFS data in all polarization modes, with PC1 and PC2 typically accounting for >99.8 % of the explained variance. PCA models were created using the global dataset (n=108), as well as buffer specific datasets containing sample in water, ABC, or PBS only (n=36 in all cases) (**Figure 6.2, Figure 8.6 & Figure 8.7 (Appendix)**).

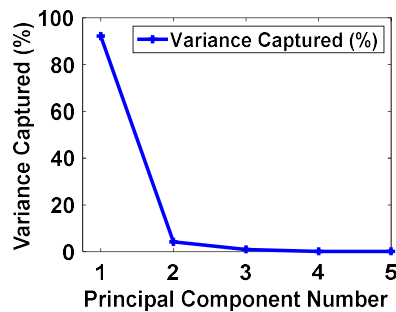


Figure 6.1: Variance captured vs. number of principle components showing 3 PC's are required to explain majority of the variance (shown for PCA analysis of t-EEM_{||} dataset of the interaction).

Table 6.1: Comparison of model parameters and components obtained for PCA modelling of intrinsic HSA emission according to the polarization of the measurement and dataset modelled (**Top-Bottom:** Global (n=108), Water (n=36), ABC (n=36), and PBS (n=36)).

Polarization setting	t-EEM	t-EEM _⊥	t-EEM _T	t-EEM	t-EEM _⊥	t-EEM _T
	Global			Water		
Variance explained (%)	99.8	99.8	99.9	99.9	99.9	99.9
PC1 Fit model (%)	99.2	99.1	99.2	99.3	99.3	99.4
PC2 Fit model (%)	0.5	0.7	0.6	0.5	0.6	0.5
PC3 Fit model (%)	0.1	0.1	0.1	0.0	0.0	0.0
	ABC			PBS		
Variance explained (%)	99.9	99.9	99.9	99.9	99.9	99.9
PC1 Fit model (%)	99.2	99.0	99.1	99.7	99.7	99.8
PC2 Fit model (%)	0.7	0.8	0.7	0.1	0.1	0.1
PC3 Fit model (%)	0.1	0.1	0.1	0.0	0.0	0.0

The PCA model of the global dataset (n=108), was chosen for discussion as it gave the best overview of all samples being analysed. Here, three PC's were required with PC1 and PC2 accounting for ~99.8 % of the explained variance in each polarization mode, with PC3 accounting for <0.1 % in all cases (**Table 6.1**). PC1 accounted for ~99.2 % of variance and appears to be arising from HSA emission showing the increasing HSA emission intensity as the concentration increases (**Figure 6.2/B**). PC2 accounted for ~0.6% of variance and appeared to represent emission spectral shifts (**Figure 6.2/C**).

The similar PC1/PC2 trajectories, and high degree of sample spread (**Figure 6.2/A**) for the water and ABC buffer samples suggested a similar type of interaction process in these environments, in PBS on the other hand, there is much less interaction occurring and the relationship between PC1 and PC2 is significantly different. In PBS,

there was much less PC2 variance and scatter in the plot which was clear evidence for a different interaction mechanism at play in this case.

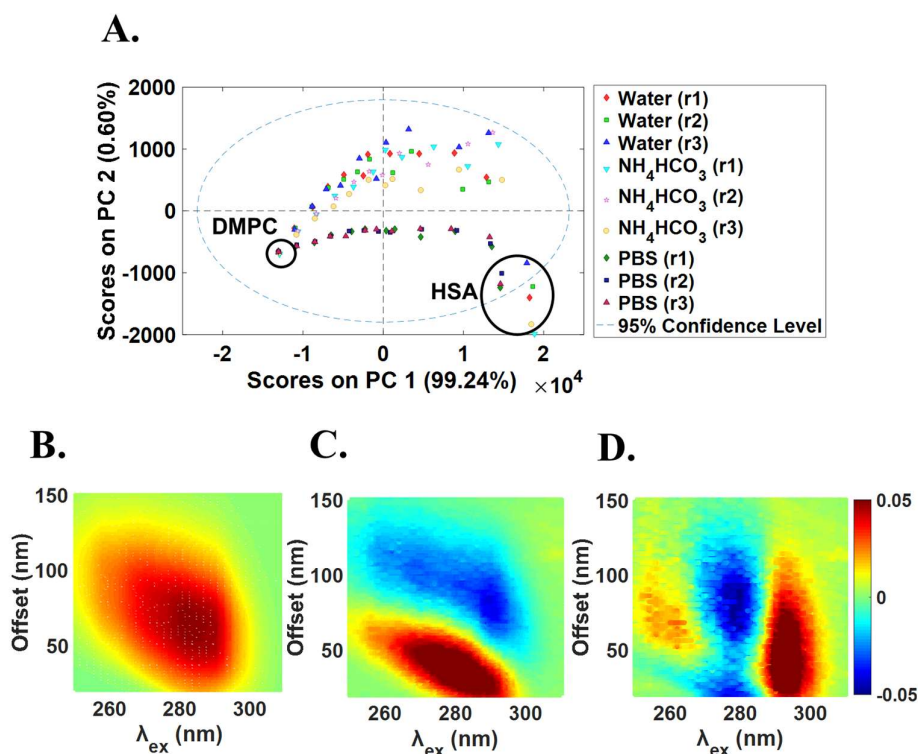


Figure 6.2: (A) PC1 vs PC2 Scores plots from three component PCA model on global dataset ($n=108$) in the total polarization mode with the samples containing DMPC liposomes only and HSA only labelled. The different markers correspond to replicate 1-3 each aqueous medium i.e., colour sets in each correspond to samples made from a single extrusion. (B-D) Show the loadings of PC 1-3 (R-L).

From PCA analysis of the sub-models (water, ABC buffer, and PBS, $n=36$ each) (Table 6.1), similar PCA loadings and relationship between PC1 and PC2 were obtained in the case of water and ABC datasets consistent with results indicating that they behaved in a similar manner (Figure 8.6/D-F & Figure 8.7/AB (Appendix)). For PBS (Figure 8.6/G-I & Figure 8.7/C (Appendix)), the PC2 component was essentially insignificant ($\sim 0.1\%$), as there was no significant spectral shift was present, indicating a different, more homogeneous, mechanism of interaction. PC3 accounted for $<0.1\%$ of emission in all cases and appears to be related to Trp emission from three different excitation wavelengths. There was probably more useful information in this

component, but the large contribution from free HSA to the measured signal prevented accurate interpretation.

It was noticeable that no significant scattered excitation light contribution (**Figure 6.3**) was observed in the TSFS_⊥ or TSFS_∥ spectra, which validated the measurement parameters selected (i.e. TSFS measurement mode with wavelength offset >20 nm and 5/5 nm excitation/emission slit widths) were appropriate for these types of samples and particle size range. However, the effect of the increased Mie scatter¹⁵ in the forward direction from the ~200 nm sized liposome manifests itself by the reduction of the Raman band in the spectrum of the liposome only samples (**Figure 6.3/B/E**) [305].

¹⁵ The scattering of electromagnetic radiation by spherical particles of any size r , relative to the wavelength, λ . Since the cases $r \ll \lambda$ and $r \gg \lambda$ are covered by Rayleigh scattering and geometric scattering theories, respectively, Mie scattering often refers to the case of $r \approx \lambda$ [304] S. Chalk, L. McEwen, The IUPAC Gold Book, Chemistry International, 39 (2017).

6.3 PARAFAC MODELLING

Next, the application of PARAFAC modelling to the intrinsic protein emission was investigated to assess what additional information could be obtained. Changes in the 3D pMDF measurements of intrinsic HSA emission ($\lambda_{\text{ex/em}} = 250\text{-}310/270\text{-}400\text{ nm}$) were evaluated in each polarization mode at varying [HSA]/[DMPC] molar ratios. Prior to PARAFAC analysis of the t-EEM data, the raw spectra of the pure components (HSA only, liposome only, and blank sample) were assessed showing the scatter affected areas (Raman scattering and random measurement noise), along with the areas of HSA emission which required interpolation prior to analysis (where $\Delta < 20\text{ nm}$) (**Figure 6.3**). This was done in order to check that the chemometric solutions obtained were not affected by artefacts present in the raw spectra. In addition, SimI was conducted on each buffer specific dataset to assess the degree of similarity between the replicate measurements and confirm samples preparation was precise and pre-processing of spectra data did not induce variation in the data. A high degree of similarity was observed between replicates ($n=3$) in all cases (>0.85) (**Figure 6.4**).

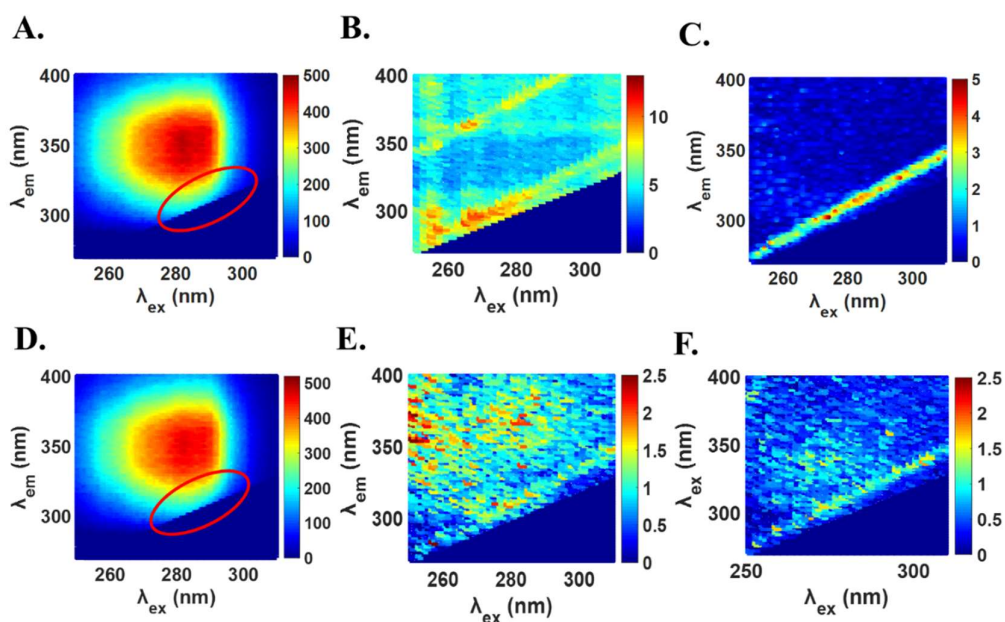


Figure 6.3: Parallel polarized t-EEM_{||} raw spectra of: (A) HSA with the area of interpolation highlighted in red, (B) DMPC liposomes showing random measurement noise and Raman scattering, and (C) Water showing the Raman scattering band. t-EEM_⊥ spectra of: (D) HSA, (E) DMPC, and (F) Water.

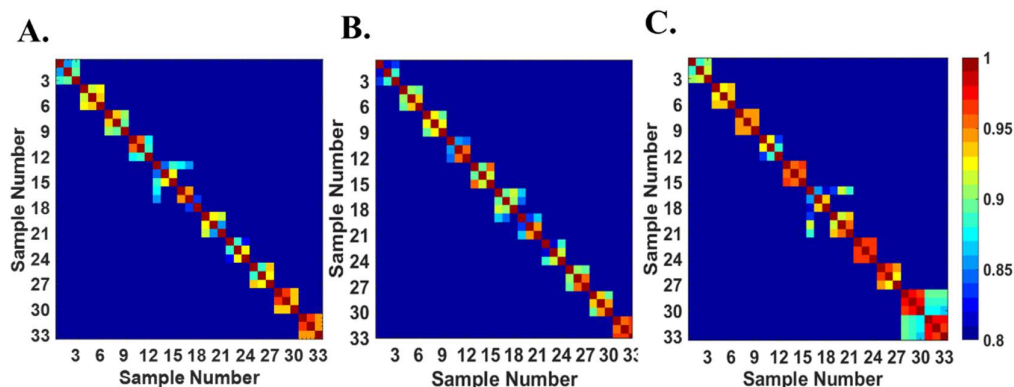


Figure 6.4: Similarity index evaluation of the HSA-DMPC datasets ($33 \times 66 \times 31$), in (A) water, (B) ABC, and (C) PBS (shown for $t\text{-EEM}_{\perp}$) showing good similarity between replicate measurements in all cases.

PARAFAC models were created using both a global dataset containing all samples from all buffers ($n=99$) (**Figure 6.7 & Table 6.4**) and three other models created on buffer specific sub-datasets containing only samples in each of the different aqueous environments: water, ABC and PBS ($n=33$ for each model) (**Figure 6.5 & Table 6.2**). In all cases, the models created using $t\text{-EEM}_{\perp}$ datasets were preferred as this polarization was minimally impacted by residual scattered light, and thus this polarization mode should represent the pure fluorescence emission only (**Figure 6.3**).

6.3.1 PARAFAC models on buffer specific datasets

From conventional spectral analysis and PCA analysis of the interactions between HSA and DMPC, we know that significantly different interaction mechanisms are at play in each of the different aqueous environments. Therefore, the buffer specific sub-models ($n=33$ in each case) were deemed the most appropriate as they allowed for more specific fitting of the underlying components of fluorescence in each of the different aqueous environments (**Figure 6.5 & Table 6.2**).

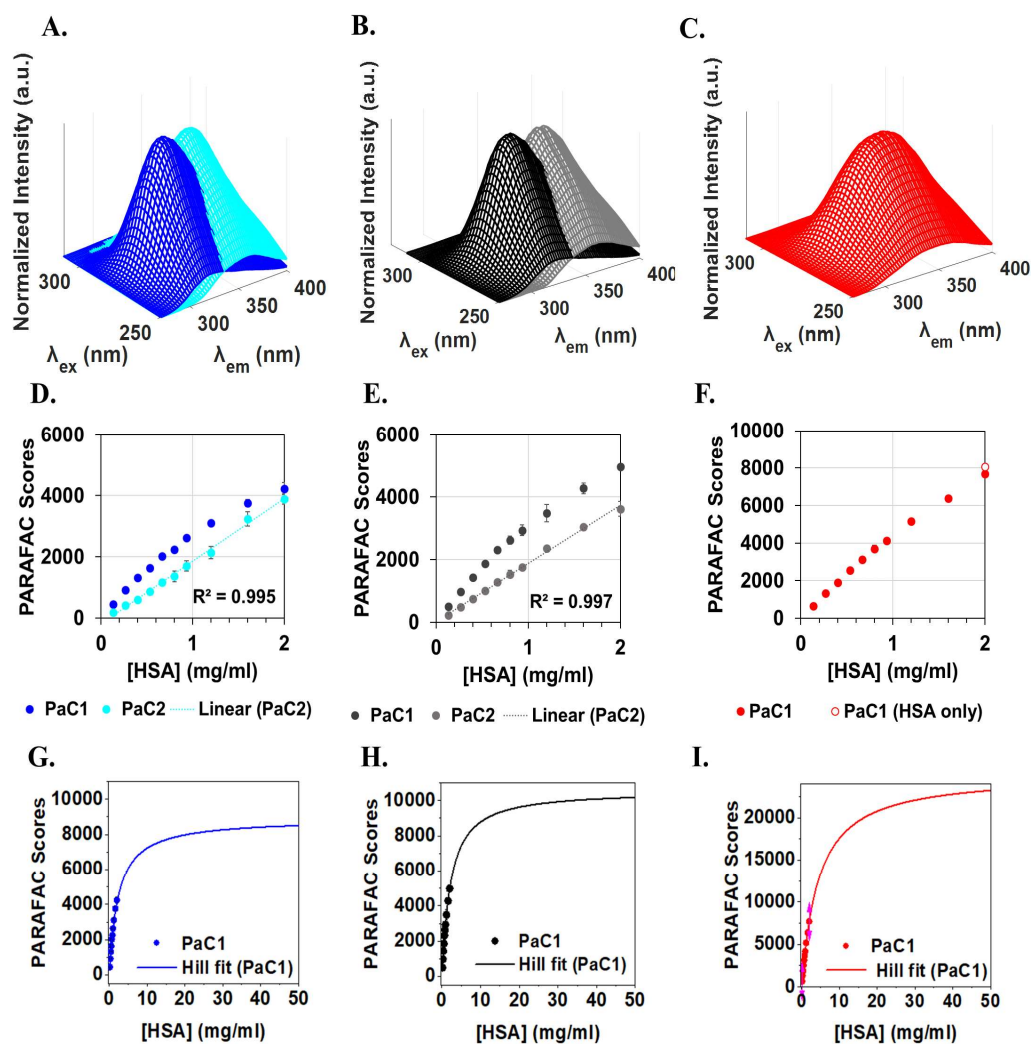


Figure 6.5: PARAFAC components resolved from sub-models ($n=33$) on the $t\text{-EEM}_{\perp}$ datasets of water, ABC and PBS (L-R). (A-B) Two-components were required in the cases of water (A) and ABC (B), whereas one-component was sufficient to describe variation in PBS (C) (resolved spectra shown for sample where [HSA]=0.8 mg/ml). (D-F) The PARAFAC scores resolved for PaC1 (and PaC2) are shown for the interaction samples in (D) water, (E) ABC, and (F) PBS. (G-I) Show the result of Hill fitting [94] the PaC1 scores in: (G) water, (H) ABC buffer, and (I) PBS.

Table 6.2: Comparison of model parameters and components obtained for PARAFAC modelling of intrinsic HSA emission according to the polarization of the measurement for the buffer specific models on datasets per interaction medium (n=33 in each case).

Polarization setting	t-EEM	t-EE M _⊥	t-EEM T	t-EEM 	t-EEM ⊥	t-EEM T	t-EEM 	t-EEM ⊥	t-EEM T
	Water			ABC			PBS		
PaC1 $\lambda_{ex}/\lambda_{em}$ (nm)	280/ 320*	280/ 324	278/ 320	280/ 318*	280/ 326	280/ 322	282/ 344	280/ 352	280/ 352
PaC1 Fit model (%)	41.5*	53.1	51.9	42.6*	60.0	65.2	100.0	100.0	100.0
PaC2 $\lambda_{ex}/\lambda_{em}$ (nm)	286/ 354*	286/ 358	284/ 358	286/ 358*	284/ 356	282/ 356	-	-	-
PaC2 Fit model (%)	58.6*	46.9	48.1	57.4*	40.0	43.1	-	-	-
Variance explained (%)	99.9	99.9	100.0	99.9	100.0	99.9	99.6	99.8	99.8
CONCORDIA (%)	99.2	99.9	100.0	96.1	100.0	99.9	100.0	100.0	100.0
Split-half analysis (%)	99.2	99.7	99.2	94.1	91.22	93.4	100.0	100.0	100.0

* For these models, the order of the components was inverted in the model output.

In the well-behaved PBS case, only one PARAFAC component is required to model HSA emission (PaC1, $\lambda_{ex}/\lambda_{em}$ (nm) = 278/352, explaining >99% of the total variance), and this tracks the change in HSA concentration (**Figure 6.5/F & Table 6.2**). This can be explained by the fact that, firstly, there is no significant penetration of the lipid bilayer to generate a large spectral change, and secondly, there is a significant amount of free, unbound HSA present here. PARAFAC modelling of this type of data could not resolve the very small spectral changes induced by adsorption of HSA on the liposome surface. A two-component PARAFAC model using PBS data was attempted, however, the components resolved differed from those resolved from ABC and water datasets indicating they may not be chemically meaningful and further confirming a one-component model was sufficient here (**Figure 6.6/C/F & Table 6.3**).

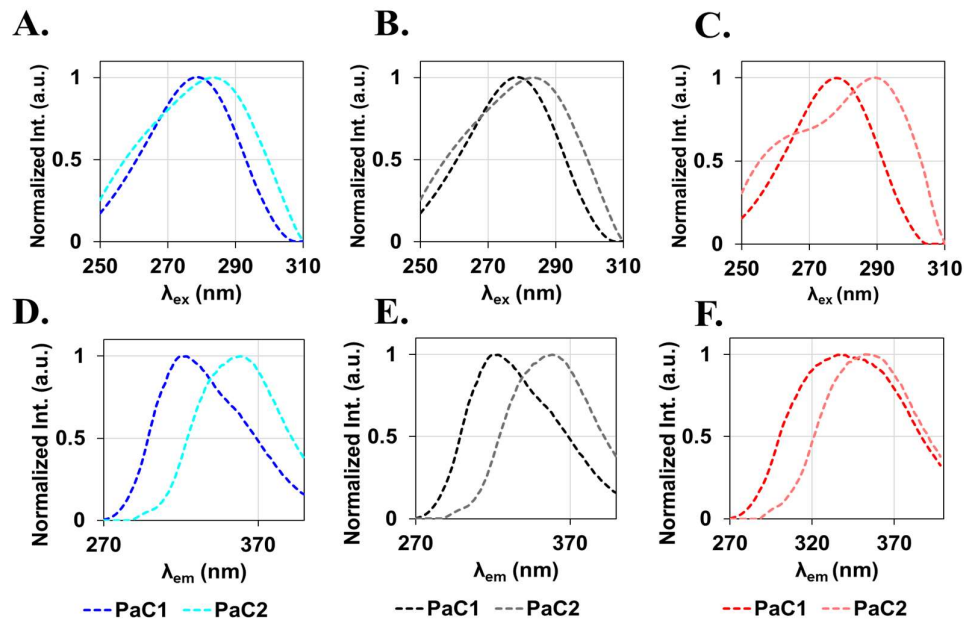


Figure 6.6: PARAFAC excitation (A-C) and emission (D-F) loadings of the 2-component model on each sub-model of water (blue/A/D), ABC (black/B/E) and PBS (red/C/F). The loadings in water and ABC are observed to be similar, while PBS loadings differ.

Table 6.3: Comparison of model parameters and components obtained for two-component PARAFAC modelling of intrinsic HSA emission for the sub-model on the PBS dataset (n=33).

Polarization setting	t-EEM	t-EEM _⊥	t-EEM _Γ
PaC1: $\lambda_{ex/em}$ (nm)	280/ 338	278/ 340	278/ 336
PaC1: Fit model (%)	65.2	77.1	72.7
PaC2: $\lambda_{ex/em}$ (nm)	292/ 352	290/354	290/ 352
PaC2: Fit model (%)	34.9	22.9	27.3
Variance explained (%)	100.0	100.0	100.0
CONCORDIA (%)	98.8	99.6	100.0
Split-half analysis (%)	96.0	92.7	97.4

In the case of water and ABC, PARAFAC analysis of the intrinsic HSA fluorescence recovered two components (explaining >99% of the total variance) for each polarization mode (**Figure 6.5 & Table 6.2**). The quality parameters indicated the model was valid and the components behaved in a trilinear fashion. PARAFAC component 1 (PaC1, ~42-65 %) appears to correspond to a combination of blue-shifted Trp-214 and tyrosine emission associated with HSA penetration into the lipid bilayer [299]. Whereas PARAFAC component 2 (PaC2, $\lambda_{ex}/\lambda_{em}$ (nm) ~284/356) was related to non-interacting, or surface bound HSA, showing a more linear relationship with an increasing concentration of HSA (**Figure 6.5/D-E**). The high PaC1 scores in water and ABC buffer prove that there is a significant population of interacting HSA (>40 %), which suggests an possibly an end-on [283] interaction based on the requirements for monolayer coverage and the protein-liposome ratios used (**Table 5.2 & Figure 5.5, Chapter 5**).

The t-EEM_⊥ polarization appears to be more sensitive towards the interacting HSA population (PaC1) with ~11.6-18.0 % more variance explained by this component (53 % and 60 % variance explained for water and ABC buffer respectively) compared to 41.5 and 42% for the t-EEM_∥ model. Two factors can explain this observation, firstly, there is better elimination of residual Mie scatter and IFE in the perpendicular polarization measurement, and secondly, there is an increased HSA emission depolarisation upon penetration of the liposome bilayer [10, 67].

From analysis of the PARAFAC scores, we expect the PaC1 scores to reach a maximum value (at a specific HSA concentration) and then decrease if only monolayers were formed. Here, the PaC1 scores show a curved behaviour with increasing HSA concentration but does not plateau within the concentration range used in the experiment (up to 2 mg/ml HSA). Here, the PaC1 behaviour was modelled using a Hill fit [306] of the scores and showed a plateau at much higher protein concentrations, predicted to be >30 mg/ml, (**Figure 6.5/G-I**). PaC2 scores on the other hand, increased linearly with protein concentration ($r^2 > 0.99$) as expected for a non-interacting population.

It is worth noting that at higher HSA concentrations primary IFE becomes more of an issue and thus the predicted concentrations are much less reliable [173]. For the HSA concentration range used here, the correlation between scores and true

concentration is also affected by quantum yield, quenching, IFE, and other photophysical processes. We have already seen both spectral shifts and lifetime changes, and therefore we cannot then use the scores to determine the precise concentrations of bound/unbound HSA in this current study, and to do so would require further study and purification of the protein-liposome complexes and implementation of IFE correction. Unfortunately for intrinsic emission this is not feasible as liposome scattering was too significant below 300 nm, however this is an area which can be further explored in future studies.

6.3.2 PARAFAC models on global datasets

A PARAFAC model was also created on the global dataset and revealed two components were required to explain the variation in HSA emission (explaining >99% of the total variance) for each polarization mode. As before, PARAFAC component 1 (PaC1, $\lambda_{\text{ex}}/\lambda_{\text{em}}$ (nm)= ~280/320) appears to correspond to a combination of Tyrosine residues of the HSA and blue-shifted emission of Trp-214 emission which is linked to penetration of HSA into the lipid bilayer and PARAFAC Component 2 (PaC2, $\lambda_{\text{ex/em}}$ (nm)=~284/356) was related to non-interacting Trp-214 and Tyr emission of HSA, which show a more linear relationship with an increased concentration of HSA (**Table 6.4**).

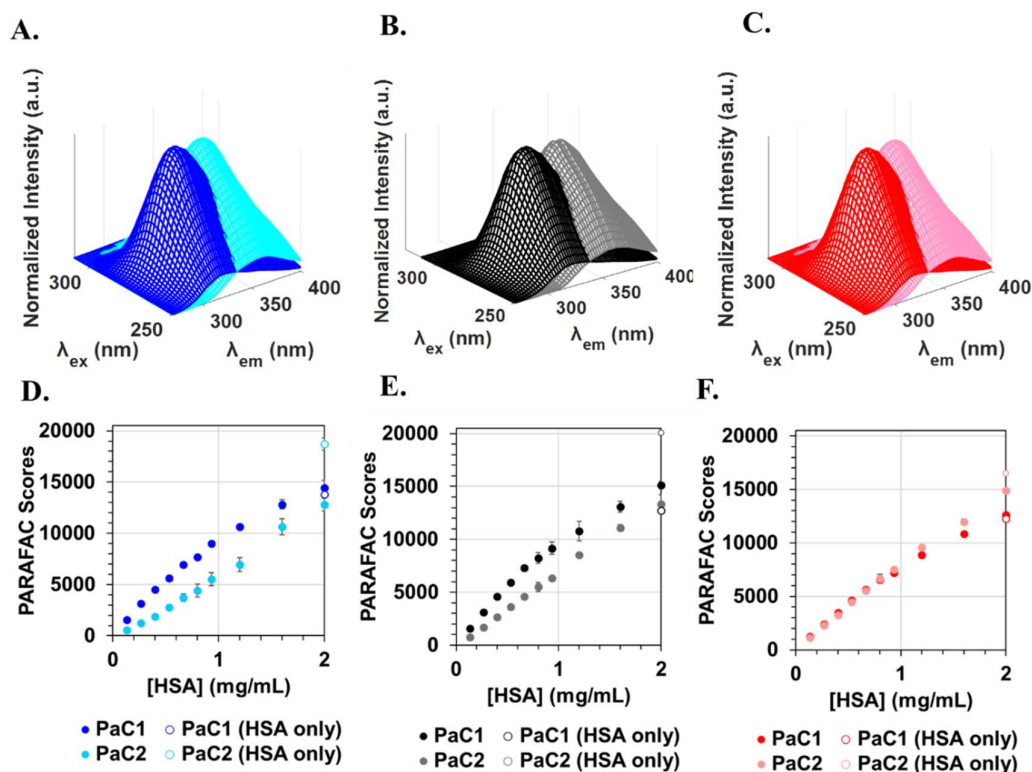


Figure 6.7: PARAFAC components resolved from global ($n=99$) on the t-EEM_T datasets (A-C) in water (A), ABC (B) and PBS (C). PaC1 corresponds to mainly Trp-214 of HSA and PaC2 corresponds to Tyrosine residues of HSA and Trp-214 which is penetrating the lipid bilayer (resolved spectra for all shown as an example for one interaction sample in water dataset, where [HSA]= 0.8 mg/ml). (D-F) The PARAFAC scores resolved for PaC1 and PaC2 are shown for the interaction samples corresponding in water (D), ABC (E) and PBS (F).

Table 6.4: Comparison of model parameters obtained for two-component PARAFAC modelling of intrinsic HSA emission according to the polarization of the measurement for the model on the global datasets (n=99).

Polarization setting	t-EEM	t-EEM_⊥	t-EEM_T
	Global		
PaC1: $\lambda_{\text{ex/em}}$ (nm)	280/ 318	280/ 324	278/ 322
PaC1: Fit model (%)	41.5	58.5	54.1
PaC2: $\lambda_{\text{ex/em}}$ (nm)	284/ 356	284/ 362	284/ 360
PaC2: Fit model (%)	58.5	41.5	45.9
Variance explained (%)	99.9	99.3	99.2
CONCORDIA (%)	97.5	100.0	99.9
Split-half analysis (%)	98.2	96.1	96.0

Although, the quality parameters indicated the model was valid (CONCORDIA >97.5 %) and the components behaved in a trilinear fashion the components resolved from the global dataset showing highly overlapping scores in the PBS data (**Figure 6.7/F**), indicating one-component is sufficient in describing the variation in emission here. In addition to the fact that a two-component model on the PBS sub-model, did not resolve chemically meaningful components (**Figure 6.6**).

6.3.3 Anisotropy analysis of PARAFAC components

Anisotropy values recovered using conventional spectroscopy, did not provide useful information because of the large amount of light scatter (**Figure 5.9, Chapter 5**), so here, the anisotropies of the resolved PARAFAC components were evaluated to see if they could provide any additional information. Anisotropy values calculated

from the PARAFAC resolved HSA components in water and ABC buffer, showed significant differences in behaviour upon interaction with liposomes. PaC1 calculated anisotropies (at the max emission of the component) were significantly lower (0.08-0.04 in water, 0.09-0.05 in ABC buffer) than the PaC2 values (~0.11-0.13 and ~0.15-0.16) which were higher than that of the free HSA. This contradicts what one might expect, (i.e., an increased anisotropy upon binding of smaller HSA (d~7 nm) to larger liposome (d~200 nm)), however, this is a very complex photophysical system and these observations can be explained as arising from a combination of factors [67].

Firstly, the large photophysical changes (i.e., spectral blue-shift and lifetime reduction) experienced by HSA on incorporation into the lipid membrane, mean comparing PaC1 anisotropy values with free HSA is not appropriate, as they are structurally and photophysically different molecules upon penetration. Secondly, radiative energy transfer from PaC1 to PaC2 (particularly since there is an excess of free HSA) can significantly reduce the anisotropy [67]. Finally, the secondary scattering IFE (i.e., of the emission) is very different for the parallel and perpendicularly polarized TSFS measurements for this particle size range, making it nearly impossible to extract true anisotropy values in a right-angle geometry measurement as undertaken here [307]. Although analysis of the anisotropy of PARAFAC resolved emission is complicated by several factors, which prevent accurate quantitative analysis, the anisotropy values recovered do confirm, at least, that two very different populations of HSA species in different environments are resolved.

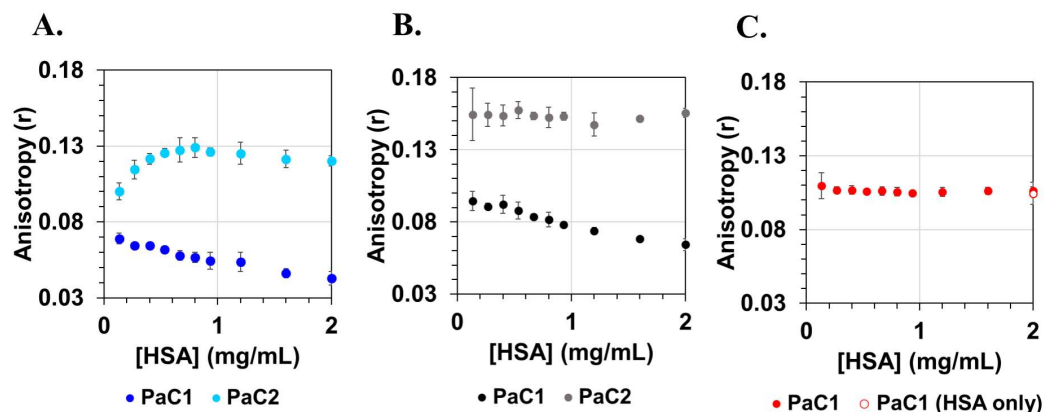


Figure 6.8: Anisotropy of PARAFAC resolved components (PaC1 & PaC2), showing samples corresponding to HSA in PBS in the absence (unfilled circle) and presence of DMPC liposomes (filled circles) in: (A) water, (B) ABC buffer, and (C) PBS buffer. The anisotropy values given were calculated at $\lambda_{\text{ex/em}}$ maxima for PaC1 and PaC2 as determined by the t-EEM_T models (for water; PaC1 $\lambda_{\text{ex/em}}$ =280/318 nm, PaC2 $\lambda_{\text{ex/em}}$ =286/358 nm, for ABC buffer; PaC1 $\lambda_{\text{ex/em}}$ =280/322 nm, PaC2 $\lambda_{\text{ex/em}}$ =282/356 nm and for PBS; PaC1 $\lambda_{\text{ex/em}}$ =280/352 nm).

6.3.4 Evaluation of PARAFAC scores

Evaluation of the different interaction mechanism at play in each of the different aqueous environments was possible using the ratio between the resolved PARAFAC components. From the buffer specific models, plotting the component score ratio versus HSA concentration showed the different interaction mechanisms for water and ABC buffer (**Figure 6.9**). The steepest slope of the ratio of PaC1/PaC2 vs. [HSA] was observed for the interaction in water, consistent with previous results indicating the greatest interaction is occurring here. Here, there is a greater amount of PaC1 (interacting component) and a lower amount of PaC2 (non-interacting Trp-214 residues), thus a steeper slope is observed.

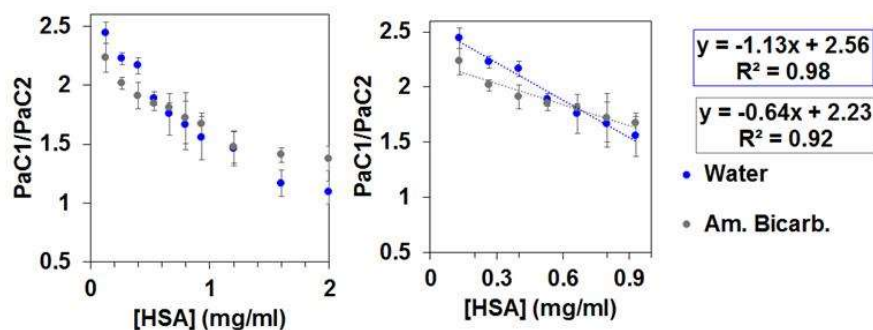


Figure 6.9: Plot of PaC1/PaC2 ratio versus HSA concentration obtained from two-component PARAFAC models of the interaction in water (blue) and ABC (grey).

Evaluation of the ratio between the resolved fluorescent components of the global model, also could reveal the different interaction mechanisms at play in each different aqueous environment and allowed comparison of the systems where HSA was penetrating the bilayer (water, ABC) and where HSA was not penetrating the bilayer possibly remaining in aqueous solution or binding to the surface of the liposome without penetration (PBS case) (**Figure 6.10**). Again, the steepest slope observed was for water, and the interaction in ABC was observed to follow the same trend. In PBS however, a very slight slope and due to the almost co-linear relationship between PaC1 and PaC2 (**Figure 6.7/F**), again indicating minimal interaction is occurring here and the HSA is not significantly penetrating the lipid bilayer.

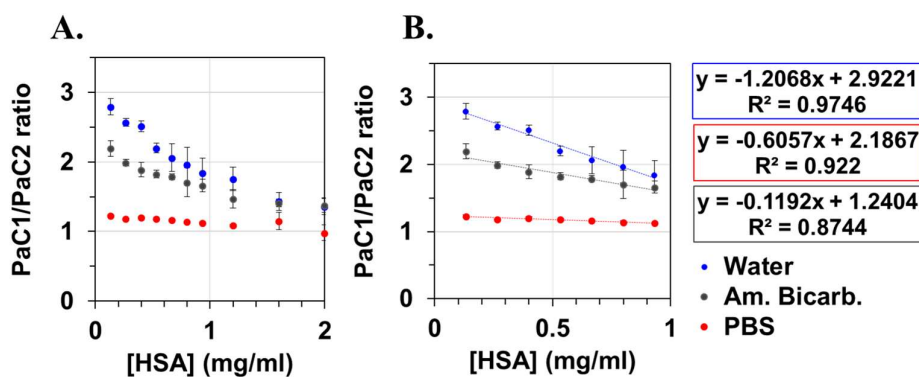


Figure 6.10: Ratio of PaC1/PaC2 components resolved from the interaction data in the three different aqueous environments; water (blue), ABC (grey), and PBS (red) from the global model of t-EEM₁ for: (A) all samples up to [HSA]= 2 mg/ml and (B) for linearly behaving region up to [HSA]= 1 mg/ml.

6.4 CONCLUSIONS

The aim of this work was to investigate if ARMES using PARAFAC analysis of intrinsic HSA emission could yield more information about the interaction of HSA with DMPC liposomes in water, ABC, and PBS. ARMES analysis showed good agreement with results from conventional absorbance, fluorescence steady-state, and lifetime spectroscopies, and Dynamic Light Scattering (DLS) measurements, presented in **Chapter 5**, and provided additional information about the interaction processes occurring, inaccessible using conventional analysis.

PARAFAC analysis of the pMDF was found to resolve two components in from the intrinsic emission of HSA from the interaction with DMPC liposomes in the aqueous environments of water and ABC buffer. The first component, PaC1 ($\lambda_{ex/em} = \sim 280/320$ nm) showed a large hypsochromic emission shift caused by a combination of penetration of the lipid bilayer and some degree of protein structure modification [289-291], whereas the second component, PaC2 ($\lambda_{ex/em} = \sim 282/356$ nm), more resembled free HSA in solution with minimal spectral changes. In contrast, for PBS, only one component was required, and when the DLS data was considered, it seems that a non-penetrating protein layer (potentially a monolayer) has formed in this case and the adsorbed HSA structure was similar to that of free HSA in solution [288]. Significant differences in the amount of fluorophores population were observed between different polarization modes, with the t-EEM $_{\perp}$ polarization appearing more sensitive towards the interacting HSA population (PaC1) with ~ 11.6 - 18.0 % more resolved in t-EEM $_{\perp}$ compared the t-EEM $_{\parallel}$ model. The difference can be explained by the better elimination of light scatter and IFE in the perpendicular polarization measurement, and the increased HSA emission depolarisation upon penetration of the liposome bilayer [10, 67]. The differences observed, highlight the different information provided by each polarization modes and the advantage of using pMDF over unpolarized measurements of fluorescence emission.

Analysis of the PARAFAC scores (relative to concentration) recovered for the interacting and non-interacting fluorophores populations resolved from HSA emission, could be used to discriminate the different interaction mechanisms at play in each aqueous environment, and showed the significantly different interaction processes at play. In theory, the PARAFAC scores could be used for quantitative analysis of the

true concentrations of the penetrating and non-penetrating populations of HSA present throughout the interaction process, however, this is complicated by a number of factors such as quantum yield, quenching, IFE, and other photophysical processes [4]. Therefore, in the current study the scores cannot be used to determine the precise concentrations of bound/unbound HSA, however this could be achieved by further study if steps were taken to purify the protein-liposome complexes and obtain quantum yield information about the different species and if an IFE correction of the data was implemented. Unfortunately, here for the intrinsic emission, this is not feasible as liposome scattering was too significant below 300 nm.

Finally, the anisotropy of the PARAFAC recovered components were significantly different confirming that the species resolved were significantly different. However, interpretation of the absolute values here is complicated by the changing photophysics of the interacting HSA [4, 67]. Here, purification to remove the free HSA contribution would be required to obtain more accurate intrinsic emission anisotropies of the species and furthermore, front surface excitation could be used reduce scattered light contamination from the liposomes [308, 309].

In conclusion, ARMES provides a new, informative spectroscopic approach for investigating protein-liposome interactions that avoids the use of extrinsic fluorophores, or labelled proteins, and facilitates in-situ monitoring of the process, discriminating penetrating and non-penetrating populations of HSA using conventional benchtop spectrometers fitted with polarizers [8]. Alternative approaches such as fluorescence lifetime measurements did provide useful information, however, this requires expensive nanosecond fluorescence lifetime instrumentation which may not be widely available.

7 CONCLUSIONS

The aim of this project was to explore the use of an analytical methodology known as ARMES [1, 2], as a tool for biophysical analysis. In this thesis work, two different projects were undertaken where the application of ARMES was explored, the first project investigated the use of ARMES in the study of FRET, and the second project evaluated the use of ARMES in the analysis of protein-liposome interactions.

The ARMES method was developed in the nanoscale biophotonics laboratory in 2015 as a new tool for the quantitative and qualitative analysis of proteins [2]. The method combines the use of 4-D polarized MDF measurements, with chemometric analysis, and offers a number of significant advantages over some of the alternate methods for protein analysis which can be destructive, time-consuming, or alter the sample [3]. In ARMES, the analysis of proteins by using intrinsic fluorescence provides a fast, sensitive, inexpensive and non-invasive approach, with good robustness, ease of use and low cost, all of which are required for use as a process analytical technology (PAT) tool [4]. Early studies in the group were made using conventional thin film polarizers, which only transmitted light over 290 nm, and prevented the accurate measurement of Tyr and Trp fluorophores [2]. However, in 2017, the method was modified to include UV transparent wire grid polarizers [8] (transmits light < 290 nm), which increased the emission space collected with pMDF and improved the ARMES method. The modified method was validated through the analysis of small molecule fluorophores [1], where accurate anisotropies were successfully recovered. However, issues arose with the modified method, when it was applied to therapeutic proteins: IgG [7] and insulin [107], which had multiple overlapping fluorophores (e.g. Tyr, Trp) [4]. The analysis and chemometric decomposition of fluorescence emission in these cases, became much more complex due to factors such as FRET and IFE causing non-linearity in the fluorescence response.

In the first part of this thesis research, the application of ARMES in the analysis of FRET (**Chapter 3 & 4**) was investigated. The relevance of this work had a two-fold impact, firstly, as mentioned, FRET is known to affect the multi-dimensional emission

of multi-fluorophore systems, and complicates chemometric analysis, therefore, understanding the effect of FRET on ARMES measurement is of significant importance. Secondly, FRET is also widely used technique to study the structure and dynamics of biomolecular systems and so accurate analysis of FRET is important for a wide of biochemical applications. A model system of human serum albumin (HSA) as a FRET donor and 1,8-anilinonaphthalene sulfonate as a FRET acceptor was used and studied using the ARMES approach. The application of ARMES provided information about intensity, emission, excitation, anisotropy in a single measurement and facilitated the collection of the full emission space of the intrinsic protein (i.e., HSA emission) probe emission (i.e., ANS), thereby giving more information about the HSA-ANS interaction system in a single measurement than conventional 2-D methods. The interaction was also assessed by absorbance spectra, combined with MCR-ALS [88], which effectively resolved the overlapping absorbance spectra three components: HSA absorbance, ANS (unbound) absorbance and HSA-ANS complex absorbance and provides a simple approach for dealing with overlapping UV spectra, which is a commonly encountered problem in absorbance spectroscopy [233-238]. Unfortunately, however, MCR-ALS analysis of the absorbance spectra was unable not resolve individual species of the bound ANS molecule, although it was determined at least two different binding sites were occupied. To improve upon this work would require higher resolution absorbance spectra (i.e., more samples, a slower scan speed ($<1,200 \text{ nm min}^{-1}$), and smaller wavelength increments ($<2 \text{ nm}$)).

The analysis of pMDF spectra showed three peaks over the full HSA-ANS emission space, and the spectra were analysed conventionally in terms of intensity changes, spectral shifts, and anisotropy (**Chapter 3**). The aniso-t-EEM map's clearly showed FRET related depolarisation of emission and provided a new way to visually represent the FRET processes occurring in the system [197, 198]. Analysis of the pMDF using the ARMES approach (**Chapter 4**), was achieved using PARAFAC [106], and restricted Tucker3 [85], to model the global HSA-ANS emission and, sub-region of HSA (FRET donor) emission, respectively. The restricted Tucker3 modelling of the global t-EEM improved upon previous work by *Kompany-Zareh et al.* [244-246], by applying the model to a larger sample set ($n=63$), collecting the emission in TSFS mode rather than EEM mode, and validating the chemometric solution achieved using the fourth dimension of anisotropy. Three components were

resolved here corresponding to: HSA (Tyr + Trp), directly excited ANS, and ANS indirectly excited via FRET, and the anisotropy values rationale values [195, 249, 253, 256]. This separation of the underlying components of a FRET interacting mixture is of interest in many scientific applications for accurate quantitative analysis of FRET parameters [239, 257], and in understanding the non-linearity of fluorescence response for spectrally overlapped, interacting multi-fluorophore mixtures such as proteins [6, 7, 107]. The analysis of the sub-region of HSA emission was achieved using PARAFAC analysis, to decompose the emission into interacting (mainly Trp-214) and non-interacting donor fluorophores (mainly Tyr), and facilitated the calculation of biochemical parameters, such as quenching constants and FRET efficiency, using the multi-dimensional signal of the individual fluorophore populations. This resolution of donor emission allowed calculation of FRET efficiency values using the multi-dimensional emission of the interacting donor fluorophores only and significantly higher values (~6-7 %) were using this new proposed PARAFAC approach over the conventional calculation, by removing the influence of non-interacting donor fluorophores.

Overall, the study of the FRET interaction HSA-ANS system using ARMES had several successful outcomes and is a first step towards understanding of FRET in more complex multi-fluorophore mixtures and how it manifests itself in the resulting MDF spectra. The decomposition of the FRET donor fluorescence using PARAFAC analysis provided a new quantitative approach for the calculation of biochemical parameters using the multi-dimensional emission of the interacting and non-interacting fluorophore populations. Secondly, restricted Tucker3 modelling shows a promising approach for the separation of FRET interacting and non-interacting species of ANS fluorescence. Although many useful outcomes were found from the study of the HSA-ANS model system using ARMES, some issues were also identified which, if addressed, could significantly improve upon results. The restricted Tucker3 modelling of the global emission did not provide a solution which could be used for accurate quantitative analysis due to the high error, and to achieve a solution which could be used for quantitative analysis lower noise spectra are required. This could be achieved by using a slower scan speed ($<1200 \text{ nm min}^{-1}$), smaller wavelength increments ($<2 \text{ nm}$) averaging spectra from multiple repeat measurements, and using higher sample numbers, which currently is currently not feasible with the current scanning-based

Agilent Cary-Eclipse system and full pTSFS or pEEM spectral measurements because of the time limitations of the measurement. The use of an alternative system, with multi-channel detector, such as Horiba Aqualog, could provide a potential solution to overcome problems, with significantly faster collection times of MDF spectra.

In the second part of my thesis research the application of ARMES (alongside a variety of orthogonal measurements) in the analysis of protein-liposome interactions was explored (**Chapters 5 & 6**). A model system of HSA and DMPC liposomes was used, and their interactions were monitored in the aqueous environments of water, ABC, and PBS. Analysis of the interaction using conventional DLS measurements, clearly showed the dramatically different interaction mechanisms at play in each aqueous environment, with extensive disruption of the liposomes observed in water [268], whereas in ABC and PBS the increased stabilisation of HSA in solution of the buffer environment resulted in a more stable interaction and disruption of the liposomes was not observed [272, 273] (**Chapter 5**). However, although useful in elucidation of the different interaction mechanisms at play, DLS did not provide any direct information about the protein and furthermore, quantitative analysis became unfeasible as the samples became less monodisperse [134, 165]. To further assess the interactions absorbance measurements were analysed, however the spectra were significantly affected by scatter arising from the liposome samples (~ 200 nm) [302, 303]. From the previous study on the HSA-ANS system, MCR-ALS was proven to be useful in the analysis of overlapping absorbance spectra, and here, successfully resolved HSA absorbance from scatter, providing an alternative approach for dealing with scatter contamination in absorbance spectra of liposomal systems [303].

PARAFAC analysis of the pTSFS data (ARMES approach) (**Chapter 6**) of HSA intrinsic emission yielded a lot more information about the interaction process and showed good agreement with results from conventional analysis. From the application of PARAFAC analysis to the pTSFS data, it was found that two components were required to explain the emission of HSA in the cases of both water and ABC aqueous environments, where the first component, PaC1 ($\lambda_{ex/em} = \sim 280/320$ nm) showed a large hypsochromic emission shift caused by a combination of penetration of the lipid bilayer and possibly modification of HSA structure [289-291]. The second component resolved, PaC2 ($\lambda_{ex/em} = \sim 282/356$ nm), more resembled the free HSA in solution with minimal spectral changes. In contrast, for PBS, only one

component was required to explain the emission of HSA, which indicate a non-penetrating protein layer (potentially a monolayer) was formed in this case and the adsorbed HSA structure was similar to that of the free HSA in solution [288]. Analysis of the PARAFAC scores (relative to concentration) recovered for the interacting and non-interacting fluorophores populations resolved from HSA emission, could be used to discriminate the different interaction mechanisms at play in each aqueous environment, and in theory, could be used for quantitative analysis of the true concentrations of the species throughout the interaction process. However unfortunately, this was complicated by a number of factors such as quantum yield, quenching, IFE, and other photophysical processes. Thus, in the current study the scores cannot be used to determine the precise concentrations of bound/unbound HSA. However, this could be achieved in future work if steps were be taken to purify the protein-liposome complexes to obtain quantum yield information about the different species and if IFE correction of the data was implemented (not feasible here as scattering was too significant <300 nm). Furthermore, the anisotropy of the PARAFAC recovered components had significantly different values, confirming significantly different species were resolved. The anisotropy values recovered had lower levels of error in comparison to anisotropy values recovered from conventional fluorescence which is essential for quantitative analysis. However, interpretation of the absolute values here is complicated by the changing photophysics of the interacting HSA [4, 67]. Here, purification to remove the free HSA contribution would be required to obtain more accurate intrinsic emission anisotropies of the species. Furthermore, the front surface excitation could be used reduce the potential for scattered light contamination from the liposomes [308, 309].

Results from this second project showed ARMES provides a new, informative spectroscopic approach for investigating protein-liposome interactions that avoids the use of extrinsic fluorophores or labelled proteins and enabled the resolution of fluorescence emission into interacting populations of HSA which had penetrated the lipid bilayer and populations of HSA which were surface bound or free in aqueous solution. To better characterise the protein-liposome structures does however require removal of the excess free HSA, the use of front-surface excitation, and IFE correction, which should enable more accurate PARAFAC modelling with recovery of more fluorescent components and calculation of correct component anisotropies. This

would allow for calculation of correct protein concentrations and anisotropies, providing a new quantitative approach for the monitoring of protein-liposome interactions. Nevertheless, for situations like this study, where we are comparing different buffers at the same concentration levels, the ARMES method as implemented provides a convenient approach to characterizing different interactions via a comprehensive analysis of the intrinsic protein emission.

In conclusion, the application of ARMES methodology for biophysical analysis on two different molecular systems is demonstrated in this thesis work. In both studies ARMES enabled resolution of the fluorescence emission into its constituent fluorophore emission and thereby facilitated a more accurate analysis of the interactions and photophysical processes occurring. These studies show ARMES has good potential as a tool of biophysical analysis of interacting molecular systems. The potential use of ARMES for FRET analysis and in analysis of protein-liposome interactions, is still limited by several factors. The results for ARMES measurements could be improved by improving SNR, with more samples and replicates to improve model resolution, and a higher throughput measurement (faster collection of 3D spectra) which are both prohibited by the time required for collection of a full 3D pMDF spectra with the Agilent Cary Eclipse used in this thesis work. Both, improved SNR, and the larger sample sets could be achieved if more samples were collected and averaged, which is not feasible in terms of time with the single detection channel system in Agilent Cary-Eclipse spectrometers. The issues could also be addressed by using a system with a multi-channel detector, such as Horiba Aqualog which has a CCD fluorescence emission detector that is >100 times faster than the current system. In addition, the Aqualog system can also collect UV-vis absorbance and EEM spectra at the same time which allows for automatic correction of IFE, Rayleigh, and Raman scatter. At present, studies are ongoing in the group to assess the use of an Aqualog system to improve the current ARMES methodology.

8 APPENDIX

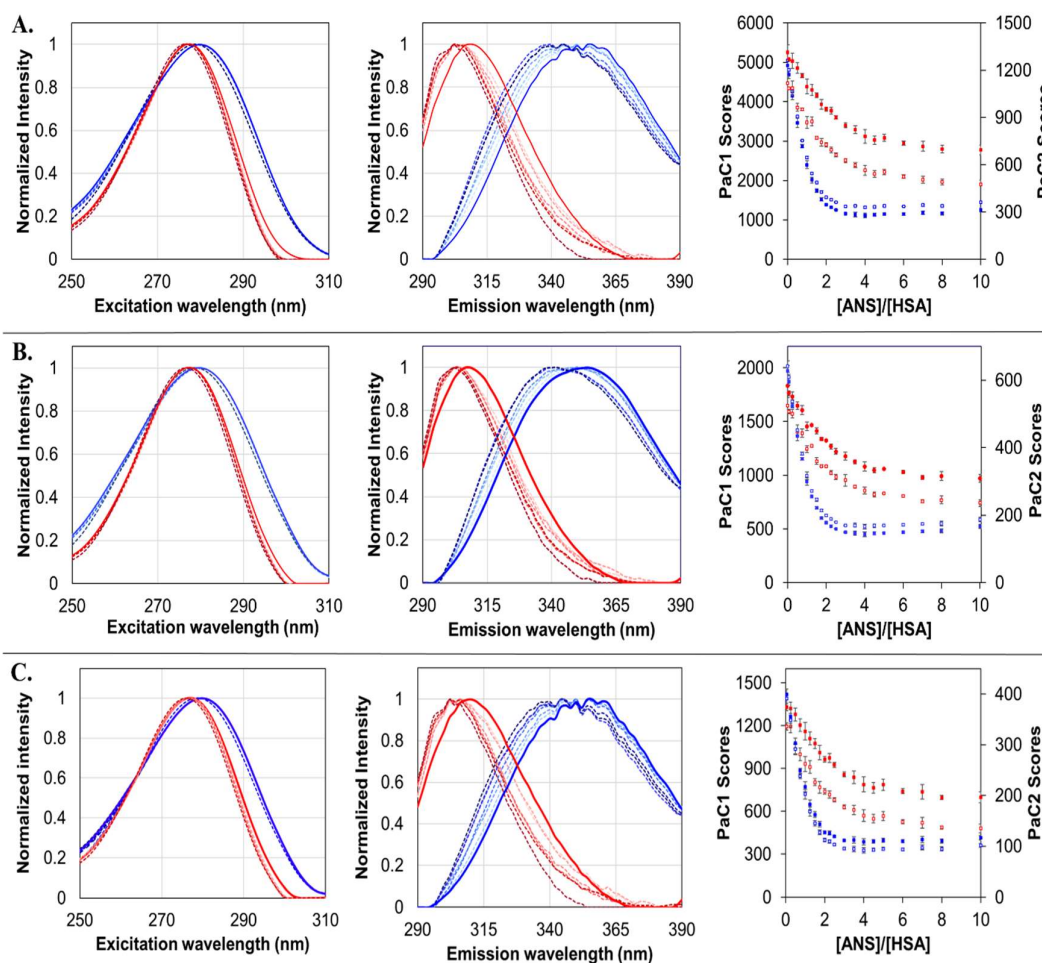


Figure 8.1: Comparison of PARAFAC models showing the (L-R) excitation and emission profiles and scores of Trp (blue in A, B and C) and Tyr (red in A, B and C) according to the (A) Total, (B) Parallel, and (C) Perpendicular polarization. PARAFAC model resolution including all samples ($n=63$) are represented by solid lines and filled squares. PARAFAC sub-models ($n=6-24$) consisting of samples at varying $[ANS]/[HSA]$ molar ratios (Table 8.1) are represented by dashed lines and open squares.

Table 8.1: Comparison of model parameters and components obtained from PARAFAC modelling of donor emission at varying [ANS]/[HSA] molar ratios.

Polarization setting	t-EEM	t-EEM _⊥	t-EEM _T
Model 1:	Dataset: 9 × 131 × 101 ([ANS]/[HSA]=0-0.25)		
PaC1 λ _{ex} /λ _{em} (nm)	280/350	280/350	350/280
PaC1 Fit model (%)	93.1	94.5	94.9
PaC2 λ _{ex} /λ _{em} (nm)	278/304	276/306	278/306
PaC2 Fit model (%)	6.9	5.5	5.1
Variance explained (%)	99.99	99.99	99.99
CONCORDIA (%)	87.74	98.39	96.16
Split-half analysis (%)	81.80	26.88	54.27
Model 2:	Dataset: 6 × 131 × 101 ([ANS]/[HSA]=0.5-0.75)		
PaC1 λ _{ex} /λ _{em} (nm)	280/352	280/350	280/350
PaC1 Fit model (%)	89.7	92.2	92.4
PaC2 λ _{ex} /λ _{em} (nm)	278/304	276/306	278/302
PaC2 Fit model (%)	10.3	7.8	7.6
Variance explained (%)	99.99	99.99	99.99
CONCORDIA (%)	98.44	96.47	98.85
Split-half analysis (%)	99.80	83.70	87.82
Model 3:	Dataset: 6 × 131 × 101 ([ANS]/[HSA]=1-1.25)		
PaC1 λ _{ex} /λ _{em} (nm)	280/350	280/350	280/350
PaC1 Fit model (%)	83.3	88.3	88.2
PaC2 λ _{ex} /λ _{em} (nm)	278/304	276/306	278/306
PaC2 Fit model (%)	15.7	11.7	11.8
Variance explained (%)	99.98	99.99	99.99
CONCORDIA (%)	92.79	69.99	82.24
Split-half analysis (%)	99.90	1.71	98.95
Model 4:	Dataset: 9 × 131 × 101 ([ANS]/[HSA]=1.5-2)		
PaC1 λ _{ex} /λ _{em} (nm)	280/342	280/344	280/344
PaC1 Fit model (%)	80.8	85.0	84.7

PaC2 $\lambda_{ex}/\lambda_{em}$ (nm)	278/302	276/306	278/302
PaC2 Fit model (%)	19.2	15.0	15.3
Variance explained (%)	99.97	99.98	99.98
CONCORDIA (%)	66.41	93.25	93.78
Split-half analysis (%)	99.90	96.5	93.89
Model 5:	Dataset: $9 \times 131 \times 101$ ([ANS]/[HSA]=2.25-3)		
PaC1 $\lambda_{ex}/\lambda_{em}$ (nm)	280/342	280/344	280/344
PaC1 Fit model (%)	79.5	83.1	82.5
PaC2 $\lambda_{ex}/\lambda_{em}$ (nm)	278/302	276/302	278/302
PaC2 Fit model (%)	20.5	16.9	17.5
Variance explained (%)	99.97	99.99	99.99
CONCORDIA (%)	90.62	98.21	82.61
Split-half analysis (%)	99.9	71.57	7.21
Model 6:	Dataset: $24 \times 131 \times 101$ ([ANS]/[HSA]=3.5-10)		
PaC1 $\lambda_{ex}/\lambda_{em}$ (nm)	278/342	278/344	278/344
PaC1 Fit model (%)	81.6	87.2	86.7
PaC2 $\lambda_{ex}/\lambda_{em}$ (nm)	276/302	276/302	276/302
PaC2 Fit model (%)	18.4	12.8	13.4
Variance explained (%)	99.87	99.89	99.88
CONCORDIA (%)	-191.11	-255.68	-216.23
Split-half analysis (%)	99.9	29.90	16.70

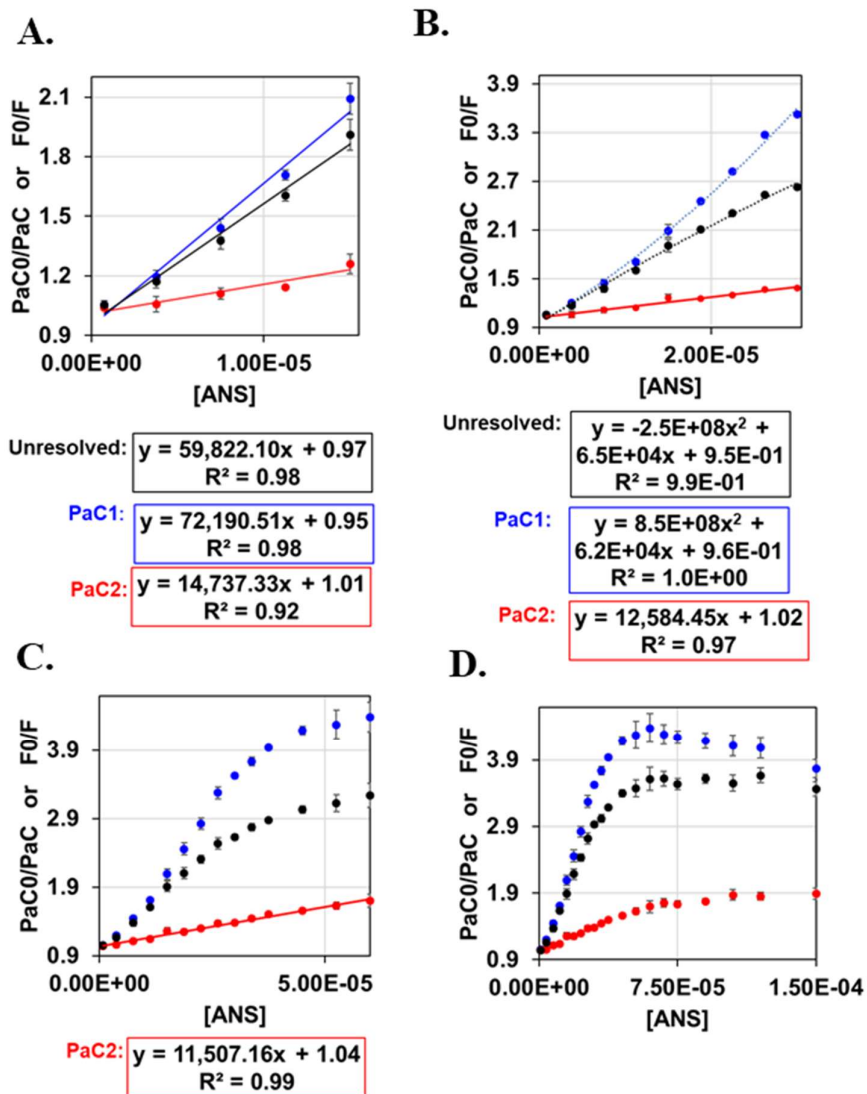


Figure 8.2: Stern-Volmer plots (F_0/F or PaC_0/PaC) using t-EEM $_{\parallel}$ for unresolved spectra (black) (based on a single point $\lambda_{ex}/\lambda_{em} = 280/350$ nm in absence and presence of quencher), and for the individual Trp (PaC1) (red) and Tyr (PaC2) (blue) populations. Stern-Volmer plots (A-D) show the quenching up to $[ANS]/[HSA]=1,2,4,10$, respectively, and the linear region is at low ANS concentrations is associated with FRET quenching.

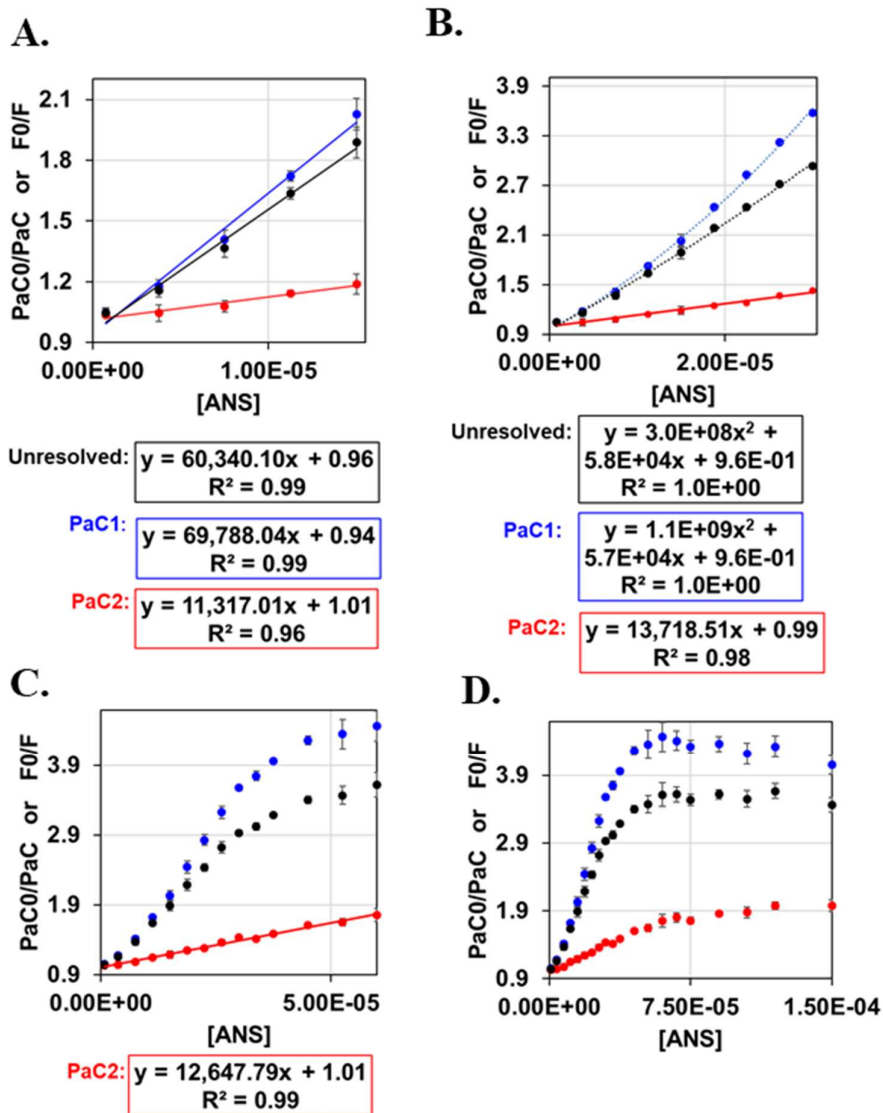


Figure 8.3: Stern-Volmer plots (F_0/F or PaC_0/PaC) using $t-EEM_{\perp}$ for unresolved spectra (black) (based on a single point $\lambda_{ex}/\lambda_{em} = 280/350$ nm in absence and presence of quencher), and for the individual Trp (PaC1) (red) and Tyr (PaC2) (blue) populations. Stern-Volmer plots (A-D) show the quenching up to $[ANS]/[HSA]=1,2,4,10$, respectively, and the linear region is at low ANS concentrations is associated with FRET quenching.

Table 8.2: Estimation of components rotational ambiguities by MCR-BANDS for MCR models presented in table S-1, using non-negativity on C and S^T as well as equality constraint on HSA spectra.

MCR model built using non-negativity (C and S^T) and equality constraint on HSA spectra		
Global	C1 (HSA)	C2 (Scatter)
f_n max	0.32	0.86
f_n min	0.32	0.86
f_n max – f_n min	0.00	0.00
Water		
f_n max	0.19	0.92
f_n min	0.19	0.92
f_n max – f_n min	0.00	0.00
ABC		
f_n max	0.42	0.72
f_n min	0.43	0.72
f_n max – f_n min	0.00	0.00
PBS		
f_n max	0.42	0.74
f_n min	0.42	0.74
f_n max – f_n min	0.01	0.00

Table 8.3: Estimation of components rotational ambiguities by MCR-BANDS for MCR models presented in table S-1, using non-negativity on C and S^T alone.

MCR model built using non-negativity (C and S^T) alone		
Global	C1 (HSA)	C2 (Scatter)
f_n max	0.71	0.59
f_n min	0.63	0.58
f_n max – f_n min	0.08	0.01
Water		
f_n max	0.62	0.81
f_n min	0.45	0.64
f_n max – f_n min	0.17	0.17
ABC		
f_n max	0.79	0.59
f_n min	0.54	0.41
f_n max – f_n min	0.25	0.18
PBS		
f_n max	0.70	0.50
f_n min	0.65	0.44
f_n max – f_n min	0.05	0.06

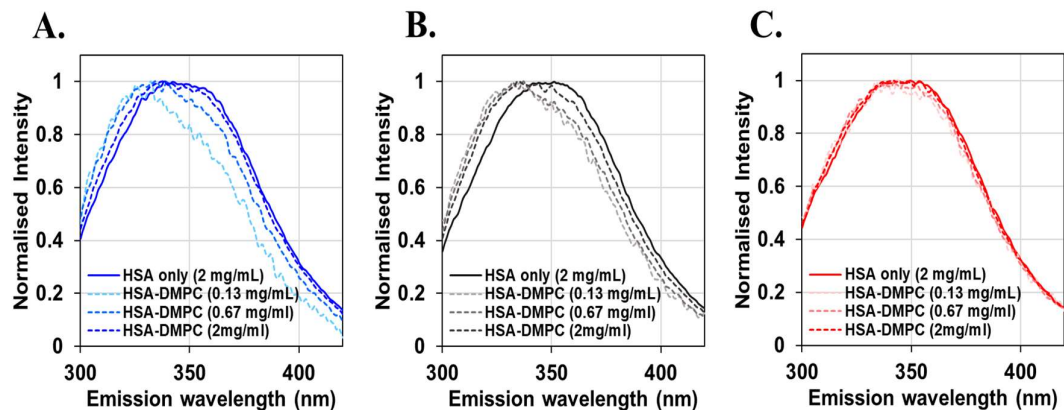


Figure 8.4: Fluorescence emission of HSA (exc. 280 nm) in vertical (\parallel) polarization mode in; (A) Water, (B) ABC, and (C) PBS, in the absence (solid lines) and presence DMPC liposomes (dashed lines).

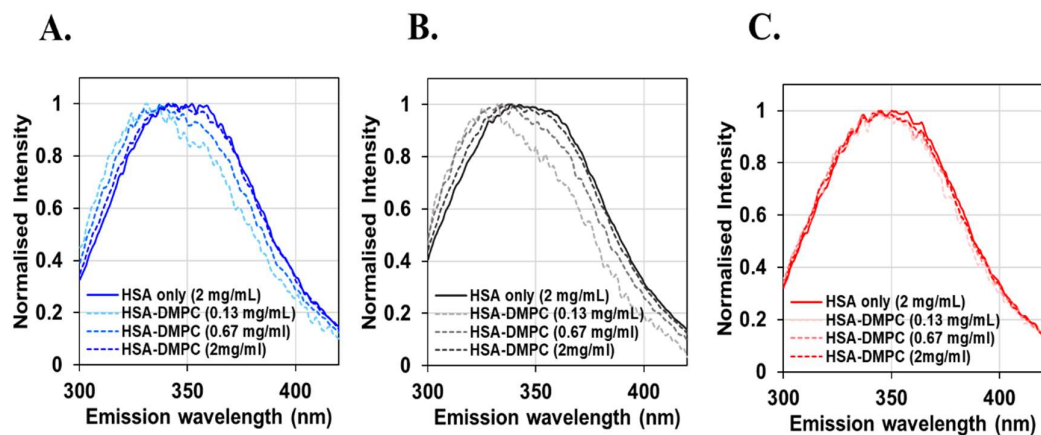


Figure 8.5: Fluorescence emission of HSA (exc. 280 nm) in perpendicular (\perp) polarization mode in; (A) Water, (B) ABC, and (C) PBS, in the absence (solid lines) and presence of DMPC liposomes (dashed lines).

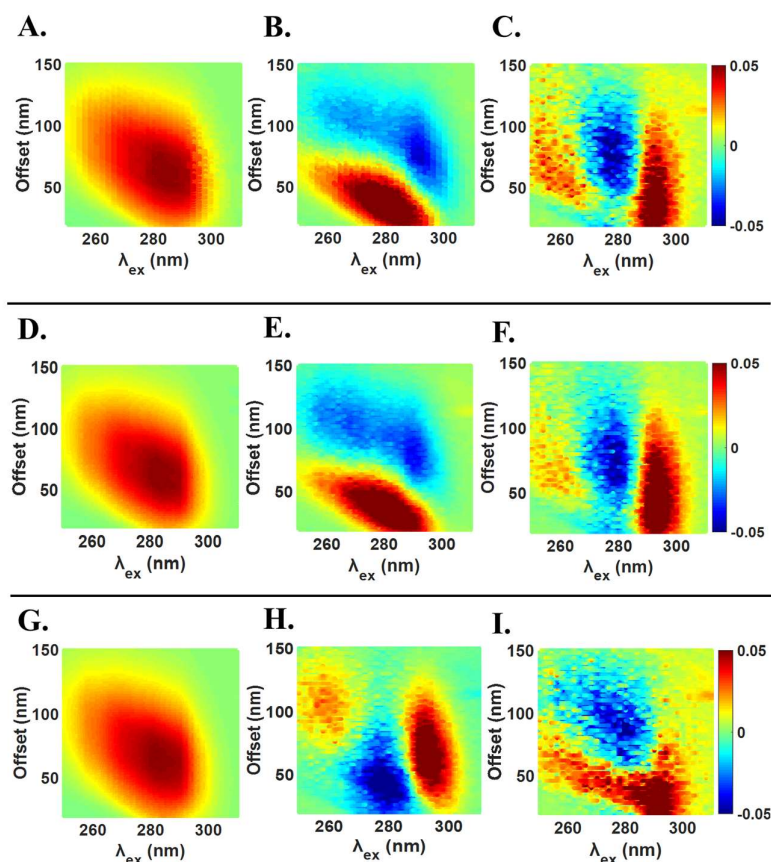


Figure 8.6: PCA loadings shown for PC's 1-3 (L-R) for PCA models on water (A-C), ABC (D-F), and PBS (G-I) using the total polarization datasets.

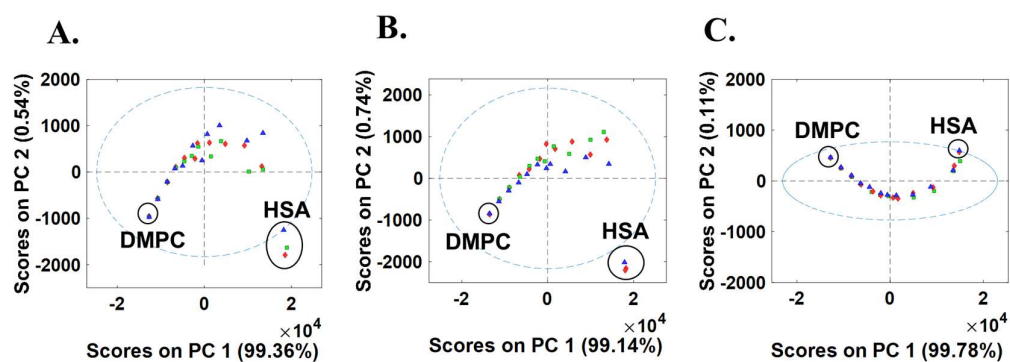


Figure 8.7: PC1 vs PC2 Scores plots from three component PCA models of the total datasets of water, ABC, and PBS (R-L) interaction samples. The samples containing DMPC liposomes only and HSA only are labelled in each plot. The red, green, and blue markers correspond to replicate measurements 1-3, respectively in each aqueous medium i.e., colour sets in each correspond to samples made from a single extrusion.

REFERENCES

- [1] Y. Casamayou-Boucau, A. Ryder, Accurate anisotropy recovery from fluorophore mixtures using Multivariate Curve Resolution (MCR), *Anal. Chim. Acta*, 1000 (2017).
- [2] R.C. Groza, B.Y. Li, A.G. Ryder, Anisotropy resolved multidimensional emission spectroscopy (ARMES): A new tool for protein analysis, *Anal. Chim. Acta*, 886 (2015) 133-142.
- [3] D.J. Houde, S.A. Berkowitz, *Biophysical characterization of proteins in developing biopharmaceuticals*, Amsterdam, Netherlands : Elsevier, Amsterdam, Netherlands, 2015.
- [4] J.R. Lakowicz, *Principles of Fluorescence Spectroscopy*, 3rd ed., Springer, New York, 2006.
- [5] B. Li, P.W. Ryan, M. Shanahan, K.J. Leister, A.G. Ryder, Fluorescence Excitation—Emission Matrix (EEM) Spectroscopy for Rapid Identification and Quality Evaluation of Cell Culture Media Components, *Appl. Spectrosc.*, 65 (2011) 1240-1249.
- [6] M. Steiner-Browne, S. Elcoroaristizabal, A.G. Ryder, Using polarized Total Synchronous Fluorescence Spectroscopy (pTSFS) with PARAFAC analysis for characterizing intrinsic protein emission, *Chemom. Intell. Lab. Syst.*, (2019) 103871.
- [7] M. Steiner-Browne, S. Elcoroaristizabal, Y. Casamayou-Boucau, A.G. Ryder, Investigating native state fluorescence emission of Immunoglobulin G using polarized Excitation Emission Matrix (pEEM) spectroscopy and PARAFAC, *Chemom. Intell. Lab. Syst.*, 185 (2019) 1-11.
- [8] Y. Casamayou-Boucau, A.G. Ryder, Extended wavelength anisotropy resolved multidimensional emission spectroscopy (ARMES) measurements: better filters, validation standards, and Rayleigh scatter removal methods, *Methods Appl. Fluoresc.*, 5 (2017) 037001.
- [9] F. Gordon, S. Elcoroaristizabal, A.G. Ryder, Modelling Förster resonance energy transfer (FRET) using anisotropy resolved multi-dimensional emission spectroscopy (ARMES), *Biochim. Biophys. Acta Gen. Subj.*, 1865 (2021) 129770.
- [10] J. Sabin, G. Prieto, J.M. Ruso, P.V. Messina, F.J. Salgado, M. Nogueira, M. Costas, F. Sarmiento, Interactions between DMPC Liposomes and the Serum Blood Proteins HSA and IgG, *J. Phys. Chem. B*, 113 (2009) 1655-1661.
- [11] R. Thakur, A. Das, A. Chakraborty, The fate of anticancer drug, ellipticine in DPPC and DMPC liposomes upon interaction with HSA: A photophysical approach, *J. Photochem. Photobiol. B*, 130 (2014) 122-131.
- [12] H. Huang, C. Zhang, S. Yang, W. Xiao, Q. Zheng, X. Song, The investigation of mRNA vaccines formulated in liposomes administrated in multiple routes against SARS-CoV-2, *J. Controlled Release*, 335 (2021) 449-456.
- [13] B. Valeur, M.N. Berberan-Santos, A Brief History of Fluorescence and Phosphorescence before the Emergence of Quantum Theory, *J. Chem. Educ.*, 88 (2011) 731-738.
- [14] G.G. Stokes, On the Change of Refrangibility of Light, *Philos. Trans. Royal Soc.*, 142 (1852) 463-562.
- [15] B. Valeur, *Introduction: On the Origin of the Terms Fluorescence, Phosphorescence, and Luminescence*, Springer Berlin Heidelberg, Berlin, Heidelberg, 2001.

- [16] G.G. Stokes, On the metallic reflection exhibited by certain nonmetallic substances, *Philos. Mag.*, 1853, pp. 393-403.
- [17] F. Perrin, La fluorescence des solutions, *Ann. Phys.*, 10 (1929) 169-275.
- [18] B. Valeur, *Molecular fluorescence: principles and applications*, 2nd Ed. ed., John Wiley & Sons, 2012.
- [19] M. Kasha, Characterization of electronic transitions in complex molecules, *Faraday Discuss.*, 9 (1950) 14-19.
- [20] J.R. Albani, *Principles and applications of fluorescence spectroscopy*, Blackwell Publishing, 2008.
- [21] L. Stryer, *Fluorescence Spectroscopy of Proteins*, *Science*, 162 (1968) 526-533.
- [22] M.R. Eftink, Fluorescence techniques for studying protein structure, *Methods Biochem. Anal.*, 35 (1991) 127-205.
- [23] A.S. Ladokhin, *Fluorescence Spectroscopy in Peptide and Protein Analysis*, in: R.A. Meyers (Ed.) *Encyclopedia of Analytical Chemistry*, John Wiley & Sons Ltd, Chichester, 2000, pp. 5762–5779.
- [24] T.Y. Tsong, Trp-59 fluorescence of ferricytochrome-C as a sensitive measure of overall protein conformation, *J. Biol. Chem.*, 249 (1974) 1988-1990.
- [25] C.D. Snow, N. Nguyen, V.S. Pande, M. Gruebele, Absolute comparison of simulated and experimental protein-folding dynamics, *Nature*, 420 (2002) 102-106.
- [26] A. Sytnik, I. Litvinyuk, Energy transfer to a proton-transfer fluorescence probe: Tryptophan to a flavonol in human serum albumin, *Proc. Natl. Acad. Sci. U. S. A.*, 93 (1996) 12959-12963.
- [27] E.A. Burstein, N.S. Vedenkina, M.N. Ivkova, Fluorescence and the location of tryptophan residues in protein molecules, *Photochem. Photobiol.*, 18 (1973) 263-279.
- [28] J.T. Vivian, P.R. Callis, Mechanisms of tryptophan fluorescence shifts in proteins, *Biophys. J.*, 80 (2001) 2093-2109.
- [29] A. Hawe, M. Sutter, W. Jiskoot, Extrinsic fluorescent dyes as tools for protein characterization, *Pharm. Res.*, 25 (2008) 1487-1499.
- [30] A.M. Weljie, H.J. Vogel, *Steady-State Fluorescence Spectroscopy*, in: H.J. Vogel (Ed.) *Calcium-Binding Protein Protocols: Volume 2: Methods and Techniques*, Springer New York, Totowa, NJ, 2002, pp. 75-87.
- [31] D.P. Millar, Time-resolved fluorescence spectroscopy, *Curr. Opin. Struct. Biol.*, 6 (1996) 637-642.
- [32] W. Becker, A. Bergmann, Multi-dimensional time-correlated single photon counting, *Reviews in Fluorescence 2005*, 2 (2005) 77-+.
- [33] J.M. Demas, Excited-state lifetime measurements: Promise and problems, *Abstr. Pap. Am. Chem. Soc.*, 219 (2000) U440-U440.
- [34] W. Becker, *The bh TCSPC Handbook*, 7th Edition ed., Becker & Hickel GmbH, 2017.
- [35] C. Fu, H. Zheng, G. Wang, Y. Zhou, H. Chen, Y. He, J. Liu, J. Sun, Z. Xu, Three-Dimensional Imaging via Time-Correlated Single-Photon Counting, *Appl. Sci.*, 10 (2020) 1930.
- [36] Förster, Zwischenmolekulare Energiewanderung und Fluoreszenz, *Annalen der Physik*, 437 (1948) 55-75.
- [37] P.G. Wu, L. Brand, *Resonance Energy Transfer: Methods and Applications*, *Anal. Biochem.*, 218 (1994) 1-13.
- [38] D.W. Piston, G.J. Kremers, Fluorescent protein FRET: the good, the bad and the ugly, *Trends Biochem. Sci.*, 32 (2007) 407-414.

- [39] J.A. Broussard, K.J. Green, Research Techniques Made Simple: Methodology and Applications of Förster Resonance Energy Transfer (FRET) Microscopy, *J. Investig. Dermatol.*, 137 (2017) e185-e191.
- [40] B. Valeur, Effects of intermolecular photophysical processes on fluorescence emission, in: J.W.a. Sons (Ed.) *Molecular Fluorescence: Principles and Applications*, Wiley-VCH Verlag GmbH, 2002.
- [41] S.E. Braslavsky, Glossary of terms used in photochemistry, 3rd edition (IUPAC Recommendations 2006), *Pure Appl. Chem.*, 79 (2007) 293-465.
- [42] F.W.J. Teale, The ultraviolet fluorescence of proteins in neutral solution, *Biochem. J.*, 76 (1960) 381-388.
- [43] L. Loura, M. Prieto, FRET in Membrane Biophysics: An Overview, *Front. physiol.*, 2 (2011).
- [44] P.D.J. Moens, M.K. Helms, D.M. Jameson, Detection of tryptophan to tryptophan energy transfer in proteins, *Protein J.*, 23 (2004) 79-83.
- [45] A.B.T. Ghisaidoobe, S.J. Chung, Intrinsic Tryptophan Fluorescence in the Detection and Analysis of Proteins: A Focus on Forster Resonance Energy Transfer Techniques, *Int. J. Mol. Sci.*, 15 (2014) 22518-22538.
- [46] M.C. Murphy, I. Rasnik, W. Cheng, T.M. Lohman, T.J. Ha, Probing single-stranded DNA conformational flexibility using fluorescence spectroscopy, *Biophys. J.*, 86 (2004) 2530-2537.
- [47] L. Yuan, W.Y. Lin, K.B. Zheng, S.S. Zhu, FRET-Based Small-Molecule Fluorescent Probes: Rational Design and Bioimaging Applications, *Accounts Chem. Res.*, 46 (2013) 1462-1473.
- [48] L. Stryer, Fluorescence Energy Transfer as a Spectroscopic Ruler, *Annu. Rev. Biochem.*, 47 (1978) 819-846.
- [49] Y. Shi, P.F.W. Stouten, N. Pillalamarri, L. Barile, R.V. Rosal, S. Teichberg, Z. Bu, D.J.E. Callaway, Quantitative determination of the topological propensities of amyloidogenic peptides, *Biophys. Chem.*, 120 (2006) 55-61.
- [50] K. Truong, M. Ikura, The use of FRET imaging microscopy to detect protein-protein interactions and protein conformational changes in vivo, *Curr. Opin. Struct. Biol.*, 11 (2001) 573-578.
- [51] S.F. Martin, M.H. Tatham, R.T. Hay, I.D. Samuel, Quantitative analysis of multi-protein interactions using FRET: application to the SUMO pathway, *Protein Sci.*, 17 (2008) 777-784.
- [52] R.B. Sekar, A. Periasamy, Fluorescence resonance energy transfer (FRET) microscopy imaging of live cell protein localizations, *J. Cell Biol.*, 160 (2003) 629-633.
- [53] B.K.-K. Fung, L. Stryer, Surface density determination in membranes by fluorescence energy transfer, *Biochem.*, 17 (1978) 5241-5248.
- [54] Q. Ni, J. Zhang, Dynamic visualization of cellular signaling, *Adv. Biochem. Eng. Biotechnol.*, 119 (2010) 79-97.
- [55] A. Buntru, T. Zimmermann, C.R. Hauck, Fluorescence resonance energy transfer (FRET)-based subcellular visualization of pathogen-induced host receptor signaling, *BMC Biol.*, 7 (2009) 81.
- [56] M.J. Lohse, S. Nuber, C. Hoffmann, Fluorescence/Bioluminescence Resonance Energy Transfer Techniques to Study G-Protein-Coupled Receptor Activation and Signaling, *Pharmacol. Rev.*, 64 (2012) 299-336.
- [57] L. Liu, F. He, Y. Yu, Y. Wang, Application of FRET Biosensors in Mechanobiology and Mechanopharmacological Screening, *Front. Bioeng. Biotechnol.*, 8 (2020).

- [58] L. Wu, C. Huang, B.P. Emery, A.C. Sedgwick, S.D. Bull, X.-P. He, H. Tian, J. Yoon, J.L. Sessler, T.D. James, Förster resonance energy transfer (FRET)-based small-molecule sensors and imaging agents, *Chem. Soc. Rev.*, 49 (2020) 5110-5139.
- [59] Y. Liu, J. Liao, Quantitative FRET (Förster Resonance Energy Transfer) analysis for SENP1 protease kinetics determination, *J. Vis. Exp.*, (2013) e4430-e4430.
- [60] T. Eilert, E. Kallis, J. Nagy, C. Röcker, J. Michaelis, Complete Kinetic Theory of FRET, *J. Phys. Chem. B*, 122 (2018) 11677-11694.
- [61] J.R. Silvius, I.R. Nabi, Fluorescence-quenching and resonance energy transfer studies of lipid microdomains in model and biological membranes, *Mol. Membr. Biol.*, 23 (2006) 5-16.
- [62] I.V. Gopich, A. Szabo, Theory of the energy transfer efficiency and fluorescence lifetime distribution in single-molecule FRET, *Proc. Natl. Acad. Sci. U.S.A.*, 109 (2012) 7747-7752.
- [63] C.M. Yengo, C.L. Berger, Fluorescence anisotropy and resonance energy transfer: powerful tools for measuring real time protein dynamics in a physiological environment, *Curr. Opin. Pharmacol.*, 10 (2010) 731-737.
- [64] M. Tramier, M. Coppey-Moisan, Fluorescence anisotropy imaging microscopy for homo-FRET in living cells, *Methods Cell Biol.*, 85 (2008) 395-414.
- [65] T. Zal, N.R.J. Gascoigne, Photobleaching-corrected FRET efficiency imaging of live cells, *Biophys. J.*, 86 (2004) 3923-3939.
- [66] E.B. Van Munster, G.J. Kremers, M.J. Adjobo-Hermans, T.W. Gadella, Jr., Fluorescence resonance energy transfer (FRET) measurement by gradual acceptor photobleaching, *J. Microsc.*, 218 (2005) 253-262.
- [67] D.M. Jameson, J.A. Ross, Fluorescence Polarization/Anisotropy in Diagnostics and Imaging, *Chem. Rev.*, 110 (2010) 2685-2708.
- [68] T.L. Mann, U.J. Krull, Fluorescence polarization spectroscopy in protein analysis, *Analyst*, 128 (2003) 313-317.
- [69] T.A. Smith, K.P. Ghiggino, A review of the analysis of complex time-resolved fluorescence anisotropy data, *Methods Appl. Fluoresc.*, 3 (2015) 15.
- [70] D.M. Jameson, S.E. Seifried, Quantification of Protein-Protein Interactions Using Fluorescence Polarization, *Methods*, 19 (1999) 222-233.
- [71] G. Weber, Polarization of the fluorescence of macromolecules 1. Theory and experimental method, *Biochem. J.*, 51 (1952) 145-155.
- [72] A.G. Ryder, C.A. Stedmon, N. Harrit, R. Bro, Calibration, standardization, and quantitative analysis of multidimensional fluorescence (MDF) measurements on complex mixtures (IUPAC Technical Report), *Pure Appl. Chem.*, 89 (2017) 1849-1870.
- [73] D. Patra, A.K. Mishra, Recent developments in multi-component synchronous fluorescence scan analysis, *Trends Analyt. Chem.*, 21 (2002) 787-798.
- [74] K. Kumar, A.K. Mishra, Application of 'multivariate curve resolution alternating least square (MCR-ALS)' analysis to extract pure component synchronous fluorescence spectra at various wavelength offsets from total synchronous fluorescence spectroscopy (TSFS) data set of dilute aqueous solutions of fluorophores, *Chemom. Intell. Lab. Syst.*, 116 (2012) 78-86.
- [75] A.V. Schenone, A. de Araújo Gomes, M.J. Culzoni, A.D. Campiglia, M.C.U. de Araújo, H.C. Goicoechea, Modeling nonbilinear total synchronous fluorescence data matrices with a novel adapted partial least squares method, *Anal. Chim. Acta*, 859 (2015) 20-28.
- [76] K. Kumar, A.K. Mishra, Application of parallel factor analysis to total synchronous fluorescence spectrum of dilute multifluorophoric solutions: addressing

- the issue of lack of trilinearity in total synchronous fluorescence data set, *Anal. Chim. Acta*, 755 (2012) 37-45.
- [77] A. Nevin, D. Comelli, G. Valentini, R. Cubeddu, Total synchronous fluorescence spectroscopy combined with multivariate analysis: method for the classification of selected resins, oils, and protein-based media used in paintings, *Anal. Chem.*, 81 (2009) 1784-1791.
- [78] M. Bahram, R. Bro, C. Stedmon, A. Afkhami, Handling of Rayleigh and Raman scatter for PARAFAC modeling of fluorescence data using interpolation, *J. Chemometr.*, 20 (2006) 99-105.
- [79] D.N. Kothawala, K.R. Murphy, C.A. Stedmon, G.A. Weyhenmeyer, L.J. Tranvik, Inner filter correction of dissolved organic matter fluorescence, *Limnol. Oceanogr. Methods*, 11 (2013) 616-630.
- [80] H. Chen, J.E. Kenny, Application of PARAFAC to a two-component system exhibiting Fluorescence Resonance Energy Transfer: from theoretical prediction to experimental validation, *The Analyst*, 137 (2012) 153-162.
- [81] S. Wold, Spline functions, a new tool in data-analysis, *Kemisk Tidskrift*, 84 (1972) 34.
- [82] B. Kowalski, S. Brown, B. Vandeginste, Editorial, *J. Chemometr.*, 1 (1987) 1-2.
- [83] E.R. Malinowski, P.H. Weiner, A.R. Levinstone, Factor analysis of solvent shifts in proton magnetic resonance, *J. Phys. Chem.*, 74 (1970) 4537--4542.
- [84] P.C. Jurs, B.R. Kowalski, T.L. Isnehour, C.N. Reilley, Investigation of combined patterns from diverse analytical data using computerized learning machines, *Anal. Chem.*, 41 (1969) 1949--1953.
- [85] L.R. Tucker, Some mathematical notes on three-mode factor analysis, *Psychometrika*, (1966) 279-311.
- [86] A.K. Smilde, *Multi-way analysis with applications in the chemical sciences*, J. Wiley, 2004.
- [87] R.G. Brereton, A short history of chemometrics: a personal view, *J. Chemometr.*, 28 (2014) 749-760.
- [88] A. de Juan, R. Tauler, Multivariate curve resolution (MCR) from 2000: Progress in concepts and applications, *Critical Rev. Anal. Chem.*, 36 (2006) 163-176.
- [89] H.A.L. Kiers, Hierarchical relations among 3-way methods, *Psychometrika*, 56 (1991) 449-470.
- [90] S. Wold, K. Esbensen, P. Geladi, *Principal component analysis*, *Chemom. Intell. Lab. Syst.*, 2 (1987) 37-52.
- [91] H.-L. Wu, T. Wang, R.-Q. Yu, Recent advances in chemical multi-way calibration with second-order or higher-order advantages: Multilinear models, algorithms, related issues and applications, *TrAC Trends in Analytical Chemistry*, 130 (2020) 115954.
- [92] P. Kroonenberg, *Three-Mode Principal Component Analysis: Theory and Applications*, DSWO Press, The Netherlands, 1983.
- [93] U. Sivarajah, M.M. Kamal, Z. Irani, V. Weerakkody, Critical analysis of Big Data challenges and analytical methods, *J. Bus. Res.*, 70 (2017) 263-286.
- [94] P. Mishra, J.-M. Roger, D. Jouan-Rimbaud-Bouveresse, A. Biancolillo, F. Marini, A. Nordon, D.N. Rutledge, Recent trends in multi-block data analysis in chemometrics for multi-source data integration, *Trends Analyt. Chem.*, 137 (2021) 116206.
- [95] A. Biancolillo, F. Marini, *Chemometric Methods for Spectroscopy-Based Pharmaceutical Analysis*, *Front. Chem.*, 6 (2018).
- [96] T. Azzouz, R. Tauler, Application of multivariate curve resolution alternating least squares (MCR-ALS) to the quantitative analysis of pharmaceutical and agricultural samples, *Talanta*, 74 (2008) 1201-1210.

- [97] J.A. Arancibia, G.M. Escandar, Second-order chromatographic photochemically induced fluorescence emission data coupled to chemometric analysis for the simultaneous determination of urea herbicides in the presence of matrix co-eluting compounds, *Anal. Methods*, 6 (2014) 5503-5511.
- [98] S.A. Bortolato, A.C. Olivieri, Chemometric processing of second-order liquid chromatographic data with UV-vis and fluorescence detection. A comparison of multivariate curve resolution and parallel factor analysis 2, *Anal. Chim. Acta*, 842 (2014) 11-19.
- [99] J. Saurina, C. Leal, R. Compañó, M. Granados, R. Tauler, M.D. Prat, Determination of triphenyltin in sea-water by excitation-emission matrix fluorescence and multivariate curve resolution, *Anal. Chim. Acta*, 409 (2000) 237-245.
- [100] H. Hotelling, Analysis of a complex of statistical variables into principal components, *J. Educ. Psychol.*, 24 (1933) 417-441.
- [101] C.J. Carroll J. D., Analysis of individual differences in multidimensional scaling via an N-way generalization of an 'Eckart-Young' decomposition, *Psychometrika*, 35 (1970) 283-319.
- [102] R.A. Harshman, Foundations of the parafac procedure: model and conditions for an 'explanatory' multi-mode factor analysis., *UCLA Work. Pap. Phon*, (1970) 1-84.
- [103] F.L. Hitchcock, The expression of a tensor or a polyadic as a sum of products, *J. Math. Phys.*, 6 (1927).
- [104] P. Kroonenberg, R. Harshman, T. Murakami, Analysing Three-way Profile Data Using the Parafac and Tucker3 Models Illustrated with Views on Parenting, *Appl. Multivar. Res*, 13 (2009) 5-41.
- [105] R.B. Cattell, "Parallel proportional profiles" and other principles for determining the choice of factors by rotation, *Psychometrika*, 9 (1944) 267-283.
- [106] R. Bro, PARAFAC. Tutorial and applications, *Chemom. Intell. Lab. Syst.*, 38 (1997) 149-171.
- [107] Y. Casamayou-Boucau, A.G. Ryder, Quantitative analysis of weakly bound insulin oligomers in solution using polarized multidimensional fluorescence spectroscopy, *Anal. Chim. Acta*, 1138 (2020) 18-29.
- [108] R. Bro, H.A.L. Kiers, A new efficient method for determining the number of components in PARAFAC models, *J. Chemometr.*, 17 (2003) 274-286.
- [109] C.M. Andersen, R. Bro, Practical aspects of PARAFAC modeling of fluorescence excitation-emission data, *J. Chemometr.*, 17 (2003) 200-215.
- [110] P.M. Kroonenberg, J.M.F. ten Berge, The equivalence of Tucker3 and Parafac models with two components, *Chemom. Intell. Lab. Syst.*, 106 (2011) 21-26.
- [111] M. Kompany-Zareh, Y. Akhlaghi, R. Bro, Tucker core consistency for validation of restricted Tucker3 models, *Anal. Chim. Acta*, 723 (2012) 18-26.
- [112] A.L. Silva, S. Elcoroaristizabal, A. Ryder, Multi-Attribute Quality Screening of Immunoglobulin G using polarized Excitation Emission Matrix Spectroscopy, *Anal. Chim. Acta*, 1101 (2019).
- [113] B. Leader, Q.J. Baca, D.E. Golan, Protein therapeutics: A summary and pharmacological classification, *Nat. Rev. Drug Discov.*, 7 (2008) 21-39.
- [114] G.A. Petsko, Protein structure and function, Oxford University Press, 2004.
- [115] F. Chiti, C.M. Dobson, Protein misfolding, functional amyloid, and human disease, *Annu. Rev. Biochem.*, 75 (2006) 333-366.
- [116] G. Walsh, Biopharmaceutical benchmarks 2014, *Nat. Biotechnol.*, 32 (2014) 992-1000.
- [117] D.V. Goeddel, D.G. Kleid, F. Bolivar, H.L. Heyneker, D.G. Yansura, R. Crea, T. Hirose, A. Kraszewski, K. Itakura, A.D. Riggs, Expression in escherichia-coli of

- chemically synthesized genes for human insulin, *Proc. Natl. Acad. Sci. U.S.A.*, 76 (1979) 106-110.
- [118] D.J.A. Crommelin, G. Storm, R. Verrijck, L. de Leede, W. Jiskoot, W.E. Hennink, Shifting paradigms: biopharmaceuticals versus low molecular weight drugs, *Int. J. Pharm.*, 266 (2003) 3-16.
- [119] D.M. Ecker, S.D. Jones, H.L. Levine, The therapeutic monoclonal antibody market, *mAbs*, 7 (2015) 9-14.
- [120] D.A. Jackson, R.H. Symons, P. Berg, Biochemical Method for Inserting New Genetic Information into DNA of Simian Virus 40: Circular SV40 DNA Molecules Containing Lambda Phage Genes and the Galactose Operon of *Escherichia coli*, *Proc. Nat. Acad. Sci.*, 69 (1972) 2904-2909.
- [121] H.A.D. Lagassé, Alexaki, A., Simhadri, V. L., Katagiri, N. H., Jankowski, W., Sauna, Z. E., & Kimchi-Sarfaty, C., Recent advances in (therapeutic protein) drug development, *F1000Research*, 113 (2017).
- [122] H. Mellstedt, Clinical considerations for biosimilar antibodies, *Eur. J. Cancer Suppl.*, 11 (2013) 1 - 11.
- [123] A.S. Rathore, Follow-on protein products: scientific issues, developments and challenges, *Trends Biotechnol.*, 27 (2009) 698-705.
- [124] K.D. Ratanji, J.P. Derrick, R.J. Dearman, I. Kimber, Immunogenicity of therapeutic proteins: Influence of aggregation, *J. Immunotoxicol.*, 11 (2014) 99-109.
- [125] J. den Engelsman, P. Garidel, R. Smulders, H. Koll, B. Smith, S. Bassarab, A. Seidl, O. Hainzl, W. Jiskoot, Strategies for the Assessment of Protein Aggregates in Pharmaceutical Biotech Product Development, *Pharm. Res.*, 28 (2011) 920-933.
- [126] M.E.M. Cromwell, E. Hilario, F. Jacobson, Protein aggregation and bioprocessing, *AAPS J.*, 8 (2006) E572-E579.
- [127] J.S. Philo, Is any measurement method optimal for all aggregate sizes and types?, *AAPS J.*, 8 (2006) E564-E571.
- [128] S. Zolls, R. Tantipolphan, M. Wiggenhorn, G. Winter, W. Jiskoot, W. Friess, A. Hawe, Particles in therapeutic protein formulations, Part 1: Overview of analytical methods, *J. Pharm. Sci.*, 101 (2012) 914-935.
- [129] R. Krishnamurthy, M. Sukumar, T. Das, N. Lacher, Emerging analytical technologies for biotherapeutics development, *Bioprocess Int.*, 6 (2008).
- [130] H. Mach, C.R. Middaugh, Ultraviolet Spectroscopy as a Tool in Therapeutic Protein Development, *J. Pharm. Sci.*, 100 (2011) 1214-1227.
- [131] D. Shajari, A. Bahari, P. Gill, Fast and simple detection of bovine serum albumin concentration by studying its interaction with gold nanorods, *Colloids Surf. A Physicochem. Eng. Asp.*, 543 (2018) 118-125.
- [132] S. Fekete, A. Beck, J.-L. Veuthey, D. Guilleme, Theory and practice of size exclusion chromatography for the analysis of protein aggregates, *J. Pharm. Biomed. Anal.*, 101 (2014) 161-173.
- [133] J.M. Walker, SDS Polyacrylamide Gel Electrophoresis of Proteins, in: J.M. Walker (Ed.) *The Protein Protocols Handbook*, Humana Press, Totowa, NJ, 2009, pp. 177-185.
- [134] J. Stetefeld, S.A. McKenna, T.R. Patel, Dynamic light scattering: a practical guide and applications in biomedical sciences, *Biophys. Rev.*, 8 (2016) 409-427.
- [135] J. Panchal, J. Kotarek, E. Marszal, E.M. Topp, Analyzing Subvisible Particles in Protein Drug Products: a Comparison of Dynamic Light Scattering (DLS) and Resonant Mass Measurement (RMM), *AAPS J.*, 16 (2014) 440-451.
- [136] N.J. Greenfield, Using circular dichroism spectra to estimate protein secondary structure, *Nat. protoc.*, 1 (2006) 2876-2890.

- [137] V. Joshi, T. Shivach, N. Yadav, A. Rathore, Circular Dichroism Spectroscopy as a Tool for Monitoring Aggregation in Monoclonal Antibody Therapeutics, *Anal. Chem.*, 86 (2014).
- [138] M. Jackson, H.H. Mantsch, The Use and Misuse of FTIR Spectroscopy in the Determination of Protein Structure, *Crit. Rev. Biochem. Mol. Biol.*, 30 (1995) 95-120.
- [139] A. Barth, Infrared spectroscopy of proteins, *Biochim. Biophys. Acta Bioenerg.*, 1767 (2007) 1073-1101.
- [140] W. Timp, G. Timp, Beyond mass spectrometry, the next step in proteomics, *Sci. Adv.*, 6 (2020).
- [141] B. Domon, R. Aebersold, Mass Spectrometry and Protein Analysis, *Science*, 312 (2006) 212-217.
- [142] S.A. Trauger, W. Webb, G. Siuzdak, Peptide and protein analysis with mass spectrometry, *Spectroscopy*, 16 (2002) 15-28.
- [143] C.R. Alving, Macrophages as targets for delivery of liposome-encapsulated antimicrobial agents, *Adv. Drug Deliv. Rev.*, 2 (1988) 107-128.
- [144] A. Sharma, U.S. Sharma, Liposomes in drug delivery: Progress and limitations, *Int. J. Pharm.*, 154 (1997) 123-140.
- [145] J.M. Berg, J.L. Tymoczko, L. Stryer, *Biochemistry*, Fifth Edition ed., W.H. Freeman, 2002.
- [146] A.D. Bangham, R.W. Horne, Negative staining of phospholipids and their structural modification by surface-active agents as observed in the electron microscope, *J. Mol. Biol.*, 8 (1964) 660-IN610.
- [147] C. Chen, S. Zhu, T. Huang, S. Wang, X. Yan, Analytical techniques for single-liposome characterization, *Anal. Methods*, 5 (2013) 2150-2157.
- [148] S.B. Kulkarni, G.V. Betageri, M. Singh, Factors affecting microencapsulation of drugs in liposomes, *J. Microencapsul.*, 12 (1995) 229-246.
- [149] B.S. Pattni, V.V. Chupin, V.P. Torchilin, New Developments in Liposomal Drug Delivery, *Chem. Rev.*, 115 (2015) 10938-10966.
- [150] D.D. Lasic, Novel applications of liposomes, *Trends Biotechnol.*, 16 (1998) 307-321.
- [151] J.N. Israelachvili, S. Marcelja, R.G. Horn, Physical principles of membrane organization, *Q. Rev. Biophys.*, 13 (1980) 121-200.
- [152] H. Pandey, R. Rani, V. Agarwal, Liposome and Their Applications in Cancer Therapy, *Braz. Arch. Biol. Technol.*, 59 (2016).
- [153] A.D. Bangham, M.M. Standish, J.C. Watkins, Diffusion of univalent ions across the lamellae of swollen phospholipids, *J. Mol. Biol.*, 13 (1965) 238-IN227.
- [154] M. Li, C. Du, N. Guo, Y. Teng, X. Meng, H. Sun, S. Li, P. Yu, H. Galons, Composition design and medical application of liposomes, *Eur. J. Med. Chem.*, 164 (2019) 640-653.
- [155] T. Oberholzer, P.L. Luisi, The Use of Liposomes for Constructing Cell Models, *J. Biol. Phys.*, 28 (2002) 733-744.
- [156] A.D. Bangham, M.W. Hill, N.G.A. Miller, Preparation and Use of Liposomes as Models of Biological Membranes, in: E.D. Korn (Ed.) *Methods in Membrane Biology: Volume 1*, Springer US, Boston, MA, 1974, pp. 1-68.
- [157] S.K. Sahoo, V. Labhasetwar, Nanotech approaches to drug delivery and imaging, *Drug Discov. Today*, 8 (2003) 1112-1120.
- [158] L. Sercombe, T. Veerati, F. Moheimani, S.Y. Wu, A.K. Sood, S. Hua, Advances and Challenges of Liposome Assisted Drug Delivery, *Front. Pharmacol.*, 6 (2015) 286-286.

- [159] J.-S. Kim, Liposomal drug delivery system, *J. Pharm. Investig.*, 46 (2016) 387-392.
- [160] Y. Barenholz, Doxil®--the first FDA-approved nano-drug: lessons learned, *J. Controlled Release*, 160 (2012) 117-134.
- [161] E. Beltrán-Gracia, A. López-Camacho, I. Higuera-Ciapara, J.B. Velázquez-Fernández, A.A. Vallejo-Cardona, Nanomedicine review: clinical developments in liposomal applications, *Cancer Nanotechnol.*, 10 (2019) 11.
- [162] U. Bulbake, S. Doppalapudi, N. Kommineni, W. Khan, Liposomal Formulations in Clinical Use: An Updated Review, *Pharmaceutics*, 9 (2017).
- [163] F. Bonté, R.L. Juliano, Interactions of liposomes with serum proteins, *Chem. Phys. Lipids*, 40 (1986) 359-372.
- [164] K. Apperson, J. Karolin, R.W. Martin, D.J.S. Birch, Nanoparticle metrology standards based on the time-resolved fluorescence anisotropy of silica colloids, *Measurement Science and Technology*, 20 (2009) 025310.
- [165] E. Tomaszewska, K. Soliwoda, K. Kadziola, B. Tkacz-Szczesna, G. Celichowski, M. Cichowski, W. Szmaja, J. Grobelny, Detection Limits of DLS and UV-Vis Spectroscopy in Characterization of Polydisperse Nanoparticles Colloids, *J. Nanomater.*, 2013 (2013) 313081.
- [166] J. Einax, Steven D. Brown, Romà Tauler, Beata Walczak (Eds.): Comprehensive chemometrics. Chemical and biochemical data analysis, *Anal. Bioanal. Chem.*, 396 (2009).
- [167] R.D. JiJi, K.S. Booksh, Mitigation of Rayleigh and Raman Spectral Interferences in Multiway Calibration–Emission Matrix Fluorescence Spectra, *Anal. Chem.*, 72 (2000) 718-725.
- [168] P.D. Wentzell, S.S. Nair, R.D. Guy, Three-way analysis of fluorescence spectra of polycyclic aromatic hydrocarbons with quenching by nitromethane, *Anal. Chem.*, 73 (2001) 1408-1415.
- [169] A. Rinnan, K.S. Booksh, R. Bro, First order Rayleigh scatter as a separate component in the decomposition of fluorescence landscapes, *Anal. Chim. Acta*, 537 (2005) 349-358.
- [170] D.J.-R. Bouveresse, H. Benabid, D.N. Rutledge, Independent component analysis as a pretreatment method for parallel factor analysis to eliminate artefacts from multiway data, *Anal. Chim. Acta*, 589 (2007) 216-224.
- [171] M. Ameloot, M. vandeVen, A.U. Acuña, B. Valeur, Fluorescence anisotropy measurements in solution: Methods and reference materials (IUPAC Technical Report), *Pure Appl. Chem.*, 85 (2013) 589-608.
- [172] W.N. Reichelt, D. Waldschitz, C. Herwig, L. Neutsch, Bioprocess monitoring: minimizing sample matrix effects for total protein quantification with bicinchoninic acid assay, *J. Ind. Microbiol. Biotechnol.*, 43 (2016) 1271-1280.
- [173] J.X. Xu, B.C.N. Vithanage, S.A. Athukorale, D. Zhang, Scattering and absorption differ drastically in their inner filter effects on fluorescence, resonance synchronous, and polarized resonance synchronous spectroscopic measurements, *Analyst*, 143 (2018) 3382-3389.
- [174] A.G. Ryder, Quantitative Analysis of Crude Oils by Fluorescence Lifetime and Steady State Measurements Using 380-nm Excitation, *Appl. Spectrosc.*, 56 (2002) 107-116.
- [175] A. Savitzky, M.J.E. Golay, Smoothing and Differentiation of Data by Simplified Least Squares Procedures, *Anal. Chem.*, 36 (1964) 1627-1639.
- [176] K. Kumar, A.K. Mishra, Parallel factor (PARAFAC) analysis on total synchronous fluorescence spectroscopy (TSFS) data sets in excitation-emission matrix

fluorescence (EEMF) layout: Certain practical aspects, *Chemom. Intell. Lab. Syst.*, 147 (2015) 121-130.

[177] A. Sillen, Y. Engelborghs, The correct use of "average" fluorescence parameters, *Photochem. Photobiol.*, 67 (1998) 475-486.

[178] P.A. Dalgarno, J. Juan-Colás, G.J. Hedley, L. Piñeiro, M. Novo, C. Perez-Gonzalez, I.D.W. Samuel, M.C. Leake, S. Johnson, W. Al-Soufi, J.C. Penedo, S.D. Quinn, Unveiling the multi-step solubilization mechanism of sub-micron size vesicles by detergents, *Sci. Rep.*, 9 (2019) 12897.

[179] J. Juan-Colás, L. Dresser, K. Morris, H. Lagadou, R.H. Ward, A. Burns, S. Tear, S. Johnson, M.C. Leake, S.D. Quinn, The Mechanism of Vesicle Solubilization by the Detergent Sodium Dodecyl Sulfate, *Langmuir*, 36 (2020) 11499-11507.

[180] T. Gadella, FRET and FLIM techniques, 1st ed., Elsevier Science, 2008.

[181] D.M. Togashi, A.G. Ryder, A fluorescence analysis of ANS bound to bovine serum albumin: Binding properties revisited by using energy transfer, *J. Fluoresc.*, 18 (2008) 519-526.

[182] D.M. Togashi, A.G. Ryder, D. O'Shaughnessy, Monitoring Local Unfolding of Bovine Serum Albumin During Denaturation Using Steady-State and Time-Resolved Fluorescence Spectroscopy, *J. Fluoresc.*, 20 (2010) 441-452.

[183] J. Ghuman, P.A. Zunszain, I. Petitpas, A.A. Bhattacharya, M. Otagiri, S. Curry, Structural basis of the drug-binding specificity of human serum albumin, *J. Mol. Biol.*, 353 (2005) 38-52.

[184] M.L. Ferrer, R. Duchowicz, B. Carrasco, J.G. de la Torre, A.U. Acuna, The conformation of serum albumin in solution: A combined phosphorescence depolarization-hydrodynamic modeling study, *Biophys. J.*, 80 (2001) 2422-2430.

[185] T. Peters, Serum Albumin, *Adv. Protein Chem.*, 37 (1985) 161 - 245.

[186] R. Joshi, M. Jadhao, H. Kumar, S.K. Ghosh, Is the Sudlow site I of human serum albumin more generous to adopt prospective anti-cancer bioorganic compound than that of bovine: A combined spectroscopic and docking simulation approach, *Bioorg. Chem.*, 75 (2017) 332-346.

[187] H. Kumar, V. Devaraji, R. Joshi, S. Wankar, S.K. Ghosh, A Chalcone-Based Potential Therapeutic Small Molecule That Binds to Subdomain IIA in HSA Precisely Controls the Rotamerization of Trp-214, *ACS Omega*, 3 (2018) 10114-10128.

[188] G. Sudlow, D.J. Birkett, D.N. Wade, The Characterization of Two Specific Drug Binding Sites on Human Serum Albumin, *Mol. Pharmacol.*, 11 (1975) 824-832.

[189] I.M. Kuznetsova, A.I. Sulatskaya, O.I. Povarova, K.K. Turoverov, Reevaluation of ANS Binding to Human and Bovine Serum Albumins: Key Role of Equilibrium Microdialysis in Ligand - Receptor Binding Characterization, *Plos One*, 7 (2012) 9.

[190] O.K. Gasymov, B.J. Glasgow, ANS fluorescence: Potential to augment the identification of the external binding sites of proteins, *Biochim. Biophys. Acta Proteins Proteom.*, 1774 (2007) 403-411.

[191] E.M. Kosower, Intramolecular donor-acceptor systems. 9. Photophysics of (phenylamino)naphthalenesulfonates: a paradigm for excited-state intramolecular charge transfer, *Accounts Chem. Res.*, 15 (1982) 259-266.

[192] E.M. Kosower, D. Huppert, Excited State Electron and Proton Transfers, *Annu. Rev. Phys. Chem.*, 37 (1986) 127-156.

[193] C. Reichardt, Solvatochromic Dyes as Solvent Polarity Indicators, *Chem. Rev.*, 94 (1994) 2319-2358.

[194] R.A. Moore, J. Lee, G.W. Robinson, Hydration dynamics of electrons from a fluorescent probe molecule, *J. Phys. Chem.*, 89 (1985) 3648-3654.

- [195] G. Weber, E. Daniel, Cooperative effects in binding by bovine serum albumin 2. Binding of 1-anilino-8-naphthalene sulfonate. Polarization of ligand fluorescence and quenching of protein fluorescence, *Biochem.*, 5 (1966).
- [196] I. Tasaki, A. Warashina, H. Pant, Studies of light emission, absorption and energy transfer in nerve membranes labelled with fluorescent probes, *Biophys. Chem.*, 4 (1976) 1-13.
- [197] I.M. Kuznetsova, A.I. Sulatskaya, O.I. Povarova, K.K. Turoverov, Reevaluation of ANS Binding to Human and Bovine Serum Albumins: Key Role of Equilibrium Microdialysis in Ligand - Receptor Binding Characterization, *Plos One*, 7 (2012).
- [198] L.A. Bagatolli, S.C. Kivatinitz, F. Aguilar, M.A. Soto, P. Sotomayor, G.D. Fidelio, Two distinguishable fluorescent modes of 1-anilino-8-naphthalenesulfonate bound to human albumin, *J. Fluoresc.*, 6 (1996) 33-40.
- [199] G. Weber, Polarization of the fluorescence of macromolecules 1. Theory and experimental method, *Biochem. J.*, 51 (1952) 145-155.
- [200] R.B. Singh, S. Mahanta, A. Bagchi, N. Guchhait, Interaction of human serum albumin with charge transfer probe ethyl ester of N,N-dimethylamino naphthyl acrylic acid: An extrinsic fluorescence probe for studying protein micro-environment, *Photochem. Photobiol. Sci.*, 8 (2009) 101-110.
- [201] S. Ranjbar, Y. Shokoohinia, S. Ghobadi, N. Bijari, S. Gholamzadeh, N. Moradi, M.R. Ashrafi-Kooshk, A. Aghaei, R. Khodarahmi, Studies of the interaction between isoimperatorin and human serum albumin by multispectroscopic method: identification of possible binding site of the compound using esterase activity of the protein, *Sci. World J.*, 2013 (2013) 305081.
- [202] J. Jaumot, R. Gargallo, A. de Juan, R. Tauler, A graphical user-friendly interface for MCR-ALS: a new tool for multivariate curve resolution in MATLAB, *Chemom. Intell. Lab. Syst.*, 76 (2005) 101-110.
- [203] S. Elcoroaristizabal, A. de Juan, J.A. García, N. Durana, L. Alonso, Comparison of second-order multivariate methods for screening and determination of PAHs by total fluorescence spectroscopy, *Chemom. Intell. Lab. Syst.*, 132 (2014) 63-74.
- [204] Z.J. Cheng, R. Liu, X.H. Jiang, Spectroscopic studies on the interaction between tetrandrine and two serum albumins by chemometrics methods, *Spectrochim Acta A*, 115 (2013) 92-105.
- [205] G. E., P. P., Einfluss der Konzentration auf die Polarisation der Fluoreszenz von Farbstofflösungen, *Physik*, 24 (1924) 24-36.
- [206] Z. Zolmajd-Haghighi, Q.S. Hanley, When One Plus One Does Not Equal Two: Fluorescence Anisotropy in Aggregates and Multiply Labeled Proteins, *Biophys. J.*, 106 (2014) 1457-1466.
- [207] U. Kragh-Hansen, V.T.G. Chuang, M. Otagiri, Practical aspects of the ligand-binding and enzymatic properties of human serum albumin, *Biol. Pharm. Bull.*, 25 (2002) 695-704.
- [208] J.S. Renny, L.L. Tomasevich, E.H. Tallmadge, D.B. Collum, Method of continuous variations: applications of job plots to the study of molecular associations in organometallic chemistry, *Angew. Chem.*, 52 (2013) 11998-12013.
- [209] P. Job, Formation and Stability of Inorganic Complexes in Solution, *Annales de Chimie*, 10 (1928) 113-203.
- [210] K. Takehara, K. Yuki, M. Shirasawa, S. Yamasaki, S. Yamada, Binding Properties of Hydrophobic Molecules to Human Serum Albumin Studied by Fluorescence Titration, *Anal. Sci.*, 25 (2009) 115-120.
- [211] G. Zolese, G. Falcioni, E. Bertoli, R. Galeazzi, M. Wozniak, Z. Wypych, E. Gratton, A. Ambrosini, Steady-state and time resolved fluorescence of albumins

interacting with N-oleylethanolamine, a component of the endogenous N-acylethanolamines, *Proteins*, 40 (2000) 39-48.

[212] M. Song, S. Liu, J. Yin, H. Wang, Interaction of human serum album and C₆₀ aggregates in solution, *Int. J. Mol. Sci.*, 12 (2011) 4964-4974.

[213] I. Cvijetić, D. Petrovic, T. Verbić, I. Juranic, B. Drakulic, Human Serum Albumin Binding of 2-[(Carboxymethyl)sulfanyl]-4-oxo-4-(4-tert-butylphenyl)butanoic Acid and its Mono-Me Ester, *ADMET & DMPK*, 2 (2014) 126-142.

[214] A.A. Salem, M. Lotfy, A. Amin, M.A. Ghattas, Characterization of human serum albumin's interactions with safranal and crocin using multi-spectroscopic and molecular docking techniques, *Biochem. Biophys. Rep.*, 20 (2019) 100670.

[215] S. Lehrer, Solute perturbation of protein fluorescence. Quenching of the tryptophyl fluorescence of model compounds and of lysozyme by iodide ion, *Biochem.*, 10 (1971) 3254-3263.

[216] Z.J. Cheng, H.M. Zhao, Q.Y. Xu, R. Liu, Investigation of the interaction between indigotin and two serum albumins by spectroscopic approaches, *J. Pharm. Anal.*, 3 (2013) 257-269.

[217] V.D. Suryawanshi, L.S. Walekar, A.H. Gore, P.V. Anbhule, G.B. Kolekar, Spectroscopic analysis on the binding interaction of biologically active pyrimidine derivative with bovine serum albumin, *J. Pharm. Anal.*, 6 (2016) 56-63.

[218] M. Mączajek-Jurczyk, J. Równicka Zubik, R. Dyja, A. Sułkowska, Comparative Analysis of KP-HSA Complex by Spectroscopic Methods, *Acta Physica Polonica A*, 123 (2013) 673-680.

[219] M. Amiri, K. Jankeje, J.R. Albani, Origin of fluorescence lifetimes in human serum albumin. Studies on native and denatured protein, *J. Fluoresc.*, 20 (2010) 651-656.

[220] J.R. Albani, New insights in the interpretation of tryptophan fluorescence : origin of the fluorescence lifetime and characterization of a new fluorescence parameter in proteins: the emission to excitation ratio, *J. Fluoresc.*, 17 (2007) 406-417.

[221] A. Sillen, J.F. Díaz, Y. Engelborghs, A step toward the prediction of the fluorescence lifetimes of tryptophan residues in proteins based on structural and spectral data, *Protein Sci.*, 9 (2000) 158-169.

[222] J. Fidy, M. Laberge, B. Ullrich, L. Polgar, Z. Szeltner, J. Gallay, M. Vincent, Tryptophan rotamers that report the conformational dynamics of proteins, *Pure Appl. Chem.*, 73 (2001) 415-419.

[223] M. Hellings, M. De Maeyer, S. Verheyden, Q. Hao, E.J.M. Van Damme, W.J. Peumans, Y. Engelborghs, The dead-end elimination method, tryptophan rotamers, and fluorescence lifetimes, *Biophys. J.*, 85 (2003) 1894-1902.

[224] C. Buehler, C.Y. Dong, P.T.C. So, T. French, E. Gratton, Time-Resolved Polarization Imaging By Pump-Probe (Stimulated Emission) Fluorescence Microscopy, *Biophys. J.*, 79 (2000) 536-549.

[225] R.F. Latypov, D. Liu, K. Gunasekaran, T.S. Harvey, V.I. Razinkov, A.A. Raibekas, Structural and thermodynamic effects of ANS binding to human interleukin-1 receptor antagonist, *Protein Sci.*, 17 (2008) 652-663.

[226] S. Maity, R.K. Gundampati, T.K. Suresh Kumar, NMR Methods to Characterize Protein-Ligand Interactions, *Nat. Prod. Commun.*, 14 (2019) 1-17.

[227] D.E. Kamen, R.W. Woody, A partially folded intermediate conformation is induced in pectate lyase C by the addition of 8-anilino-1-naphthalenesulfonate (ANS), *Protein Sci.*, 10 (2001) 2123-2130.

- [228] W. Kirk, The binding of 1,8 ANS congeners to I-FABP and comparison of some hypotheses about ANS' spectral sensitivity to environment, *Biochim. Biophys. Acta*, 1748 (2005) 84-93.
- [229] K. Singh, I. Hussain, V. Mishra, M.S. Akhtar, New insight on 8-anilino-1-naphthalene sulfonic acid interaction with TgFNR for hydrophobic exposure analysis, *Int. J. Biol. Macromol.*, 122 (2019) 636-643.
- [230] D. Essassi, R. Zini, J.P. Tillement, Use of 1-anilino-8-naphthalene sulfonate as a fluorescent probe in the investigation of drug interactions with human alpha-1-acid glycoprotein and serum albumin, *J. Pharm. Sci.*, 79 (1990) 9-13.
- [231] E. Schönbrunn, S. Eschenburg, K. Luger, W. Kabsch, N. Amrhein, Structural basis for the interaction of the fluorescence probe 8-anilino-1-naphthalene sulfonate (ANS) with the antibiotic target MurA, *Proc. Natl. Acad. Sci.*, 97 (2000) 6345-6349.
- [232] O.K. Gasyimov, A.R. Abduragimov, B.J. Glasgow, Characterization of fluorescence of ANS-tear lipocalin complex: evidence for multiple-binding modes, *Photochem. Photobio.*, 83 (2007) 1405-1414.
- [233] F. Sánchez Rojas, C. Bosch Ojeda, Recent development in derivative ultraviolet/visible absorption spectrophotometry: 2004–2008: A review, *Anal. Chim. Acta*, 635 (2009) 22-44.
- [234] C. Bosch Ojeda, F. Sanchez Rojas, Recent applications in derivative ultraviolet/visible absorption spectrophotometry: 2009–2011: A review, *Microchem. J.*, 106 (2013) 1-16.
- [235] M.M. Sebaiy, S.M. El-Adl, A.A. Mattar, Different techniques for overlapped UV spectra resolution of some co-administered drugs with paracetamol in their combined pharmaceutical dosage forms, *Spectrochim. Acta A Mol. Biomol. Spectrosc.*, 224 (2020) 117429.
- [236] C.M. El-Maraghy, N.T. Lamie, Three smart spectrophotometric methods for resolution of severely overlapped binary mixture of Ibuprofen and Paracetamol in pharmaceutical dosage form, *BMC Chem.*, 13 (2019) 99.
- [237] L. Antonov, D. Nedeltcheva, Resolution of overlapping UV–Vis absorption bands and quantitative analysis, *Chem. Soc. Rev.*, 29 (2000) 217-227.
- [238] Y. Hu, W. Li, J. Hu, Resolving overlapped spectra with curve fitting, *Spectrochim. Acta A Mol Biomol. Spectrosc.*, 62 (2005) 16-21.
- [239] A.D. Hoppe, B.L. Scott, T.P. Welliver, S.W. Straight, J.A. Swanson, N-Way FRET Microscopy of Multiple Protein-Protein Interactions in Live Cells, *Plos One*, 8 (2013).
- [240] C.A. Stedmon, S. Markager, R. Bro, Tracing dissolved organic matter in aquatic environments using a new approach to fluorescence spectroscopy, *Mar. Chem.*, 82 (2003) 239-254.
- [241] L. Lenhardt, R. Bro, I. Zekovic, T. Dramicanin, M.D. Dramicanin, Fluorescence spectroscopy coupled with PARAFAC and PLS DA for characterization and classification of honey, *Food Chem.*, 175 (2015) 284-291.
- [242] J.B. Kruskal, Three-way arrays: Rank and uniqueness of trilinear decompositions, with application to arithmetic complexity and statistics, *Linear Algebra Appl.*, 18 (1977) 95–138.
- [243] A. de Juan, R. Tauler, Comparison of three-way resolution methods for non-trilinear chemical data sets, *J. Chemom.*, 15 (2001) 749-772.
- [244] Y. Akhlaghi, M. Kompany-Zareh, S. Ebrahimi, Model-based approaches to investigate the interactions between unmodified gold nanoparticles and DNA strands, *Sens. Actuator B-Chem.*, 221 (2015) 45-54.

- [245] Y. Akhlaghi, M. Kompany-Zareh, M.R. Hormozi-Nezhad, Multiway Investigation of Interaction between Fluorescence Labeled DNA Strands and Unmodified Gold Nanoparticles, *Anal. Chem.*, 84 (2012) 6603-6610.
- [246] M. Kompany-Zareh, S. Gholami, Soft and hard multiway FRET-based investigation of interaction between drug and QD labeled DNA, *Chemom. Intell. Lab. Syst.*, 139 (2014) 33-41.
- [247] A.G.R. Boyan Li, Similarity index: a rapid classification method for multivariate data arrays, in: U.S. Patent (Ed.), National University of Ireland Galway (NUI Galway), 2011, pp. 12.
- [248] T. Sen, S. Mandal, S. Haldar, K. Chattopadhyay, A. Patra, Interaction of Gold Nanoparticle with Human Serum Albumin (HSA) Protein Using Surface Energy Transfer, *J. Phys. Chem. C*, 115 (2011) 24037-24044.
- [249] D. Fuentealba, H. Kato, M. Nishijima, G. Fukuhara, T. Mori, Y. Inoue, C. Bohne, Explaining the Highly Enantiomeric Photocyclodimerization of 2-Anthracenecarboxylate Bound to Human Serum Albumin Using Time-Resolved Anisotropy Studies, *J. Am. Chem. Soc.*, 135 (2013) 203-209.
- [250] S. Zorrilla, G. Rivas, A.U. Acuna, M.P. Lillo, Protein self-association in crowded protein solutions: A time-resolved fluorescence polarization study, *Protein Sci.*, 13 (2004) 2960-2969.
- [251] F.N. Castellano, J.D. Dattelbaum, J.R. Lakowicz, Long-lifetime Ru(II) complexes as labeling reagents for sulfhydryl groups, *Anal. Biochem.*, 255 (1998) 165-170.
- [252] P. Sarkar, S.V. Koushik, S.S. Vogel, I. Gryczynski, Z. Gryczynski, Photophysical properties of Cerulean and Venus fluorescent proteins, *J. Biomed. Opt.*, 14 (2009) 034047-034047.
- [253] X. Shi, J. Basran, H.E. Seward, W. Childs, C.R. Bagshaw, S.G. Boxer, Anomalous Negative Fluorescence Anisotropy in Yellow Fluorescent Protein (YFP 10C): Quantitative Analysis of FRET in YFP Dimers, *Biochem.*, 46 (2007) 14403-14417.
- [254] Y. Casamayou-Boucau, A.G. Ryder, Accurate anisotropy recovery from fluorophore mixtures using Multivariate Curve Resolution (MCR), *Anal. Chim. Acta*, 1000 (2018) 132-143.
- [255] S. Khrapunov, N. Pastor, M. Brenowitz, Solution Structural Studies of the *Saccharomyces cerevisiae* TATA Binding Protein (TBP), *Biochem.*, 41 (2002) 9559-9571.
- [256] I.M. Vlasova, V.V. Zhuravleva, A.M. Saletsky, Denaturation of bovine serum albumin initiated by sodium dodecyl sulfate as monitored via the intrinsic fluorescence of the protein, *Russ. J. Phys. Chem. B*, 8 (2014) 385-390.
- [257] C. Berney, G. Danuser, FRET or No FRET: A Quantitative Comparison, *Biophys. J.*, 84 (2003) 3992-4010.
- [258] G.W. Gordon, G. Berry, X.H. Liang, B. Levine, B. Herman, Quantitative fluorescence resonance energy transfer measurements using fluorescence microscopy, *Biophys J*, 74 (1998) 2702-2713.
- [259] A. Akbarzadeh, R. Rezaei-Sadabady, S. Davaran, S.W. Joo, N. Zarghami, Y. Hanifehpour, M. Samiei, M. Kouhi, K. Nejati-Koshki, Liposome: classification, preparation, and applications, *Nanoscale Res. Lett.*, 8 (2013) 102-102.
- [260] P. Aggarwal, J.B. Hall, C.B. McLeland, M.A. Dobrovolskaia, S.E. McNeil, Nanoparticle interaction with plasma proteins as it relates to particle biodistribution, biocompatibility and therapeutic efficacy, *Adv. Drug Delivery Rev.*, 61 (2009) 428-437.

- [261] S.C. Semple, A. Chonn, P.R. Cullis, Interactions of liposomes and lipid-based carrier systems with blood proteins: Relation to clearance behaviour in vivo, *Adv. Drug Delivery Rev.*, 32 (1998) 3-17.
- [262] T. Ishida, H. Harashima, H. Kiwada, Liposome Clearance, *Biosci. Rep.*, 22 (2002) 197-224.
- [263] M. Gekle, Renal tubule albumin transport, *Annu. Rev. Physiol.*, 67 (2005) 573-594.
- [264] A. Tojo, S. Kinugasa, Mechanisms of Glomerular Albumin Filtration and Tubular Reabsorption, *Inter. J. Nephrol.*, 2012 (2012) 481520.
- [265] M. Anderson, A. Omri, The Effect of Different Lipid Components on the In Vitro Stability and Release Kinetics of Liposome Formulations, *Drug Delivery*, 11 (2004) 33-39.
- [266] V. Weissig, *Liposomes*, 1 ed., Humana Press, 2010.
- [267] W. Yan, L. Huang, The effects of salt on the physicochemical properties and immunogenicity of protein based vaccine formulated in cationic liposome, *Int. J. Pharm.*, 368 (2009) 56-62.
- [268] S.K. Kandasamy, R.G. Larson, Effect of salt on the interactions of antimicrobial peptides with zwitterionic lipid bilayers, *Biochim. Biophys. Acta*, 1758 (2006) 1274-1284.
- [269] V.S. Stoll, J.S. Blanchard, Buffers: principles and practice, *Methods Enzymol.*, 182 (1990) 24-38.
- [270] W. Kunz, J. Henle, B.W. Ninham, 'Zur Lehre von der Wirkung der Salze' (about the science of the effect of salts): Franz Hofmeister's historical papers, *Curr. Opin. Colloid & Interface Sci.*, 9 (2004) 19-37.
- [271] T.J. Zbacnik, R.E. Holcomb, D.S. Katayama, B.M. Murphy, R.W. Payne, R.C. Cocco, G.J. Evans, J.E. Matsuura, C.S. Henry, M.C. Manning, Role of Buffers in Protein Formulations, *J. Pharm. Sci.*, 106 (2017) 713-733.
- [272] G. Pabst, A. Hodzic, J. Štrancar, S. Danner, M. Rappolt, P. Laggnier, Rigidity of Neutral Lipid Bilayers in the Presence of Salts, *Biophys. J.*, 93 (2007) 2688-2696.
- [273] R.A. Böckmann, A. Hac, T. Heimburg, H. Grubmüller, Effect of sodium chloride on a lipid bilayer, *Biophys. J.*, 85 (2003) 1647-1655.
- [274] J. Dufourcq, J.-F. Faucon, Intrinsic fluorescence study of lipid-protein interactions in membrane models. Binding of melittin, an amphipathic peptide, to phospholipid vesicles, *Biochim. Biophys. Acta Biomembr.*, 467 (1977) 1-11.
- [275] C.A. Kraft, J.L. Garrido, L. Leiva-Vega, G. Romero, Quantitative analysis of protein-lipid interactions using tryptophan fluorescence, *Sci. Signal*, 2 (2009) p14.
- [276] H.I. Petrache, S. Tristram-Nagle, D. Harries, N. Kucerka, J.F. Nagle, V.A. Parsegian, Swelling of phospholipids by monovalent salt, *J. Lipid Res.*, 47 (2006) 302-309.
- [277] M. Danaei, M. Dehghankhold, S. Ataei, F. Hasanzadeh Davarani, R. Javanmard, A. Dokhani, S. Khorasani, M.R. Mozafari, Impact of Particle Size and Polydispersity Index on the Clinical Applications of Lipidic Nanocarrier Systems, *Pharmaceutics*, 10 (2018) 57.
- [278] V.A. Parsegian, B.W. Ninham, Application of the Lifshitz Theory to the Calculation of Van der Waals Forces across Thin Lipid Films, *Nature*, 224 (1969) 1197-1198.
- [279] M. Mozafari, E. Mazaheri, K. Dormiani, Simple Equations Pertaining to the Particle Number and Surface Area of Metallic, Polymeric, Lipidic and Vesicular Nanocarriers, *Sci. Pharm.*, 89 (2021) 15.

- [280] N.A. Kim, I.B. An, D.G. Lim, J.Y. Lim, S.Y. Lee, W.S. Shim, N.G. Kang, S.H. Jeong, Effects of pH and buffer concentration on the thermal stability of etanercept using DSC and DLS, *Biol. Pharm. Bull.*, 37 (2014) 808-816.
- [281] P. Taboada, S. Barbosa, E. Castro, V. Mosquera, Amyloid Fibril Formation and Other Aggregate Species Formed by Human Serum Albumin Association, *J. Phys. Chem. B*, 110 (2006) 20733-20736.
- [282] A. Chubarov, A. Spitsyna, O. Krumkacheva, D. Mitin, D. Suvorov, V. Tormyshev, M. Fedin, M.K. Bowman, E. Bagryanskaya, Reversible Dimerization of Human Serum Albumin, *Molecules*, 26 (2020).
- [283] D.M. Togashi, A.G. Ryder, G. Heiss, Quantifying adsorbed protein on surfaces using confocal fluorescence microscopy, *Colloids Surf. B*, 72 (2009) 219-229.
- [284] Y. Xia, J. Sun, D. Liang, Aggregation, fusion, and leakage of liposomes induced by peptides, *Langmuir*, 30 (2014) 7334-7342.
- [285] C. Corbo, R. Molinaro, F. Taraballi, N.E. Toledano Furman, M.B. Sherman, A. Parodi, F. Salvatore, E. Tasciotti, Effects of the protein corona on liposome-liposome and liposome-cell interactions, *Inter. J. Nanomedicine*, 11 (2016) 3049-3063.
- [286] F. Giulimondi, L. Digiacomo, D. Pozzi, S. Palchetti, E. Vulpis, A.L. Capriotti, R.Z. Chiozzi, A. Laganà, H. Amenitsch, L. Masuelli, G. Peruzzi, M. Mahmoudi, I. Screpanti, A. Zingoni, G. Caracciolo, Interplay of protein corona and immune cells controls blood residency of liposomes, *Nature Comm.*, 10 (2019) 3686.
- [287] V. Džupponová, G. Žoldák, Salt-dependent passive adsorption of IgG1 κ -type monoclonal antibodies on hydrophobic microparticles, *Biophys. Chem.*, 275 (2021) 106609.
- [288] S.A. Johnstone, D. Masin, L. Mayer, M.B. Bally, Surface-associated serum proteins inhibit the uptake of phosphatidylserine and poly(ethylene glycol) liposomes by mouse macrophages, *Biochim. Biophys. Acta Biomembr.*, 1513 (2001) 25-37.
- [289] C. Sweet, J.E. Zull, Activation of glucose diffusion from egg lecithin liquid crystals by serum albumin, *Biochim. Biophys. Acta*, 173 (1969) 94-103.
- [290] S.L. Law, W.Y. Lo, S.H. Pai, G.W. Teh, F.Y. Kou, The adsorption of bovine serum albumin by liposomes, *Int. J. Pharm.*, 32 (1986) 237-241.
- [291] R.L. Juliano, H.K. Kimelberg, D. Papahadjopoulos, Synergistic effects of a membrane protein (spectrin) and Ca²⁺ on the Na⁺ permeability of phospholipid vesicles, *Biochim. Biophys. Acta*, 241 (1971) 894-905.
- [292] K. Hoekstra, J. van Renswoude, R. Tomasini, G. Scherphof, Interaction of phospholipid vesicles with rat hepatocytes: further characterization of vesicle-cell surface interaction; use of serum as a physiological modulator, *Membr. Biochem.*, 4 (1981) 129-147.
- [293] L.J. Lis, J.W. Kauffman, D.F. Shriver, Raman spectroscopic detection and examination of the interaction of amino acids, polypeptides and proteins with the phosphatidylcholine lamellar structure, *Biochim. Biophys. Acta Biomembr.*, 436 (1976) 513-522.
- [294] A. Kyrychenko, Using fluorescence for studies of biological membranes: a review, *Methods Appl. Fluoresc.*, 3 (2015) 042003.
- [295] E.C. Jensen, Use of Fluorescent Probes: Their Effect on Cell Biology and Limitations, *The Anatomical Record*, 295 (2012) 2031-2036.
- [296] Andrey S. Klymchenko, R. Kreder, Fluorescent Probes for Lipid Rafts: From Model Membranes to Living Cells, *Chemistry & Biology*, 21 (2014) 97-113.
- [297] B. Christiaens, S. Symoens, S. Verheyden, Y. Engelborghs, A. Joliot, A. Prochiantz, J. Vandekerckhove, M. Rosseneu, B. Vanloo, Tryptophan fluorescence

- study of the interaction of penetratin peptides with model membranes, *Eur. J. Biochem.*, 269 (2002) 2918-2926.
- [298] Y. Chen, M.D. Barkley, Toward Understanding Tryptophan Fluorescence in Proteins, *Biochem.*, 37 (1998) 9976-9982.
- [299] R. Thakur, A. Das, A. Chakraborty, Interaction of human serum albumin with liposomes of saturated and unsaturated lipids with different phase transition temperatures: a spectroscopic investigation by membrane probe PRODAN, *RSC Adv.*, 4 (2014) 14335-14347.
- [300] D. Toptygin, R.S. Savtchenko, N.D. Meadow, S. Roseman, L. Brand, Effect of the Solvent Refractive Index on the Excited-State Lifetime of a Single Tryptophan Residue in a Protein, *J. Phys. Chem. B*, 106 (2002) 3724-3734.
- [301] C.P. Pan, P.L. Muiño, M.D. Barkley, P.R. Callis, Correlation of tryptophan fluorescence spectral shifts and lifetimes arising directly from heterogeneous environment, *J. Phys. Chem. B*, 115 (2011) 3245-3253.
- [302] M.M. Elmer-Dixon, B.E. Bowler, Rapid quantification of cardiolipin and DOPC lipid and vesicle concentration, *Anal. Biochem.*, 520 (2017) 58-61.
- [303] G. Dorrington, N.P. Chmel, S.R. Norton, A.M. Wemyss, K. Lloyd, D. Praveen Amarasinghe, A. Rodger, Light scattering corrections to linear dichroism spectroscopy for liposomes in shear flow using calcein fluorescence and modified Rayleigh-Gans-Debye-Mie scattering, *Biophys. Rev.*, 10 (2018) 1385-1399.
- [304] S. Chalk, L. McEwen, *The IUPAC Gold Book*, Chemistry International, 39 (2017).
- [305] W.C. Mundy, J.A. Roux, A.M. Smith, Mie scattering by spheres in an absorbing medium*, *J. Opt. Soc. Am.*, 64 (1974) 1593-1597.
- [306] R. Gesztelyi, J. Zsuga, A. Kemeny-Beke, B. Varga, B. Juhasz, A. Tosaki, The Hill equation and the origin of quantitative pharmacology, *Archive for History of Exact Sciences*, 66 (2012) 427-438.
- [307] M. Ameloot, M. vandeVen, A.U. Acuna, B. Valeur, Fluorescence anisotropy measurements in solution: Methods and reference materials (IUPAC Technical Report), *Pure Appl. Chem.*, 85 (2013) 589-608.
- [308] K.S. Babu, J.K. Amamcharla, Application of front-face fluorescence spectroscopy as a tool for monitoring changes in milk protein concentrate powders during storage, *J. Dairy Sci.*, 101 (2018) 10844-10859.
- [309] S. Mounier, R. Redon, G. Nicolodelli, D. Milori, Front-face fluorescence spectroscopy of tryptophan and fluorescein using laser induced fluorescence and excitation emission matrix fluorescence, *RSC Adv.*, 7 (2017) 56117-56122.

PUBLICATIONS AND RESEARCH PRESENTATIONS

Peer-reviewed publications

- F. Gordon, Y. Casamayou-Boucau, A.G. Ryder, Evaluating the interaction of human serum albumin (HSA) and 1,2-dimyristoyl-sn-glycero-3-phosphocholine (DMPC) liposomes in different aqueous environments using Anisotropy Resolved Multi-Dimensional Emission Spectroscopy (ARMES), *Colloids Surf. B*, *In revision Oct. 2021*.
- F. Gordon, S. Elcoroaristizabal, A.G. Ryder, Modelling Förster resonance energy transfer (FRET) using anisotropy resolved multi-dimensional emission spectroscopy (ARMES), *Biochim. Biophys. Acta Gen. Subj.*, 1865 (2021) 129770. (DOI: [10.1016/j.bbagen.2020.129770](https://doi.org/10.1016/j.bbagen.2020.129770))
- M. Prokopowicz, A. Jarmuła, Y. Casamayou-Boucau, F. Gordon, A. Ryder, J. Sobich, P. Maj, J. Cieśla, Z. Zieliński, P. Fita, W. Rode, Advanced Spectroscopy and APBS Modeling for Determination of the Role of His190 and Trp103 in Mouse Thymidylate Synthase Interaction with selected dUMP Analogues, *Int. J. Mol. Sci.*, 22 (2021) 2661. (DOI: [10.3390/ijms22052661](https://doi.org/10.3390/ijms22052661))

International presentations

- Oral presentation- Platform talk: “Anisotropy Resolved Multidimensional Emission Spectroscopy (ARMES) for chemometric modelling to study Förster Resonance Energy Transfer (FRET) processes”, F. Gordon, S. Elcoroaristizabal, A.G. Ryder. 64th Biophysical Society Annual Meeting, San Diego, **USA**, 15-19 February **2020**.
- Poster presentation: " Using Anisotropy Resolved Multidimensional Emission Spectroscopy (ARMES) and PARAFAC chemometric modelling to study energy transfer from HSA intrinsic fluorescence upon addition of 1,8-ANS”, F. Gordon, S. Elcoroaristizabal, A.G. Ryder. Joint 12th EBSA 10th ICBP-IUPAP Biophysics Congress, Madrid, **Spain**, 20-24 July **2019**.

National presentations

- Oral presentation: “ARMES as a tool for biophysical analysis”, F. Gordon and A.G. Ryder, Eli Lilly Postgraduate Prize 2020 (3rd prize), Galway, **Ireland**, 1st

July 2021 (https://www.linkedin.com/posts/alan-ryder-31a0639_research-science-phd-activity-6817728657604317184-TIUg).

- Oral presentation: “ARMES as a tool for biophysical analysis”, F. Gordon and A.G. Ryder, BOC Gases Postgraduate Prize 2020 (1st prize), Galway, **Ireland**, 6th July 2021 (https://www.linkedin.com/posts/alan-ryder-31a0639_research-science-phd-activity-6820644317737074688-utr5).
- Oral presentation (*Eurachem 1st prize for overall best oral presentation*): “Modelling Förster Resonance Energy Transfer (FRET) using Anisotropy Resolved Multi-Dimensional Emission Spectroscopy (ARMES)”, F. Gordon, S. Elcoroaristizabal, and A.G. Ryder. ICI Postgraduate Chemistry Research Symposium, **online** conference held on Zoom (*due to COVID-19*), 9th Sept. 2020.
- Oral presentation: "Anisotropy Resolved Multidimensional Emission Spectroscopy (ARMES) for modelling FRET processes”, F. Gordon, S. Elcoroaristizabal, and A.G. Ryder. Chemistry Research Day 2019, Dillion Theatre NUI Galway, **Ireland**, 17th January 2020.
- Poster presentation: " Using Anisotropy Resolved Multidimensional Emission Spectroscopy (ARMES) and PARAFAC chemometric modelling to study energy transfer from HSA intrinsic fluorescence upon addition of 1,8-ANS”, F. Gordon, S. Elcoroaristizabal, A.G. Ryder, *Chemistry Research Day 2019*, NUI Galway, Galway, **Ireland**, 9th January 2019.
- Oral presentation: “Fluorescence Spectroscopy for the analysis of Protein Therapeutics”, *Threesis competition 2018*, NUI Galway, Galway, **Ireland**, 5th Oct 2018.
- Oral presentation: "Anisotropy Resolved Multidimensional Emission Spectroscopy (ARMES) for the photo-physical analysis of proteins”, F. Gordon and A.G. Ryder. Chemistry Research Day 2019, NCBES Seminar room, NUI Galway, **Ireland**, 24th April 2018.

Travel Awards

- Awarded a *Researcher Mobility Grant* from the RSC (to the value of £3000) to undertake a 2-month research visit to the Physics of Life Group at the

University of York, in collaboration with Dr. Steven Quinn. *Grant no.: MP19-0529 (Unable to complete due to COVID-19 travel restrictions).*

- Awarded an *Overseas Conference Travel Award* (to the value of £750) from the Analytical Chemistry Trust Fund of the RSC to attend the 64th Biophysical Society Meeting in San Diego, USA.

Research Visits

- Completed a 3-day research visit to the Physics of Life Group in the University of York, in preparation for the proposed 2-month visit.